University of Nevada, Reno

Controlling Electrocatalytic Interfaces using Thin Films and Nanostructures for Energy Applications

A dissertation submitted in partial fulfillment of the requirements for the degree of Doctor of Philosophy in Chemistry

by

Rajendra Prasad Gautam

Dr. Christopher J. Barile/Dissertation Advisor

May, 2022

THE GRADUATE SCHOOL

We recommend that the dissertation
prepared under our supervision by

entitled

be accepted in partial fulfillment of the
requirements for the degree of

Advisor

Committee Member

Committee Member

Committee Member

Graduate School Representative

David W. Zeh, Ph.D., Dean
Graduate School

Abstract

The release of greenhouse gases such as CO_2 due to various human activities and the use of fossil fuels causes climate change and increases global temperature. For this reason, we must create new technologies that help shift energy production away from fossil fuels to renewable energy sources. Over the past few decades, researchers in academia and industry have focused on developing novel techniques for clean and renewable energy, which could in part be mediated by H_2 fuel cells. The oxygen reduction reaction (ORR) occurs at the cathode of fuel cells and is the rate-limiting reaction. Water can be electrolyzed using electricity from renewable sources to generate H_2 in a green manner. The oxygen evolution reaction (OER) is the rate-limiting reaction for water electrolysis. Unfortunately, catalysts based on Pt and Ir have the best performance for the ORR and OER, respectively. However, the widespread application of these catalysts is limited because of the high cost and scarcity of Pt- and Ir-based catalysts. Non-precious metal catalysts such as those based on Cu and Ni are promising alternatives.

In this dissertation, I have developed a new electrochemical platform that allows for the study of the control of electron and proton transfer in the ORR. Specifically, I use Cu as one of the non-precious metal catalysts to study the ORR. I prepared a dinuclear Cu ORR catalyst that can be covalently attached to thiol-based self-assembled monolayers (SAMs) on Au electrodes using azide-alkyne click chemistry. Using this architecture, the electron transfer rate to the catalyst is modulated by changing the length of the SAM, and the proton transfer rate to the catalyst is controlled with an appended lipid membrane modified with proton carriers. By tuning the relative rates of proton and electron transfer,

the current density of the lipid-covered catalyst was enhanced significantly without altering its core molecular structure. Also, I utilized designer small-molecule proton carriers bearing nitrile functional groups that mimic naturally occurring protonophores. These bio-inspired CN-based proton carriers with tailorable proton kinetics were used to turn on the ORR activity of a Cu-based non-precious metal electrocatalyst supported on a modular hybrid bilayer membrane platform under alkaline conditions.

In addition, I designed and developed OER electrocatalysts using non-precious metals for energy conversion and storage processes. Hydrogen gas is an alternative fuel that is produced from the electrolysis of water, but technical challenges have heretofore limited the efficiency of water electrolyzers. In order for hydrogen gas to achieve widespread use, it is critical to develop electrocatalysts for the OER that are more cost-effective and widely available than the current state of the art. Thus, I prepared bimetallic electrocatalysts based on Ni and Cu for the OER. I used thin films of Cu_2O modified with an overlayer of Ni to construct novel electrocatalysts and determined the optimal ratio of Ni to cuprous oxide for performing the OER in alkaline conditions by tuning the amount of Ni electrodeposited on the Cu_2O. Moreover, I developed nanostructured Ni-Cu systems by synthesizing both metallic and bimetallic Ni-Cu nanoclusters and nanoparticles. I found that, for both nanoclusters and nanoparticles, the ratio of Ni to Cu is highly associated with OER electrocatalysis efficiency.

Furthermore**,** I modified carbon electrodes using different compositions of alkyl amine SAMs with various chain lengths and diluent ratios. I investigated the role of defect sites in the SAMs to understand the electron-transfer properties of the appended ferrocene molecules by modifying the SAMs with ZnO electrodeposits. Interestingly, I found that

there is a significant change in the electron-transfer rates as a function of SAM linker length when the SAM defect sites are blocked with ZnO electrodeposits. The surface modification protocols used in this study are important in a wide range of applications such as energy catalysis, electroanalysis, and biosensors.

Acknowledgments

My Ph. D. journey would not have been completed without significant input from many people. It would not be possible without love, support, motivation, encouragement, and kindness of many individuals around me. First and foremost, I would like to express my sincere gratitude to my academic advisor, Dr. Christopher J. Barile, for his valuable guidance, suggestions, and encouragement over the years. His support, guidance, encouragement, and assistance always have been of immense value, and he will remain as an inspiration to me throughout my life.

I would also like to extend my deepest sense of gratitude to my advisory committee members, Dr. Sean M. Casey, Dr. Mario A. Alpuche, Dr. Vaidyanathan (Ravi) Subramanian, and Dr. David Cantu for their valuable time, support, encouragement, insights, and suggestions.

I am grateful to Department of Chemistry, University of Nevada, Reno (UNR) for providing me a teaching assistantship. I would also like to express my sincere thanks to all faculty and staff of the Department of Chemistry, UNR for their support and co-operation. I am also thankful to all past and present members of Barile Research group for their help, support, and encouragement during my study in UNR. I would like to thank Dr. Shakirul Islam and Jason Mennel for their support and motivation.

The work performed in this dissertation could not have been accomplished without the help of my co-authors, which include Yi Teng Lee, Gabriel L. Herman, Cynthia M. Moreno, Hanqing Pan, Farzaneh Chalyavi, Alexis A. Palma, Tian Zeng.

I would like to acknowledge our collaborators Dr. Edmund C. M. Tse, Dr. Ying Li, and Dr. Mathew J. Tucker. The work done in this dissertation was supported by Research and Innovation at the UNR, American Chemical Society Petroleum Research Fund (ACS PRF), National Science Foundation (NSF), National Institute of Health (NIH), Hong Kong (HK) Research Grants Council (RGC), EU/RGC Co-Funding Mechanism (RGC: E-HKU704/19).

Also, I would like to acknowledge J. Desormeau for his kind assistance in SEM-EDS analysis which was performed in the Mackay Microbeam Laboratory at the UNR. I would also like to acknowledge Dr. Stephen Spain for his assistance to operate some instruments in the Shared Instrumentation Laboratory in the Department of Chemistry at the UNR.

Lastly, I have received unmeasurable support from people outside my academic community. I would like to remember my late parents, Chandra kala and Tanka Prasad Gautam, who were my role model and I have no words how I missed them. I would like to express my gratitude to my brothers (Nanda and Shasidhar) , sisters (Man Kumari and Devi) , and in-laws (Shiva and Gita Sharma) for their motivation and support throughout the entire period of my life. I would also like to thank all my teachers, and friends for their support.

I would like to express my deep love to my daughter Rajasi Gautam and son Reyansh Gautam. Their smile and funny words made me to forget all the stress and help to remain calm and productive. Finally, I am thankful to the love of my life, Sanjeeta Sharma Gautam, for her continuous love, support, encouragement, and sacrifice.

Table of Contents

List of Tables

List of Figures

Chapter 1: Introduction

1.1. Energy Demand, Production and Storage

Energy is one of the most important concerns of the twenty-first century due to increasing global energy demand and the rapid depletion of fossil fuels.[1-2] In addition to adverse effects on human health due to air pollution, the use of fossil fuels such as coal, oil, and natural gas with an increase in emissions of greenhouse gases such as CO_2 has an adverse impact on the Earth's environment due to global warming, sea level rise, and rapidly changing climate.[3-5] The current level of CO_2 in the Earth's atmosphere has increased abruptly after the industrial revolution in the mid-1700s. The CO_2 level in the atmosphere is nearly 413 parts per million (ppm), which is about 130 ppm greater compared to the pre-industrial era. If fossil fuels continued to be burned at their current rate, the level of CO_2 will exceed 1500 ppm in a few centuries.[5-6] This increase in CO_2 will result in a further increase in the global temperature, melting of polar ice caps, and a huge portion of land on the earth will go below sea level.[7]

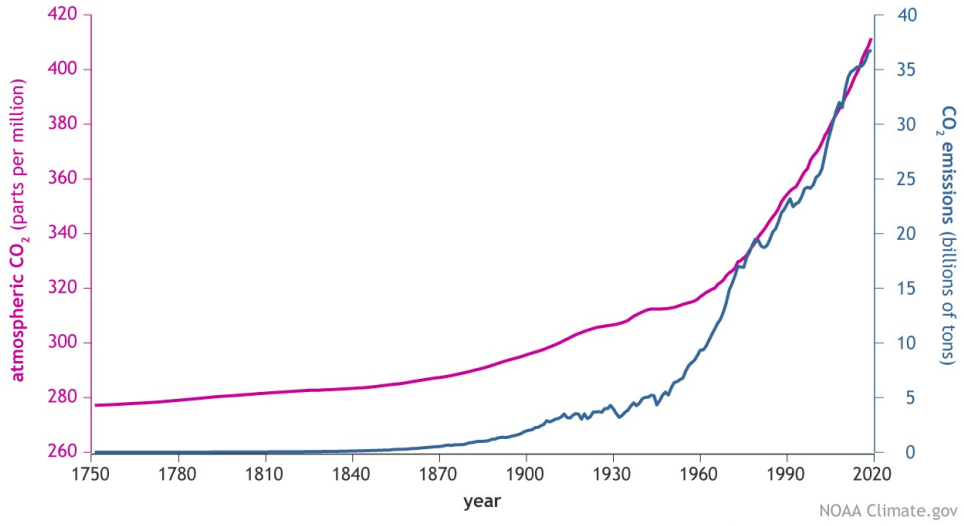

Figure 1.1. CO_2 emissions and concentrations[5]

The electrification of vehicles and a shift to renewable energy sources, such as solar and wind, for electricity production, can play a huge role in solving the global CO_2 emission problem.[1] Renewable energy sources like windmills and solar cells are non-continuous and therefore there is a need for an efficient energy storage solution. H_2 gas can be used as an energy carrier in energy converting/storage systems such as fuel cells. Rechargeable grid-scale batteries are another technology that could play a vital role in overcoming the intermittent nature of solar and wind energy.[8,9]

Figure 1.2. Global electric car registrations and automobile market share[10]

1.2. Fuel Cells

Due to the rapid increase in population growth worldwide and depletion of carbonaceous fuels, the demand for clean, renewable, and sustainable energy increases day

by day.[11] Over the past few decades, researchers have focused on developing novel techniques for clean and renewable energy, which could in part be mediated by H_2 fuel cells. Fuel cells are electrochemical devices that convert chemical energy into electrical energy by the use of fuels such as methanol.[9] In fuel cells, the two electrodes are separated by a thin membrane or some other electrolyte and contain the catalyst materials necessary for the oxidation and reduction reaction.[12,13]

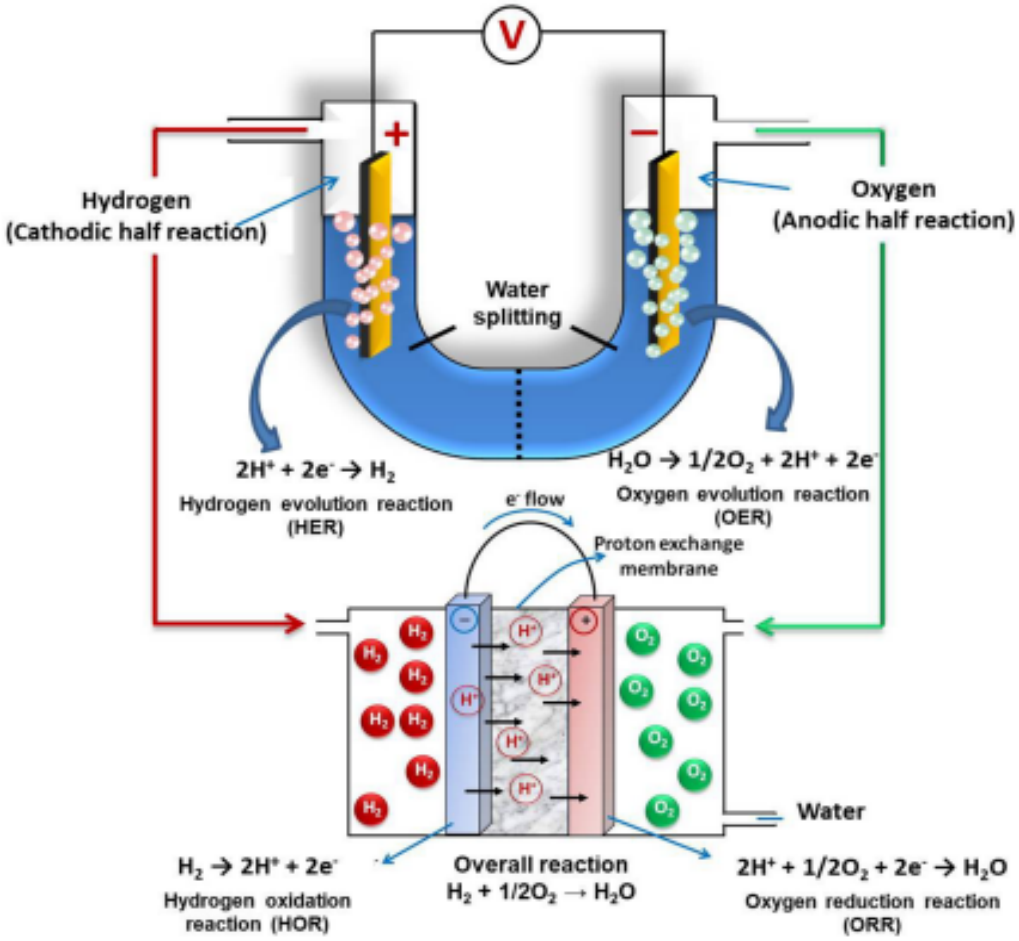

Figure 1.3. Schematic representation of the oxygen reduction reaction in a fuel cell and the oxygen evolution and hydrogen evolution reactions for water splitting[14]

In a fuel cell, generally H_2 is used as fuel. However, methanol, ethanol, formic acid, and phosphoric acid have also been used in fuel cells. Recently, fuel cells have been gaining much attention because the thermodynamic efficiency of fuel cells is not limited by the Carnot cycle, which is the case with an internal combustion engine. However, the efficiency of the fuel cell is directly related to the overpotential. The overpotential is the potential difference between the experimental and thermodynamic potential of the half-reactions occurring at each electrode.

The thermodynamic efficiency of fuel cells has been as high as 90%, but the burning of H_2 in an internal combustion engine typically results in efficiencies around 10-20%.[13] However, it is hard to achieve such a high efficiency in fuel cells in practice. Current state-of-the-art fuel cells used in vehicles achieve efficiencies close to 60% that do not account for losses that occur when preparing and storing H_2.

1.3. Non-precious Metal Catalysts for O_2 Reduction Reaction

The oxygen reduction reaction (ORR) occurs at the cathode of fuel cells and is the rate-limiting reaction in fuel cells. The ORR is a complex multi-step reaction with various numbers of electrons and protons involved.[15-16] The ORR can occur through competing pathways to produce O_2^- , H_2O_2, and H_2O. The production of undesired products such as O_2^- and H_2O_2 degrade the catalyst, so it is very important to develop a catalyst that produces the desired product H_2O.[2,17,18]

Precious metals such as Pt are used as catalysts in both of the electrodes in a fuel cell. These Pt-based catalysts have the best performance for the ORR.[13,19,20] However, the widespread application of fuel cells is limited because of the high cost, less-than-ideal stability, and high overpotential of Pt-based catalysts.[21,22] As Pt is the best catalyst for

ORR, different strategies have been adopted to reduce the amount of Pt used. Some strategies include fabricating Pt alloys with other non-precious metals such as Ni, Co, Mn, and Fe.[13,23] Incorporating these non-precious metals improves the ORR activity, showing the beneficial effect of doping the Pt lattice. The cost of fuel cell vehicles would be substantially reduced and become easily accessible to the public if chemists develop a highly active and stable ORR catalyst that does not require or contain any precious metals such as Pt. Recently, non-precious metal catalysts such as those based on Cu have been explored as a promising alternative for ORR.[2,12,24,25]

Much effort has been devoted to developing novel electrocatalysts for the ORR, which is inspired by biological enzymes such as laccase[24,25] and cytochrome c oxidase.[26] Cytochrome c oxidase catalyzes the ORR and contains the non-precious metals Fe and Cu in its active site. Laccase is another biological enzyme that catalyzes the ORR. The laccase contains three Cu atoms in its active site. It has been observed that the laccase catalyzes the ORR with smaller overpotentials as Pt.[27] However, the fuel cells developed using laccase-decorated electrodes suffer from low power densites[28] as these enzymes are much larger than Pt atoms. As such, there is a need to develop better ORR catalysts to address this problem.

One of the approaches to overcome this problem is to design and prepare more cost-effective small-molecule catalysts containing non-precious metals that mimic the active site of laccase or cytochrome c oxidase.[17,18,23] The search for active and durable ORR catalysts that contain non-precious metals such as Cu, Fe, Mn, Co, and Ni started with the discovery of the ORR activity of transition metal phthalocyanines.[29,30] Since then, a lot of non-precious metal catalysts have been explored, such as those containing metal

porphyrins,[31] N-containing heterocycles,[25] doped carbon nanotubes,[32] and N-rich polymers as precursors.[16] Researchers have explored many different synthetic ways to prepare non-precious metal catalysts for the ORR. However, significant improvement in catalyst performance has been hindered by a lack of understanding of the mechanistic details of this reaction.

Recently, the Barile group developed a novel electrochemical platform in which the kinetics of proton and electron transfer can be quantitatively controlled to a molecular electrocatalyst. The electrodes utilize self-assembled monolayers to alter electron transfer rates and lipid monolayers with proton carriers to modulate proton transfer rates. By tuning the relative rates of proton and electron transfer, we demonstrate enhanced catalytic activity of a Cu-diaminotriazole catalyst for the ORR.

1.4. Non-precious Metal Catalysts for O_2 Evolution Reaction

H_2 gas is considered a promising alternative fuel that can be produced in a clean and renewable manner from water electrolysis if the electricity utilized comes from renewable resources such as solar energy.[33,34] Currently, H_2 production primarily relies on fossil fuels such as natural gas, oil, and coal. Currently, 48% of H_2 production comes from natural gas, 30% comes from oil, and 18% comes from coal. Only a very small fraction of total H_2 production (4%) comes from the electrolysis of water.[33-35] To generate H_2 in a clean and renewable manner, water can be electrolyzed using electricity from renewable sources.

Electrochemical water splitting consists of the oxygen evolution reaction (OER) at the anode and the H_2 evolution reaction (HER) at the cathode. The OER is the rate-limiting reaction for water electrolysis.[36,37] Catalysts based on Ru and Ir have the best performance for the OER. However, the widespread application of these catalysts is limited because of

the high cost and scarcity of these two precious metals.[38,39]. Non-precious metal catalysts such as those based on Ni, Fe, Co, and Mn are promising alternatives. Ni-based compounds have been known as active OER catalysts since the last century.[40,41]

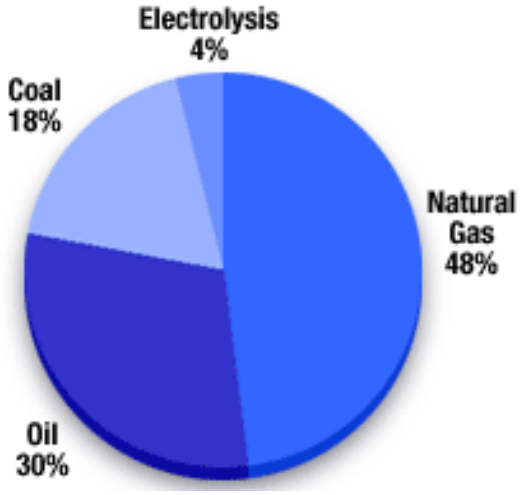

Figure 1.4. Resources used for global H_2 production[42]

A tremendous amount of effort has been invested in attempts to prepare active and stable Ni-based catalysts for the OER. Specifically, Ni-based materials such as Ni-based phosphides,[40,43] NiFe alloys,[44] NiFe oxides,[45] NiFe layered double hydroxides,[46] bimetallic Ni-Mn compounds, Ni-Co compounds,[47] Ni oxides, and hydroxides have been used for water splitting in alkaline media.[48]

Metals are always some of the first candidates for catalysis. Mainly, transition metal oxides catalysts have been known to be active catalysts for OER for a long time.[49,50] A great deal of research efforts has been devoted to improving the performance of these catalysts. The transition metal oxides are excellent candidates for OER due to their multivalent oxidation states. The OER activities of these metal oxides depend on their

morphology, composition, and d electron count. These catalysts can be cost-effective and possess good corrosion resistance.[51]

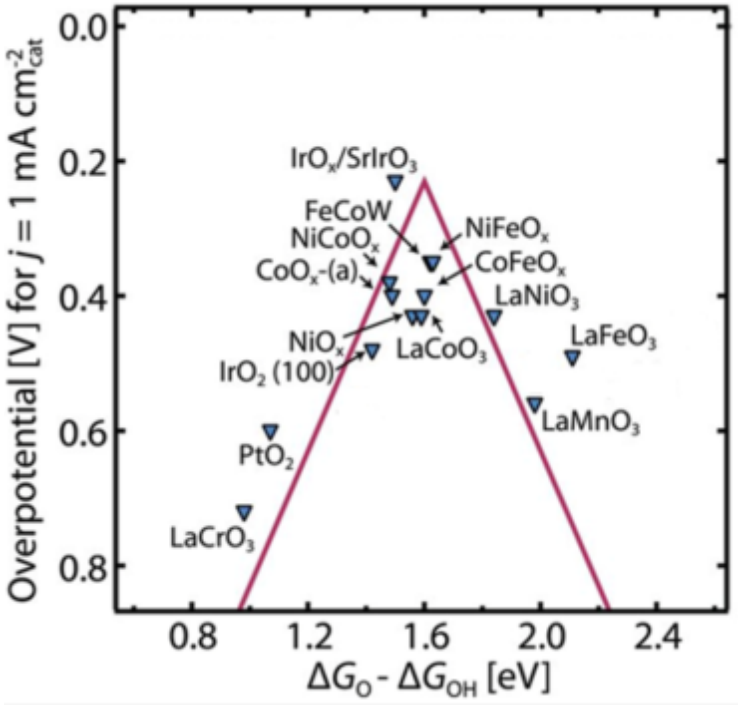

Figure 1.5. Volcano plot of transition metal oxides for OER[52]

A large amount of effort has been devoted to substituting precious metal catalysts with non-precious metal catalysts. Figure 1.5 is a volcano plot of some transition metal oxide catalysts for the OER, in which the optimal catalysts are at the peak of the volcano. Specifically, the transition metals such as NiO_x, CoO_x, and FeO_x are considered potential OER catalysts, but they are not stable in acidic media. NiO_x, however, is stable under alkaline conditions. Therefore, NiO and related transition metal oxides are among the most promising OER catalysts.

Recently, the Barile group developed novel OER electrocatalysts based on Ni and Cu. These catalysts were synthesized via the electrodeposition of Ni and Cu_2O on tin-doped indium oxide (ITO) substrate. Furthermore, in search of inexpensive catalysts for the OER

in alkaline media, we designed and developed nanostructured Ni and Cu systems. These catalysts exhibited superior performance for the OER in basic media.

1.5. Chapter Overview

This dissertation includes the following five chapters that describe each of the author's five papers published in different journals.

Chapter 2, entitled "Controlling Proton and Electron Transfer Rates to Enhance the Activity of an Oxygen Reduction Electrocatalyst," was published in ***Angewandte Chemie***, **2018**.[20] In this work, we prepared a catalyst consisting of a Cu complex of benzyl triazole alkyne by covalently attaching it to a Au electrode with differing chain lengths of thiol-linked self-assembled monolayers (SAMs). We used phospholipid 1,2-dimyristoyl-sn-glycerol-3-phosphocholine to form a thin film held to the SAM catalyst with weak Van der Waals interactions. These interactions allowed for the completion of the electrode architecture by appending a lipid monolayer with 1-dodecylboronic acid as a proton carrier to the top of the SAM. This novel architecture modulates the electron transfer rate to a given catalyst by altering the length of the SAM and controls the proton transfer rate to the catalyst by appending a lipid membrane modified with proton carriers. This electrochemical platform allows for the identification of the optimal kinetic and thermodynamic parameters for ORR catalysts.

Chapter 3, entitled "Nitrile-Facilitated Proton Transfer for Enhanced Oxygen Reduction by Hybrid Electrocatalysts," was published in ***ACS Catalysis***, **2021**.[21] In this research work, we synthesized proton carriers with nitrile groups that can be found in protonophores. These bioinspired proton carriers can enable transmembrane proton delivery to a hybrid bilayer membrane (HBM)-supported Cu oxygen reduction reaction

electrocatalyst under basic conditions. HBM is an electrochemical platform in which a lipid layer is appended on top of SAMs covalently attached to the substrate. The stimuli-responsive proton regulators switch on the activity of the oxygen reduction reaction electrocatalyst. This work explores how proton transfer kinetics control the performance of electrocatalysts for clean and renewable energy converting systems.

Chapter 4, entitled "Nanostructured Ni-Cu Electrocatalysts for the Oxygen Evolution Reaction," was published in **Catalysis Science & Technology**, **2020**.[53] In this work, we prepared metallic and bimetallic OER electrocatalysts based on Ni and Cu. Specifically, we synthesized various compositions of Ni and Cu nanostructured systems for the OER. The prepared Ni-Cu nanoparticles, nanoclusters, and OER electrocatalysts found that Ni-Cu nanoclusters with a 52:48 mol% Ni: Cu bimetallic composition exhibited superior OER performance compared to other compositions.

Chapter 5, entitled "Cuprous Oxide Electrodeposited with Nickel for the Oxygen Evolution Reaction in 1M NaOH," was published in the ***Journal of Physical Chemistry C***, **2019**.[54] This work describes the preparation of OER electrocatalysts using Cu_2O thin films modified with different Ni overlayers on ITO substrates. We synthesized OER electrocatalysts based on Ni and Cu via the electrodeposition of Ni and Cu_2O. We then revealed the optimal ratio of Ni to Cu_2O for OER in alkaline conditions by electrodepositing various amounts of Ni on Cu_2O, discovering that the top-performing catalyst possessed an onset overpotential of 150 mV. We utilized advanced analytical techniques including XRD, SEM, EDS, and AFM to perform surface characterization, finding that differences in the amount of Ni electrodeposited determined the composition, morphology, and performance of the catalyst.

Chapter 6, entitled “Preparation and Electron Transfer Properties of Self-Assembled Monolayers of Ferrocene on Carbon Electrodes,” was published in the **Journal of Physical Chemistry C**, **2021**.[55] In this research work, we modified glassy carbon electrodes using various compositions of alkyl amine SAMs, and then amide coupling reactions were performed between ferrocene carboxylic acid and the amine groups of the SAM. Furthermore, we also studied the role of defect sites in electron transfer to the appended ferrocene molecules by modifying the SAMs with ZnO electrodeposits. The SAM-modified carbon electrodes protocol used in this work could be applicable in energy catalysis, biosensors, and electroanalysis.

1.6 References

1. Luderer, G.; Madeddu, S.; Merfort, L.; Ueckerdt, F.; Pehl, M.; Pietzcker, R.; Rottoli, M.; Schreyer, F.; Bauer, N.; Baumstark, L.; Bertram, C.; Dirnaichner, A.; Humpenöder, F.; Levesque, A.; Popp, A.; Rodrigues, R.; Strefler, J.; Kriegler, E. Impact of Declining Renewable Energy Costs on Electrification in Low-Emission Scenarios. *Nat. Energy* **2022**, *7*, 32–42.
2. Barile, C. J.; Tse, E. C. M.; Li, Y.; Sobyra, T. B.; Zimmerman, S. C.; Hosseini, A.; Gewirth, A. A. Proton Switch for Modulating Oxygen Reduction by a Copper Electrocatalyst Embedded in a Hybrid Bilayer Membrane. *Nat. Mater.* **2014**, *13*, 619–623.
3. Nitopi, S.; Bertheussen, E.; Scott, S. B.; Liu, X.; Engstfeld, A. K.; Horch, S.; Seger, B.; Stephens, I. E. L.; Chan, K.; Hahn, C.; Nørskov, J. K.; Jaramillo, T. F.; Chorkendorff, I. Progress and Perspectives of Electrochemical CO2 Reduction on Copper in Aqueous Electrolyte. *Chem. Rev.* **2019**, *119*, 7610–7672.
4. Gautam, Rajendra P.; Pokhrel, Megh Raj., "Removal of Chromium (VI) from Aqueous Solution using Charred Pomegranate Waste", Journal of Nepal Chemical Society, **2012**, *29*, 81-88.
5. Buis, A. The Atmosphere: Getting a Handle on Carbon Dioxide. *NASA's Jet Propuls. Lab.* **2019**, 1–12.
6. NOAA. Climate Change: Atmospheric Carbon Dioxide. *NOAA Clim.* **2020**, 1–5.
7. Solomon, S.; Plattner, G. K.; Knutti, R.; Friedlingstein, P. Irreversible Climate Change Due to Carbon Dioxide Emissions. *Proc. Natl. Acad. Sci. U. S. A.* **2009**, *106*, 1704–1709.
8. Wunderling, N.; Willeit, M.; Donges, J. F.; Winkelmann, R. Global Warming Due to Loss of Large Ice Masses and Arctic Summer Sea Ice. *Nat. Commun.* **2020**, *11*, 1–8.
9. Navarro, R. M.; Peña, M. A.; Fierro, J. L. G. Hydrogen Production Reactions from Carbon Feedstocks: Fossil Fuels and Biomass. *Chem. Rev.* **2007**, *107*, 3952–3991.
10. Liu, M.; Xiao, X.; Li, Q.; Luo, L.; Ding, M.; Zhang, B.; Li, Y.; Zou, J.; Jiang, B. Recent Progress of Electrocatalysts for Oxygen Reduction in Fuel Cells. *J. Colloid Interface Sci.* **2022**, *607*, 791–815.
11. International Energy Agency (IEA) Global EV Outlook. **2021**, 1–11.
12. Nikolaidis, P.; Poullikkas, A. A Comparative Overview of Hydrogen Production Processes. *Renew. Sustain. Energy Rev.* **2017**, *67*, 597–611.
13. Jiao, K.; Xuan, J.; Du, Q.; Bao, Z.; Xie, B.; Wang, B.; Zhao, Y.; Fan, L.; Wang, H.; Hou, Z.; Huo, S.; Brandon, N. P.; Yin, Y.; Guiver, M. D. Designing the next Generation of Proton-Exchange Membrane Fuel Cells. *Nature* **2021**, *595*, 361–369.
14. Gewirth, A. A.; Thorum, M. S. Electroreduction of Dioxygen for Fuel-Cell Applications: Materials and Challenges. *Inorg. Chem.* **2010**, *49*, 3557–3566.
15. Vij, V.; Sultan, S.; Harzandi, A. M.; Meena, A.; Tiwari, J. N.; Lee, W. G.; Yoon, T.; Kim, K. S. Nickel-Based Electrocatalysts for Energy-Related Applications: Oxygen Reduction, Oxygen Evolution, and Hydrogen Evolution Reactions. *ACS Catal.* **2017**, *7*, 7196–7225.

16. Gautam, R. P.; Lee, Y. T.; Herman, G. L.; Moreno, C. M.; Tse, E. C. M.; Barile, C. J. Controlling Proton and Electron Transfer Rates to Enhance the Activity of an Oxygen Reduction Electrocatalyst. *Angew. Chemie* **2018**, *130*, 13668–13671.
17. Jaouen, F.; Proietti, E.; Lefèvre, M.; Chenitz, R.; Dodelet, J. P.; Wu, G.; Chung, H. T.; Johnston, C. M.; Zelenay, P. Recent Advances in Non-Precious Metal Catalysis for Oxygen-Reduction Reaction in Polymer Electrolyte Fuel Cells. *Energy Environ. Sci.* **2011**, *4*, 114–130.
18. Tse, E. C. M.; Barile, C. J.; Kirchschlager, N. A.; Li, Y.; Gewargis, J. P.; Zimmerman, S. C.; Hosseini, A.; Gewirth, A. A. Proton Transfer Dynamics Control the Mechanism of O2 Reduction by a Non-Precious Metal Electrocatalyst. *Nat. Mater.* **2016**, *15*, 754–759.
19. Thorseth, M. A.; Tornow, C. E.; Tse, E. C. M.; Gewirth, A. A. Cu Complexes That Catalyze the Oxygen Reduction Reaction. *Coord. Chem. Rev.* **2013**, *257*, 130–139.
20. Igarashi, H.; Fujino, T.; Zhu, Y.; Uchida, H.; Watanabe, M. CO Tolerance of Pt Alloy Electrocatalysts for Polymer Electrolyte Fuel Cells and the Detoxification Mechanism. *Phys. Chem. Chem. Phys.* **2001**, *3*, 306–314.
21. Knupp, S. L.; Vukmirovic, M. B.; Haldar, P.; Herron, J. A.; Mavrikakis, M.; Adzic, R. R. Platinum Monolayer Electrocatalysts for O 2 Reduction: Pt Monolayer on Carbon-Supported PdIr Nanoparticles. *Electrocatalysis* **2010**, *1*, 213–223.
22. Zeng, T.; Gautam, R. P.; Barile, C. J.; Li, Y.; Tse, E. C. M. Nitrile-Facilitated Proton Transfer for Enhanced Oxygen Reduction by Hybrid Electrocatalysts. *ACS Catal.* **2020**, *10*, 13149–13155.
23. Nagappan, S.; Duraivel, M.; Hira, S. A.; Prabakar, K.; Ha, C. S.; Joo, S. H.; Nam, K. M.; Park, K. H. Heteroatom-Doped Nanomaterials/Core–Shell Nanostructure Based Electrocatalysts for the Oxygen Reduction Reaction. *J. Mater. Chem. A* **2022**, *10*, 987–1021.
24. Higgins, D. C.; Chen, Z. Recent Progress in Non-Precious Metal Catalysts for PEM Fuel Cell Applications. *Can. J. Chem. Eng.* **2013**, *91*, 1881–1895.
25. Yaropolov, A. I.; SKOROBOGATKO, O. V.; VARTANOV, S. S.; VARFOLOMEYEV, S. . La Cease. *Appl. Biochem. Biotechnol.* **1994**, *49*, 257–280.
26. Tse, E. C. M.; Schilter, D.; Gray, D. L.; Rauchfuss, T. B.; Gewirth, A. A. Multicopper Models for the Laccase Active Site: Effect of Nuclearity on Electrocatalytic Oxygen Reduction. *Inorg. Chem.* **2014**, *53*, 8505–8516.
27. Michel, H.; Behr, J.; Harrenga, A.; Kannt, A. Cytochrome c Oxidase: Structure and Spectroscopy. *Annu. Rev. Biophys. Biomol. Struct.* **1998**, *27*, 329–356.
28. Rahman, M. A.; Noh, H. B.; Shim, Y. B. Direct Electrochemistry of Laccase Immobilized on Au Nanoparticles Encapsulated-Dendrimer Bonded Conducting Polymer: Application for a Catechin Sensor. *Anal. Chem.* **2008**, *80*, 8020–8027.
29. Thorum, M. S.; Anderson, C. A.; Hatch, J. J.; Campbell, A. S.; Marshall, N. M.; Zimmerman, S. C.; Lu, Y.; Gewirth, A. A. Direct, Electrocatalytic Oxygen Reduction by Laccase on Anthracene-2-Methanethiol-Modified Gold. *J. Phys. Chem. Lett.* **2010**, *1*, 2251–2254.

30. Oberst, J. L.; Thorum, M. S.; Gewirth, A. A. Effect of PH and Azide on the Oxygen Reduction Reaction with a Pyrolyzed Fe Phthalocyanine Catalyst. *J. Phys. Chem. C* **2012**, *116*, 25257–25261.
31. Cárdenas-Jirón, G. I. Substituent Effect in the Chemical Reactivity and Selectivity of Substituted Cobalt Phthalocyanines. *J. Phys. Chem. A* **2002**, *106*, 3202–3206.
32. Kuwana, T.; Fujihira, M.; Sunakawa, K.; Osa, T. Catalytic Electroreduction of Molecular Oxygen Using Water Soluble Iron Porphyrin. *J. Electroanal. Chem.* **1978**, *88*, 299–303.
33. Xiong, C.; Wei, Z.; Hu, B.; Chen, S.; Li, L.; Guo, L.; Ding, W.; Liu, X.; Ji, W.; Wang, X. Nitrogen-Doped Carbon Nanotubes as Catalysts for Oxygen Reduction Reaction. *J. Power Sources* **2012**, *215*, 216–220.
34. Kalamaras, C. M.; Efstathiou, A. M. Hydrogen Production Technologies: Current State and Future Developments. *Conf. Pap. Energy* **2013**, *2013*, 1–9.
35. Suen, N. T.; Hung, S. F.; Quan, Q.; Zhang, N.; Xu, Y. J.; Chen, H. M. Electrocatalysis for the Oxygen Evolution Reaction: Recent Development and Future Perspectives. *Chem. Soc. Rev.* **2017**, *46*, 337–365.
36. Lyu, F.; Wang, Q.; Choi, S. M.; Yin, Y. Noble-Metal-Free Electrocatalysts for Oxygen Evolution. *Small* **2019**, *15*, 1–17.
37. Fabbri, E.; Habereder, A.; Waltar, K.; Kötz, R.; Schmidt, T. J. Developments and Perspectives of Oxide-Based Catalysts for the Oxygen Evolution Reaction. *Catal. Sci. Technol.* **2014**, *4*, 3800–3821.
38. Fabbri, E.; Schmidt, T. J. Oxygen Evolution Reaction - The Enigma in Water Electrolysis. *ACS Catal.* **2018**, *8*, 9765–9774.
39. Reier, T.; Oezaslan, M.; Strasser, P. Electrocatalytic Oxygen Evolution Reaction (OER) on Ru, Ir, and Pt Catalysts: A Comparative Study of Nanoparticles and Bulk Materials. *ACS Catal.* **2012**, *2*, 1765–1772.
40. Varnell, J. A.; Sotiropoulos, J. S.; Brown, T. M.; Subedi, K.; Haasch, R. T.; Schulz, C. E.; Gewirth, A. A. Revealing the Role of the Metal in Non-Precious-Metal Catalysts for Oxygen Reduction via Selective Removal of Fe. *ACS Energy Lett.* **2018**, *3*, 823–828.
41. Stern, L. A.; Feng, L.; Song, F.; Hu, X. Ni2P as a Janus Catalyst for Water Splitting: The Oxygen Evolution Activity of Ni2P Nanoparticles. *Energy Environ. Sci.* **2015**, *8*, 2347–2351.
42. Zhou, Q.; Chen, Y.; Zhao, G.; Lin, Y.; Yu, Z.; Xu, X.; Wang, X.; Liu, H. K.; Sun, W.; Dou, S. X. Active-Site-Enriched Iron-Doped Nickel/Cobalt Hydroxide Nanosheets for Enhanced Oxygen Evolution Reaction. *ACS Catal.* **2018**, *8*, 5382–5390.
43. Voldsund, M.; Jordal, K.; Anantharaman, R. Hydrogen Production with CO2 Capture. *Int. J. Hydrogen Energy* **2016**, *41*, 4969–4992.
44. Bhanja, P.; Kim, Y.; Paul, B.; Lin, J.; Alshehri, S. M.; Ahamad, T.; Kaneti, Y. V.; Bhaumik, A.; Yamauchi, Y. Facile Synthesis of Nanoporous Transition Metal-Based Phosphates for Oxygen Evolution Reaction. *ChemCatChem* **2020**, *12*, 2091–2096.

45. Lim, D.; Oh, E.; Lim, C.; Shim, S. E.; Baeck, S. H. Bimetallic NiFe Alloys as Highly Efficient Electrocatalysts for the Oxygen Evolution Reaction. *Catal. Today* **2020**, *352*, 27–33.
46. Huang, W.; Chen, C.; Ling, Z.; Li, J.; Qu, L.; Zhu, J.; Yang, W.; Wang, M.; Owusu, K. A.; Qin, L.; Zhou, L.; Mai, L. Ni/Fe Based Bimetallic Coordination Complexes with Rich Active Sites for Efficient Oxygen Evolution Reaction. *Chem. Eng. J.* **2021**, *405*, 126959.
47. Zhao, J. W.; Shi, Z. X.; Li, C. F.; Gu, L. F.; Li, G. R. Boosting the Electrocatalytic Performance of NiFe Layered Double Hydroxides for the Oxygen Evolution Reaction by Exposing the Highly Active Edge Plane (012). *Chem. Sci.* **2021**, *12*, 650–659.
48. Liu, P. P.; Zheng, Y. Q.; Zhu, H. L.; Li, T. T. Mn2O3 Hollow Nanotube Arrays on Ni Foam as Efficient Supercapacitors and Electrocatalysts for Oxygen Evolution Reaction. *ACS Appl. Nano Mater.* **2019**, *2*, 744–749.
49. Bonomo, M.; Dini, D.; Decker, F. Electrochemical and Photoelectrochemical Properties of Nickel Oxide (NiO) with Nanostructured Morphology for Photoconversion Applications. *Front. Chem.* **2018**, *6*, 1–16.
50. Gao, L.; Cui, X.; Sewell, C. D.; Li, J.; Lin, Z. Recent Advances in Activating Surface Reconstruction for the High-Efficiency Oxygen Evolution Reaction. *Chem. Soc. Rev.* **2021**, *50*, 8428–8469.
51. Yu, M.; Budiyanto, E.; Tüysüz, H. Principles of Water Electrolysis and Recent Progress in Cobalt-, Nickel-, and Iron-Based Oxides for the Oxygen Evolution Reaction. *Angew. Chemie - Int. Ed.* **2022**, *61* 1-5.
52. Konkena, B.; Masa, J.; Botz, A. J. R.; Sinev, I.; Xia, W.; Koßmann, J.; Drautz, R.; Muhler, M.; Schuhmann, W. Metallic NiPS3@NiOOH Core-Shell Heterostructures as Highly Efficient and Stable Electrocatalyst for the Oxygen Evolution Reaction. *ACS Catal.* **2017**, *7*, 229–237.
53. She, Z. W.; Kibsgaard, J.; Dickens, C. F.; Chorkendorff, I.; Nørskov, J. K.; Jaramillo, T. F. Combining Theory and Experiment in Electrocatalysis: Insights into Materials Design. *Science.* **2017**, *355*, 6321.
54. Gautam, R. P.; Pan, H.; Chalyavi, F.; Tucker, M. J.; Barile, C. J. Nanostructured Ni-Cu Electrocatalysts for the Oxygen Evolution Reaction. *Catal. Sci. Technol.* **2020**, *10*, 4960–4967.
55. Lee, Y. T.; Gautam, R. P.; Islam, S. M.; Barile, C. J. Cuprous Oxide Electrodeposited with Nickel for the Oxygen Evolution Reaction in 1 M NaOH. *J. Phys. Chem. C* **2019**, *123*, 1287–1292.
56. Gautam, R. P.; Barile, C. J. Preparation and Electron-Transfer Properties of Self-Assembled Monolayers of Ferrocene on Carbon Electrodes. *J. Phys. Chem. C* **2021**, *125*, 8177-8184.

Chapter 2: Controlling Proton and Electron Transfer Rates to Enhance the Activity of an Oxygen Reduction Electrocatalyst

2.1. Introduction

Reactions involving the transfer of multiple protons and electrons are instrumental in many renewable energy conversion schemes and biological processes.[1-7] One of the most important redox reactions that involves proton transfer is the O_2 reduction reaction (ORR), which occurs at the cathode of fuel cells and in mitochondria present in all aerobic life.[8-11] Unfortunately, the mechanistic details of the ORR are difficult to elucidate because of the complex interplay between the thermodynamics and kinetics of the multiple proton and electron transfer steps involved.[12]

In this work, we design an electrochemical platform that allows for the control of the thermodynamics and kinetics of proton and electron transfer to a Cu-based molecular ORR catalyst. It is well known that the electrode potential dictates the thermodynamics of electron transfer and that the pH of the bulk solution controls the thermodynamics of proton transfer in many metal-centered proton transfer reactions.[13-16] The kinetics of electron transfer can be modulated to a molecular catalyst through the use of self-assembled monolayers (SAMs) with varying alkyl chain lengths.[17-19] However, there are few methods to control the kinetics of proton transfer to a catalyst in an unconvoluted manner. Gewirth and coworkers recently developed proton-permeable lipid membranes to alter the proton transfer kinetics to a catalyst without perturbing its molecular identity. [20,21] These membranes contain amphiphilic alkyl proton carriers that deliver protons via a flip-flop diffusion process. [22]

Here, we develop an electrode architecture containing an ORR catalyst that allows for both the control of proton transfer rates through the use of lipid membranes and the control of electron transfer rates through the use of a modular SAM scaffold that takes advantage of azide-alkyne click chemistry. The click chemistry approach enables us to attach a synthesized ORR catalyst to a SAM surface. The length of the catalyst-modified SAM can be facilely modified without changing the identity of the catalyst. Together, this click platform provides a means to control electron transfer kinetics to the catalyst. By altering the amount of proton carrier in the lipid layer of the same platform, proton transfer kinetics can also be tuned.

2.2. Experimental Section

2.2.1. General Procedures

All starting materials and electrolyte chemicals were obtained from commercially available sources and used without further purification. The benzyl triazole alkyne (BTA) ligand and the azide-terminated thiols were synthesized following procedures described in the "Synthetic Procedures" section. Electrochemical studies were carried out using a VSP-300 Biologic potentiostat. For electrochemical studies, a three-electrode system was used with a Pt counter electrode, a Ag/AgCl reference electrode, and Au or glassy carbon as the working electrode. Au working electrodes were prepared according to a literature procedure. [23]

2.2.2. Experiments with Au Electrodes

A 1 mM thiol solution in ethanol containing either 1-azido-11-undecanethiol or 1-azido-5-pentanethiol with 100 mM $LiClO_4$ was added to the Au electrodes. The self-assembled monolayers (SAMs) were formed electrochemically by cycling between 0 V and -0.7 V four times at a scan rate of 10 mV/s. Similar electrochemical procedures have been used to form thiol-based SAMs previously.[24] The Au electrodes were subsequently rinsed three times with ethanol and DI water. The azide-alkyne click solution was prepared by combining 2.3 mL 3:1 vol % DMSO and water, 300 µL of 8 mM aqueous $Cu(NO_3)_2$, 300 µL 8 mM tris[(1-benzyl-1*H*-1,2,3-triazol-4-yl)methyl]amine (TBTA) in DMSO, 300 µL 100 mM sodium ascorbate, and 72 µL of 4 mM BTA in DMSO. About 300 µL of the click solution was added on each surface and allowed to sit on the surfaces for 1 hour in the dark. The Au electrodes were rinsed twice with DI water and soaked in about 300 µL of 100 mM aqueous Cu $(NO_3)_2$ solution for 1 hour. The Au electrodes were then rinsed three times with DI water before lipid formation.

The lipid film was prepared by adding 5 mg 2-dimyristoyl-sn-glycero-3-phosphocholine (DMPC) with and without varying amounts of 1-dodecylboronic acid (DBA) as a proton carrier in a 20 mL vial. The vial containing DMPC with or without DBA was dissolved in 1-1.5 mL of $CHCl_3$. The $CHCl_3$ was removed under a gentle stream of air, and the film was further dried in a vacuum desiccator for 30 minutes. 83 µL of isopropanol, followed by 10.5 mL of 100 mM potassium phosphate pH 7 buffer was added to the vial drop wise via syringe, and the solution was sonicated for 30 minutes. pH 7 buffer solutions were sparged with O_2 for 15 minutes prior to running each O_2 reduction

experiment. For all experiments with a lipid layer, an electrochemical blocking experiment was conducted in an aqueous solution containing 1 mM $K_3Fe(CN)_6$ and 100 mM NaCl to confirm the integrity of the lipid monolayer as demonstrated previously.[25] All experiments were carried out at room temperature (25 ± 1) °C.

2.2.3. Experiments on Glassy Carbon Electrodes

Experiments on glassy carbon electrodes were conducted using a modified literature protocol.[26] 1.0 g of Vulcan XC-72 and 0.2 g of $CuSO_4 \cdot 5H_2O$ were added to a vial. 20.0 mL of DI water was added to the vial, and the resulting suspension was sonicated to form a viscous suspension. 0.159 g of 3,5-diamino-1,2,4-triazole or 0.11 g of 1,2,3-triazole was dissolved in 10.0 mL DI water and then this solution was added dropwise with constant stirring to the previously prepared solution. The combined mixture was stirred for 18 hours followed by suction filtration. The solids formed were collected, dried in a vacuum oven for 3 hours at 90°C, and pulverized using a mortar and pestle.

A stock solution was prepared by combining 1 mg of the Cu complex and Vulcan mixture and 4 µL of Nafion in 1.0 mL of DI water. About 20 µL of this stock solution was drop-casted onto a glassy carbon electrode and dried under a stream of air for 10-15 minutes. O_2 reduction experiments were then performed using the modified glassy carbon electrode as the working electrode.

2.2.4. Cu Coverage Calculations

The cross-sectional area calculated with Spartan '08 (Wavefunction, Inc.) v. 1.2.0 of a Cu complex of BTA is 395 $Å^2$. The surface coverage using this area and assuming a smooth Au surface is 4.2 x 10^{-11} mol cm^{-2}, which is similar to the experimentally observed Cu coverage.

2.2.5. Synthetic Procedures

Dichloromethane (DCM), dimethyl sulfoxide (DMSO), ethyl acetate (EtOAc), and methanol (MeOH) were of reagent grade and used without further purification. Column chromatography was performed using 230-400 mesh silica gel. Ratios of solvents for chromatography are reported as volume ratios. NMR spectra were obtained using a Varian 400 MHz NMR Spectrometer in the Shared Instrument Laboratory (SIL) in the Department of Chemistry at the University of Nevada, Reno (UNR). ^{1}H NMR spectra were recorded in $CDCl_3$ and referenced to the residual protio solvent peak at 7.26 parts per million (ppm). ^{13}C NMR spectra were recorded in CD_3OD and referenced to the residual protio solvent peak at 49 ppm. Chemical shifts (δ) and coupling constants (J) are reported in ppm and hertz (Hz), respectively. High-resolution mass spectrometry with electrospray ionization (ESI-HRMS) analysis was obtained using an Agilent G6230B time-of-flight mass spectrometer in the SIL at UNR.

The azide-terminated thiols, 1-azido-11-undecanethiol and 1-azido-5-pentanethiol, were synthesized according to previously reported literature procedures. [27, 28] N^3-benzyl-N^5-(but-3-yn-1-yl)-1*H*-1,2,4-triazole-3,5-diamine (BTA) was synthesized in four steps starting from benzylamine. BTA was synthesized from N^5-benzyl-1H-1,2,4-triazole-3,5-

diamine and but-3-yn-1-yl methanesulfonate starting materials. N^5-benzyl-1H-1,2,4-triazole-3,5-diamine was synthesized in two steps from benzylamine following a literature protocol.[29] A previously reported procedure was used to synthesize but-3-yn-1-yl methanesulfonate from but-3-yn-1-ol.[30]

To synthesize BTA, a solution of N^5-benzyl-1H-1,2,4-triazole-3,5-diamine (1.09 mg, 5.8 mmol) in DMF (8 mL) was added dropwise to but-3-yn-1-ol (385 mg, 2.6 mmol). The solution was refluxed under N_2 for 48 hr. After cooling, the reaction mixture was poured into water (10 mL) and extracted with DCM (3x 100 mL). The organic layers were washed with brine (10 mL), dried over Na_2SO_4, and removed under reduced pressure. The resulting residue was purified by gradient column chromatography (EtOAc:MeOH = 1:0 to 9:1) to give the final product as a yellow solid (75 mg, 12%). ^{1}H NMR δ 7.28-7.40 (m, 5 H), 4.40 (s, 2 H), 3.92 (t, 2 H, J = 6.4), 2.67 (td, 2 H, J_1 = 6.4, J_2 = 2.6), 2.05 (t, 1 H, J = 2.6), ^{13}C NMR δ 163.2, 129.5, 129.3, 128.8, 128.6, 128.3, 81.4, 72.0, 47.2, 46.0, 24.0, ESI-HRMS (*m/z*): calc for $[M+H]^+$ 242.1406, found 242.1392.

^{1}H NMR Spectrum of BTA:

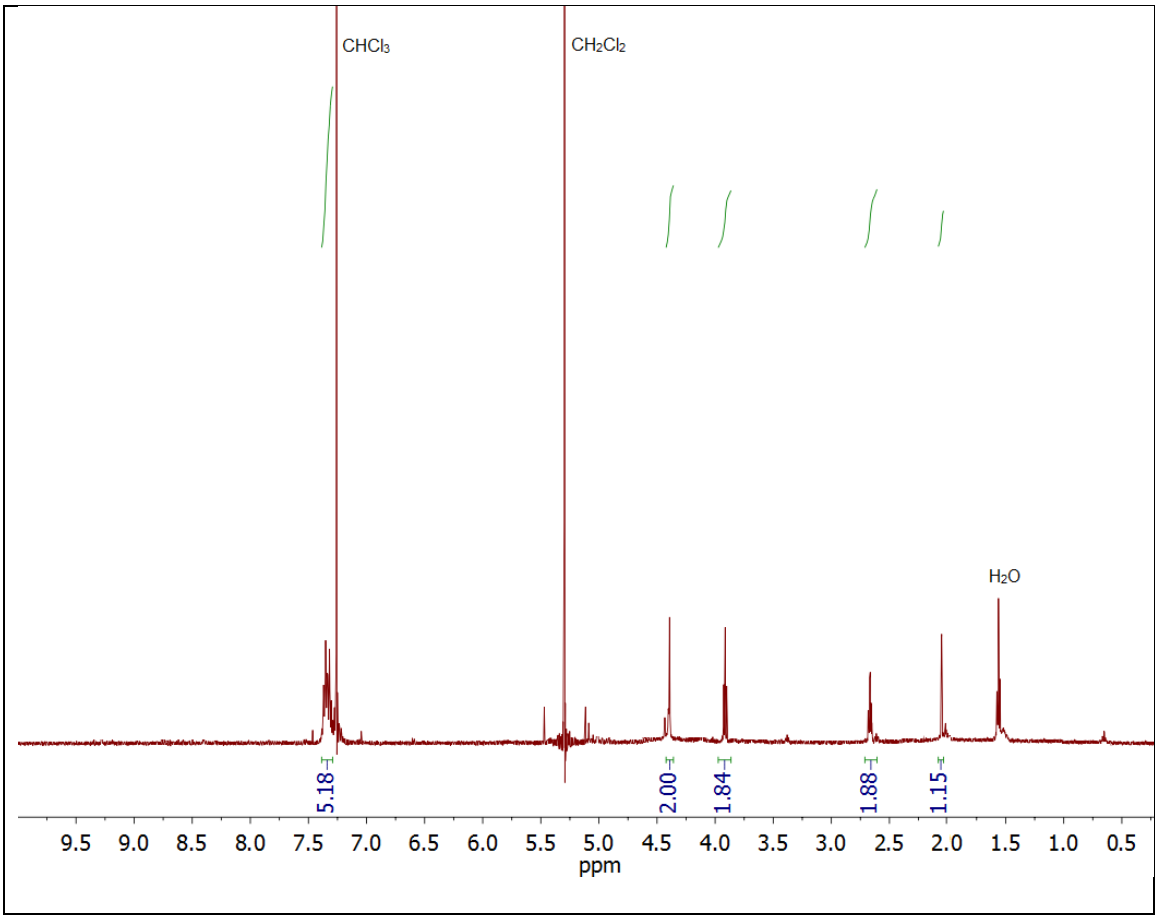

^{13}C NMR Spectrum of BTA:

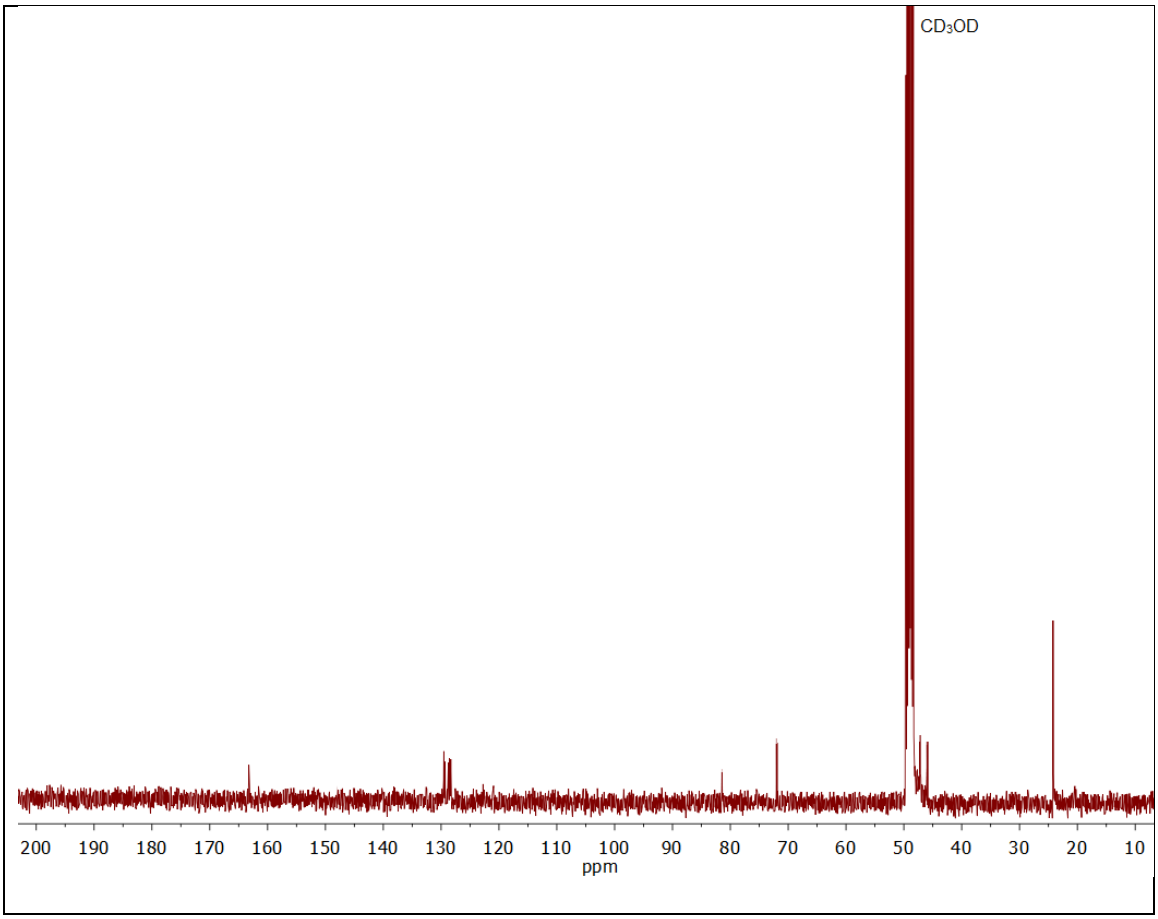

2.3. Results and Discussion

We first designed a ligand that supports an active ORR catalyst that can be incorporated into an electrode architecture with tunable proton and electron transfer kinetics. The ligand, N^3-benzyl-N^5-(but-3-yn-1-yl)-1*H*-1,2,4-triazole-3,5-diamine (BTA), was synthesized in four steps from benzylamine and contains three important features (Figure 2.1.). First, the BTA ligand contains a diaminotriazole core which upon

coordination to Cu forms a highly active ORR catalyst. This core is inspired by previous studies with a dinuclear Cu complex of 3,5-diamino-1,2,4-triazole, which in terms of overpotential is one of the most active molecular Cu ORR catalysts known. [31-33] Second, BTA contains an alkyne moiety, which allows it to undergo the azide-alkyne click reaction with azide-terminated SAMs. Lastly, BTA possesses a benzyl group, which enables lipid monolayers to assemble on top of a BTA SAM. [20] The hydrophobic tails of the lipid monolayer are appended to the hydrophobic benzyl groups of the BTA SAM via Van der Waals interactions.

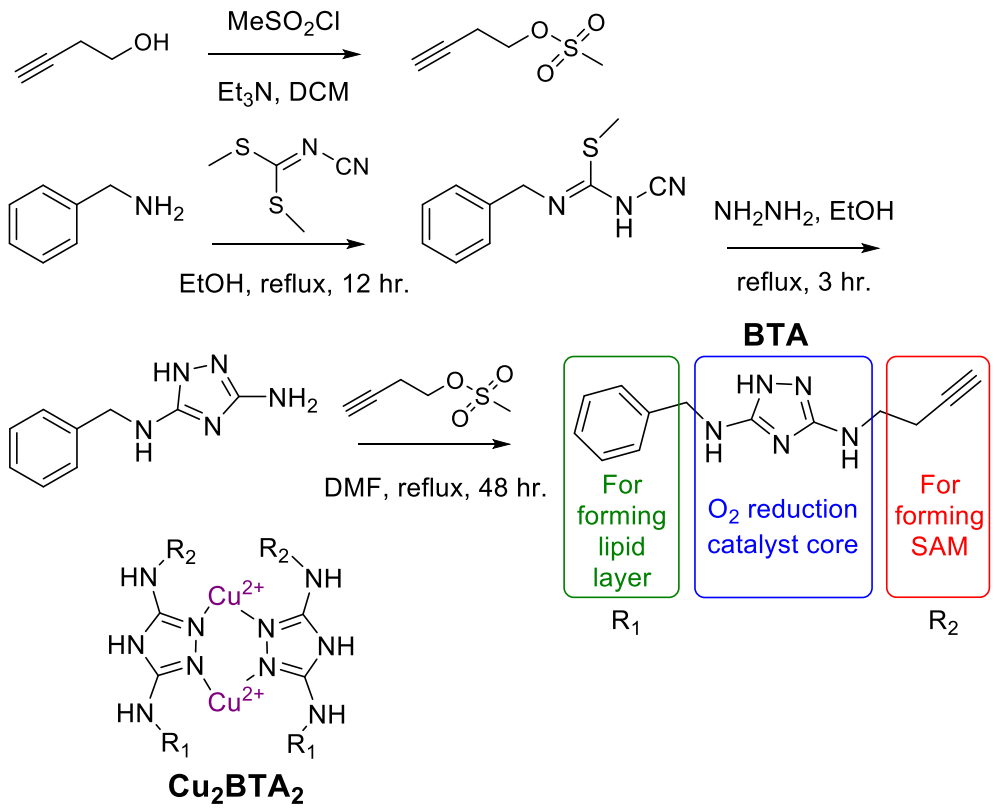

Figure 2.1. Synthesis of BTA with three important features highlighted along with the structure of the dinuclear CuBTA complex.

Electrodes containing the CuBTA ORR catalyst with tunable proton and electron transfer rates were constructed in three steps (Figures 1 and S2.1). First, Au electrodes were modified with SAMs of azide-terminated thiols with different alkyl chain lengths. Next, the BTA ligand was covalently attached to the SAM using azide-alkyne click chemistry and subsequently immersed in a Cu^{2+} solution to form the active dinuclear Cu complex. Lastly, a lipid monolayer containing 1-dodecylboronic acid (DBA) as a proton carrier was appended on top of the SAM to complete the electrode architecture.

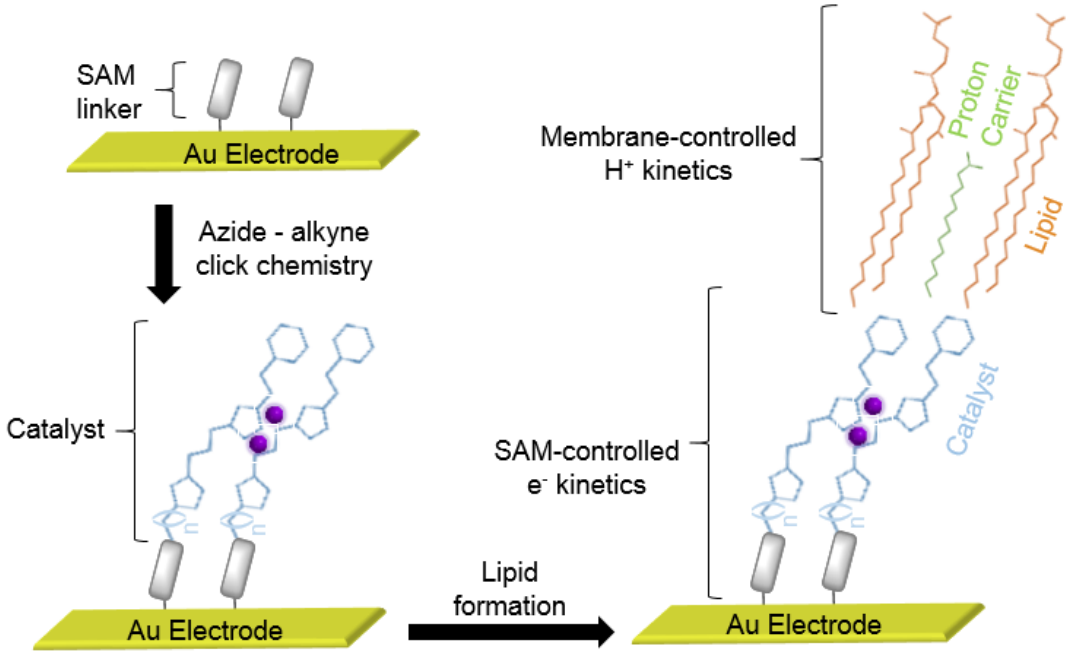

Figure 2.2. Schematic of the fabrication of lipid-modified SAMs used to control the electron and proton transfer rates to a molecular O_2 reduction catalyst.

Electrochemical techniques were used to assess the chemical structure of the electrodes at each fabrication stage. Electrodes containing the CuBTA catalyst were first assembled using an azide-terminated thiol containing 5 methylene groups (Figures 2.1 and S2.1, n = 5). The presence of Cu in the catalyst was confirmed by a Cu(I)/Cu(II) couple in

cyclic voltammetry (CV) experiments (Figure S2.2). By integrating the charge of the Cu couple in the CV, the amount of Cu catalyst on the surface was determined to be 1.3 x 10^{-11} mol cm^{-2}, a value that matches what is expected for a full monolayer of Cu (see SI). A linear sweep voltammogram (LSV) of the CuBTA assembly without a lipid layer demonstrates that CuBTA is an active ORR catalyst that exhibits an onset potential of about 0 V vs. Ag/AgCl and an O_2 diffusion-limited peak current density of about -900 µA cm^{-2} in O_2-sparged pH 7 buffer (Figure 2.3, black line).

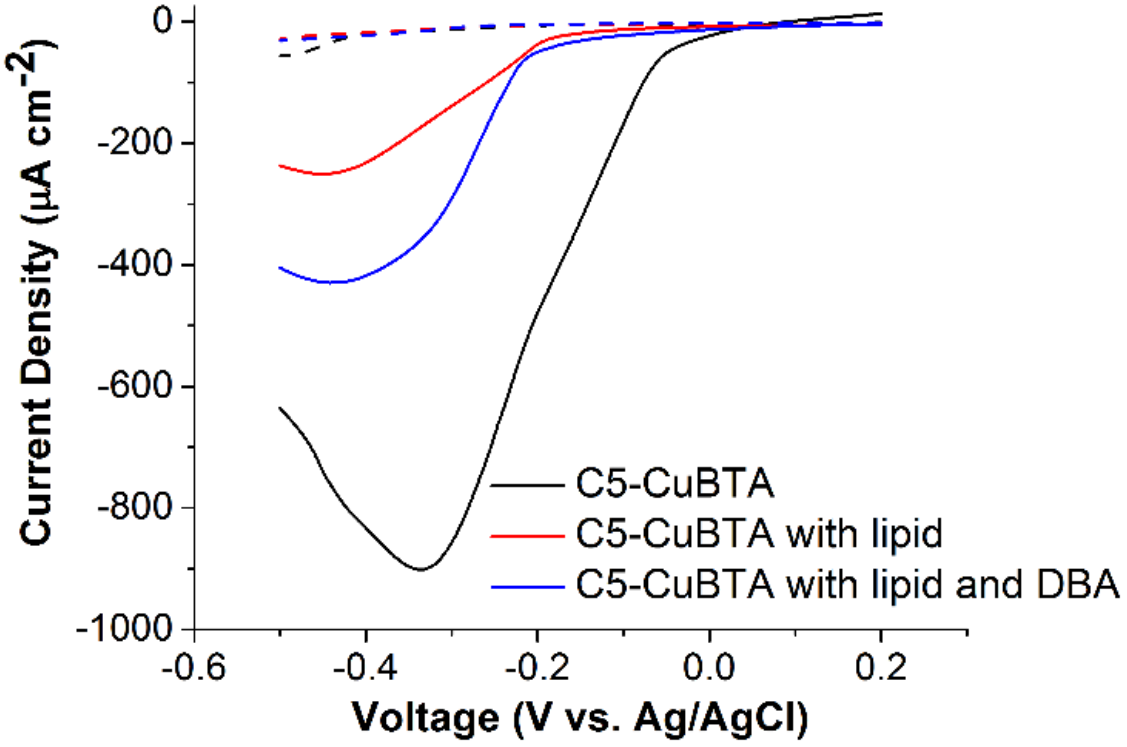

Figure 2.3. Linear sweep voltammograms of O_2 reduction by the CuBTA catalyst using an azide-terminated thiol SAM containing 5 methylene groups (black line) covered by a DMPC lipid monolayer (red line) with 10 mol% DBA proton carrier (blue line) at 10 mV/s in O_2-saturated pH 7 buffer. Dashed lines are the corresponding voltammograms in N_2-saturated pH 7 buffer.

Control experiments in the absence of O_2 (Figures 2.3 and 2.4, dashed lines), with Zn, or without performing the click chemistry do not exhibit significant ORR activity, further demonstrating that Cu is necessary to produce an active catalyst (Figures S2.3 and S2.4). Further control experiments comparing the activity of Cu complexes of 3,5-diamino,1,2,4-triazole and 1,2,3-triazole indicate that the Cu-1,2,3-triazole complex is not a competent ORR catalyst, demonstrating that the 1,2,3-triazole linker formed from the azide-alkyne click chemistry is not contributing to the ORR activity measured (Figure S2.5).

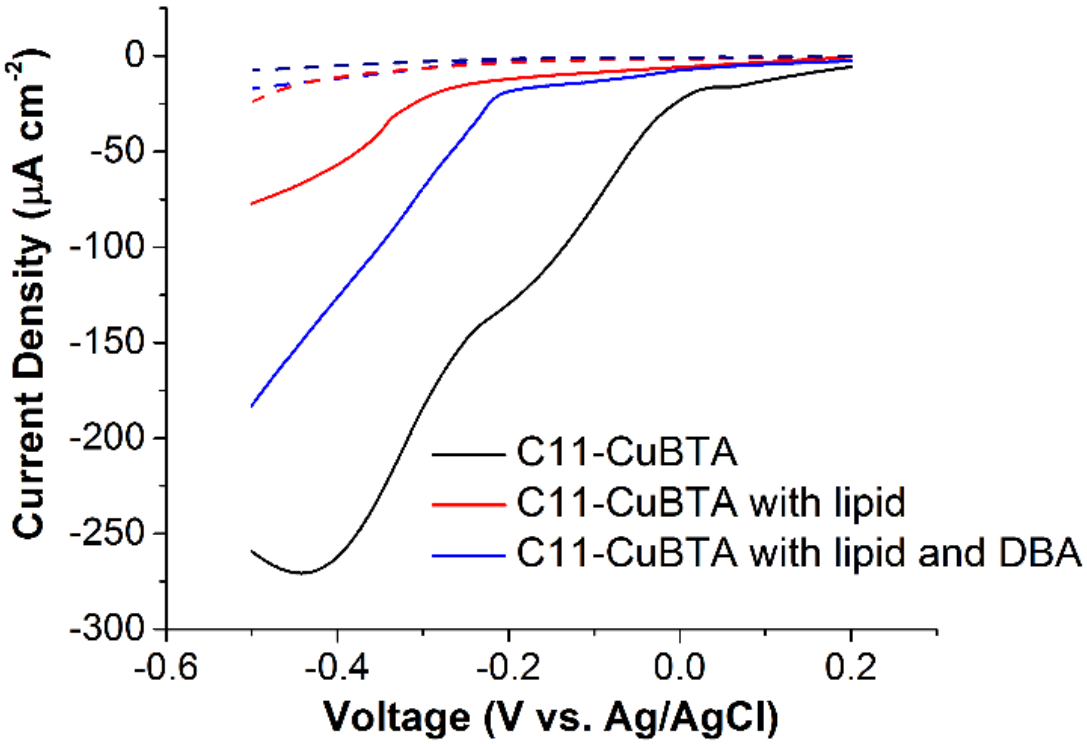

Figure 2.4. Linear sweep voltammograms of O_2 reduction by the CuBTA catalyst using an azide-terminated thiol SAM containing 11 methylene groups (black line) covered by a DMPC lipid monolayer (red line) with 10 mol% DBA proton carrier (blue line) at 10

mV/s in O_2-saturated pH 7 buffer. Dashed lines are the corresponding voltammograms in N_2-saturated pH 7 buffer.

Having established that the CuBTA complex catalyzes the ORR, we next evaluated the ORR activity of CuBTA when the SAM is covered by a monolayer of 1,2-dimyristoyl-*sn*-glycero-3-phosphocholine (DMPC) lipid. A LSV of CuBTA in the presence of lipid displays an onset potential of about -0.2 V and a peak current density of about -250 μA cm^{-2} (Figure 2.3, red line). The negative shift in onset potential and reduction in current density indicates that the ORR activity of CuBTA significantly decreases upon lipid formation. This inhibition of catalytic activity arises from impeded proton transport across the hydrophobic lipid membrane as has been observed in other lipid-covered electrodes[34] and is also manifested by an about 50 mV negative shift in the midpoint potential of the Cu(I)/Cu(II) couple (Figure S2.2). O_2 diffusion through the lipid monolayer is fast, and hence the ORR by lipid-covered CuBTA is not limited by a lack of O_2 (Figure S2.6). Results obtained from electrochemical impedance spectroscopy demonstrate that the molecular length of the system increases upon performing the click reaction and further increases upon lipid formation, as expected (Figure S2.7). Upon incorporating the DBA proton carrier in the lipid, the CuBTA catalytic current density increases to about -425 μA cm^{-2}, but the onset potential does not change considerably (Figure 2.3, blue line). This result demonstrates that the presence of the proton carrier enhances the kinetics of the ORR without significantly altering the thermodynamics of the reaction. The peak in the LSV in the presence of lipid and proton carrier is due to kinetically limited proton transfer. DBA delivers protons across the lipid membrane via flip-flop diffusion in a kinetically-controlled

fashion as discussed previously.[21] Electrochemical blocking experiments using $Fe(CN)_6^{3-}$ demonstrate that the ORR does not compromise the integrity of the lipid layer regardless of whether the proton carrier is present (Figure S2.8).

To modify the electron transfer kinetics to the CuBTA catalyst, we changed the SAM to an azide-terminated thiol containing 11 methylene groups (Figures 2.2 and S2.1, n = 11). As measured using Laviron analysis [35] (Figure S2.9), this longer-chained SAM, which possesses a greater barrier for electron tunneling, exhibits about 30 times slower electron transfer than the previously described thiol containing 5 methylene groups ((1.2 ± 0.2) s^{-1} and (39 ± 3) s^{-1} for the C_{11} and C_5 SAMs, respectively). A LSV of O_2 reduction by CuBTA attached to the C_{11} SAM displays an onset potential of about 0 V and a peak current density of about -275 μA cm^{-2} (Figure 2.4, black line). The onset potentials for ORR using C_{11} and C_5 SAMs are similar because the active catalyst is the same in both cases, which means that the thermodynamics for catalyzing the ORR do not change when altering the SAM. However, the peak current density is significantly less for the C_{11} SAM due to the slower electron transfer rate. Also, the Tafel slope of the LSV for the C_{11} SAM is significantly higher than that of the C_5 SAM, further indicating that electron transfer kinetics are impeded in the C_{11} case (Figure S2.10). Upon covering the C_{11}-linked catalyst with lipid, the current density decreases and the onset potential shifts negative in a manner similar to what is observed with the lipid-covered catalyst on C_5 SAM (Figure 2.3, red line). Incorporation of the proton carrier also enhances the catalytic current, but does not significantly alter the onset potential for catalysis (Figure 2.4, blue line). In short, similar

changes in the ORR voltammetry occur using both the C_{11} and C_5 SAMs, but the slower electron transfer rate for the C_{11} SAM decreases the overall kinetics of catalysis.

To complement the modulation of electron transfer rates using SAMs, we also varied the proton transfer rate to the CuBTA catalyst by changing the concentration of proton carrier in the lipid layer. The data in Figure S2.11 show that as the amount of proton carrier in the lipid layer increases, the current enhancement afforded by the lipid layer compared to the lipid-only case correspondingly increases. The current enhancement observed saturates when around 10 mol% of proton carrier is added to the lipid membrane, which is the maximum amount of DBA that can incorporate in the lipid during vesicle formation.[21] Since proton transfer rates across this lipid membrane have already been measured (Figure S2.12),[21] we calculated the ratio of the proton and electron transfer rates to CuBTA (k_{H+}/k_{e-}). The ORR current density enhancement by the proton carrier increases as a function of k_{H+}/k_{e-} (Figure 2.5).

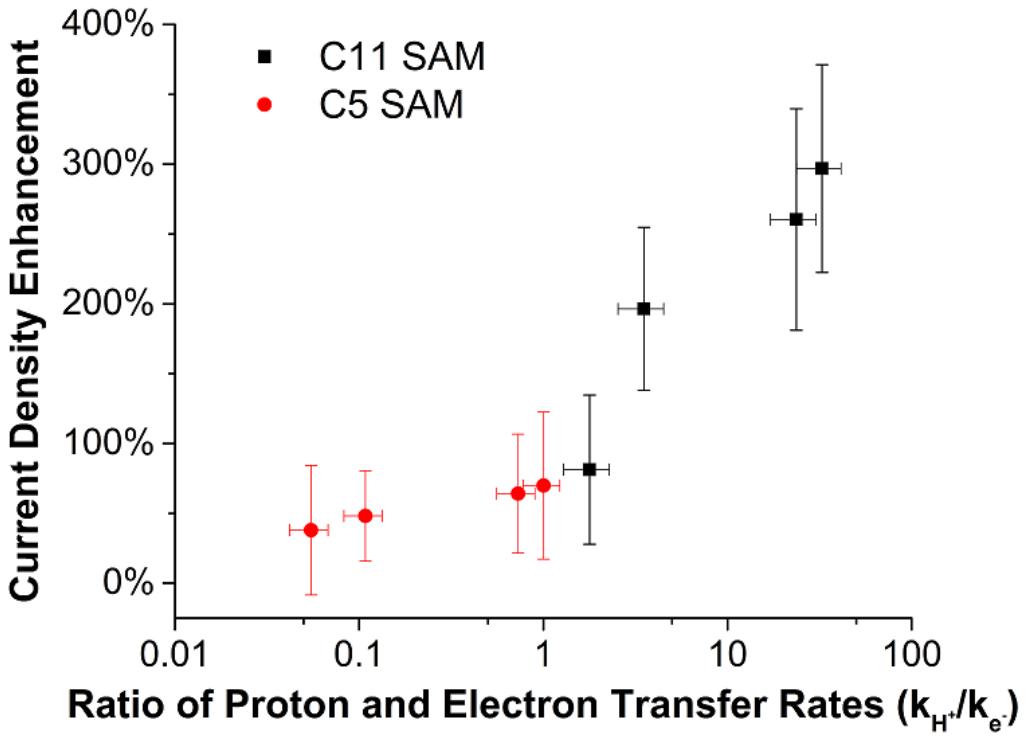

Figure 2.5. O_2 reduction current density enhancement by CuBTA imparted by the incorporation of the DBA proton carrier in the lipid as a function of the ratio of proton and electron transfer rates (k_{H+}/k_{e-}) using an azide-terminated thiol SAM containing 5 (red points) and 11 (black points) methylene groups.

In the absence of the proton carrier, proton transfer to the catalyst is almost entirely blocked by the hydrophobic lipid layer, and as a result, the 1 e^- reduction of O_2 to superoxide predominantly occurs.[36] With added proton carrier, k_{H+}/k_{e-} increases, which favors the 4 e^- reduction of O_2 to H_2O as evidenced by dye-based spectroelectrochemical experiments quantifying the amount of partially reduced oxygen species (Figure S2.13) and results in increased current density (Figure S2.14). Therefore, the addition of proton carrier changes the rate-determining step (RDS) for the ORR. In particular, the RDS changes from electron transfer with lipid in the absence of proton carrier to proton transfer in the presence of proton carrier as discussed previously.[20] The use of both the C_{11} and C_5 SAMs with different electron transfer rates allows for two orders of magnitude of k_{H+}/k_{e-}

to be accessed. The current enhancement using the C_{11} SAM is greater than the enhancement measured on the C_5 SAM regardless of the amount of proton carrier in the lipid layer (compare black points to red points, Figure 2.5). The greater enhancement with the C_{11} SAM occurs because the accelerated proton transfer rate with the proton carrier has a larger relative impact on the catalytic current density when the electron transfer rate to the catalyst is slow. In contrast, with a C_5 SAM in which relatively fast electron transfer occurs, the proton carrier's ability to enhance the ORR activity is not as pronounced. Strikingly, the current density enhancements are similar for the C_5 SAM with the maximum amount of proton carrier (10 mol%) and the C_{11} SAM with the minimum amount of proton carrier (0.2 mol%) because the two cases have similar k_{H+}/k_{e-} values (compare rightmost red point and leftmost black point, Figure 2.5). These results demonstrate that the interplay between proton and electron transfer rates dictates the overall activity of the ORR catalyst. We note that relative changes in the peak current density do not strictly reflect changes in the catalytic rate due to small shifts in the position of the peaks, but these effects are minimal.

2.4. Conclusions

To the best of our knowledge, this work is the first example of an electrochemical platform that allows for the quantitative control of both the electron and proton transfer rates to a single molecular catalyst without changing its identity. For the CuBTA ORR catalyst studied here, tuning the relative rates of proton and electron transfer enable the catalytic activity to be substantially enhanced by (297 ± 73)% compared to the lipid-only case. We envision that this sort of electrode scheme will enable researchers to elucidate the kinetic parameters needed for optimal catalysis, not only for the ORR, but for any reaction involving the transfer of protons and electrons.

2.5. References

1. C. J. Chang, M. C. Y. Chang, N. H. Damrauer, D. G. Nocera, *Biochim. Biophys. Acta* **2004**, *1655*, 13-28.
2. D. R. Weinberg, C. J. Gagliardi, J. F. Hull, C. F. Murphy, C. A. Kent, B. C. Westlake, A. Paul, D. H. Ess, D. G. McCafferty, T. J. Meyer, *Chem. Rev.* **2012**, *112*, 4016-4093.
3. J. M. Mayer, I. J. Rhile, *Biochim. Biophys. Acta* **2004**, *1655*, 51-58.
4. C. A. Farberow, A. Godinez-Garcia, G. Peng, J. F. Perez-Robles, O. Solorza-Feria, M. Mavrikakis, *ACS Catalysis* **2013**, *3*, 1622-1632.
5. L. Trotochaud, S. L. Young, J. K. Ranney, S. W. Boettcher, *J. Am. Chem. Soc.* **2014**, *136*, 6744-6753
6. C. M. Che, K. Lau, T. C. Lau, C. K. Poon, *J. Am. Chem. Soc.* **1990**, *112*, 5176-5181.
7. K.-F. Chin, K.-Y. C.-M. Wong, *J. Chem. Soc. Dalton* **1993**, *1*, 197-198.
8. A. M. Pasqualeti, E. Padgett, D.-Y. Kuo, D. A. Muller, F. H. B. Lima, J. *J.* Suntivich, *Electrochem. Soc.* **2017**, *164*, F645-F650.
9. J. Suntivich, H. A. Gasteiger, N. Yabuuchi, H. Nakanishi, J. B. Goodenough, Y. Shao-Horn, *Nat. Chem.* **2011**, *3*, 546.
10. J. A. Herron, J. Jiao, K. Hahn, G. Peng, R. R. Adzic, M. Mavrikakis, *Electrocatalysis* **2012**, *3*, 192-202.
11. D. Banham, F. Feng, K. Pei, S. Ye, V. *J.* Birss, *Mater. Chem. A* **2013**, *1*, 2812-2820.
12. A. A. Gewirth, M. S. Thorum, *Inorg. Chem.* **2010**, *49*, 3557-3566.
13. A. J. Bard, L. R. Faulkner, *Electrochemical Methods: Fundamentals and Applications*, 2nd ed., John Wiley & Sons, Inc. Hoboken, NJ, 2001.
14. J. L. Oberst, M. S. Thorum, A. A. Gewirth, *J. Phys. Chem. C* **2012**, *116*, 25257-25261.
15. R. Boulatov, J. P. Collman, I. M. Shiryaeva, C. J. Sunderland, *J. Am. Chem. Soc.* **2002**, *124*, 11923-11935.
16. C. C. L. McCrory, X. Ottenwaelder, T. D. P. Stack, C. E. D. Chidsey, *J. Phys. Chem. A* **2007**, *111*, 12641-12650.
17. C. E. D. Chidsey, *Science* **1991**, *251*, 919.
18. J. P. Collman, N. K. Devaraj, T. P. A. Eberspacher, C. E. D. Chidsey, Langmuir **2006**, *22*, 2457-2464.
19. N. K. Devaraj, R. A. Decreau, W. Ebina, J. P. Collman, C. E. D. Chidsey, *J. Phys. Chem. B* **2006**, *110*, 15955-15962.
20. C. J. Barile, E. C. M. Tse, Y. Li, T. B. Sobyra, S. C. Zimmerman, A. Hosseini, A. A. Gewirth, *Nat. Mater.* **2014**, *13*, 619-623.
21. E. C. M. Tse, C. J. Barile, N. A. Kirchschlager, Y. Li, J. P. Gewargis, S. C. Zimmerman, A. Hosseini, A. A. Gewirth, *Nat. Mater.* **2016**, *15*, 754-759.
22. C. J. Barile, E. C. M. Tse, Y. Li, J. P. Gewargis, N. A. Kirchschlage, S. C. Zimmerman, A. A. Gewirth, *Biophys. J.* **2016**, *110*, 2451-2462.
23. L. Angnes, E. M. Richter, M. A. Augelli, G. H. Kume, *Anal. Chem.* **2000**, *72*, 5503-5506.

24. J. P. Collman, R. A. Decréau, H. Lin, A. Hosseini, Y. Yang, A. Dey, T. A. Eberspacher, *P. Natl. Acad. Sci. U.S.A.* **2009**, *106*, 7320.
25. E. C. M. Tse, C. J. Barile, J. P. Gewargis, Y. Li, S. C. Zimmerman, A. A. Gewirth, *Anal. Chem.* **2015**, *87*, 2403-2409.
26. M. S. Thorum, J. Yadav, A. A. Gewirth, *Angew. Chem. Int. Edit.* **2009**, *48*, 165-167.
27. N. K. Devaraj, R. A. Decreau, W. Ebina, J. P. Collman, C. E. D. Chidsey, *J. Phys. Chem. B* **2006**, *110*, 15955-15962.
28. X. Han, S. Bian, Y. Liang, K. N. Houk, A. B. Braunschweig, *J. Am. Chem. Soc.* **2014**, *136*, 10553-10556.
29. Y. Li, E. C. M. Tse, C. J. Barile, A. A. Gewirth, S. C. Zimmerman, *J. Am. Chem. Soc.* **2015**, *137*, 14059-14062.
30. M. S. Thorum, J. Yadav, A. A. Gewirth, *Angew. Chem. Int. Edit.* **2009**, *48*, 165-167.
31. L. Iannazzo, D. Soroka, S. Triboulet, M. Fonvielle, F. Compain, V. Dubée, J.-L. Mainardi, J.-E. Hugonnet, E. Braud, M. Arthur, M. Etheve-Quelquejeu, *J. Med. Chem.* **2016**, *59*, 3427-3438.
32. M. A. Thorseth, C. E. Tornow, E. C. M. Tse, A. A. Gewirth, *Coordin. Chem. Rev.* **2013**, *257*, 130-139.
33. A. A. Gewirth, J. A. Varnell, A. M. DiAscro. *Chem. Rev.* **2018**, *118*, 2313-2339.
34. Y. Li, E. C. M. Tse, C. J. Barile, A. A. Gewirth, S. C. Zimmerman, *J. Am. Chem. Soc.* **2015**, *137*, 14059-14062.
35. E. Laviron, *J. Electroanal. Chem. Interf. Electrochem.* **1974,** *52*, 355-393.
36. A. Hosseini, C. J. Barile, A. Devadoss, T. A. Eberspacher, R. A. Decreau, J. P. Collman, *J. Am. Chem. Soc.* **2011**, *133*, 11100-11102.

Chapter 3: Nitrile-Facilitated Proton Transfer for Enhanced Oxygen Reduction by Hybrid Electrocatalysts

3.1. Introduction

Energy catalysis powered by alternative energy sources holds the promise to a sustainable society.[1-6] Broadly speaking, energy catalysis encompasses renewable fuel generation and utilization as well as electrochemical energy conversion and storage.[7-12] Low-temperature polymer electrolyte membrane fuel cells (PEMFCs) are considered to be a next-generation technology for the transportation sector, and the oxygen reduction reaction (ORR) is the chemical reaction occurring at a PEMFC cathode that fundamentally limits the overall performance of a PEMFC.[13-15] The ORR is challenging to optimize because multiple proton and electron transfer steps are involved while partially reduced oxygen species (PROS) such as hydrogen peroxide and superoxide can be generated as deleterious side products.[16-20] Currently, state-of-the-art catalysts consist of Pt on carbon (Pt/C), which is scarce and thus expensive.[21-23] Non-precious metal (NPM) alternatives have been actively explored as alternatives to Pt as ORR electrocatalysts.[24-27] Although commercial PEMFCs operate under acidic conditions to enhance the proton conductance of the Nafion membranes, Fe/N/C nanomaterials under alkaline conditions possess selectivity and activity for the ORR that rivals those of Pt/C catalysts.[28-30] However, when compared to ORR enzymes such as laccase in nature,[31] there is still plenty of room for improvements regarding the activity and selectivity of artificial catalysts.[32-34]

To enhance the activity and selectivity of ORR electrocatalysts, more thorough understanding and control of the proton and electron transfer steps involved in the ORR is necessary.[1, 35-37] Immense spectroscopic and theoretical efforts have been invested to reveal that both proton transfer and electron transfer play major roles in dictating the ORR mechanism.[38-43] Recently, hybrid bilayer membranes (HBMs) have been developed as an

experimental platform to regulate independently the thermodynamics and kinetics of proton and electron transfer steps (Figure 3.1).[44-48] A HBM consists of a lipid monolayer appended on top of a self-assembled monolayer (SAM),[49] thereby allowing us to take advantage of the knowledge gained through biophysical and spectroscopic membrane studies.[50-53] HBMs with transition metal complexes installed at the SAM-lipid interface have been utilized as versatile electrochemical platforms to regulate electrocatalytic processes that involve multiple proton and electron transfer steps.[54] The catalytic sites embedded in HBM systems usually contain NPM ORR catalysts or ferrocene- or quinone-based redox probes.[55-57] Previously, HBM constructs containing 1,2-dimyristoyl-*sn*-glycero-3-phosphocholine (DMPC) lipid with catalytic amounts of 1-dodecylboronic acid (DBA) added in the lipid layer were used to regulate reaction pathways and product selectivity of the ORR.[45] DBA undergoes a "flip-flop" diffusion mechanism to deliver protons from the external bulk solution through the hydrophobic tail region of the lipid layer to the embedded ORR catalytic unit.[58] Control over ORR activity and selectivity is achieved by tuning the thermodynamics and kinetics of proton and electron transfer processes independently.[59]

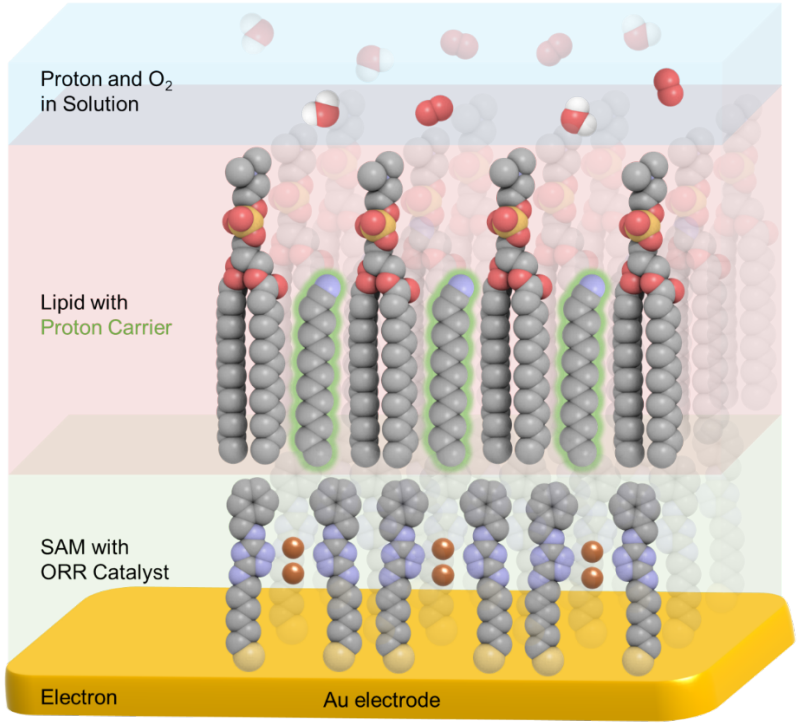

Figure 3.1. Schematic of the HBM electrochemical platform utilized to widen the pH window for proton delivery across lipid membranes for O_2 reduction.

HBMs can be used to turn on and off the ORR activity of an embedded catalytic unit via several means. A light-triggered proton switch was achieved using a stiff-stilbene proton transfer agent incorporated into the lipid layer of a HBM.[60] A pH-sensitive proton switch has also been realized by using mono-*N*-dodecylphosphate (MDP) as the proton carrier.[44] However, up until now, no proton switch can be turned on in basic condition and off in acidic condition. This limitation is due to the mode of proton delivery used in HBMs. Known proton transfer agents rely on protonation of acidic head groups to form neutral moieties that are hydrophobic enough to penetrate the hydrophobic tail region of the lipid layer. This protonation-based working principle renders the transmembrane proton

delivery process unfavourable in basic conditions. New modes of proton transfer in HBMs could overcome this limitation.

In this work, we utilize a bioinspired strategy to design HBMs with active proton carriers under alkaline conditions. In nature, protonophores uncouple oxidative phosphorylation by decreasing the inner mitochondria membrane potential via proton translocation through lipids across a wide pH range.[61] Here, inspired by the cyano (CN) functional groups found in typical protonophores, alkyl-CN molecules are designed and synthesized as membrane-associated proton carriers in HBM platforms. In our HBM construct, the ORR catalyst is a dinuclear Cu complex of a benzyltriazolethiol (BTT) ligand, which is similar in structure to one of the best performing artificial di-Cu molecular ORR catalysts.[62-64] The BTT unit is also equipped with a hexylthiolate arm to form a uniform SAM on Au with an electron transfer rate fast enough to support the ORR as well as a phenyl prosthetic group to facilitate Van der Waal's interaction between the hydrophobic DMPC lipid tail and the aromatic ring (Figure. 3.2). ORR activity is then used to gauge the proton transfer performance of the new class of CN-based proton delivery agents. The overall goal is to develop unique CN-based proton carriers with a new proton transfer mechanism to deliver protons, thereby filling this knowledge gap and facilitating ORR investigations under basic conditions.

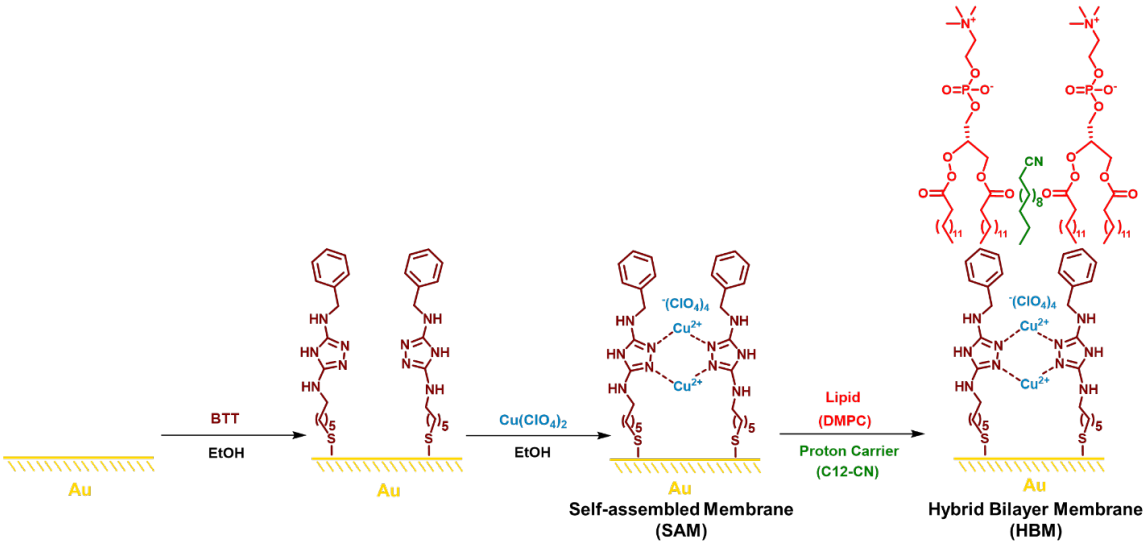

Figure 3.2. Preparation scheme of hybrid bilayer membrane (HBM) platform containing bio-inspired CN-based proton carriers with tailorable transmembrane proton delivery rates to a non-precious Cu ORR electrocatalyst under basic conditions.

3.2. Methods and Materials

Chemicals were obtained from commercial sources and used without further purification unless otherwise specified. For experiments from pH 6 to 9, potassium phosphate buffer solutions (100 mM) were prepared using Milli-Q water (> 18 MΩ cm) and adjusted to the desired pH using H_3PO_4 (85 wt % ACS reagent grade, Sigma-Aldrich) and NaOH (analytical grade, Dieckmann Chemical). Solutions were sparged with N_2 (99.995% high purity grade, Linde HKO) and O_2 (99.995% high purity grade, Linde HKO) for 30 min prior to each experiment.

Electrochemical studies were carried out using a 660E Electrochemical Workstation (CH Instruments). For studies in aqueous solutions a three-electrode cell was used with a carbon counter electrode. Electrochemical potentials are measured and reported with respect to a “no-leak” Ag/AgCl (3 M KCl, ESA Inc.) reference electrode. A Ti adhesion layer (20 nm), followed by an Au layer (100 nm), was deposited on microscope

glasses (11 mm in length × 11 mm in width × 1 mm in thickness) as electrodes using an electron-beam vacuum evaporator (Kao Duen Tech. Corp.). The Au working electrodes were rinsed with water and EtOH prior to use.

The experiments were conducted at room temperature (26 ± 1) °C and low temperature (4±1) °C. For voltammetry collected under N_2 and O_2, the scan rate was 100 and 10 mV/s, respectively. For blocking experiments using 1 mM $K_3Fe(CN)_6$ in 100 mM KCl solution, the scan rate was 50 mV/s.

Preparation of the HBM system was reported elsewhere.[44, 45] In short, 6-((3-(benzylamino)-1,2,4-triazol-5-yl)amino)hexane-1-thiol (BTT) was synthesized and deposited as a SAM on an Au working electrode. Cu ions were incorporated into the BTT-modified Au surface using an ethanolic solution of $Cu(ClO_4)_2$, which was then embedded inside a monolayer of 1,2-dimyristoyl-*sn*-glycero-3-phosphocholine (DMPC) with 1 equivalent of tridecanenitrile (C12-CN) molecule. HBMs incorporated with other proton carriers mentioned in this paper were all prepared in the same manner.

Caution! Perchlorate salts are potentially explosive. Only small amounts of materials should be prepared.

3.3. Results and Discussion

3.3.1. Designing an Active Proton Carrier under Alkaline Conditions

To widen the effective pH range for proton delivery in HBM, C12-CN was chosen as a potential proton carrier candidate based on its molecular features and favorable lipid permeable parameter (LPP), which suggests it easily diffuses across lipid membranes (see SI note 3.1 and Figure S3.1).[49] C12-CN exhibits an alkyl tail length similar to previous

proton transfer agents such as DBA and MDP that work well with DMPC-appended HBM systems [44, 45] C12-CN also displays a LPP value larger than DBA and MDP, potentially rendering C12-CN more efficient at proton delivery.

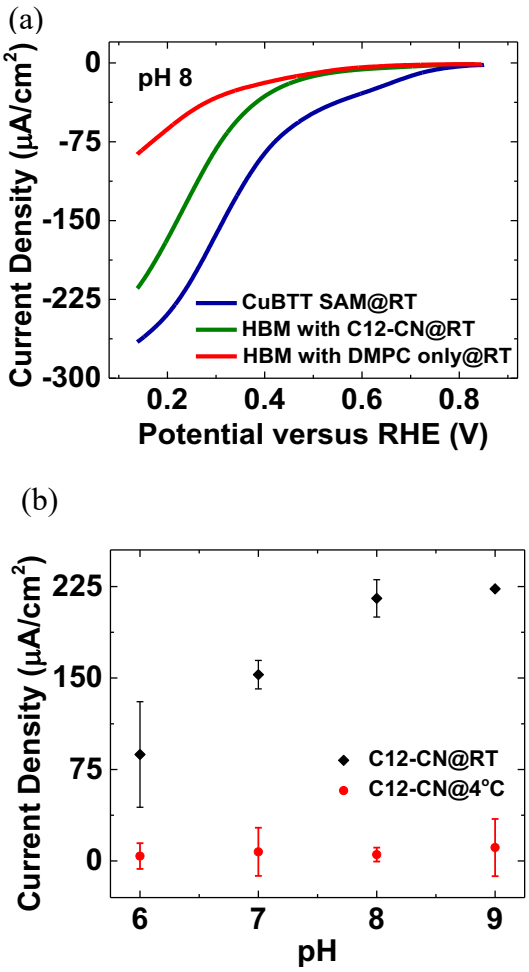

Figure 3.3. (a) O_2 reduction reaction (ORR) linear sweep voltammograms (LSVs) of a SAM of CuBTT (blue), with a monolayer of DMPC appended (red), and with 1 equivalent of C12-CN in the lipid layer (green) in O_2-saturated pH 8 phosphate buffer at a scan rate of 10 mV s^{-1}. (b) Maximum cathodic current densities measured at 0.137 V vs. RHE of a SAM of CuBTT covered by a monolayer of DMPC with 1 equivalent of C12-CN added to the DMPC layer on Au at room temperature (RT, black) and 4 °C (red) as a function of pH.

Taking these molecular design features into consideration, we conducted electrochemical experiments to investigate the proton delivery ability of C12-CN in a HBM construct. Here, ORR was used as a proxy readout to quantify the effectiveness of C12-CN at ferrying protons across DMPC membrane because ORR contains PCET steps. Figure 3.3a shows LSVs of the HBM system with C12-CN in pH 8 aqueous solutions saturated with O_2. The CuBTT electrocatalyst displays an ORR onset potential at (0.718 ± 0.001) V vs. RHE and a current density of (270 ± 36) μA/cm^2 at 0.137 V vs. RHE (Figure 3.3a, blue line) at pH 8. Upon appending a DMPC lipid layer on top of the CuBTT SAM, the onset potential shifts to (0.487 ± 0.042) V vs. RHE and the current density measured decreased to (88 ± 8) μA/cm^2 (Figure 3a, red line). This (181 ± 27) μA/cm^2 decrease in current density is likely caused by the hydrophobicity of the DMPC layer, which limits proton availability to CuBTT. The integrity of the DMPC layer before and after ORR was verified by an electrochemical blocking test using ferrocyanide (Figure S2.2c). Upon incorporating C12-CN into the lipid layer, the ORR onset potential remains at (0.528 ± 0.006) V vs. RHE (Figure 3.3a, green line), suggesting that there is minimal change to the thermodynamics of the HBM system. Intriguingly, the ORR current density of CuBTT embedded inside a HBM containing C12-CN is revived to (215 ± 15) μA/cm^2, a value higher than the DMPC only case by (126 ± 6) μA/cm^2 and lower than the CuBTT-SAM system by (55 ± 20) μA/cm^2. This recovery in ORR activity is likely due to C12-CN facilitating proton delivery from the bulk solution through the DMPC layer to the underlying CuBTT SAM. These results suggest that C12-CN restores the proton transfer kinetics across a lipid membrane at pH 8, a property not observed in previously used proton carriers such as DBA or MDP.

We next investigated the ability of C12-CN to deliver protons across membranes in pH 6, 7, and 9. Figure 3.3b shows the ORR current density measured at 0.137 V vs. RHE using HBM systems bearing C12-CN as the proton carrier. HBM containing C12-CN exhibits a low ORR current density of around (87 ± 43) μA/cm^2 at pH 6, indicating that transmembrane proton transfer by C12-CN is limited under a mildly acidic condition. The ORR activity observed increases as the pH of the bulk solution increases to 7, reaches a maximum at pH 8, and plateaus at pH 9 at ca. (223 ± 1) μA/cm^2 (Figure 3.3b and S3.3). Low temperature studies at 4 °C in pH 6-9 demonstrate that the ORR activity of HBMs containing C12-CN in the lipid layer is suppressed at temperatures below the gel-phase transition temperature of DMPC,[44, 65] corroborating that protons are delivered via a flip-flop diffusion mechanism (Figure S3.4).[44, 45, 58] Electrochemical blocking experiments with ferrocyanide confirmed that the integrity of the lipid layer in the HBMs containing C12-CN remains intact and relatively pinhole-free between pH 6-9 (Figure S3.2). Taken together, these results demonstrate that enhanced transmembrane proton transfer can be achieved under alkaline conditions in a HBM system for the first time.

3.3.2. Identifying the Molecular Site Responsible for Proton Delivery

C12-CN was chosen as a proton carrier due to the presence of the CN group that is found in CN-containing protonophores in nature. However, for C12-CN, there is no obvious protonation site for proton transfer due to the high pKa of tridecanenitrile. In lieu of the lack of a basic function group to bind a proton, other molecular features that might lead to proton delivery are then explored. The protons on the carbon next to the CN group are potential candidates, though the mechanism of such proton delivery is ambiguous. Molecular modifications to C12-CN were then designed to probe the role of these α-

protons, and C12-CN will be termed as C12-CN-2H in the sections 3.2.2 and 3.2.3 to highlight the structural modifications used as well as make the comparison among the C12-CN derivatives easier to follow.

We synthesized additional proton carriers in which the α-protons of C12-CN-2H are switched to methyl groups to test the hypothesis that α-protons are responsible for transmembrane proton transfer activities. Figure 3.4 displays LSVs of HBMs containing C12-CN with 0, 1, or 2 α-protons replaced by methyl groups, which are named as C12-CN-2H, C12-CN-H-Me, and C12-CN-2Me, respectively. Compared to C12-CN-2H, C12-CN-H-Me displays a (39 ± 11) % decrease in ORR activity (Figure 3.4, orange line), while C12-CN-2Me exhibits a (65 ± 12) % decrease in ORR activity. The current density measured for C12-CN-2Me is similar to DMPC only, indicating that C12-CN with 2 α-methyl groups lacks any significant proton transfer capability. The proportional trend observed between proton transfer capacity and number of α-methyl groups adjacent to the CN chain-end groups suggest that the α-protons in C12-CN-2H are associated with delivering protons across the lipid membrane of HBMs.

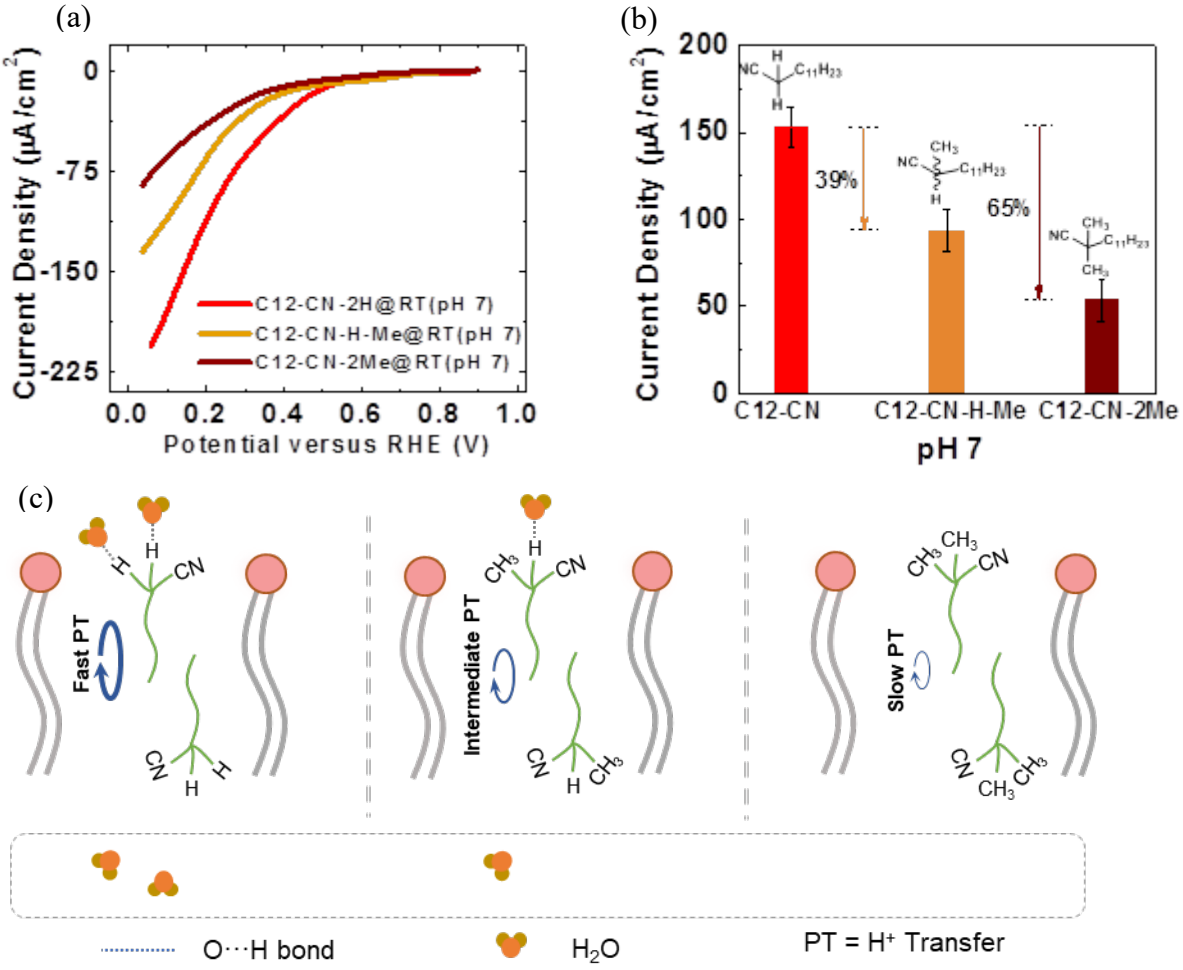

Figure 3.4. (a) O_2 reduction CVs of a HBM containing C12-CN-2H (red), C12-CN-HMe (orange), and C12-CN-2Me (brown) in O_2-saturated pH 7 phosphate buffer at a scan rate of 10 mV s^{-1}. (b) ORR current density measured at 0.137 V vs. RHE of HBMs containing C12-CN (red), C12-CN-H-Me (orange), and C12-CN-2Me (brown) in O_2-saturated pH 7 phosphate buffer. (c) Schematic depicting how C12-CN-2H delivers protons at a higher rate than C12-CN-HMe, which is in turn faster than C12-CN-2Me across the lipid layer of a HBM for O_2 reduction.

3.3.3. Elucidating the Mechanism of Proton Transfer via Deuterated Studies

To investigate if the enhanced proton transfer activity is due to a direct or indirect involvement of the α-protons, we also synthesized nitrile proton carriers with selectively deuterated α-protons. The synthesized C12-CN carriers with 1 or 2 α-protons replaced by

deuterons (C12-CN-HD and C12-CN-2D) were used to examine if direct deprotonation and re-protonation occurs at the α position. Solid lines in Figure 3.5a-c represent the ORR LSVs in pH 7 buffer of HBMs containing C12-CN-2H, C12-CN-HD, and C12-CN-2D, respectively. Compared to C12-CN-2H (Figure 3.5a, solid line), C12-CN-HD displays a (43 ± 3) % decrease in ORR activity (Figure 3.5b, solid line), while C12-CN-2D exhibits a (64 ± 4) % decrease in ORR activity (Figure 3.5c, solid line). The current density measured for C12-CN-2D is similar to DMPC only, indicating that C12-CN with 2 α-deuterons lacks any significant proton transfer capability (Figure S3.5). The proportional trend observed between proton transfer capacity and number of α-deuterons adjacent to the CN chain-end groups suggest that the α-protons in C12-CN-2H are required for efficient proton delivery across the lipid membrane of HBMs.

Now that the importance of the α-protons in C12-CN-2H for transmembrane proton transfer has been established, we next explore the potential proton transfer mechanism of CN-based proton carriers. One possible mechanism requires the *direct* consumption of the α-protons, and the other mechanism involves an *indirect* involvement of the α-protons.

(a)

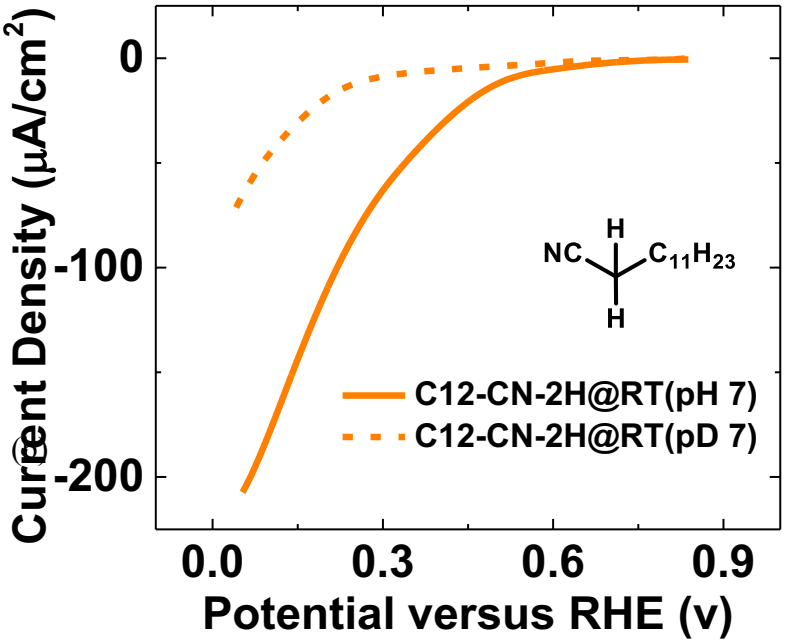
0
-100
-200
Current Density (μA/cm²)
0.0
0.3
0.6
0.9
Potential versus RHE (v)
NC
H
C11H23
H
C12-CN-2H@RT(pH 7)
C12-CN-2H@RT(pD 7)

(b)

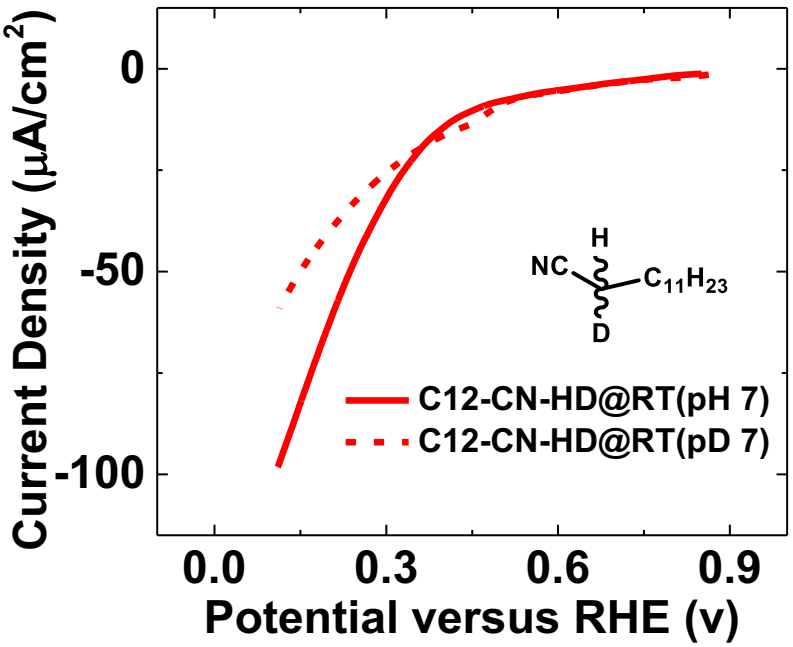
0
-50
-100
Current Density (μA/cm²)
0.0
0.3
0.6
0.9
Potential versus RHE (v)
NC
H
D
C11H23
C12-CN-HD@RT(pH 7)
C12-CN-HD@RT(pD 7)

(c)

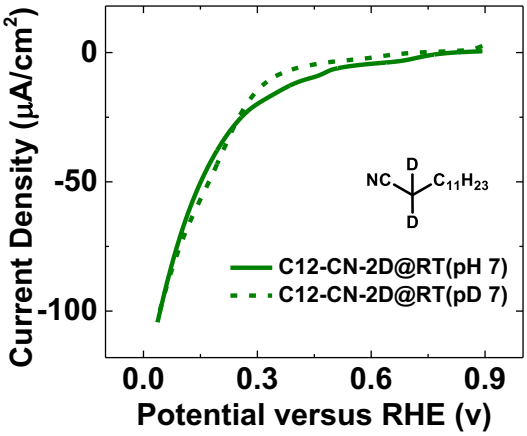
Current Density (μA/cm²)
0
-50
-100
0.0
0.3
0.6
0.9
Potential versus RHE (v)
NC
D
C11H23
D
C12-CN-2D@RT(pH 7)
C12-CN-2D@RT(pD 7)

(d)

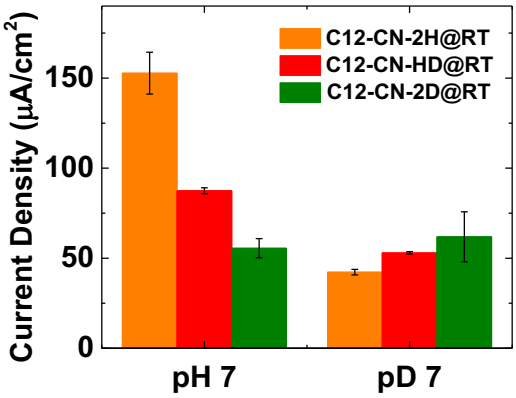
Current Density (μA/cm²)
150
100
50
0
C12-CN-2H@RT
C12-CN-HD@RT
C12-CN-2D@RT
pH 7
pD 7

(e)

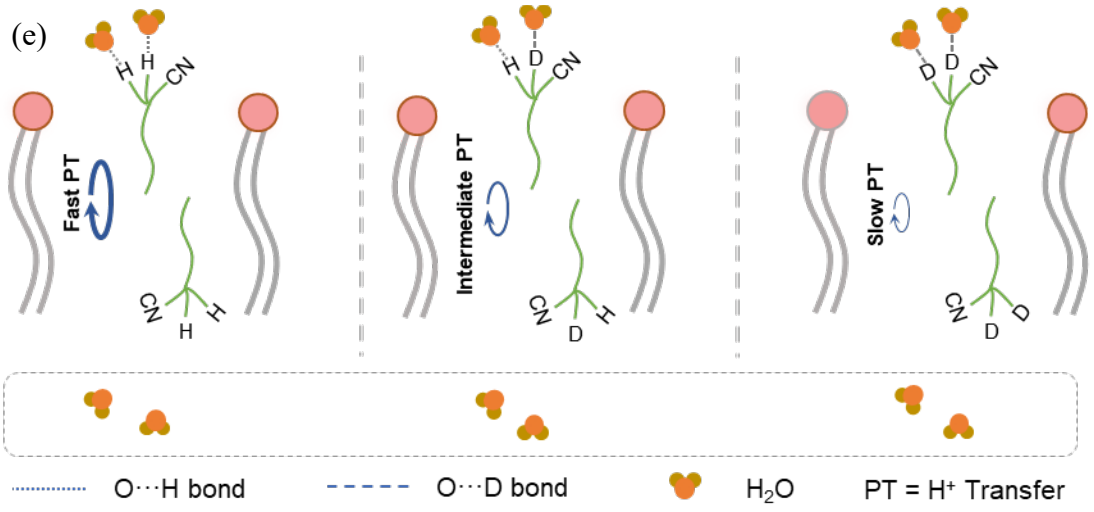
Fast PT
Intermediate PT
Slow PT
O···H bond
O···D bond
H2O
PT = H+ Transfer

Figure 3.5. O_2 reduction CVs of HBMs containing one equivalent of (a) C12-CN-2H (orange), (b) C12-CN-HD (red), and (c) C12-CN-2D (green) in O_2-saturated pH 7 and pD 7 phosphate buffer at a scan rate of 10 mV s^{-1}. (d) ORR current density measured at 0.137 V vs. RHE of HBMs containing C12-CN-2H (orange), C12-CN-HD (red), and C12-CN-2D (green) in O_2-saturated pH 7 and pD 7 phosphate buffer. (e) Schematic illustrating how C12-CN-2H delivers protons at a higher rate than C12-CN-HD, which is in turn faster than C12-CN-2D across the lipid layer of a HBM for O_2 reduction.

We first explore whether the direct consumption of the α-protons is a viable mechanism. If the α-protons are consumed during the proton delivery process, the α-position of these proton carriers would be replenished by protons in the bulk solution. For the case of C12-CN-2D in pH 7 buffer shown in Figure 3.5c, if the direct consumption of α-protons mechanism is at play, the α-deuterons would be exchanged by protons in the protic bulk solution. As only a catalytic amount of proton carrier is present in the lipid layer (see Appendices SI note 3.6 and Figure S3.6), if deprotonation occurs at the α-position, the deuteron would be expected to be removed and then replaced by a proton available in the bulk solution, thereby leading to an anticipated revival of the ORR current to a level similar to that of C12-CN-2H. However, the ORR activity of C12-CN-2D did not recover after passing a current density of (5.2 ± 0.1) μA/cm^2, the point at which all the deuterons in C12-CN-2D would have been replaced if the α-deuterons were consumed directly. Analogous logic can be applied to the C12-CN-HD case to demonstrate that α-protons and α-deuterons were not consumed and replaced during ORR in HBM. Together with the trend observed across Figure 3.5a-c in which an increasing number of deuterons result in a decrease in proton delivery activity, these results suggest that α-protons do not undergo direct deprotonation during proton transfer to the CuBTT ORR catalytic site.

The next possible mechanism for proton transfer by alkyl nitriles is for it to be mediated by water molecules associated to the nitrile head groups via hydrogen bonds. To interrogate if CN-based proton carriers transport water across lipid membranes, ORR LSVs of HBMs containing C12-CN-2H, C12-CN-HD, and C12-CN-2D were recorded in pD 7 buffer solutions (Figure 3.5a-c, dashed lines). The ORR current densities found for HBMs with C12-CN-2H and C12-CN-HD in pD 7 were found to be less than those in pH 7. In all cases, upon using a deuterated buffer solution, the proton transfer abilities observed of C12-CN-2H, C12-CN-HD, and C12-CN-2D were similar to that found for the DMPC only case in pH 7 (Figure S3.7), suggesting that proton/deuteron delivery was significantly inhibited in pD 7.

Figure 3.5d summarizes two major effects of deuterating the α-position and the bulk solution on the ORR current densities recorded at 0.137 V vs. RHE. First, deuteration at the α-position decreases the ORR current density measured in pH 7 while minimally affecting that in pD 7. Second, all ORR current densities observed in pD 7 are similar to the case with C12-CN-2D in pH 7 and the DMPC-only control case. These observed trends are a consequence of stronger deuteron bonding as compared to hydrogen bonding, a phenomenon that has been observed previously.[66-69] Previous studies have established that the rate-determining step (RDS) of the ORR in a HBM system is the physical flip-flop diffusion step of the proton carrier going through the lipid layer of the HBM.[44,45] Combining these two pieces of information, we posit that D_2O is bound to proton carriers in all pD 7 cases more tightly than H_2O bound to proton carriers in all pH 7 cases. Specifically, slow deuteron dissociation from the proton carrier to the embedded CuBTT catalytic unit is expected in pD 7. Analogously, in pH 7 cases, deuteration at the α-position

results in forming tighter H_2O…D bonds, thereby lowering the deprotonation step in which a proton from H_2O is transferred to the CuBTT catalytic moiety. Taken together, we propose that alkyl nitrile proton carriers utilize hydrogen-bonded water as a proton carrier to deliver protons across lipid membranes from bulk solution to the CuBTT active site embedded in the HBM.

(a)

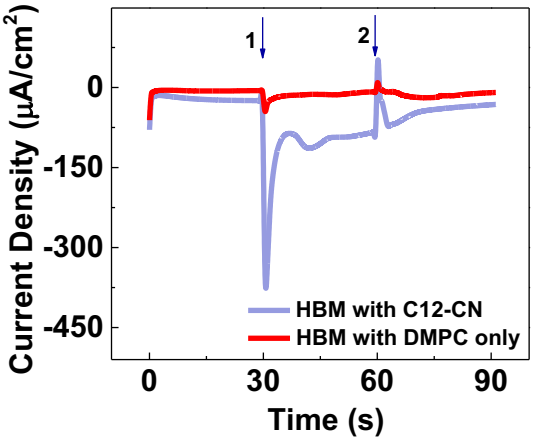

(b)

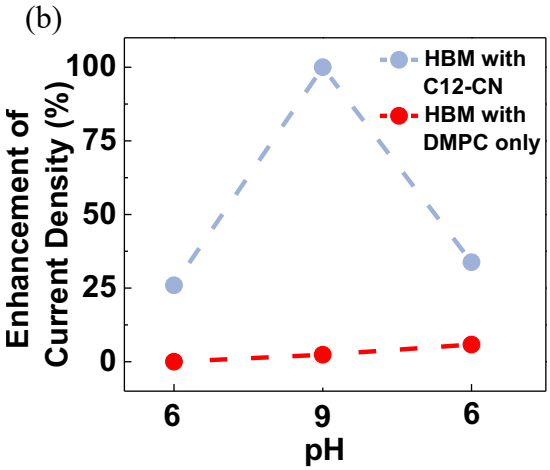

Figure 3.6. (a) Chronoamperometry of CuBTT on Au covered by lipid (red) with C12-CN incorporated (blue) in O_2-saturated pH 6 buffer solution at 0.137 V vs. RHE. NaOH was added after 30 s (arrow 1) to adjust the solution to pH 9 and H_3PO_4 was added after 60 s (arrow 2) to adjust the solution to pH 6. (b) pH-dependent ORR current density enhancement of CuBTT on Au covered by lipid (red) with C12-CN incorporated (blue).

Each data point is averaged across the current density observed over the 5 s period right before each pH jump is triggered.

To demonstrate the feasibility of switching on proton delivery under alkaline conditions, a HBM containing C12-CN in the lipid layer is subjected to a pH-jump experiment in which the pH of the solution is toggled between pH 6 and 9. Figure 3.6a shows the ORR current response of HBMs with and without C12-CN in the lipid layer over a period of 90 s while holding the electrode potential at 0.137 V vs. RHE with the solution initially set to pH 6. Base was added after 30 s (arrow 1) to adjust the solution pH from 6 to 9, and subsequently acid was added after 60 s (arrow 2) to adjust the solution pH from 9 back to 6. For the control case without C12-CN, the ORR activity remains relatively constant throughout the whole 90 s period (Figure 3.6a, red line). This observation indicates that a change in pH does not alter the transmembrane proton kinetics as no proton carrier is present in the lipid layer of the HBM (Figure 3.6b, red).

For the case with C12-CN added to the DMPC layer of a HBM, the ORR activity recorded for the HBM with C12-CN is similar to the DMPC only case between 0 and 30 s (Figure 3.6a, blue line). This observation matches with the trend observed in Figure 3.3b that C12-CN does not transfer protons efficiently across the DMPC lipid layer in pH 6. After switching to pH 9 at 30 s, the ORR activity of the HBM containing C12-CN increases significantly (Figure 3.6a, blue line). The observed 70% boost in current density enhancement indicates that the proton switch is in the “on” state and that C12-CN delivers protons from the bulk solution across the lipid membrane to the CuBTT ORR catalytic site efficiently at pH 9 (Figure 3.6b, blue). Upon switching the solution pH back to 6 at 60 s, the ORR activity decreases to a level similar to the case at “0 s” time point. This observation

indicates that the proton switch is turned off and proton transfer at pH 6 is inhibited. Taken together, a unique proton switch that operates by turning off under acidic condition and turning on under basic condition is constructed and its utility in regulating the activity of an ORR catalyst is demonstrated.

3.4. Conclusions

In this report, a major bottleneck in the field of artificial transmembrane proton transfer has been overcome. Previously, proton switches could only be turned on upon acidification in hybrid bilayer membrane (HBM) electrocatalytic platforms. Here, a protonophore-inspired alkyl-CN has been developed to trigger and facilitate proton delivery across the lipid membrane of a HBM upon basification with high H^+ transfer kinetics under pH 8 and 9 against the proton gradient. Supported by low temperature, selective methylation, and isotopic labelling studies, the proton transfer mechanism was found to be consistent with the "flip-flop" diffusion mechanism. Unlike previous boronic acid and phosphate-based proton carriers, the alkyl-CN proton transfer agent was determined to facilitate proton delivery through bound water molecules that were hydrogen-bonded to the α-protons immediately adjacent to the CN functional group. The applicability of this unique proton gate was demonstrated through an "on-off-on" experiment. The alkyl-CN proton switch can be turned from the "off" state to the "on" state by adjusting the pH from 6 to 9 and vice versa in an *in-situ* fashion. The breakthroughs achieved by the designer proton carriers synthesized in this study represent the first example of enhancing proton delivery under basic conditions in an HBM for oxygen reduction electrocatalysis, and these proton regulators are envisioned to be broadly useful for studying other redox processes that involve electron and proton transfer steps.

3.5. References

1. W. Cheng, X. Zhao, H. Su, F. Tang, W. Che, H. Zhang, Q. Liu, *Nat. Energy* **2019**, *4*, 115-122.
2. G. Wu, K. L. More, C. M. Johnston, P. Zelenay, *Science* **2011**, *332*, 443-447.
3. B. Demir, T. Kropp, K. R. Rivera-Dones, E. B. Gilcher, G. W. Huber, M. Mavrikakis, J. A. Dumesic, *Proc. Natl. Acad. Sci. U.S.A.* **2020**, *117*, 3446-3450.
4. G. Liu, A. W. Robertson, M. M.-J. Li, W. C. H. Kuo, M. T. Darby, M. H. Muhieddine, Y.-C. Lin, K. Suenaga, M. Stamatakis, J. H. Warner, S. C. E. Tsang, *Nat. Chem.* **2017**, *9*, 810-816.
5. C. Di Giovanni, W.-A. Wang, S. Nowak, J.-M. Grenèche, H. Lecoq, L. Mouton, M. Giraud, C. Tard, *ACS Catalysis* **2014**, *4*, 681-687.
6. C. Costentin, C. Di Giovanni, M. Giraud, J.-M. Savéant, C. Tard, *Nat. Materials* **2017**, *16*, 1016.
7. L. Fan, C. Xia, F. Yang, J. Wang, H. Wang, Y. Lu, *Sci. Adv.* **2020**, *6*, eaay3111.
8. F. Jaouen, E. Proietti, M. Lefèvre, R. Chenitz, J.-P. Dodelet, G. Wu, H. T. Chung, C. M. Johnston, P. Zelenay, *Energy Environ. Sci.* **2011**, *4*, 114-130.
9. M. Faustini, M. Giraud, D. Jones, J. Rozière, M. Dupont, T. R. Porter, S. Nowak, M. Bahri, O. Ersen, C. Sanchez, C. Boissière, C. Tard, J. Peron, *Advanced Energy Materials* **2019**, *9*, 1802136.
10. S. I. Chan, S. S. F. Yu, *Nat. Catal.* **2019**, *2*, 286-287.
11. T. Liu, Z. Zhou, Y. Guo, D. Guo, G. Liu, *Nat. Commun.* **2019**, *10*, 675.
12. C. Costentin, S. Drouet, G. Passard, M. Robert, J.-M. Savéant, *J. Am. Chem. Soc.* **2013**, *135*, 9023-9031.
13. J. Wu, X. Z. Yuan, J. J. Martin, H. Wang, J. Zhang, J. Shen, S. Wu, W. Merida, *J. Power Sources* **2008**, *184*, 104-119.
14. M. A. Thorseth, C. E. Tornow, E. C. M. Tse, A. A. Gewirth, *Coord. Chem. Rev.* **2013**, *257*, 130-139.
15. C. Chen, Y. Kang, Z. Huo, Z. Zhu, W. Huang, H. L. Xin, J. D. Snyder, D. Li, J. A. Herron, M. Mavrikakis, M. Chi, K. L. More, Y. Li, N. M. Markovic, G. A. Somorjai, P. Yang, V. R. Stamenkovic, *Science* **2014**, *343*, 1339-1343.
16. C. Costentin, M. Robert, J.-M. Savéant, *Chem. Rev.* **2010**, *110*, PR1-PR40.
17. D. R. Weinberg, C. J. Gagliardi, J. F. Hull, C. F. Murphy, C. A. Kent, B. C. Westlake, A. Paul, D. H. Ess, D. G. McCafferty, T. J. Meyer, *Chem. Rev.* **2012**, *112*, 4016-4093.
18. C. J. Chang, M. C. Y. Chang, N. H. Damrauer, D. G. Nocera, *BBA - Bioenergetics* **2004**, *1655*, 13-28.
19. J. M. Mayer, *Annu. Rev. Phys. Chem.* **2004**, *55*, 363-390.
20. J. P. Collman, A. Dey, C. J. Barile, S. Ghosh, R. A. Decréau, *Inorg. Chem.* **2009**, *48*, 10528-10534.
21. H. Yano, M. Watanabe, A. Iiyama, H. Uchida, *Nano Energy* **2016**, *29*, 323-333.
22. Y. Shao-Horn, W. C. Sheng, S. Chen, P. J. Ferreira, E. F. Holby, D. Morgan, *Top. Catal.* **2007**, *46*, 285-305.
23. X. Yang, L. T. Roling, M. Vara, A. O. Elnabawy, M. Zhao, Z. D. Hood, S. Bao, M. Mavrikakis, Y. Xia, *Nano Lett.* **2016**, *16*, 6644-6649.

24. A. A. Gewirth, J. A. Varnell, A. M. DiAscro, *Chem. Rev.* **2018**, *118*, 2313-2339.
25. Y.-J. Wu, Y.-C. Wang, R.-X. Wang, P.-F. Zhang, X.-D. Yang, H.-J. Yang, J.-T. Li, Y. Zhou, Z.-Y. Zhou, S.-G. Sun, *ACS Appl. Mater. Interfaces* **2018**, *10*, 14602-14613.
26. J. S. Kang, J. Kim, M. J. Lee, Y. J. Son, D. Y. Chung, S. Park, J. Jeong, J. M. Yoo, H. Shin, H. Choe, H. S. Park, Y.-E. Sung, *Adv. Sci.* **2018**, *5*, 1700601.
27. X. Mo, K. C. Chan, E. C. M. Tse, *Chem. Mater.* **2019**, *31*, 8230-8238.
28 U. I. Kramm, J. Herranz, N. Larouche, T. M. Arruda, M. Lefèvre, F. Jaouen, P. Bogdanoff, S. Fiechter, I. Abs-Wurmbach, S. Mukerjee, J.-P. Dodelet, *Phys. Chem. Chem. Phys.* **2012**, *14*, 11673-11688.
29. Z. Chen, D. Higgins, A. Yu, L. Zhang, J. Zhang, *Energy Environ. Sci.* **2011**, *4*, 3167-3192.
30. J. A. Varnell, E. C. M. Tse, C. E. Schulz, T. T. Fister, R. T. Haasch, J. Timoshenko, A. I. Frenkel, A. A. Gewirth, *Nat. Commun.* **2016**, *7*, 12582.
31. S. M. Jones, E. I. Solomon, *Cell. Mol. Life Sci.* **2015**, *72*, 869-883.
32. C. H. Choi, H.-K. Lim, M. W. Chung, G. Chon, N. Ranjbar Sahraie, A. Altin, M.-T. Sougrati, L. Stievano, H. S. Oh, E. S. Park, F. Luo, P. Strasser, G. Dražić, K. J. J. Mayrhofer, H. Kim, F. Jaouen, *Energy Environ. Sci.* **2018**, *11*, 3176-3182.
33. E. C. M. Tse, D. Schilter, D. L. Gray, T. B. Rauchfuss, A. A. Gewirth, *Inorg. Chem.* **2014**, *53*, 8505-8516.
34. N. Thiyagarajan, D. Janmanchi, Y.-F. Tsai, W. H. Wanna, R. Ramu, S. I. Chan, J.-M. Zen, S. S.-F. Yu, *Angew. Chem. Int. Ed.* **2018**, *57*, 3612-3616.
35. A. Jain, Y. Shin, K. A. Persson, *Nat. Rev. Mater.* **2016**, *1*, 15004.
36. Z. W. Seh, J. Kibsgaard, C. F. Dickens, I. Chorkendorff, J. K. Nørskov, T. F. Jaramillo, *Science* **2017**, *355*.
37. E. C. M. Tse, A. A. Gewirth, *J. Phys. Chem. A* **2015**, *119*, 1246-1255.
38. J. Rosenthal, D. G. Nocera, *Acc. Chem. Res.* **2007**, *40*, 543-553.
39. J. M. Mayer, I. J. Rhile, *BBA - Bioenergetics* **2004**, *1655*, 51-58.
40. M. H. V. Huynh, T. J. Meyer, *Chem. Rev.* **2007**, *107*, 5004-5064.
41. A. Soudackov, S. Hammes-Schiffer, *J. Chem. Phys.* **2000**, *113*, 2385-2396.
42. S. Hammes-Schiffer, A. V. Soudackov, *J. Phys. Chem. B* **2008**, *112*, 14108-14123.
43. E. C. M. Tse, J. A. Varnell, T. T. H. Hoang, A. A. Gewirth, *J. Phys. Chem. Lett.* **2016**, *7*, 3542-3547.
44. C. J. Barile, E. C. M. Tse, Y. Li, T. B. Sobyra, S. C. Zimmerman, A. Hosseini, A. A. Gewirth, *Nat. Mater.* **2014**, *13*, 619-623.
45. E. C. M. Tse, C. J. Barile, N. A. Kirchschlager, Y. Li, J. P. Gewargis, S. C. Zimmerman, A. Hosseini, A. A. Gewirth, *Nat. Mater.* **2016**, *15*, 754-759.
46. M. Wang, W. Zhan, *Acc. Chem. Res.* **2016**, *49*, 2551-2559.
47. L. Liu, W. Zhan, *Langmuir* **2012**, *28*, 4877-4882.
48. Z. Su, J. J. Leitch, J. Lipkowski, *Curr. Opin. Electrochem.* **2018**, *12*, 60-72.
49. E. C. M. Tse, C. J. Barile, J. P. Gewargis, Y. Li, S. C. Zimmerman, A. A. Gewirth, *Anal. Chem.* **2015**, *87*, 2403-2409.
50. P. J. Chung, H. L. Hwang, K. Dasbiswas, A. Leong, K. Y. C. Lee, *Langmuir* **2018**, *34*, 13000-13005.

51. J.-Y. Wang, W. Chen, M. Nagao, P. Shelat, B. A. G. Hammer, G. T. Tietjen, K. D. Cao, J. M. Henderson, L. He, B. Lin, B. Akgun, M. Meron, S. Qian, S. Ward, J. D. Marks, T. Emrick, K. Y. C. Lee, *Biomacromolecules* **2019**, *20*, 3385-3391.
52. Z. Su, D. Ho, A. R. Merrill, J. Lipkowski, *Langmuir* **2019**, *35*, 8452-8459.
53. Z. Su, X. Ran, J. J. Leitch, A. L. Schwan, R. Faragher, J. Lipkowski, *Langmuir* **2019**, *35*, 16935-16943.
54. T. Zeng, H.-L. Wu, Y. Li, E. C. M. Tse, C. J. Barile, *Electrochim. Acta* **2019**, *320*, 134611.
55. A. Hosseini, C. J. Barile, A. Devadoss, T. A. Eberspacher, R. A. Decreau, J. P. Collman, *J. Am. Chem. Soc.* **2011**, *133*, 11100-11102.
56. A. Hosseini, J. P. Collman, A. Devadoss, G. Y. Williams, C. J. Barile, T. A. Eberspacher, *Langmuir* **2010**, *26*, 17674-17678.
57. E. C. M. Tse, C. J. Barile, Y. Li, S. C. Zimmerman, A. Hosseini, A. A. Gewirth, *Phys. Chem. Chem. Phys.* **2017**, *19*, 7086-7093.
58. C. J. Barile, E. C. M. Tse, Y. Li, J. P. Gewargis, N. A. Kirchschlager, S. C. Zimmerman, A. A. Gewirth, *Biophys. J.* **2016**, *110*, 2451-2462.
59. R. P. Gautam, Y. T. Lee, G. L. Herman, C. M. Moreno, E. C. M. Tse, C. J. Barile, *Angew. Chem. Int. Ed.* **2018**, *57*, 13480-13483.
60. Y. Li, E. C. M. Tse, C. J. Barile, A. A. Gewirth, S. C. Zimmerman, *J. Am. Chem. Soc.* **2015**, *137*, 14059-14062.
61. S. Demine, P. Renard, T. Arnould, *Cells* **2019**, *8*, 795.
62. B. van Dijk, J. P. Hofmann, D. G. H. Hetterscheid, *Phys. Chem. Chem. Phys.* **2018**, *20*, 19625-19634.
63. S. N. Supakul, C. J. Barile, *Front. Chem.* **2018**, *6*.
64. M. S. Thorum, J. Yadav, A. A. Gewirth, *Angew. Chem. Int. Ed.* **2009**, *48*, 165-167.
65. K. John, S. Schreiber, J. Kubelt, A. Herrmann, P. Müller, *Biophys. J.* **2002**, *83*, 3315-3323.
66. M. J. Weaver, S. M. Nettles, *Inorg. Chem.* **1980**, *19*, 1641-1646.
67. M. J. Weaver, P. D. Tyma, S. M. Nettles, *J. Electroanal. Chem. Interf. Electrochem.* **1980**, *114*, 53-72.
68. J. R E Weston, *Annu. Rev. Nucl. Sci.* **1961**, *11*, 439-460.
69. M. Gómez-Gallego, M. A. Sierra, *Chem. Rev.* **2011**, *111*, 4857-4963.

Chapter 4: Nanostructured Ni-Cu Electrocatalysts for the Oxygen Evolution Reaction

Reprinted with permissions from Gautam, Rajendra P.; Pan, H.; Chalyavi, F.; Tucker, M. J.; Barile, Christopher. J. *Catalysis Science & Technology,* **2020**, *10*, 4960–4967.

4.1. Introduction

The production of hydrogen gas from renewable energy is at the center of hydrogen-based energy storage schemes. One method of producing hydrogen in a clean and renewable manner is from the electrolysis of water. However, the efficiency of current water electrolyzers is limited by the slow kinetics of the oxygen evolution reaction (OER).[1-2] Although there are several possible OER mechanisms, all pathways involve several proton and electron transfer steps, which give rise to large reaction barriers and necessitate the application of high overpotentials to drive the reaction at reasonable rates. Noble metal OER catalysts such as RuO_2, IrO_2, and Pt exhibit high OER activity, but their scarcity and high cost make large-scale utilization impractical.[3-5] Therefore, the development of inexpensive OER catalysts from nonprecious metals that possess high activity and good durability is still an unresolved challenge.

Ni-based bimetallic systems such as Ni-Co, Ni-Mn, and Ni-Fe are commonly explored classes of nonprecious metal OER catalysts that exhibit low overpotentials and enhanced activity compared to pure Ni. For example, Antar *et al.* electrodeposited Ni-Co thin film OER catalysts with a conducting polymer.[6] Fu *et al.* synthesized a series of Ni-Co phosphides with a cage-like structure.[7] Similarly, Qiu *et al.* designed Ni-Co phosphide nanocages by tuning the molar ratio of Ni/Co atoms that led to catalysts with an overpotential of 300 mV at 10 mA cm^{-2}.[2] Cheng *et al.* reported bimetallic Ni-Fe catalysts on N-doped carbon nanotubes that significantly enhanced OER activity by forming bridged Ni-Fe bimetallic dual atom active sites for the OER.[8] Both Nai *et al.* and Zhu *et al.* reported on porous and hollow Ni-Co oxide nanostructures that demonstrated enhanced OER activity by varying the Ni-Co composition.[9-10]

Our group recently demonstrated that Ni-Cu surfaces are another promising class of bimetallic Ni catalysts.[11] To construct Ni-Cu catalysts, we electrodeposited Ni overlayers of different thicknesses on top of Cu_2O thin films. OER catalysts with an optimal Ni:Cu_2O ratio exhibit an onset overpotential of only 150 mV. Although these catalysts display promising onset overpotentials, they do not operate at low overpotentials at high current densities because they are bulk materials incapable of supporting high reaction rates. In this manuscript, to overcome the current density issue of the electrodeposited Ni-Cu OER catalysts, we developed nanostructured Ni-Cu systems. We synthesized bimetallic Ni-Cu nanoclusters (<20 metal atoms) and nanoparticles (20-50 nm) to increase the current density for catalysis while maintaining the low OER overpotential intrinsic to Ni-Cu systems. For both the nanoparticles and the nanoclusters, the Ni to Cu ratio significantly affects the efficiency of OER electrocatalysis. The Ni-Cu nanocluster catalyst with a 52:48 Ni-Cu mol % exhibits an onset overpotential of only ~50 mV and an overpotential of only ~150 mV at an industrially relevant rate (10 mA cm^{-2}).

4.2. Experimental Section

4.2.1. General Procedures

Chemicals were obtained from commercially available sources and used without further purification. Electrochemical studies were carried out using a VSP-300 Biologic potentiostat using a three-electrode system with a Pt counter electrode, a Ag/AgCl reference electrode, and a glassy carbon working electrode. All experiments were conducted at room temperature (26 ± 1) °C in 1 M NaOH at a scan rate of 10 mV/s unless otherwise noted. Most experiments were conducted in unpurified NaOH (Oakwood

Chemicals, 99%) electrolytes. For some experiments, NaOH electrolytes were purified following a literature protocol.[12] The purified and unpurified electrolytes contained 2 ppb and 115 ppb of Fe, respectively, as determined by inductively coupled plasma-mass spectrometry (ICP-MS). The OER LSVs reported were IR corrected using the solution resistance value obtained from electrochemical impedance spectroscopy. All LSV experiments were at least triplicated. Onset potentials were calculated by determining the potential at which the current density reached 10% of its maximum current density. Tafel slopes were calculated using a voltage range of 1.2-1.8 V.

4.2.2. Synthesis of Nanoparticles

Nanoparticles were synthesized through a procedure modified from the work of Argueta-Figueroa *et al.*[13] For the synthesis of Cu and Ni metallic and bimetallic nanoparticles, varying amounts of $CuSO_4$ and $NiSO_4 \cdot 6H_2O$ were dissolved in 100 mL water. For the synthesis of pure Cu or Ni metallic nanoparticles, 1.596 g of $CuSO_4$ or 2.809 g of $NiSO_4 \cdot 6H_2O$ was dissolved in 100 mL water, and the pH of the solution was adjusted to 8 with 0.1 M NaOH. For the synthesis of 59:41 mol % Ni-Cu bimetallic nanoparticles, 1.404 g of $NiSO_4 \cdot 6H_2O$ and 0.798 g $CuSO_4$ was used. Similarly, for the synthesis of 46:54 mol % Ni-Cu bimetallic nanoparticles, 0.702 g of $NiSO_4 \cdot 6H_2O$ and 1.197 g $CuSO_4$ was taken. Finally, for the synthesis of 71:29 mol % Ni-Cu bimetallic nanoparticles, 2.107 g of $NiSO_4 \cdot 6H_2O$ and 0.040 g $CuSO_4$ was taken. The pH of the solutions were adjusted to 8 with 0.1 M NaOH and bubbled with N_2 for at least 30 minutes. Next, 0.5 mL of 0.04 M $NaBH_4$ was added quickly under vigorous stirring and stirred for 2 hours to complete the reaction. The precipitate was then collected by vacuum filtration and washed three times

with distilled water and once with acetone. Finally, the obtained nanoparticles were collected and stored under isopropyl alcohol.

4.2.3. Synthesis of Nanoclusters

The synthesis procedure described by Gao *et al.* was used with slight modification.[14] For the synthesis of Cu and Ni metallic and bimetallic nanoclusters, varying amounts of $CuCl_2$ and $NiCl_2$ were dissolved in 25 mL water. For the synthesis of pure Cu and Ni metallic nanoclusters, 0.169 g of $CuCl_2$ and 0.163 g of $NiCl_2$ were used. For the synthesis of 43:57 mol % Ni-Cu bimetallic nanoclusters, 0.163 g of $NiCl_2$ and 0.169 g $CuCl_2$ was taken. Similarly, for the synthesis of 25:75 mol % Ni-Cu bimetallic nanoclusters, 0.163 g of $NiCl_2$ and 0.338 g $CuCl_2$ was used. For the synthesis of 52:48 mol % Ni-Cu bimetallic nanoclusters, 0.326 g of $NiCl_2$ and 0.169 g $CuCl_2$ was taken. After dissolving the salts in 25 mL water, the metal salt solution was added to 16.5 mL aqueous solution containing 0.765 g of glutathione while stirring. After the pH of the solution dropped to 2-3, 250 µL of 50 mmol NaOH was added slowly. After 10 minutes, 0.5 mL hydrazine monohydrate was added dropwise to the reaction mixture. After 3 hours of stirring, the resulting solution was stored at 5 °C overnight. The obtained nanoclusters were then centrifuged at 3300 rpm for 3-5 minutes and washed once with ethanol. The final nanoclusters were collected by centrifugation and stored in water for further use.

4.2.4. Experiments on Glassy Carbon Electrodes

The catalysts were loaded onto a glassy carbon electrode (0.196 cm^2 geometric area) by mixing 0.11 g of Vulcan XC-72, 0.04 g of polyvinylidene fluoride (PVDF, Kynar Flex 2751-00), and 0.01 g of catalyst in a small vial. Acetone (1.0 mL) was added to the

vial and the resulting mixture was sonicated for 10 minutes. This solution (20 μL) was dropcasted onto a glassy carbon electrode and dried under a gentle stream of air for 5 minutes. Electrodes using TiO_2 nanoparticles (Anatase, ~21 nm, Sigma Aldrich) were fabricated by dropcasting a suspension of TiO_2 (10 mg/mL in acetone) onto a carbon support. After the TiO_2 has dried, Ni-Cu nanoclusters (10 mg/mL in acetone) were then dropcasted on the TiO_2/carbon substrate and dried in air.

4.3. FTIR Characterization

The FTIR spectrum of the as-synthesized 52:48 mole % Ni-Cu glutathione-nanocluster complex was collected in D_2O. The same nanocluster complex was subjected to OER catalysis in 1 M NaOH for 1 hr of chronopotentiometry at 10 mA cm^{-2} in H_2O using a glassy carbon working electrode. After catalysis, the nanoclusters were lyophilized and suspended in D_2O before FTIR was conducted. Additionally, the FTIR spectrum of the glutathione ligand in D_2O was collected to determine the signatures of free ligand in solution. All IR spectra were collected on a ThermoNicolet 6700 FTIR spectrometer, equipped with a liquid nitrogen cooled mercury cadmium telluride (MCT) detector, at 1 cm^{-1} resolution using a homemade two-compartment CaF_2 sample cell with a 56 μm Teflon spacer. The cell was divided into two compartments to collect IR measurements of the reference and the sample under similar experimental conditions and to eliminate laser drift. An automated translation stage moved the sample cell between the reference and the sample side collecting a single beam spectrum for each side, and the final IR spectrum was processed as a ratio of the sample and reference single beam.

4.3.1. Other Materials Characterization

Scanning electron microscope (SEM) images were obtained using a Hitachi S-4700 II Field Emission SEM with an Energy Dispersive Spectrometer (EDX) at an acceleration voltage of 15 kV. X-ray diffraction (XRD) was performed using a Bruker D2 X-ray Diffractometer using carbon paper as a substrate (Fuel Cell Store, AvCarb EP40T). ICP-MS was conducted by Western Environmental Testing Laboratory (Sparks, NV). All Ni:Cu ratios reported in this manuscript come from ICP-MS results as opposed to the nominal ratios of the Ni and Cu salts used during synthesis. The Faradaic efficiency for O_2 evolution was determined using a SRI 8610C gas chromatograph equipped with a thermal conductivity detector and a previously described custom-built electrochemical cell.[15] Matrix-assisted laser desorption/ionization time of flight (MALDI-TOF) mass spectra were recorded on a Bruker microflex MALDI-TOF spectrometer using 2,5-dihydroxybenzoic acid as the matrix. High-resolution mass spectrometry with electrospray ionization (ESI-MS) analysis was obtained using an Agilent G6230B time-of-flight mass spectrometer. Fluorescence spectroscopy was performed with a Jobin Yvon Horiba FluoroMax-3 using an excitation wavelength of 365 nm and ethanol as a solvent.

4.4. Results and Discussion

Ni and Cu metallic and bimetallic nanoparticles were synthesized from aqueous solutions of $NiSO_4$ and $CuSO_4$ using $NaBH_4$ as a reducing agent through a modified literature procedure.[13] SEM-EDX analysis of the bimetallic Ni-Cu nanoparticles demonstrates that the nanoparticles were successively synthesized with particle diameters ranging between 20-50 nm (Figure S4.1, Appendices). To compare the effect of particle size on the OER electrocatalytic activity, we also synthesized metallic and bimetallic Ni-

Cu nanoclusters. To form the smaller nanoclusters, glutathione is used as a stabilizing ligand that kinetically traps the particles such that they form nanoclusters containing 5-20 metal atoms. Furthermore, glutathione is a small enough ligand that it should not significantly impede electron transfer rates relative to typical OER turnover frequencies.[16] Fluorescence spectroscopy (Figure S4.2, Appendices) indicates that the Cu nanoclusters emit visible light upon ultraviolet radiation, as has been previously shown for similar systems.[17-19] We quantified the Ni:Cu ratio of both the nanoparticles and nanoclusters using ICP-MS.

The size and composition of the Ni-Cu bimetallic nanoclusters were further characterized by MALDI-TOF MS and high resolution ESI-MS. MALDI-TOF MS of pure Cu nanoclusters synthesized using glutathione (GS) is known to yield a series of ions corresponding to bare Cu nanoclusters and Cu nanoclusters bound to the glutathione ligands.[20] The MADLI-TOF MS of pure Cu nanoclusters we synthesized also has peaks ascribable to a similar set of ions (Figure S4.3, Table S4.1, Appendices). More importantly, we also conducted mass spectrometry of the bimetallic Ni-Cu nanoclusters. The most intense mass peak in the MALDI-TOF spectrum of the 52:48 mol % Ni-Cu nanoclusters occurs at a m/z of 1078.5 (Figure 4.1A), which within the resolution of MADLI m/z values (2-3 amu) can be assigned to either the bimetallic ion $[Cu_9Ni_3GS + Na]^+$ or the monometallic $[Cu_7GS_2 + Na]^+$ ion. The most intense peak at a similar m/z value in the MALDI-TOF spectrum of the pure Cu nanoclusters (Figure S4.3, Appendices) suggests that the peak is due to the monometallic $[Cu_7GS_2 + Na]^+$ species. However, several other peaks in the MALDI-TOF spectrum of the 52:48 mol % Ni-Cu nanoclusters can only be assigned to ions corresponding to bimetallic species. For example, one of the most intense

peaks in the spectrum occurs at a m/z of 1343.8 (Figure 4.1A) and can only be ascribed to bimetallic ions such as $[Cu_6Ni_6GS_2 + H]^+$. To confirm the presence of bimetallic species, we performed high-resolution ESI-MS on the bimetallic nanoclusters (Figure 4.1B). The top panel in Figure 4.1B shows the theoretical isotopic splitting pattern for a 1:1:1 mixture of $[Cu_7Ni_5GS_2 + H]^+$, $[Cu_6Ni_6GS_2 + H]^+$, and $[Cu_5Ni_7GS_2 + H]^+$ ions. The experimental ESI-MS spectrum from 1340-1360 m/z matches well with this theoretical spectrum (bottom panel, Figure 4.1B), indicating that bimetallic species are indeed present in the bimetallic nanoclusters.

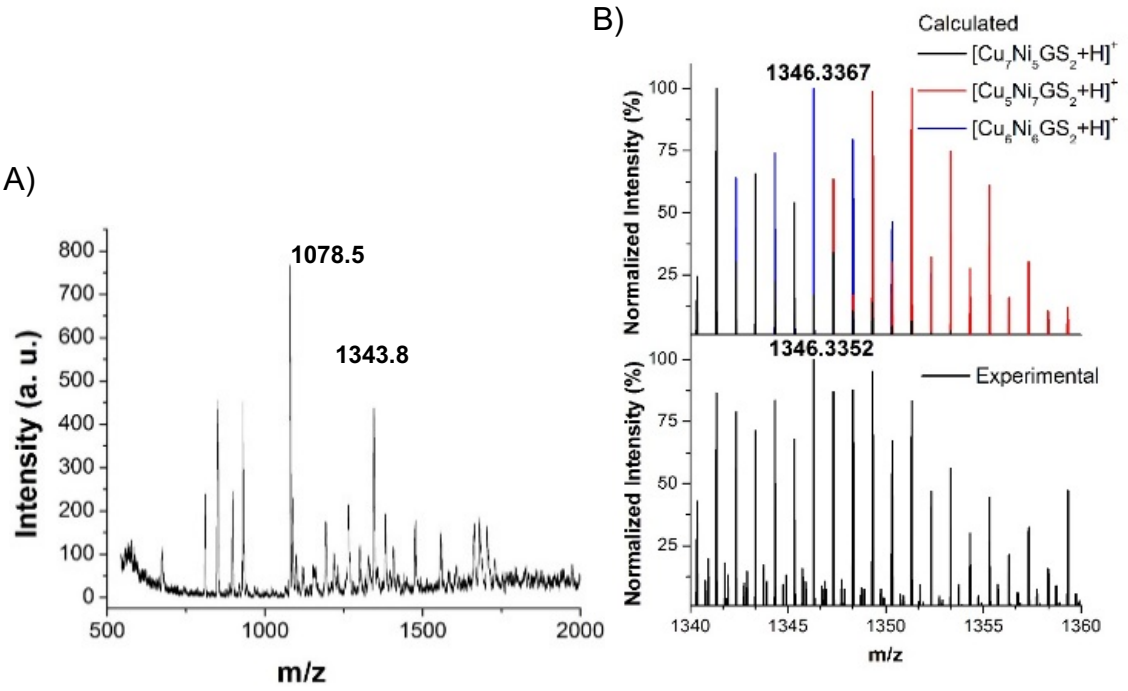

Figure 4.1. Positive-mode MALDI-TOF mass spectrum of the as-synthesized 52:48 mol % Ni-Cu nanoclusters (A). Calculated (B, top panel) isotopic pattern and experimental mass spectrum obtained from high resolution ESI mass spectrometry (B, bottom panel) of the nanoclusters.

A thorough assignment of peaks in the MALDI-TOF spectra (Figures S4.4-S4.6, Appendices) for both the monometallic and bimetallic Ni-Cu nanoclusters is presented in Table S4.1, Appendices. For all of the bimetallic nanoclusters, several additional peaks are present in the mass spectra that can only be assigned to bimetallic clusters (bold entries in Table S4.1, Appendices). Because these same peaks are absent from the spectra of the monometallic nanoclusters, this analysis further demonstrates that heterobimetallic clusters were formed, not just composites of individual Ni and Cu nanoclusters. MALDI-TOF MS of the Ni-Cu bimetallic nanoclusters after immersing them overnight in the 1 M NaOH electrolyte used for our OER electrocatalytic studies shows that the composition of the bimetallic nanoclusters remains the same after electrolyte immersion (Figure S4.7, Appendices).

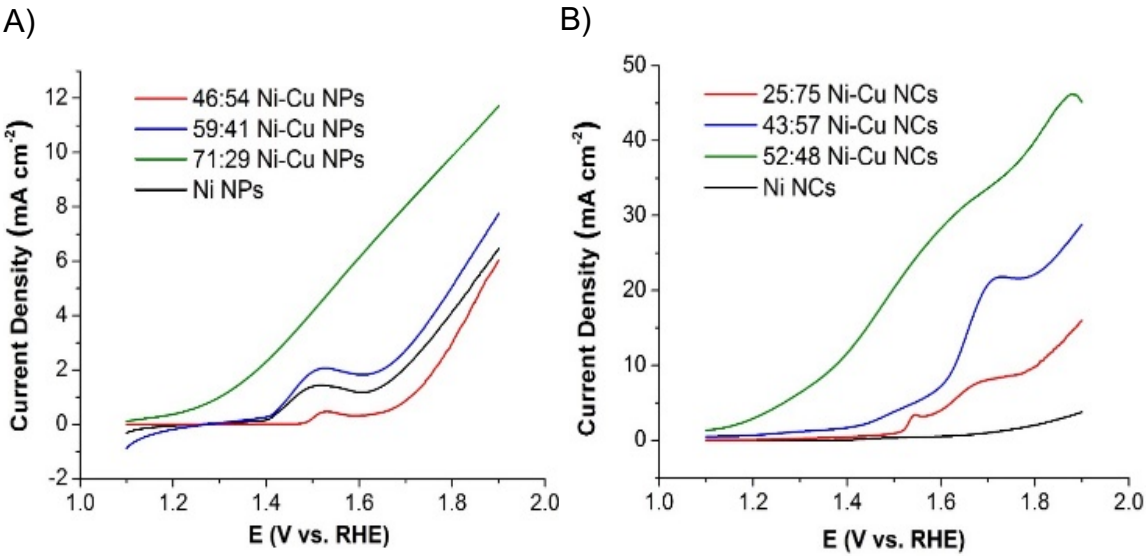

Figure 4.2. Linear sweep voltammograms at 10 mV s^{-1} of the oxygen evolution reaction in 1 M NaOH using a glassy carbon working electrode modified with a mixture of Ni-Cu bimetallic nanoparticles (NPs, A) or nanoclusters (NCs, B), Vulcan XC-72, and PVDF. Ni-Cu bimetallic NPs and NCs with various molar ratios were tested (colored lines) along with pure Ni (black lines) and pure Cu (Figure S11, ESI) NPs and NCs. Current densities are reported against the geometric electrode area.

Having synthesized an array of Cu and Ni nanostructured systems, we next assessed their ability to function as OER electrocatalysts. Catalysts were prepared on glassy carbon working electrodes, and linear sweep voltammograms (LSVs) in 1 M NaOH were conducted at a scan rate of 10 mV s^{-1}. For all catalysts, O_2 bubbles vigorously evolved from the electrode surface at voltages above 1.4 V vs. RHE. The LSVs show that the molar composition of the nanoparticles dramatically affects their OER activity (Figure 4.2A). The current density is highest for the 71:29 mol % Ni-Cu bimetallic nanoparticles (green line) as compared to other compositions of bimetallic nanoparticles. For the Ni (black line), 59:41 mol % Ni-Cu (blue line), and 46:54 mol % Ni-Cu nanoparticles (red line), there is a peak at approximately 1.5 V vs. RHE. This peak has been observed previously in other Ni-based OER catalysts and is due to the electrochemical oxidation of $Ni(OH)_2$, which spontaneously forms when Ni is immersed in alkaline solutions, to NiOOH.[21] Cyclic voltammetry experiments in the appropriate voltage range demonstrate that this NiOOH can be converted back to $Ni(OH)_2$ upon reduction (Figure S4.8, Appendices). The reason for the lack of a NiOOH peak in the LSV for the 71:29 mol % Ni-Cu is not clear. Furthermore, prominent peaks near 1.5 V are not present in the LSVs of the Ni-Cu nanoclusters. The Ni in these cases is bonded to the thiol group in the glutathione ligand, and we hypothesize that this added stability inhibits the $Ni(OH)_2$/NiOOH wave. Analagous experiments with Ni-Cu nanoclusters show that the OER current density measured is much greater than the nanoparticles due to an increase in the surface area of the small nanoclusters, which results in a greater number of active catalytic sites (Figure 4.2B). The results also demonstrate that like the nanoparticles, the catalytic activity of the nanoclusters depends strongly upon the molar ratio of Ni and Cu present. In particular, nanoclusters

with 52:48 mol % Ni-Cu possess the highest OER current density (Figure 4.2B, green line). An OER LSV of the 52:48 mol % Ni-Cu nanoclusters in a purified NaOH electrolyte that contained only 2 ppb Fe is similar to the analagous LSV in an unpurified electrolyte with 115 ppb Fe (Figure S4.9, Appendices). This finding demonstrates that possible Fe incorporation into the Ni-based catalysts from electrolyte impurities does not play a significant role in dictating catalyst activity. However, there is a small peak at approximately 1.85 V in the LSV with the unpurified electrolyte that is not present in the LSV with the purified electrolyte. These results suggest that the peak at about 1.85 V is due to the activity of a Ni-Fe species. A LSV of the 52:48 mol % Ni-Cu nanoclusters at a slower scan rate of 2 mV s^{-1} exhibits less current density as expected, but possesses a similar onset potential as the corresponding LSV at 10 mV s^{-1} (Figure S4.10, Appendices). Lastly, we note that the OER current densities obtained for the monometallic systems are much less than those of any of the bimetallic systems and are about 10 times less than those of the bimetallic systems with optimal compositions (Figures 4.2 and S4.11, Appendices). In other words, bimetallic Ni-Cu nanoparticles and nanoclusters exhibit far superior performance than either of their pure Ni or pure Cu counterparts.

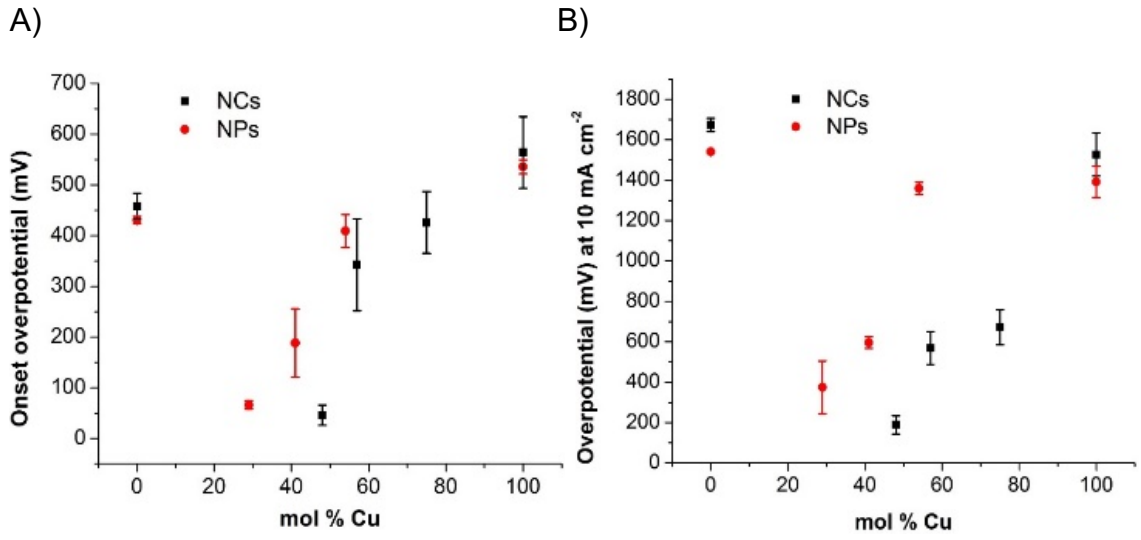

Figure 4.3. Plots of onset overpotentials (A) and overpotentials at 10 mA cm^{-2} (B) for the oxygen evolution reaction in 1 M NaOH using various compositions of Ni-Cu bimetallic nanoclusters (NCs, black) or nanoparticles (NPs, red) on a glassy carbon working electrode.

The onset overpotentials of the Ni-Cu electrocatalysts also depend strongly on the ratio of Ni and Cu present. The lowest overpotentials obtained for both the nanoparticles and nanoclusters is about 50 mV (Figure 4.3A). This result suggests that the intrinsic surface chemistry that enables catalysis for the nanoparticles and nanoclusters is similar, although the optimal molar composition to achieve this surface chemistry differs when the catalyst size changes. We also evaluated the overpotentials of the nanoparticles and nanoclusters at a current density of 10 mA cm^{-2} because the overpotential at this current density is the primary figure of merit for a practical water-splitting device.[22] Among the Ni-Cu nanoparticles, the particles with 71:29 mol % Ni-Cu possess the lowest overpotential of ~350 mV at 10 mA cm^{-2}. However, the nanoclusters with 52:48 mol % Ni-Cu exhibit the lowest overpotential of only ~150 mV at 10 mA cm^{-2}, 200 mV less than that of the nanoparticles and among the lowest reported for any OER electrocatalyst (Table S4.2).

Although the nanoparticles and nanoclusters with the lowest overpotentials at 10 mA cm^{-2} have two different molar ratios, the optimal nanoclusters possess a lower overpotential than the nanoparticles. The enhanced activity of the Ni-Cu nanostructured catalysts can be attributed to synergistic effects between Ni and Cu, resulting from differences in bimetallic surface reactivity towards oxygen radical intermediates.[7] For other Ni-Cu materials, it has been demonstrated that oxygen in the form of O_2^{2-}/O^- on the catalyst surface are strongly electrophilic reactants that are very active towards oxidation. These oxygen species are coordinatively unsaturated oxygen complexes that enhance catalyst activity.[23-25] These species also contribute to an increased number of oxygen defects on the catalyst, which act as charge traps and adsorption sites that facilitate charge transfer.[26]

In addition to determining reaction overpotentials, we also evaluated the Tafel slopes of the catalysts from the OER LSVs (Figure S4.12, Appendices). The Ni nanoclusters and nanoparticles possess Tafel slopes near 120 mV dec^{-1}, a value indicative of a rate-limiting single electron transfer step as has been reported for other OER catalysts based on Ni and Ni-Fe.[5] For most of the bimetallic Ni-Cu catalysts, however, the Tafel slopes are much greater than 120 mV dec^{-1}. Large Tafel slopes like these observed with previous OER catalysts typically are indicative of impeded electron transfer kinetics due to surface passivation. The exact origin of surface passivation in these Ni-Cu catalysts is unknown but given that these large Tafel slope values are not seen in the Ni only catalysts, it is possible that surface passivation results from Cu oxide species formed during catalysis.

We also assessed catalyst activity of the nanoclusters and nanoparticles when taking into account the electrochemically active surface area (ECSA) of the catalysts. The ECSAs of the catalysts were calculated using Pb underpotential (Figure S4.13, Appendices), which

is widely used to measure the ECSAs of Cu and Ni systems.[27-29] Because of their smaller diameters, the nanoclusters were found to have ECSAs ~250 times greater than the nanoparticles. When the currents of the OER LSVs of the catalysts are normalized using the ECSAs, the current densities of the nanoclusters are ~10 times less than that of the nanoparticles (Figure S4.14, Appendices). The decreased intrinsic activity of the nanoclusters, at least in terms of reaction kinetics, could be caused by impeded mass transfer arising from the tightly packed layer of capping glutathione ligands that stabilizes nanocluster formation. Nonetheless, the nanoclusters still exhibit lower reaction overpotentials and enhanced geometric current densities as compared to the nanoparticles as discussed earlier.

In addition to catalyst activity, catalyst stability is an important consideration when developing OER electrocatalysts. To assess stability, a series of chronopotentiometry tests of the nanoclusters with the highest OER activity (52:48 mole % Ni-Cu) were performed at a current density of 10 mA cm^{-2} for 1 hour in 1 M NaOH (Figure 4.4). We first tested the nanoclusters on a typical carbon support (Vulcan XC-72) on a glassy carbon electrode. In this case, the voltage increased quickly and reached 3 V vs. RHE in less than 6 minutes (blue line), indicating that the nanoclusters are highly unstable under these conditions. The instability of the nanoclusters is also demonstrated by cyclic voltammetry (Figure S4.15, Appendices), which shows that the catalytic current density decreases significantly during multiple cycles. To enhance the stability of the nanoclusters, we turned to TiO_2 nanoparticles on carbon paper as an electrode support. Control experiments with bare carbon paper (black line) and TiO_2 nanoparticles on bare carbon paper (red line) show excellent stability over 1 hour, requiring a voltage of 2.6 and 2.4 V vs. RHE for bare carbon

and TiO_2 on bare carbon, respectively. When the nanoclusters are supported by TiO_2 on carbon, the voltage decreased to 1.6 V vs. RHE (green line) and increased much less than without TiO_2 (blue line) over the course of 1 hour. Gas chromatography experiments indicate that the Faradaic efficiency for O_2 production by these Ni-Cu nanoclusters on TiO_2 is 95%. SEM-EDX images of the nanoclusters supported on TiO_2 reveal that the ~20 nm diameter TiO_2 particles were successfully deposited on the carbon paper electrode (Figure S4.16, Appendices). We attribute the enhanced stability of the nanoclusters on TiO_2 to the bonding that occurs between the oxygen in TiO_2 and the carboxylate groups in the glutathione-capped nanoclusters. Analogous TiO_2-carboxylate interactions are widely used in dye-sensitized solar cells and other electrode architectures to enhance device stability.[30-32] The bonding of the nanoclusters to the TiO_2 nanoparticles likely enhances stability by preventing nanocluster aggregation and subsequent catalyst inhibition. Future work will explore other conjugate chemistries that could improve the covalent tethering of the nanocluster catalysts to electrode surfaces with the goal of further increasing the stability of these catalysts.

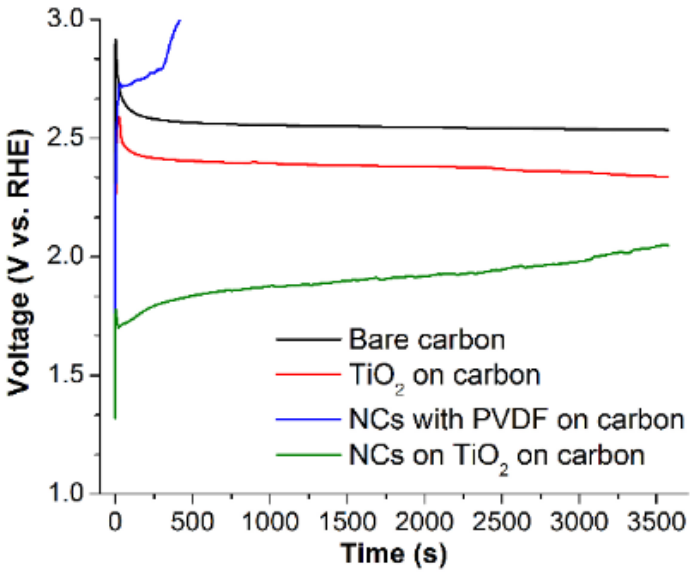

Figure 4.4. Chronopotentiometry curves of carbon (black line), TiO_2 nanoparticles on carbon (red line), Ni-Cu nanoclusters with PVDF on carbon (blue line), and Ni-Cu nanoclusters on TiO_2 nanoparticles on carbon (green line) electrodes at a current density of 10 mA cm^{-2} in 1 M NaOH.

Although the improved catalytic stability of the nanoclusters when anchored to TiO_2 suggests that one degradation mechanism of the catalysts is their detachment from the electrode, electrochemical corrosion of the metals and/or ligand scaffold could also be operative. To evaluate these possibilities, we first conducted MALDI-TOF MS of the 52:48 mol % Ni-Cu nanoclusters after catalysis (Figure S4.17, Appendices). The peak positions in the mass spectra before and after catalysis are similar, indicating that intact glutathione-nanocluster complexes still exist after catalysis. We also performed XRD analysis of the Ni-Cu nanoclusters as-deposited on carbon paper and after ten OER voltammetry cycles (Figure 4.5). Before catalysis, the XRD spectrum contains peaks ascribable to Ni, Cu, carbon, and polytetrafluoroethylene (PTFE), the last of which is present on the commercially-obtained carbon paper.[15] After catalysis, in addition to the metallic Ni and

Cu peaks, additional peaks arising from NiOOH and Cu_2O appear in the spectrum. These results, coupled with the previously discussed voltammetry of the $Ni(OH)_2$/NiOOH redox couple (Figure S4.8), suggest that the active form of the catalyst consists, at least partially, of NiOOH and Cu_2O. The Cu Pourbaix diagram indicates that Cu_2O and CuO_2^{2-} are the thermodynamically preferred Cu species under the conditions of the OER LSVs.[33] It is therefore possible that in addition to Cu_2O formation, soluble CuO_2^{2-} is leached from the electrolyte after prolonged catalysis.

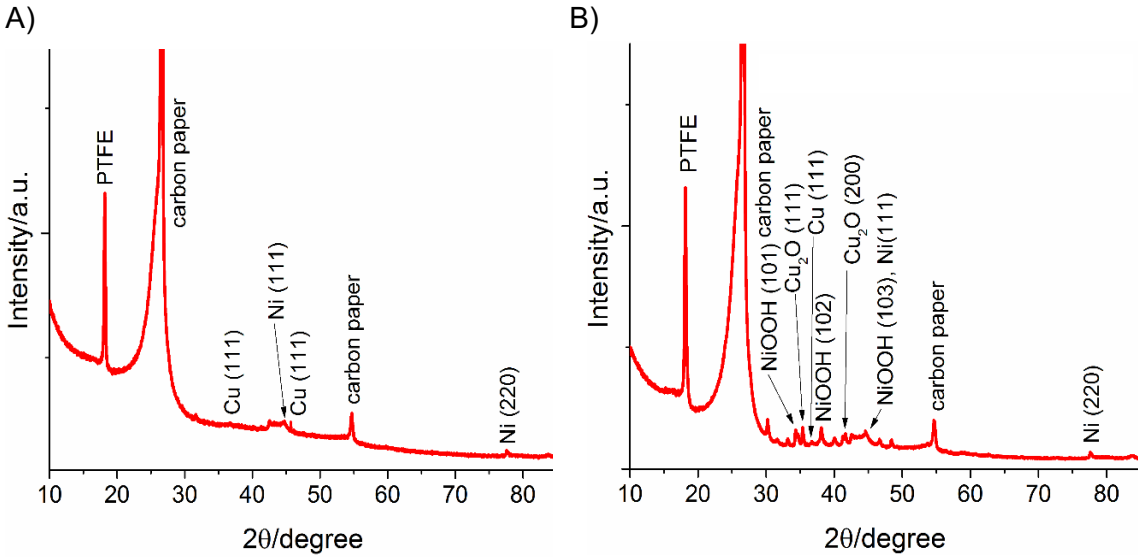

Figure 4.5. XRD spectra of the 52:48 mol % Ni-Cu nanoclusters before (A) and after (B) OER catalysis.

Although the MS and XRD results reveal important structural details of the Ni-Cu nanoclusters, the data do not give information about the structure of the glutathione ligand network, which could dictate catalytic activity. To investigate ligand structure, the FTIR spectra of the nanoclusters were collected in the amide I region. The amide I region (1600-1700 cm^{-1}) of IR spectra are routinely used to determine peptide secondary structures in

solution.[34-36] The IR spectrum of the glutathione-nanocluster complex in solution before catalysis (Figure 4.6, blue) has three distinct peaks at 1620 cm^{-1}, 1636 cm^{-1}, and 1673 cm^{-1}. The peak at 1636 cm^{-1} is assigned to the formation of beta-sheets in small peptides as has been observed previously.[37] Furthermore, a sharp, narrow, intense peak at ~1680 cm^{-1} and a second weaker band at lower frequency are characteristic of peptide aggregation.[38-40] These findings suggest that the as-synthesized nanoclusters contain a well-packed ligand network. In contrast, the IR spectrum of the nanoclusters after catalysis does not show the signature aggregation band at 1673 cm^{-1} (Figure 4.6, gray). Instead, the major spectral feature, a distinct band at 1641 cm^{-1} is indicative of a random coil structure. Because the catalyst degrades, these results suggest that the catalysts facilitate the OER at a lower overpotential with a well-ordered ligand network. As a control experiment, the IR spectrum of glutathione by itself was measured (Figure 4.6, orange). The spectrum has similar spectral features to the complex after catalysis, indicating that the ligand structure of the nanoclusters depends upon catalyst activity. Taken together, from IR analysis and the TiO_2 experiments, we conclude that nanocluster degradation on carbon electrodes occurs both because the catalysts detach from the electrodes and because of changes in ligand structure. Despite these degradation pathways however, the nanoclusters remain largely intact after catalysis as is evidenced by the similarity of the mass spectra before and after catalysis.

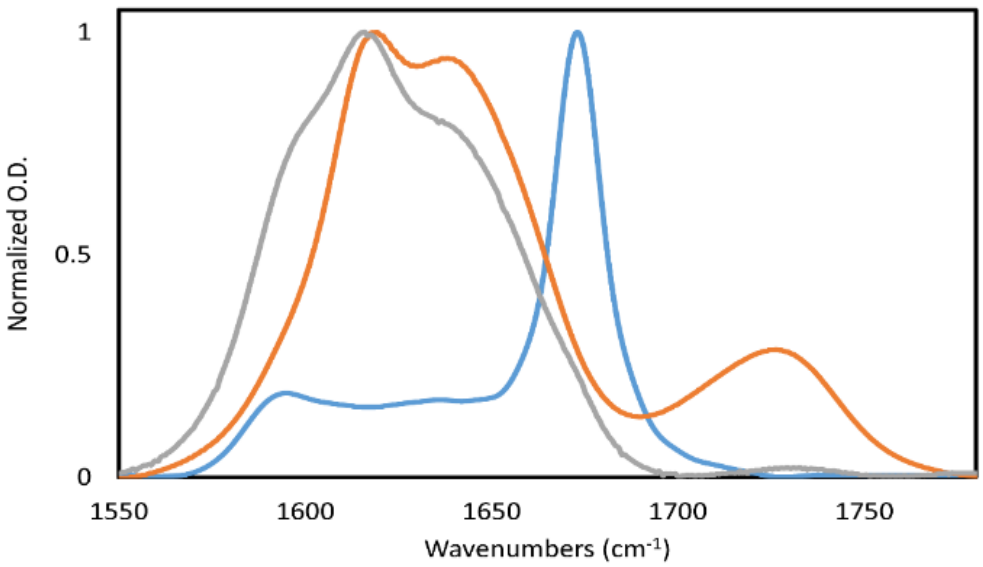

Figure 4.6. Normalized FTIR spectra of the 52:48 mole % Ni-Cu nanoclusters before (blue) and after (gray) catalysis along with the spectrum of glutathione (orange).

4. 5. Conclusions

In conclusion, we synthesized various compositions of metallic and bimetallic Ni-Cu nanostructured electrocatalysts for the OER. MALDI-TOF MS, high resolution ESI-MS, ICP-MS, XRD, FTIR, and SEM-EDX measurements confirmed the size, molar ratio, and morphology of the nanoclusters and nanoparticles. An optimal molar ratio of Ni-Cu bimetallic nanoclusters (52:48 mol % Ni-Cu NCs) possess an overpotential of ~150 mV at 10 mA cm^{-2}, making it one of the most efficient nonprecious metal OER catalysts reported. The durability of the nanoclusters for OER catalysis can be improved by tethering them via glutathione ligands to an electrode modified with TiO_2 nanoparticles. The promising performance of the Ni-Cu nanoclusters with controllable size and composition opens up future research on this new class of OER electrocatalysts.

4.6. References

1. H. Zhou, F. Yu, J. Sun, R.He, S. Chen, C.Chu, Z. Ren, *P. Natl. Acad. Sci.* USA 2017, **114**, 5607-5611.
2. B. Oiu, L. Cai, Y.Wang, Z.Lin, Y. Zou, M.Wang, Y,Chai, *Adv. Func. Mater.* 2018, **28**, 1706008-1706018.
3. Q. Shi, C. Zhu, D. Du, Y. Lin, *Chem. Soc. Rev.,* 2019, **48**, 3181-3192.
4. M. Jamesh, X. Sun, *J. Power Sources,* 2018, **400**, 31-68.
5. N. Suen, Hung, S. Hung, Quan, Q. Quan, N. Zhang, Y.Xu, H. M. Chen, *Chem. Soc. Rev.,* 2017, **46**, 337-365.
6. A. Antar, Y. Naimi, D. Takky, IOP Conference Series: Earth and Environmental Science 2018, **161**, 012027.
7. S. Fu, C. Zhu, J. Song, M. H. Engelhard, X. Li, D. Du, Y. Lin, *ACS Energy Lett.,* 2016, **1**, 792-796.
8. Y. Cheng, S. He, J. Veder, R. De Marco, S. Yang, S. Ping Jiang, *ChemElectroChem*., 2019, ***6*,** 3478-3487.
9. J. Nai, H. Yin, T. You, L. Zheng, J. Zhang, P. Wang, Z. Jin, Y. Tian, J. Liu, Z. Tang, L. Guo, *Adv. Energy Mater.* , 2015, **5**, 1401880-1401884.
10. C. Zhu, D. Wen, S. Leubner, M. Oschatz, W. Liu, M. Holzschuh, F. Simon, S. Kaskel, A. Eychmüller, *Chem. Commun.*, 2015, **51**, 7851-7854.
11. Y. T. Lee, R. P. Gautam, S. M. Islam, C. J. Barile, *J. Phys. Chem. C,* 2019, **123**, 1287-1292.
12. M. P. Browne, S. Stafford, M. O'Brien, H. Nolan, N. C. Berner, G. S. Duesberg, P. E. Colavita, M. E. G. Lyons, *J. Mater. Chem. A* 2016, **4** 11397-11407.
13. L. Argueta-Figueroa, T. A. Morales-Luckie, R. J. Scougall-Vilchis, O. F. Olea-Mejia, *Prog. Nat. Sci. Mater.* 2014, ***24*,** 321-328.
14. X. Gao, Y. Lu, M. Liu, S. He, W. Chen, *J. Mater. Chem. C* 2015, **3**, 4050-4056.
15. H. Pan, C. J. Barile, *J. Mater. Chem. A* 2020, **8**, 1741-1748.
16. C. E. D. Chidsey, *Science* 1991, **251**, 919-922.
17. C. Y. Huang, Z. Getahun, Y. Zhu, J. W. Klemke, W. F. DeGrade, F. Gai, *Proc. Natl. Acad. Sci.* 2002, **99**, 2788-2793.
18. N. Wang, L. Ga, M. Jia, J. Ai, *J. Nanomater.* 2019, **2019**, 1-5.
19. K. Basu, S. Paul, R. Jana, A. Datta, A. Banerjee, *ACS Sus. Chem. Eng.* 2019, **7**, 1998-2007.
20. Y. Li, L. Feng, W. Yan, I. Hussain, L. Su, B. Tan, *Nanoscale* 2019, **11**, 1286-1294.
21. T. T. H. Hoang, A. A. Gewirth, *ACS Catal.* 2016, **6**, 1159-1164.
22. C.C. L. McCrory, S. Jung, J.C. Peters, T. F. Jaramillo, *J. Am. Chem. Soc.* 2013, **135**, 16977-16987.

23. L. Wang, X. Ge, Y. Li, J. Liu, L. Huang, L. Feng, Y. Wang, *J. Mater. Chem. A* 2017, **5**, 4331-4334.
24. J. Fan, Z. Chen, H. Shi, G. Zhao, *Chem. Commun.* 2016, **52**, 4290-4293.
25. Y. Wang, J. Ren, Y. Wang, F. Zhang, X. Liu, Y. Guo, G. Lu, *J. Phys. Chem. C* 2008, **112**, 15293-15298.
26. J. Bao, X. D. Zhang, B. Fan, J. J. Zhang, M. Zhou, W. L. Yang, X. Hu, H. Wang, B. C. Pan, Y. Xie, *Angew. Chem. Int. Ed.* 2015, **54**, 7399-7404.
27. G. Y. Wu, S. E. Bae, A. A. Gewirth, J. Gray, X. D. Zhu, T. P. Moffat, W. Schwarzacher, *Surf. Sci.,* 2007, **601**, 1886-1891.
28. M. Seo, K. Fushimi, H. Habazaki, T. Nakayama, *Corros. Sci.*, 2008, **50**, 3139-3146.
29. Y. Song, R. Peng, D. K. Hensley, P. V. Bonnesen, L. Liang, Z. Wu, H. M. Meyer, M. Chi, C. Ma, B. G. Sumpter, A. J. Rondinone, *ChemistrySelect* 2016, **1**, 6055-6061.
30. W. Chen, S. Nachimuthu, J. Jiang, *Sci. Reports* 2017, **7**, 4979-4991.
31. L. Zhang, J. M. Cole, *ACS Appl. Mater. Inter.*, 2015, **7**, 3427-3455.
32. M. Pastore, T. Etienne, F. De Angelis, *J. Mater. Chem. C* 2016, **4**, 4346-4373.
33. Y. Oh, G. Park, C. Chung, *J. Electrochem. Soc.* 2006, **153**, G617-G621.
34. L. P. DeFlores, Z. Ganim, R. A. Nicodemus, A. Tokmakoff, *J. Am. Chem. Soc.* 2009, **131**, 3385-3391.
35. A. Barth, C. Zscherp, *Q. Rev. Biophys.* 2002, **35**, 369-430.
36. P. Hamm, M. Lim, R. M. Hochstrasser, *J. Phys. Chem. B* 1998, **102**, 6123-6138.
37. C. M. Davis, R.B. Dyer, *J. Am. Chem. Soc.*, 2016, **138**, 1456-1464.
38. Z. Ganim, H.S. Chung, A. W. Smith, L.P. DeFlores, K. C. Jones, A. Tokmakoff, *Acc. Chem. Res.*, 2008, **41**, 432-441.
39. V. Koppaka, P. H. Axelsen, *Biochemistry* 2000, **39**, 10011-10016.
40. S.D. Moran, M.T. Zanni, *J. Phys. Chem. Lett.*, 2014, **5**, 1984-1993.

Chapter 5: Cuprous Oxide Electrodeposited with Nickel for the Oxygen Evolution Reaction in 1 M NaOH

5.1. Introduction

Energy storage technologies are instrumental in facilitating our transition away from fossil fuels and towards renewable energy sources. Hydrogen gas is an attractive fuel for clean energy storage if the hydrogen utilized is produced using renewable processes.[1] Hydrogen could be produced in a green manner via the electrolysis of water.[2] However, the design of robust and inexpensive electrocatalysts for the oxygen evolution reaction (OER) is a key hurdle in developing practical water electrolyzers.[3] High-performing OER catalysts are also critical in the design of metal-air batteries.[4,5]

In an effort to develop superior OER electrocatalysts, various metal and metal oxide materials for the OER have been studied.[6] Despite much theoretical and experimental research, the discovery of an ideal OER catalyst, one that is durable, inexpensive, and operates at a low overpotential with high current density, remains elusive. Traditional OER catalysts are based on Ru and Ir, but the precious nature of these metals limits their practical utility.[7] As an alternative, metal oxides containing Ni, Co, Fe, and Mn have been developed as stable OER electrocatalysts at high pH.[8] Regardless of the catalyst employed, the high overpotential for the OER limits the efficiency of water electrolysis. Recently, bimetallic catalysts have been explored as a strategy to reduce the overpotential for the OER.[9,10] Studies show that bimetallic Ni-Fe and Ni-Co electrocatalysts are particularly effective at lowering the OER overpotential.[11-13] Other examples of bimetallic Ni-based catalysts include those that contain Ce or W.[14-17]

In this manuscript, we develop bimetallic OER electrocatalysts based on Ni and Cu that operate under basic conditions. These catalysts are synthesized via the

electrodeposition of Ni and Cu_2O. We chose to electrodeposit Ni because Ni-based OER catalysts are among the most active known due to an optimal difference in the free energy associated with the adsorption of O and OH species on NiO_x surfaces.[18] Furthermore, previous studies have shown that bimetallic Ni-based catalysts modified with Fe and Co exhibit improved performance.[19] With the proper composition and morphology, the Ni-Cu_2O catalysts developed here rival those containing Ni-Fe and Ni-Co in terms of minimizing the OER overpotential.

5.2. Experimental

5.2.1. Chronoamperometric Electrodeposition of Cuprous Oxide

Cu_2O was electrodeposited onto a tin-doped indium oxide (ITO, Xin Yan, Inc.) glass slide at 50°C for 30 minutes using a published procedure.[20] A one-compartment, three-electrode electrochemical cell was used with ITO as the working electrode, Cu foil as the counter electrode, and Ag/AgCl (3 M KCl, eDaq, Inc.) as the reference electrode. The sheet resistance of the ITO electrode was 10 Ω/sq, and the immersed geometric surface area of the electrode was 2 cm^2. The electrodeposition bath consisted of 7.5 M lactic acid and 0.66 M $CuSO_4$ adjusted to pH 12 with NaOH. The electrodeposition was carried out in the dark at a constant voltage of -0.45 V vs. Ag/AgCl. The thin film was left to dry in ambient atmosphere after electrodeposition and rinsed gently with DI water to remove any residual $CuSO_4$ on the surface. Then, the thin film was either electrodeposited with Ni or directly studied using linear sweep voltammetry (LSV).

5.2.2. Chronopotentiometric Electrodeposition of Nickel

Ni was electrodeposited on top of the Cu_2O thin film at room temperature. Similar to the Cu_2O electrodeposition method, a three-electrode cell was used except that a Pt wire was used as the counter electrode instead of Cu foil. The electrodeposition bath consisted of 0.5 M $NiSO_4$ and 0.4 M boric acid (H_3BO_3) that was adjusted to pH 3 using H_2SO_4. Chronopotentiometry at -4 mA/cm^2 for varying time periods was conducted to electrodeposit Ni films of different thicknesses. Next, the ITO electrodeposited with Ni on top of Cu_2O was left to dry in ambient air.

5.2.3. Electrochemical Measurements

To evaluate the OER activity of the thin films, the working electrodes were studied using LSV in 1 M NaOH at room temperature using a one-compartment, three-electrode configuration. The thin film on ITO functioned as the working electrode, a Pt wire was used as a counter electrode, and a Ag/AgCl electrode was used as the reference electrode. The OER LSVs reported are IR corrected using the solution resistance value obtained from electrochemical impedance spectroscopy as discussed previously.[21] All values are reported versus the reversible hydrogen electrode (RHE). Onset potentials for the OER are determined when the slope of the I-V curve reaches 17 Ω^{-1} cm^{-2}. The onset overpotential (η) is defined as the difference in the measured onset potential (E_{onset}) and the thermodynamic potential (E° = 1.23 V vs. RHE) for the oxygen evolution reaction such that $\eta = E_{onset} - E^\circ$. All electrochemical measurements were performed using a VSP-300 Biologic Potentiostat. All experimental results were at least triplicated. Error bars presented

signify one standard deviation of experimental results. Representative voltammograms are shown.

5.2.4. Material Characterization

Scanning electron microscope (SEM) images were obtained for each sample using a Hitachi S-4700 II Field Emission SEM with an Energy Dispersive Spectrometer (EDS) at an acceleration voltage of 15 kV. X-Ray diffraction (XRD) was performed using a Bruker D2 X-Ray Diffractometer. Atomic force microscopy (AFM) images were obtained using a Nanosurf EasyScan 2 microscope operated in contact mode using a silicon tip with an aluminium reflective coating (ContAl-G, TedPella, Inc.).

5.3. Results and Discussion

5.3.1. Electrodeposition of Ni-Cu_2O Thin Films

Cu_2O thin films were formed on ITO electrodes using an electrodeposition procedure reported previously.[20] To modify these films with Ni, Ni was electrodeposited on top of the Cu_2O thin films using chronopotentiometry at -4 mA/cm^2 in a Ni plating bath. By varying the electrodeposition time, the thickness of Ni on top of the Cu_2O can be tuned. Assuming a uniform Ni overlayer, we calculate the thickness of the layer from the charge passed during chronopotentiometry using equation 1 below

$$\text{Thickness} = \frac{QM}{AF\rho n} \quad (1)$$

in which Q is charge, M is molecular weight, A is electrode area, F is Faraday's constant, ρ is the density of Ni, and $n = 2$ is the number of electrons transferred in the reaction

$Ni^{2+} + 2\ e^- \rightarrow Ni_{(s)}$. Table 1 lists the calculated thicknesses of the Ni overlayer for five different plating times studied in this work. We note that SEM images (*vide infra*) indicate that the Ni layer electrodeposited is not uniform, and thus the calculated thickness values can only be interpreted as average thicknesses across the entire sample area.

Time (s)	Calculated Ni Thickness (μm)	Calculated Cu_2O:Ni Mass Ratio
20	0.7	38.5:1
100	3.2	8.4:1
160	5.3	5.1:1
200	6.8	4.0:1
500	15	1.8:1

Table 5.1. Calculated thicknesses of Ni obtained during electrodeposition for various plating times and calculated Cu_2O:Ni mass proportions of the samples.

5.3.2. OER Activity of Ni-Cu_2O Thin Films

Figure 5.1 compares IR-corrected LSVs of an unmodified Cu_2O thin film with Cu_2O substrates that have been electrodeposited with Ni for 100 s and 500 s. In all three voltammograms, the current abruptly rises once a positive enough potential is reached to allow the OER to commence. At high current densities (> ~5 mA cm^{-2}), O_2 bubbles are vigorously generated from the electrode surface. However, the onset potentials of the LSVs

for the samples with Ni are about 130 mV more negative than the unmodified Cu_2O electrode (Figure 1B). Therefore, the addition of Ni to the electrode enhances the activity of the OER catalyst in terms of overpotential.

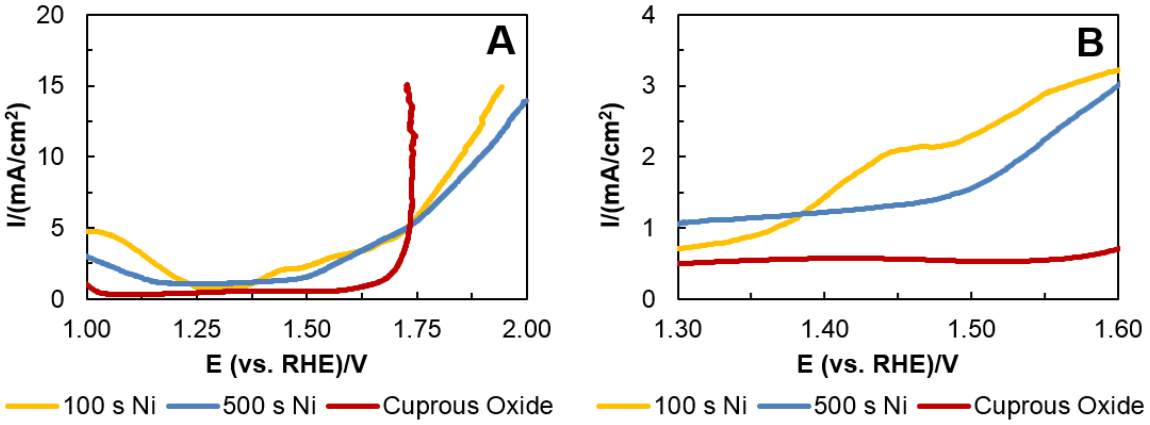

Figure 5.1. Linear sweep voltammograms of the oxygen evolution reaction in 1 M NaOH using Cu_2O on ITO working electrodes that have been electrodeposited with Ni for 0 s (red line), 100 s (orange line), and 500 s (blue line) at a scan rate of 10 mV/s. Panel B is an inset of panel A.

We tested three additional Ni electrodeposition times (20 s, 160 s, and 200 s) in an effort to determine the optimal Ni thickness for the Ni-Cu_2O catalyst (Figure 5.2A). These three catalysts also exhibited more negative onset potentials for the OER as compared to the unmodified Cu_2O control, although the extent of the enhancement varied. Importantly, control experiments measuring the LSVs of Cu and Ni foils both show much more positive OER onset potentials as compared to any of the Ni-Cu_2O electrodes (Figure 5.2B).

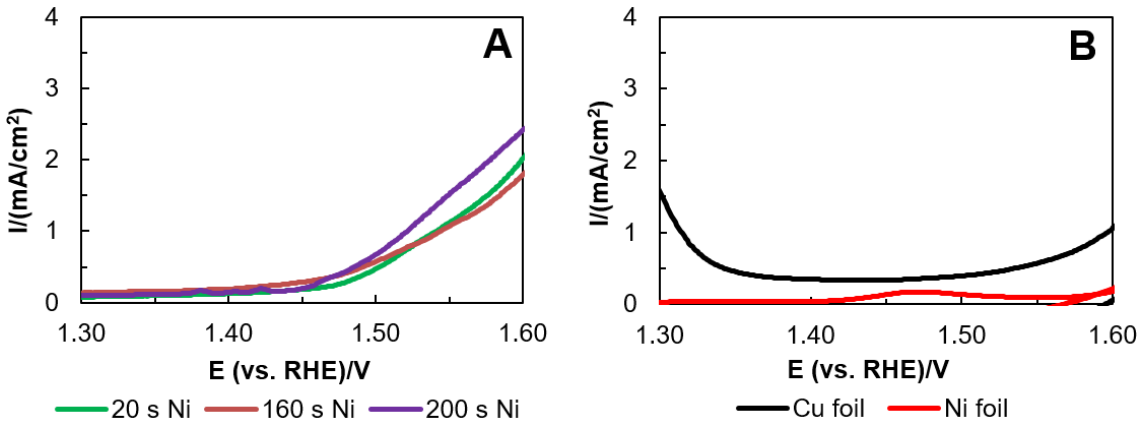

Figure 5.2. Linear sweep voltammograms of the oxygen evolution reaction in 1 M NaOH using Cu_2O on ITO working electrodes that have been electrodeposited with Ni for 20 s (A, green line), 160 s (A, red line), and 200 s (A, purple line) at a scan rate of 10 mV/s. Analogous experiments were also performed with Cu (B, black line) and Ni (B, red line) foils.

Figure 5.3 plots the calculated overpotential for the onset of the OER for Ni-Cu_2O catalysts with five different Ni overlayer thicknesses along with the overpotentials for control experiments. First, all of the Ni-Cu_2O catalysts possess an overpotential for the OER that is less than that of the Cu_2O, Cu, and Ni control experiments. Second, as the Ni electrodeposition time increases from 0 s to 20 s to 100 s, the OER overpotential decreases. However, once the Ni electrodeposition time exceeds 100 s, the OER overpotential increases. These results demonstrate that there is an optimal Ni to Cu_2O ratio to minimize the OER overpotential. The 100 s sample has the lowest overpotential (0.15 V), which is among the lowest for an OER catalyst operated under either acidic or basic conditions. Table S5.1 summarizes the overpotentials and current densities for a wide range of OER catalysts reported in the literature. The Ni-Cu_2O catalyst we developed has a comparable or lower overpotential than previously developed Ni-based OER catalysts.

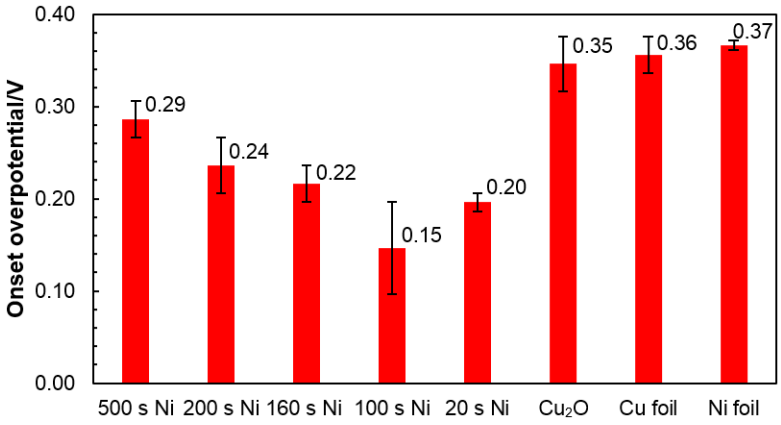

Figure 5.3. Plot of overpotentials for the onset of the oxygen evolution reaction using various working electrodes in 1 M NaOH.

5.3.3. Surface Characterization of Ni-Cu_2O Thin Films

In an effort to determine why the Ni-Cu_2O catalyst formed via 100 s of Ni electrodeposition has the optimal amount of Ni for decreasing the OER overpotential, we characterized the composition and structure of the catalysts using XRD, SEM-EDS, and AFM. We performed these characterization techniques on the samples after Ni electrodeposition but before OER voltammetry was conducted. The XRD spectrum of the Ni-Cu_2O catalyst confirms the presence of the ITO substrate and the electrodeposited films of Cu_2O and Ni on the electrode surface as expected (Figure 5.4). The positions of the peaks match the values previously reported for these three components.[20,22,23]

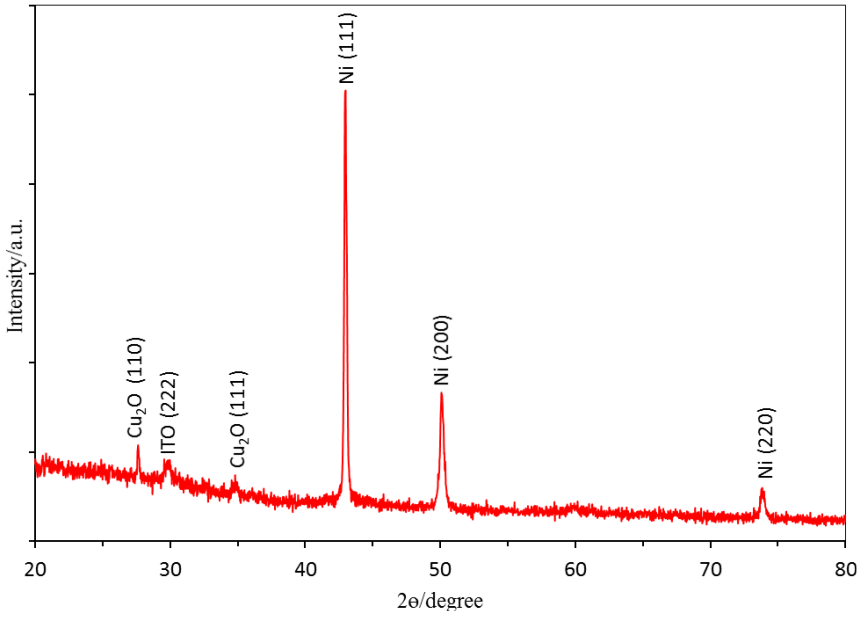

Figure 5.4. XRD spectrum of a Cu_2O on ITO electrode with a Ni overlayer formed using 100 s of Ni electrodeposition.

We next analyzed the morphology of Cu_2O electrodes modified with varying amounts of electrodeposited Ni using SEM. The unmodified electrodeposited Cu_2O thin film consists of triangular-shaped crystallites (Figure 5.5A) with (111) faces exposed as shown previously.[24] Figures 5.5B-5.5F show SEM images of Ni-Cu_2O thin films in order of increasing thicknesses of electrodeposited Ni. In all of these cases, the morphology obtained is different from the triangular facets observed without Ni. As the Ni electrodeposition time increases, the facets become sphere-like and agglomerate into larger-sized particles. We hypothesize that this agglomeration takes place due to etching of the Cu_2O crystals by the boric acid present in the Ni electrodeposition bath since Cu_2O is not stable in acid. Indeed, simply soaking a Cu_2O thin film in boric acid causes its original triangular morphology to change (Figure S5.1A). However, the morphological

change induced by the boric acid does not significantly affect the OER onset potential of the Cu_2O thin film (Figure S5.1B), indicating that Ni plays a role in the enhanced activity of the Ni-Cu_2O catalysts.

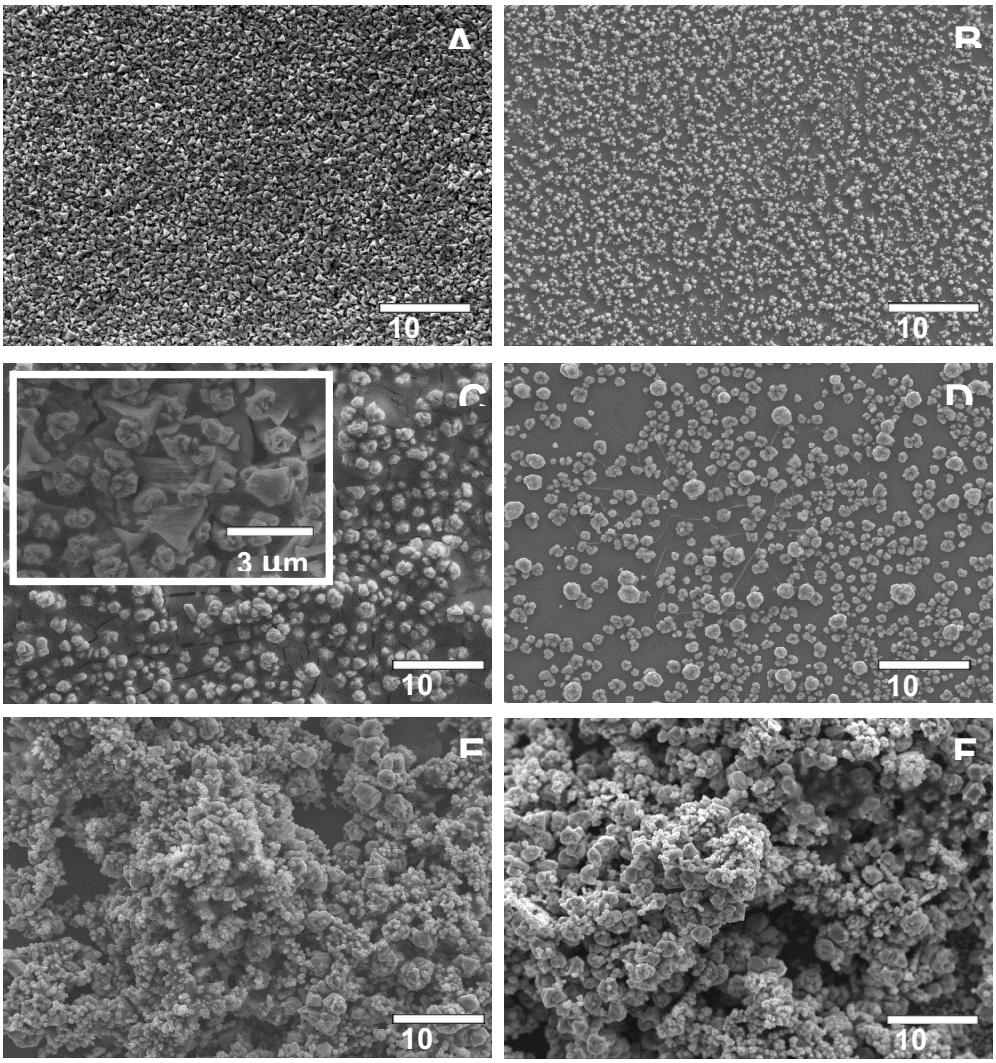

Figure 5.5. SEM images of Cu_2O on ITO electrodes with a Ni overlayer formed via 0 s (A), 20 s (B), 100 s (C), 160 s (D), 200 s (E), and 500 s (F) of Ni electrodeposition.

Since the Ni-Cu_2O catalyst formed using 100 s of Ni electrodeposition was found to have the lowest OER overpotential, we performed SEM-EDS mapping of this electrode (Figures 5.6, S5.2 and S5.3). As a whole, the SEM-EDS mapping results indicate that the electrode contains Ni-modified Cu_2O particles. The overall EDS spectrum of the SEM image in Figure 5.6A is given in Figure 5.6B. The spectrum contains peaks associated with Ni, Cu, O, and S along with unlabelled In and Sn peaks from the ITO substrate. The first two elements come from the Ni and Cu_2O thin films, the O arises from both Cu_2O and ITO, and the S originates from $NiSO_4$ used in the Ni electrodeposition bath. An elemental map of the Cu content of the electrode shows that the bright sphere-like particles on the surface are Cu_2O (Figure 5.6C). Unlike the Cu coverage, the Ni distribution does not consist of discrete particles. Instead, Figure 5.6D shows that the Ni layer is fairly uniform across the surface although it is noticeably absent where the ITO substrate is exposed (e.g. see the top left of the image). The S elemental map mostly overlaps with the Ni distribution because the S originates from the Ni electrodeposition bath (Figure 5.6E). Lastly, the O content detected by EDS is greatest where bare ITO is present, and hence is roughly inversely correlated with the Ni distribution (Figure 5.6F).

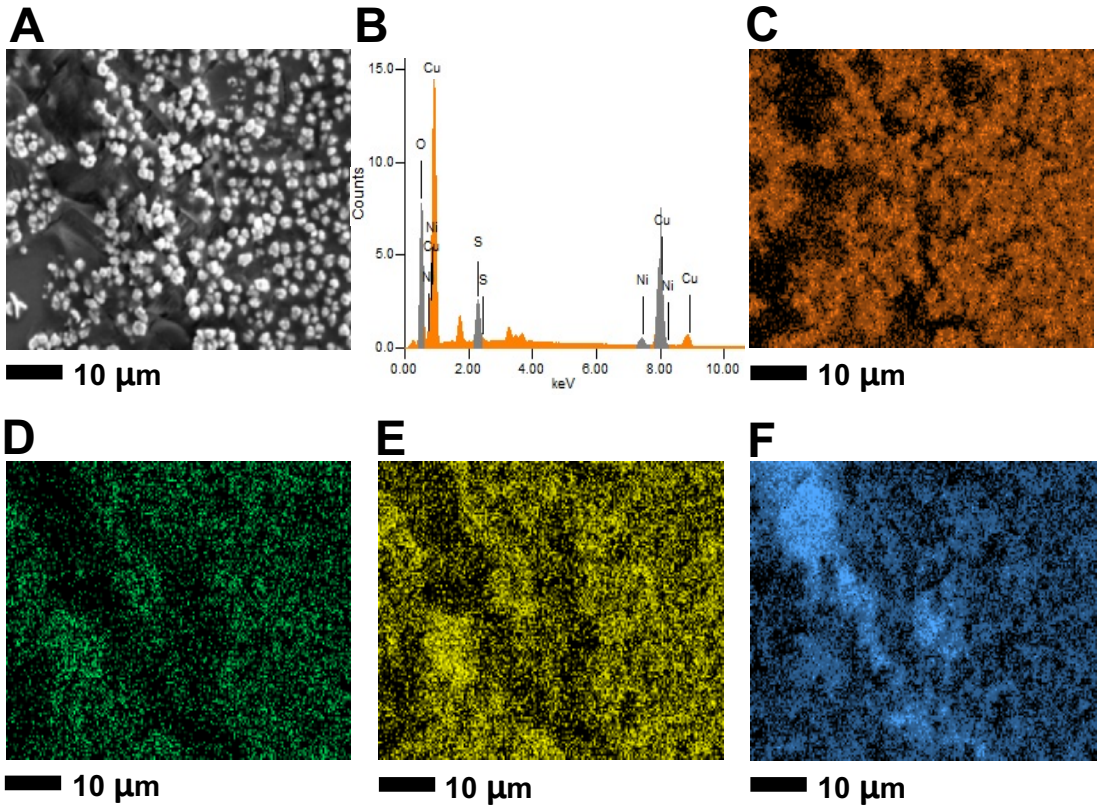

Figure 5.6. SEM image (A), EDS spectrum (B), and corresponding elemental distribution maps (C-F) as determined by EDS of a Cu_2O on ITO electrode with a Ni overlayer formed using 100 s of Ni electrodeposition. Brighter colors in the EDS maps represent higher relative elemental concentrations.

Lastly, we conducted AFM images of the Ni-Cu_2O electrode formed using 100 s of Ni electrodeposition (Figure S5.4). The AFM images confirm that there are low, smooth spots on the electrodes where bare ITO is present. The high-lying sphere-like particles are the agglomerates of Ni and Cu_2O.

Taking together the SEM, EDS mapping, and AFM results, we can now more fully understand the chemical identity of the components present in the SEM image of the optimal Ni-Cu_2O catalyst presented in Figure 5.5C formed via 100 s of Ni

electrodeposition. The sphere-like particles can be assigned to Cu_2O, and the wispy-like platelets are Ni (Figure 5.5C, inset). This morphology contains a fairly uniform mixture of Cu_2O and Ni components, and this even distribution with many bimetallic sites may explain why this surface structure leads to optimal OER electrocatalysis. Previous studies with OER catalysts have shown that bimetallic active sites often lead to lower OER overpotentials and outperform their monometallic counterparts.[25] For example, a synergistic effect between Ni and Fe sites in Fe-doped NiOOH leads to enhanced OER electrocatalysis.[26] Finally, we note that metallic Ni is unstable in the NaOH electrolyte we used for conducting the OER voltammetry.[27] The active catalyst during OER is therefore a mixture of Ni/Cu (oxy)hydroxides.

5.4. Conclusions

We synthesized a series of Ni-Cu_2O electrocatalysts for the OER by sequentially electrodepositing Cu_2O and Ni on ITO substrates. By altering the amount of Ni on the surface, the activity of the electrocatalysts varies substantially. An optimal thickness of Ni yields a catalyst with an improved onset overpotential of 0.15 V. Characterization using XRD, SEM, EDS, and AFM demonstrates that the composition and morphology of the electrocatalysts are dependent upon the amount of Ni electrodeposition and dictate catalyst performance.

5.5. References

1. Marbán, G.; Valdés-Solís, T., Towards the Hydrogen Economy? *Int. J. Hydrogen Energ.* **2007**, *32*, 1625-1637.

2. Carmo, M.; Fritz, D. L.; Mergel, J.; Stolten, D., A Comprehensive Review on PEM Water Electrolysis. *Int. J. Hydrogen Energ.* **2013**, *38*, 4901-4934.

3. Tahir, M.; Pan, L.; Idrees, F.; Zhang, X.; Wang, L.; Zou, J.; Wang, Z. L., Electrocatalytic Oxygen Evolution Reaction for Energy Conversion and Storage: A Comprehensive Review. *Nano Energy* **2017**, *37*, 136-157.

4. Li, Y.; Lu, J., Metal-Air Batteries: Will They Be the Future Electrochemical Energy Storage Device of Choice? *ACS Energy Lett.* **2017**, *2*, 1370-1377.

5. Weng, W.; Barile, C. J.; Du, P.; Abouimrane, A.; Assary, R. S.; Gewirth, A. A.; Curtiss, L. A.; Amine. K., Polymer Supported Organic Catalysts for O_2 Reduction in Li-O_2 Batteries. *Electrochim. Acta* **2014**, *119*, 138-143.

6. McCrory, C. C. L.; Jung, S.; Peters, J. C.; Jaramillo, T. F., Benchmarking Heterogeneous Electrocatalysts for the Oxygen Evolution Reaction. *J. Am. Chem. Soc.* **2013**, *135*, 16977-16987.

7. Reier, T.; Oezaslan, M.; Strasser, P., Electrocatalytic Oxygen Evolution Reaction (OER) on Ru, Ir, and Pt Catalysts: A Comparative Study of Nanoparticles and Bulk Materials. *ACS Catal.* **2012**, *2*, 1765-1772.

8. Sapountzi, F. M.; Gracia, J. M.; Weststrate, C. J.; Fredriksson, H. O. A.; Niemantsverdriet, J. W., Electrocatalysts for the Generation of Hydrogen, Oxygen and Synthesis Gas. *Prog. Energ. Combust.* **2017**, *58*, 1-35.

9. Song, F.; Hu, X., Exfoliation of Layered Double Hydroxides for Enhanced Oxygen Evolution Catalysis. *Nat. Comm.* **2014**, *5*, 4477-4485.

10. Hirai, S.; Yagi, S.; Seno, A.; Fujioka, M.; Ohno, T.; Matsuda, T., Enhancement of the Oxygen Evolution Reaction in Mn^{3+}-based Electrocatalysts: Correlation between Jahn–Teller Distortion and Catalytic Activity. *RSC Adv.* **2016**, *6*, 2019-2023.

11. Zhang, Y.; Cui, B.; Zhao, C.; Lin, H.; Li, J., Co–Ni Layered Double Hydroxides for Water Oxidation in Neutral Electrolyte. *Phys. Chem. Chem. Phys.* **2013**, *15*, 7363-7369.

12. Lu, Z.; Qian, L.; Tian, Y.; Li, Y.; Sun, X.; Duan, X., Ternary NiFeMn Layered Double Hydroxides as Highly-efficient Oxygen Evolution Catalysts. *Chem. Comm.* **2016**, *52*, 908-911.

13. Qiu, Y.; Xin, L.; Li, W., Electrocatalytic Oxygen Evolution over Supported Small Amorphous Ni–Fe Nanoparticles in Alkaline Electrolyte. *Langmuir* **2014**, *30*, 7893-7901.

14. Favaro, M.; Drisdell, W. S.; Marcus, M. A.; Gregoire, J. M.; Crumlin, E. J.; Haber, J. A.; Yano, J., An Operando Investigation of (Ni-Fe-Co-Ce)O_x System as Highly Efficient Electrocatalyst for Oxygen Evolution Reaction. *ACS Catal.* **2017**, *7*, 1248-1258.

15. Haber, J. A.; Guevarra, D.; Jung, S.; Jin, J.; Gregoire, J. M., Disocvery of a New Oxygen Evolution Reaction Electrocatalysts by Combinatorial Investigation of the Ni-La-Co-Ce Oxide Composition Space. *Chem. Electro. Chem.* **2014**, *1*, 1613-1617.

16. Xi, Z.; Mendoza-Garcia, A.; Zhu, H.; Chi, M.; Su, D.; Erdosy, D. P.; Li, J.; Sun, S., $Ni_xWO_{2.72}$ Nanorods as an Efficient Electrocatalyst for Oxygen Evolution Reaction. *Green Energy Environ.* **2017**, *2*, 119-123.

17. Nsanzimana, J. M. V.; Peng, Y.; Miao, M.; Reddu, V.; Zhang, W.; Wang, H.; Xia, B. Y.; Wang, X. An Earth-Abundant Tungsten-Nickel Alloy Electrocatalyst for Superior Hydrogen Evolution. *ACS Appl. Nano. Mater.* **2018**, *1*, 1228-1235.

18. Seh, Z. W.; Kibsgaard, J.; Dickens, C. F.; Chorkendorff, I.; Norskov, J. K.; Jaramillo, T. F., Combining Theory and Experiment in Electrocatalysis: Insights into Materials Design. *Science* **2017**, *355*, 147-159.

19. Man, I. C.; Su, H.; Calle-Vallejo, F.; Hansen, H. A.; Martinez, J. I.; Inoglu, N. G.; Kitchin, J.; Jaramillo, T. F.; Norskov, J. K.; Rossmeisl, J., Universality in Oxygen Evolution Electrocatalysis on Oxide Surfaces. *Chem. Cat. Chem.* **2011**, *3*, 1159-1165.

20. Golden, T. D.; Shumsky, M. G.; Zhou, Y.; VanderWerf, R. A.; Van Leeuwen, R. A.; Switzer, J. A., Electrochemical Deposition of Copper(I) Oxide Films. *Chem. Mater.* **1996**, *8*, 2499-2504.

21. van der Vliet, D.; Strmcnik, D. S.; Wang, C.; Stamenkovic, V. R.; Markovic, N. M.; Koper, M. T. M., On the Importance of Correcting for the Uncompensated Ohmic Resistance in Model Experiments of the Oxygen Reduction Reaction. *J. Electrochem. Soc.* **2010**, *647*, 29-34.

22. Du, L. X.; Jiao, Y.; Niu, S.; Miao, H.; Yao, H.; Wang, K.; Hu, X.; Fan, H., Control of Morphologies and Properties of Zinc Oxide Nanorod Arrays by Slightly Adjusting their Seed Layers. *Nanomater. Nanotechno.* **2016**, *6*, 1847980416663674-1847980416663681.

23. Yaddanapudi, H. S.; Tian, K.; Teng, S.; Tiwari, A., Facile Preparation of Nickel/carbonized Wood Nanocomposite for Environmentally Friendly Supercapacitor Electrodes. *Sci. Rep.-UK* **2016**, *6*, 33659-33667.

24. DeHority, K.; Budin, N.; Hilston, S. S.; Zhang, Y.; Fillinger, A., Deposition of Nickel on Electrodeposited Cu_2O Films at Potentials More Positive than the Nernst Potential of Ni^{2+}/Ni0. *J. Electrochem. Soc.* **2017**, *164*, H615-H620.

25. Kim, J. S.; Kim, B.; Kim, H.; Kang, K., Recent Progress on Multimetal Oxide Catalysts for the Oxygen Evolution Reaction. *Adv. Energy Mater.* **2018**, *8*, 1702774-1702799.

26. Xiao, H.; Shin, H.; Goddard, W. A., Synergy Between Fe and Ni in the Optimal Performance of (Ni,Fe)OOH Catalysts for the Oxygen Evolution Reaction. *P. Natl. Acad. Sci. USA* **2018**, *115*, 5872-5877.

27. Beverskog, B.; Puigdomenech, I., Revised Pourbaix Diagrams for Nickel at 25–300 °C. *Corros. Sci.* **1997**, *39*, 969-980.

Chapter 6: Preparation and Electron Transfer Properties of Self-Assembled Monolayers of Ferrocene on Carbon Electrodes

6.1. Introduction

Carbon and its compounds are important materials due to their good chemical, electrochemical, and thermal stability. Because of these properties, carbon materials have been widely used in electroanalysis, chemical and biological sensing, energy storage and conversion, and catalysis.[1-6] The functionalization of carbon electrodes in a controlled manner is important for many of these applications, both from a technological and scientific standpoint.[7] One method of modifying glassy carbon electrodes is through self-assembled monolayers (SAMs). SAMs can be used to modulate the surface reactivity, hydrophobicity, and wettability among other attributes.[8,9] In addition, SAMs can function as stable anchors for other molecules to electrode surfaces through covalent bonds.[8,10] SAMs on carbon covalently modified with molecules vastly increase the functionality of carbon electrodes and for appended species that are redox active, the electrodes can be used to study electron transfer properties. [7-9,11]

In this work, the electron transfer properties of ferrocene attached to SAMs on carbon electrodes are studied. The SAMs are fabricated electrochemically from alkyl diamines as was first pioneered by Sanchez et al.[12] and Deinhammer et al.[13] After SAM formation, amide coupling is elicited between ferrocenecarboxylic acid and the terminal amine groups of the SAM. This coupling reaction, mediated by 1-ethyl-3-(3-(dimethylamino) propyl) carbodiimide hydrochloride (EDC) and *N*-hydroxysuccinimide (NHS) in aqueous solution, goes to completion quickly at room temperature and is experimentally straightforward to perform.[1,14-16]

Previous studies have applied this coupling reaction to SAMs on both carbon and Au electrodes.[2,8,11,17-19,20] EDC/NHS coupling is one of the most popular and widely used

methods for the covalent attachment of small molecules, nanoparticles, and various biomolecules such as proteins and nucleic acids to SAMs. These SAMs have found numerous applications in biosensors due to their biocompatibility and ability to offer molecular level control over surface chemistry and dynamics.[6,13,14,21-23]

Taken together, the amine-SAM formation step followed by EDC/NHS coupling provides a facile route to the preparation of ferrocene-modified carbon electrodes. We modify the glassy carbon electrode with various compositions and chain lengths of SAMs to study how these variables affect surface coverage and electron transfer properties. In addition, we interrogate the role of defect sites in the SAMs on electron transfer to the appended ferrocene by further modifying the SAMs with ZnO electrodeposits.

6.2. Methods

6.2.1. General Procedures

All chemicals were purchased from commercially available sources and used without further purification. All electrochemical studies were carried out using a VSP-300 Biologic potentiostat. Electrochemical studies were conducted using a three-electrode system in which a Pt wire was used as the counter electrode, Ag/AgCl/3 M KCl (Edaq, Inc.) as the reference electrode, and a bare or modified glassy carbon surface (5 mm diameter) as the working electrode. The voltammetry data were collected using a potassium phosphate (100 mM) pH 7 aqueous buffer solution at various scan rates. For studies with other types of carbon, glassy carbon electrodes were modified with 0.11 mg of single-walled carbon nanotubes (Tuball, OCSiAl, Inc.) or 0.11 mg of Vulcan XC-72 and 0.04 g polyvinylidene fluoride (PVDF, Kynar Flex 2751-00) dropcast in acetone (1.0 mL) or

Nafion 117 (FuelCellStore, Inc., 5 μL). All of the cyclic voltammograms (CVs) reported are the second scan unless specified otherwise. Atomic force microscopy (AFM) images were obtained using a Nanosurf EasyScan 2 microscope operated in contact mode using silicon tips with an aluminum reflective coating (ContAl-G, TedPella, Inc.). X-ray photoelectron spectroscopy (XPS) was conducted with a PHI 5600 spectrometer with monochromatic Al Kα radiation and a diameter of analysis of 800 μm.

6.2.2. Experiments on Glassy Carbon Electrodes

Prior to their modification, glassy carbon electrodes were polished with an alumina (0.05 μm in diameter) slurry followed by cleaning with DI water. Then the electrodes were sonicated in DI water for 10 minutes and allowed to dry at room temperature. For solutions of C2 and C6 SAMs, aqueous solutions were prepared using different proportions of ethylenediamine, ethanolamine, hexamethylenediamine, hexylamine, and 6-amino-1-hexanol with a total concentration of 100 mM. For solutions of C12 SAMs, 1,12-diaminododecane and dodecylamine were added in different proportions in acetonitrile with a total concentration of 10 mM. Tetrabutylammonium tetrafluoroborate (100 mM) was also added for the C12 SAM solutions.

The SAMs were formed using chronoamperometry at 1.6 V for various times. After SAM formation, EDC and NHS solutions were prepared by mixing them in a 1:1 molar ratio (20 mM total concentration) and vortexing for 2 minutes. Ferrocenecarboxylic acid (Fc-COOH) solutions (250 μM) were freshly prepared in dimethyl sulfoxide (DMSO) for each experiment.[15] The electrode was then soaked in a mixture of the EDC/NHS (1.5 mL)

and Fc-COOH solutions (0.5 mL) for 18 hours. Lastly, the glassy carbon electrodes were rinsed with pH 7 buffer solution followed by DI water, and voltammetry was conducted.

6.2.3. ZnO Electrodeposition

ZnO electrodeposition on SAM-modified glassy carbon electrodes was carried out in an aqueous solution containing KCl (100 mM) and $Zn(NO_3)_2$ (50 mM) using chronoamperometry at -1.2 V for 20 s, unless the amount of time was otherwise specified.[24] After ZnO electrodeposition, the glassy carbon electrodes were gently rinsed with DI water and soaked in the same mixture of EDC/NHS/Fc-COOH described above for 18 hours. Afterward, the glassy carbon electrodes were rinsed with pH 7 buffer solution followed by DI water, and voltammetry was conducted.

6.3. Results and Discussion

6.3.1. SAM Chain Length and Diluent Effects

Glassy carbon electrodes were modified with different compositions of SAMs having various alkyl chain lengths (Figure 6.1). In the first step, chronoamperometry was performed to oxidize the alkyl amines and attach the SAMs to the glassy carbon electrodes. In some experiments, we used a mixture of alkyl monoamines and diamines to control surface coverage. These mixed monolayers with monoamine diluents create a SAM with a controllable density of terminal amine groups that in turn affect the density of ferrocene appended to the surface in the subsequent coupling step. SAMs with low surface coverages can be, for example, used to delineate the effect of intermolecular reactions of appended species because, at low surface coverages, the species will be site isolated.[2,15,25] In the

second surface attachment step, the SAM-modified glassy carbon electrodes were soaked in a mixture of EDC/NHS/Fc-COOH to attach the ferrocene.

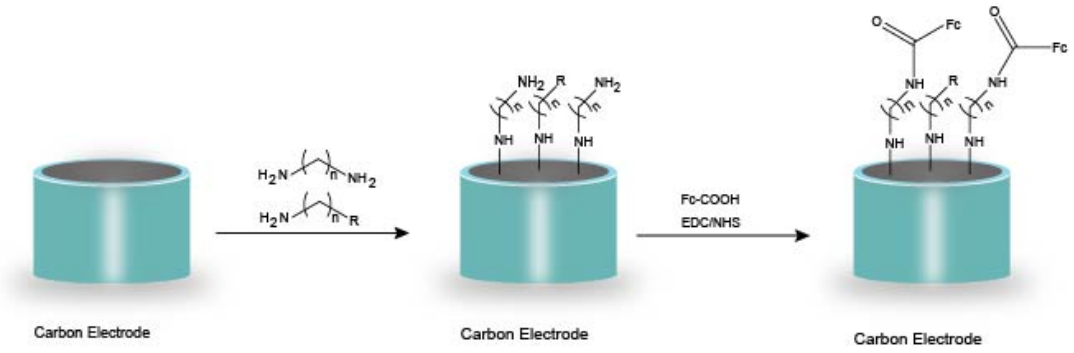

Figure 6.1. Schematic of the modification of carbon electrodes with various chain lengths of SAMs to attach ferrocene with controllable surface coverage.

The black line in Figure 6.2A shows a cyclic voltammogram at a scan rate of 300 mV s^{-1} of a diamine SAM containing 2 methylene groups (C2 SAM) without monoamine diluent. The CV shows one set of peaks corresponding to the reversible Fe^{3+}/Fe^{2+} couple of ferrocenes. Randles-Sevcik analysis of experiments performed at different scan rates demonstrate that the ferrocene is attached to the surface as opposed to freely diffusing in solution (Figure S6.1). Control experiments show that unmodified electrodes, electrodes subjected to EDC/NHS/Fc-COOH without a SAM, and SAM-modified electrodes subjected to Fc-COOH without EDC/NHS all do not exhibit any redox peaks (Figure S6.2). These findings demonstrate that ferrocene is attached to the glassy carbon electrodes only when all of the reaction components are present. The lack of redox activity in the control experiments indicates that ferrocene is not simply physisorbed and instead is covalently bound to the electrode via the SAM.

We soaked the electrodes in the EDC/NHS/Fc-COOH mixture for 18 hours to perform the amide coupling reaction. Experiments conducted with a longer immersion time (e.g. 48 hours) did not result in a significant increase in surface coverage compared to the 18 hours experiments (Figure S6.3), indicating that 18 hours is enough time for the coupling reaction to go to completion. We also modulated the voltage range scanned during the CV experiments. When extending the anodic sweep limit to 1.0 V vs. Ag/AgCl, there is a rise in the anodic current at voltages greater than 0.8 V, indicating that a second electrochemical process occurs (Figure S6.4). Because further cycling of the electrode under these conditions leads to a decrease in the current density of the ferrocene redox couple, we ascribe this anodic feature starting at 0.8 V to the irreversible oxidation and decomposition of the amine SAM.

To control the surface coverage of ferrocene, ferrocene was attached to C2 SAMs on glassy carbon electrodes using $NH_2(CH_2)_2NH_2$ and the diluent $NH_2(CH_2)_2OH$ in various molar ratios. With 50 mol % diluent (Figure 6.2A, red line), the peak shape in the CV sharpens as compared to the CV of the SAM without diluent (Figure 6.2B, black line). Without diluent, adjacent ferrocene molecules are closer to one another than when they are spaced with the diluent. Ferrocenes adjacent to one another can undergo intermolecular electron transfer, which results in a wider distribution of voltages at which electron transfer occurs, yielding a broader peak in the CV. In contrast, with 50 mol % diluent, more of the ferrocenes are site-isolated, which gives rise to a narrower peak. Further increasing the concentration of the diluent results in a decrease in the peak current density due to lower surface coverages of ferrocene (Figure 6.2A blue and pink lines and Figure S6.5).

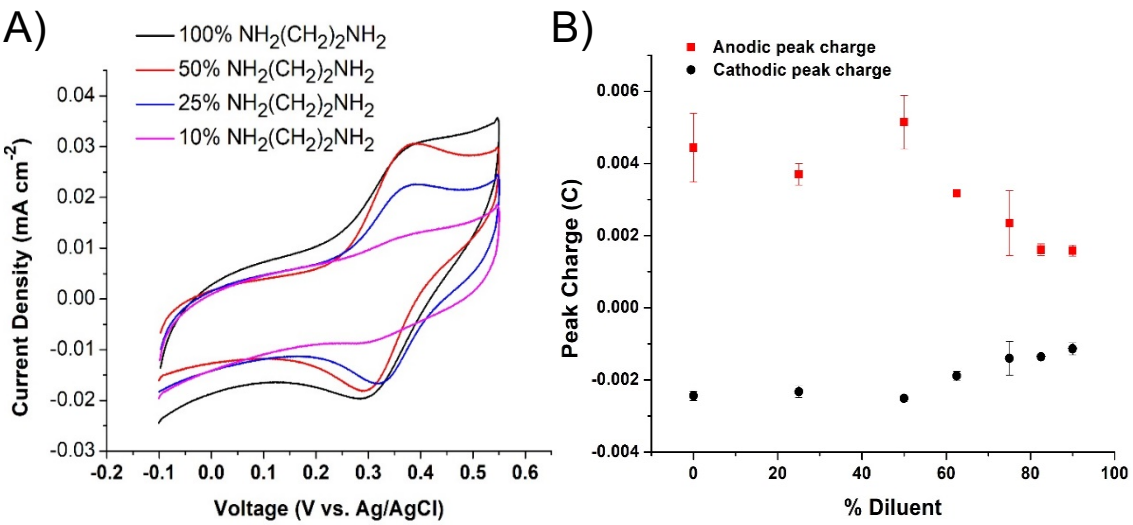

Figure 6.2. Cyclic voltammograms at 300 mV s^{-1} in pH 7 buffer of ferrocene attached to C2 SAMs on glassy carbon electrodes using 100 mM $NH_2(CH_2)_2NH_2$ and $NH_2(CH_2)_2OH$ in various molar ratios (A). Plot of anodic peak charge (red) and cathodic peak charge (black) of ferrocene attached to C2 SAMs with different molar ratios of $NH_2(CH_2)_2NH_2$ and $NH_2(CH_2)_2OH$ diluent.

Figure 6.2B plots the integrated charges for the anodic and cathodic peaks of the ferrocene modified C2 SAMs as a function of the amount of diluent. From 0% to 50% diluent, the integrated charge remains fairly constant because there is a maximum amount of ferrocene that can sterically fit onto the electrode. At diluent proportions greater than 50%, the magnitudes of the integrated charges decrease with increasing diluent due to lower surface coverages of ferrocene. We note that the absolute value of the cathodic charges are significantly less than those of the anodic charges. For a reversible redox couple such as ferrocene, these two values are expected to be the same.[26] The origin of this discrepancy arises from the relatively large background current caused by the capacitance of the glassy carbon electrode, which disproportionately affects the integration calculations of the cathodic peaks. The anodic charges for the SAMs range from 1.6 mC to 5.2 mC

across the different diluent ratios, which corresponds to a ferrocene surface density ranging between 2.8 x 10^{-7} mol cm^{-2} to 8.5 x 10^{-8} mol cm^{-2}.

Many previous works have established that the CVs of SAMs of ferrocene on Au electrodes exhibit zero peak separation for a reversible system.[27-33] Additionally, theoretical analysis of the peak shape indicates that for a monolayer of non-interacting redox active species, the full width at half maximum (FWHM) of the peak is 90.6 mV.[34-36] The CVs obtained in this study for a monolayer of ferrocene using $NH_2(CH)_2NH_2$ without diluent possess a peak separation of (142 ± 14) mV and a FWHM of (150 ± 15) mV. These values are both higher than the theoretical values and those obtained on Au monolayers because the appended ferrocenes are not site-isolated and hence interact with one another. Furthermore, as discussed later in the manuscript, the monolayers are not well ordered, and the resulting inhomogeneity in the monolayer causes variations in the chemical environment of each ferrocene, which leads to peak broadening. Dilution of the monolayers with $NH_2(CH)_2OH$ decreases both the peak separation and FWHM values of the CVs (Figure S6.6) due to decreased ferrocene-ferrocene interactions. However, the values measured are still significantly higher than the theoretical values, indicating that the diluted monolayers are still highly heterogeneous.

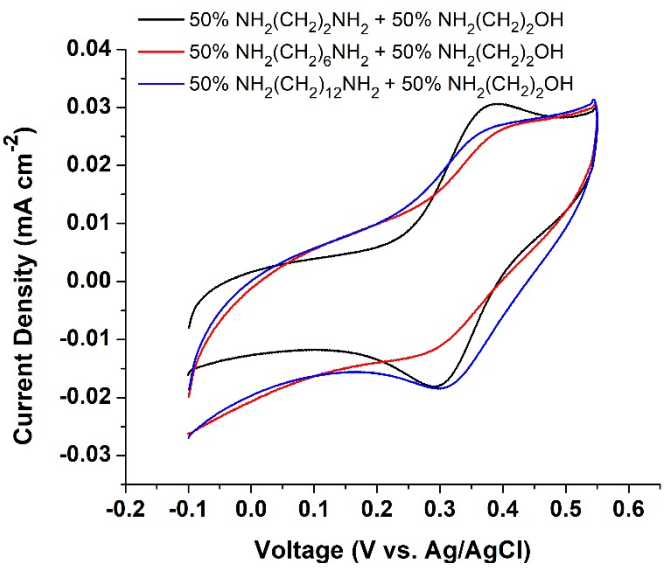

Figure 6.3. Cyclic voltammograms at 300 mV s^{-1} in pH 7 buffer of ferrocene attached to SAMs on glassy carbon electrodes using 50 mM $NH_2(CH_2)_2OH$ diluent and 50 mM $NH_2(CH_2)_2NH_2$ (black), 50 mM $NH_2(CH_2)_6NH_2$ (red), and 50 mM $NH_2(CH_2)_{12}NH_2$ (blue).

To understand the effect of chain length on the surface coverage of ferrocene, in addition to C2 SAMs, we performed experiments using SAMs containing 6 and 12 methylene groups. Whereas both the C2 and C6 SAM solutions are soluble in water and thus can be attached using the same chronoamperometry conditions, the C12 SAM is not soluble in water due to its long hydrophobic tail. For this reason, we prepared C12 SAM solutions in acetonitrile and first optimized the amount of time (8 hours) needed during chronoamperometry to maximize the surface coverage of ferrocene (Figure S6.7). The CVs of the ferrocene C12 SAMs at different scan rates are shown in Figure S6.8.

Figure 6.3 shows cyclic voltammograms of ferrocene attached to SAMs containing 2, 6, and 12 methylene groups with 50 mol % of the $NH_2(CH_2)_2OH$ diluent at 300 mV s^{-1}. The Fe 2p XPS spectra of these SAMs match previous literature reports[2,37] of ferrocene-modified carbon electrodes and indicate that ferrocene was successfully attached to the

electrodes regardless of the number of methylene groups in the SAMs (Figure S6.9). Interestingly, the peak separations between the anodic and cathode waves of the three CVs are fairly similar to one another. This result is in sharp contrast to what is observed when ferrocene and other redox active molecules are attached to SAMs of alkanethiols on Au electrodes.[20] In this case, longer-chained SAMs exhibit slower electron transfer kinetics, resulting in a larger peak-to-peak separation as compared to shorter-chained SAMs. The slower electron transfer kinetics arise from electron tunneling that occurs through the insulating alkyl chains in the well-packed SAMs. With the SAMs studied here on carbon, however, the similar peak separation values across the three different chain lengths suggest that the electron transfer rates through the three SAMs are also similar. Quantification of these electron transfer rates using Laviron analysis confirms that the SAMs possess similar transfer kinetics (*vide infra*). We propose that disorder in the SAMs allows for the alkyl chains of the SAM to bend, which enables the ferrocene molecules to be in close contact with defect sites on the electrode. Compared to well-defined Au electrodes such as Au(111), carbon is a much more poorly-defined surface that contains a high defect density. Moreover, the use of a short C2 diluent in the SAMs used for the CVs in Figure 6.3 further contributes to a high degree of structural disorder in these systems. Longer chain lengths of SAMs are known to have greater packing densities and less defect sites due to a greater number of Van der Waals interactions between the alkyl chains. For the C6 and C12 experiments (Figure 6.3, red and blue lines), the large difference in lengths between the linker and the diluent and the resulting disordered SAMs with increased ferrocene-ferrocene interactions may explain the broadening of the peaks of the ferrocene redox couple as compared to the CV of the SAM with the C2 linker (Figure 6.3, black line).

Taken together, these attributes of the SAMs allow the appended ferrocene molecules to orient themselves close to the electrode surface, which results in fast electron transfer rates, regardless of the linker length in the SAM used.

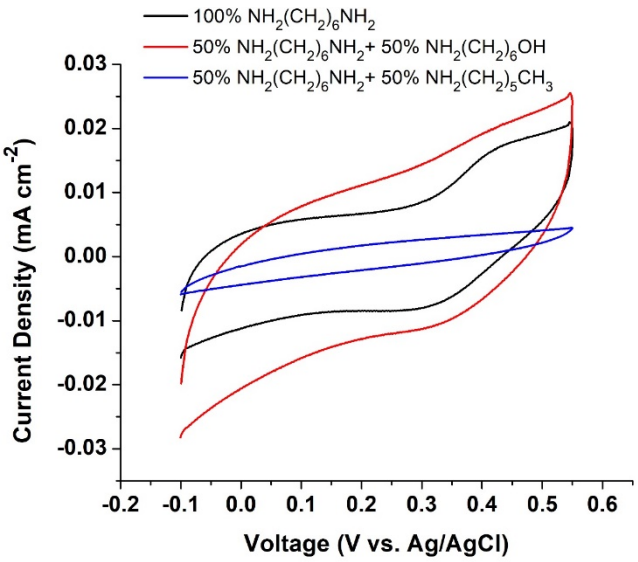

Figure 6.4. Cyclic voltammograms at 300 mV s^{-1} in pH 7 buffer of ferrocene attached to C6 SAMs on glassy carbon electrodes using 100 mM $NH_2(CH_2)_6NH_2$ (black), 50 mM $NH_2(CH_2)_6NH_2$ and 50 mM $NH_2(CH_2)_6OH$ (red), and 50 mM $NH_2(CH_2)_6NH_2$ and 50 mM $NH_2(CH_2)_5CH_3$ (blue).

To fabricate SAMs with less disorder, we increased the chain of the length of the diluent. The red line in Figure 6.4 displays a CV of a ferrocene-modified SAM with a C6 linker and 50 mol % of a diluent of similar length ($NH_2(CH_2)_6OH$). Compared to a ferrocene modified C6 SAM without diluent (Figure 6.4, black line), the CV shows that ferrocene was attached with a significantly lower surface coverage. This result suggests that the C6 diluent impedes the attachment of ferrocene to the SAM, likely through unfavorable steric interactions during the amide coupling reactions. We also compared the effect of modifying the electrodes with diluents with a hydrophobic methyl head group as opposed to a hydrophilic alcohol head group. With 50 mol % of a hydrophobic C6 diluent,

the ferrocene-modified SAM shows only a negligible amount of ferrocene attachment (Figure 6.4, blue line). A similar result is obtained with a C12 SAM and 50 mol% of a hydrophobic C12 diluent (Figure S6.10). Evidently, the hydrophobic head groups of the SAMs further impede ferrocene attachment because it is unfavorable for the hydrophilic reactants and products of the amide coupling chemistry to react at the hydrophobic SAM interface. The non-Faradaic current density of the CV with the hydrophobic C6 diluent (Figure 6.4, blue line) is also significantly less than that of the hydrophilic C6 diluent (Figure 6.4, red line). This difference arises from the lower quantity of hydrophilic ions that accumulate at the SAM-water interface when the SAM is hydrophobic. A smaller number of ions gives rise to a smaller non-Faradaic capacitive current density. In summary, both the length and functionality of the diluent have a profound effect on the dynamics of ferrocene attachment.

6.3.2. Defect Blocking Experiments with ZnO Electrodeposits

In the previous section, we established a hypothesis as to why the electron transfer rate to ferrocene did not vary with the chain length of the SAM linker. We suggested that perhaps defect sites not modified with SAM on the carbon electrode allow the alkyl groups of the SAM linker to bend towards the electrode surface, enabling electron transfer to occur directly from the electrode to ferrocene, instead of via a tunneling mechanism through the insulating SAM linkers. To further explore this hypothesis, here we investigate the role of defect sites in the SAMs on ferrocene electron transfer dynamics by modifying the SAMs with ZnO electrodeposits. Because electrodeposition is preferred on portions of the electrode that are not modified with SAM, the ZnO electrodeposition can be elicited

selectively on the unmodified defect sites. In this way, the defect sites of the SAM can be blocked, and their role in ferrocene electron transfer dynamics can be probed.

Towards this end, we first optimized the amount of time needed to conduct ZnO electrodeposition to block the defect sites (Figure S6.11). If too much ZnO is electrodeposited, the ZnO buries the ferrocene, thus rendering it redox inactive (Figure S6.11, dark blue line). On the other hand, if too little ZnO is electrodeposited, not all of the defect sites are blocked, and the resulting CV is similar in appearance to a CV without any ZnO electrodeposits (Figure S6.11, red line). Under the chronoamperometry conditions used for ZnO electrodeposition, 20 s was the maximum amount of electrodeposition time that did not result in a significant decrease in ferrocene surface coverage, thus implying that the majority of the defect sites on the SAM are blocked by the ZnO electrodeposits. In addition to voltammetry experiments, we used AFM to characterize the electrodes with and without ZnO electrodeposits. Images of a bare glassy carbon electrode are relatively smooth, but reveal the presence of scratches caused by polishing the surface with alumina during the cleaning procedure (Figure S6.12). Similar morphologies of glassy carbon electrodes have been reported previously.[38] Upon attaching a SAM of ferrocene on the electrode (Figure S6.13) and subsequently electrodepositing ZnO (Figure S6.14), the roughness of the surfaces progressively increases. In particular, high-lying particles in the AFM image of the ZnO-modified electrode (Figure S6.14A) indicate the presence of ZnO electrodeposits, which presumably nucleated in the exposed defect sites of the SAM. The Fe 2p XPS data of the ZnO-modified electrode demonstrate that ferrocene remains attached to the surface after ZnO electrodeposition (Figure S6.15). The positions of the Fe 2p peaks are not perturbed by the ZnO electrodeposits, indicating that the short-range chemical

environment of the attached ferrocene is not altered by the ZnO. Furthermore, the Zn 2p XPS and Zn Auger LMM peaks match previous literature values for ZnO electrodeposits,[39] which together demonstrate that ZnO was successfully electrodeposited (Figure S6.16).

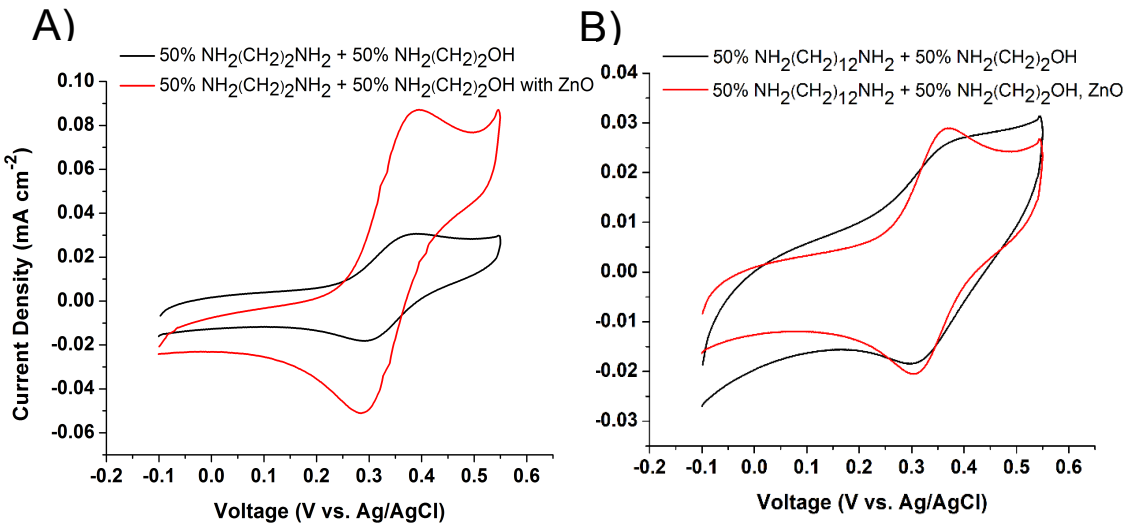

Figure 6.5. Cyclic voltammograms at 300 mV s^{-1} in pH 7 buffer of ferrocene attached to SAMs on glassy carbon electrodes using 50 mM $NH_2(CH_2)_2OH$ diluent and 50 mM $NH_2(CH_2)_2NH_2$ (A) or 50 mM $NH_2(CH_2)_{12}NH_2$ (B) with (red) and without (black) 20 s of ZnO electrodeposition.

Figure 6.5A displays a CV of a ferrocene modified C2 SAM with 50 mol % C2 diluent with (red line) and without (black line) ZnO electrodeposits. After ZnO electrodeposition, there is a large increase in electrode capacitance. This increase can be ascribed to the addition of high surface area ZnO electrodeposits to the surface. In contrast, on C6 and C12 SAMs with 50 mol % C2 diluent, this same increase in capacitance is not observed (Figures 6.5B and S6.17). Presumably, the C6 and C12 SAMs are more ordered and well-packed, and so there are not as many ZnO electrodeposits on the surface, or the electrodeposits are more compact and have less surface area.

Although there is a change in capacitance, the CVs of the ferrocene-modified C2 SAMs with and without ZnO electrodeposits exhibit similar peak broadness (Figure 6.5A). In the case of the C12 SAMs, however, the peaks in the CV with the ZnO electrodeposits are much sharper than in the CV without ZnO (Figure 6.5B). In the absence of ZnO, we hypothesize that bending of the alkyl linking groups enables ferrocene molecules to not only directly interact with the electrode but with one another. The resulting ferrocene-ferrocene interactions give rise to peak broadness. Upon electrodeposition of ZnO in the defect sites of the SAM, this bending does not occur as readily, which prevents ferrocene-ferrocene interactions and thus results in a sharper peak in the CV.

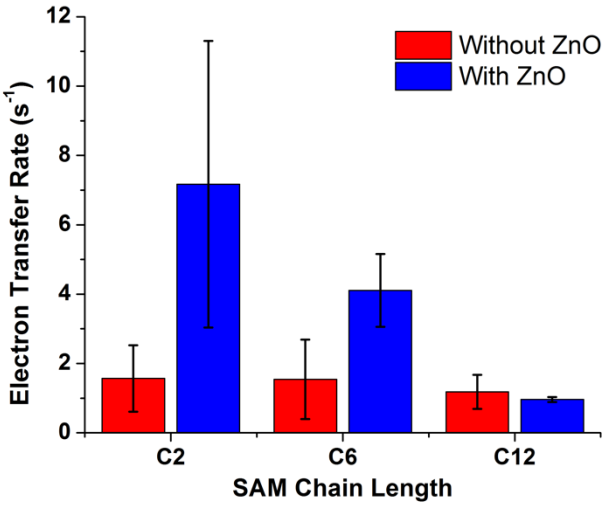

Figure 6.6. Calculated cathodic electron transfer rates using the Laviron equation of ferrocene SAMs using 50 mM of different chain length of diamines and 50 mM $NH_2(CH_2)_2OH$ with (blue) and without (red) 20 s of ZnO electrodeposition.

Using the Laviron method,[36] we calculated the electron transfer rates to ferrocene on SAMs with and without ZnO electrodeposits (Figures 6.6 and S6.18). As mentioned before, the Laviron rates are similar for all three SAM linker lengths in the absence of ZnO electrodeposits (Figure 6.6, red bars). This result is consistent with previous studies on

vertically aligned carbon nanofibers modified with ferrocene SAMs.[2] We hypothesize that relatively fast electron transfer occurs regardless of the SAM linker length because in these disordered SAMs, the alkyl linkers can bend towards the electrode and allow the ferrocene molecules to directly interact with the electrode through defect sites in the SAM.

Interestingly, there is significant change in the electron transfer rates versus SAM linker lengths with the ZnO electrodeposits (Figure 6.6, blue bars). In particular, as the chain length increases, the electron transfer rate decreases. This trend matches what is observed with ferrocene appended to alkyl SAMs on well-ordered Au electrodes.[19, 22] On Au electrodes, electron transfer to ferrocene occurs via electron tunneling through the insulating alkyl linkers of the SAM (Figure 6.7A), and so longer chain lengths result in slower electron transfer. Our finding that ZnO electrodeposits cause the ferrocene-modified SAMs on glassy carbon to behave more like those on Au implies that ZnO electrodeposits are blocking the defect sites on the carbon surfaces (Figure 6.7B). Furthermore, these experiments are consistent with an electron transfer mechanism in the absence of ZnO electrodeposits in which ferrocene directly interacts with the electrode through these defect sites as opposed to electron tunneling through the alkyl linkers (Figure 6.7C).

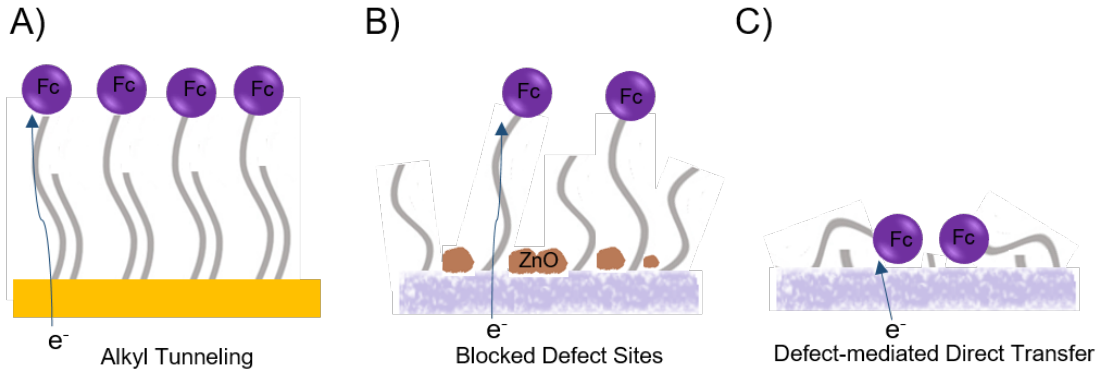

Figure 6.7. Schematic showing the tunneling mechanism of electron transfer to ferrocene on Au SAMs (A) and how ZnO electrodeposits block defect sites on carbon electrodes (B). In the absence of ZnO, electron transfer occurs directly from the carbon electrode to ferrocene (C).

Aside from these mechanistic findings, we now comment on some other aspects of these electron transfer rates. First, compared to ferrocene-modified SAMs on Au, the electron transfer rate with the C12 linker with ZnO electrodeposits is still very fast. This finding suggests that the ZnO electrodeposits do not block all of the electrode defect sites and that the electron transfer rate measured is reflective of a combination of tunneling and defect-mediated pathways or alternatively, ZnO-mediated charge transfer. Second, the electron transfer rates to ferrocene on C2 and C6 SAMs with ZnO electrodeposits are faster than without ZnO. This effect could be due to electron transfer occurring through the semiconducting ZnO electrodeposits to ferrocene.

We also compare our results to those found by Ruther et al., who analyzed the electron transfer kinetics of ferrocene SAMs attached to boron-doped diamond electrodes.[40] In a manner similar to the results reported here, the authors found that there was not a strong dependence of the electron transfer rates on the length of the alkyl linker used in the SAM. The authors attributed these findings to conformational flexibility within the disordered SAMs. The ZnO electrodeposition studies conducted here that suggest defect-mediated electron transfer agree well with the conclusions reported by Ruther et al. Although the electron transfer rates measured in this work are similar to those previously measured on ferrocene SAMs on vertically-aligned carbon nanotubes,[2] the electron transfer rates measured on boron-doped diamond electrodes are approximately three orders of magnitude faster. These results suggest that the enhanced conductivity of boron-doped

diamond electrodes as compared to carbon electrodes contributes to this electron transfer rate enhancement.[41,42]

6.3.3. Ferrocene-modified SAMs on other Types of Carbon Electrodes

We also attached ferrocene to three different types of carbon electrodes to complement our studies on glassy carbon electrodes. Ferrocene was attached via SAMs formed using 50 mol % $NH_2(CH_2)_2NH_2$ and 50 mol % $NH_2(CH_2)_2OH$ diluent on glassy carbon electrodes that were modified with Vulcan XC-72 and PVDF, carbon nanotubes and Nafion, and Vulcan XC-72 and Nafion (Figure 6.8). The reversible CVs obtained in all cases show that the ferrocene modification strategy developed in this work is applicable to a wide range of carbon surfaces.

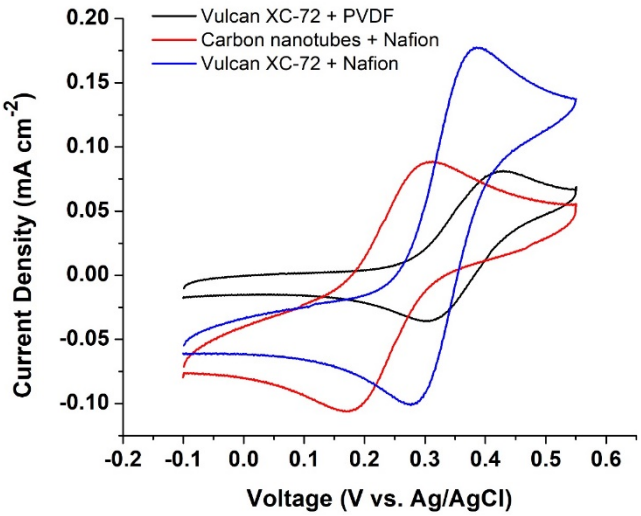

Figure 6.8. Cyclic voltammograms at 300 mV s^{-1} in pH 7 buffer of ferrocene attached to SAMs using 50 mM $NH_2(CH_2)_2NH_2$ and 50 mM $NH_2(CH_2)_2OH$ diluent on glassy carbon electrodes modified with Vulcan XC-72 and PVDF (black), carbon nanotubes and Nafion (red), and Vulcan XC-72 and Nafion (blue).

The surface coverages of ferrocene increase as follows for the four carbon substrates: Vulcan XC-72/Nafion > Carbon nanotubes/Nafion > Vulcan XC-72/PVDF > unmodified glassy carbon electrode. CVs of the Fe(II)/Fe(III) couple in aqueous $K_3Fe(CN)_6$ using these four carbon electrodes without ferrocene SAMs exhibit current densities with magnitudes in this same order (Figure S6.19). This finding demonstrates that the different surface coverages of ferrocene observed on the four carbon electrodes are due to the varying electrochemically active surface areas of the carbons.

6.4. Conclusions

SAM-modified carbon electrodes are important in a wide range of applications, including electroanalysis, biosensors, and catalysis. We modified glassy carbon electrodes with ferrocene using different compositions of alkyl amine SAMs with various chain lengths and diluents. An amide coupling reaction was carried out between Fc-COOH and the terminal amine groups of the SAMs using EDC and NHS in an aqueous solution. In addition, we investigated the role of defect sites in the SAMs to understand the electron transfer properties to the appended ferrocene by modifying the SAMs with ZnO electrodeposits. Our results show that the electron transfer rates increase as the SAM linker chain length increases with ZnO electrodeposits, but there is no significant change in the electron transfer rates without ZnO electrodeposits. These studies were used to discriminate between defect-mediated electron transfer and electron tunneling mechanisms.

6.5. References

1. Sam, S.; Touahir, L.; Salvador Andresa, J.; Allongue, P.; Chazalviel, J. N.; Gouget-Laemmel, A. C.; De Villeneuve, C. H.; Moraillon, A.; Ozanam, F.; Gabouze, N.; et al. Semiquantitative Study of the EDC/NHS Activation of Acid Terminal Groups at Modified Porous Silicon Surfaces. *Langmuir* **2010**, *26*, 809–814.
2. Landis, E. C.; Hamers, R. J. Covalent Grafting of Ferrocene to Vertically Aligned Carbon Nanofibers: Electron-Transfer Processes at Nanostructured Electrodes. *J. Phys. Chem. C* **2008**, *112*, 16910–16918.
3. Yang, W.; Auciello, O.; Butler, J. E.; Cai, W.; Carlisle, J. A.; Gerbi, J. E.; Gruen, D. M.; Knickerbocker, T.; Lasseter, T. L.; Russell, J. N.; et al. DNA-Modified Nanocrystalline Diamond Thin-Films as Stable, Biologically Active Substrates. *Nat. Mater.* **2002**, *1*, 253–257.
4. Pleskov, Y. V. Synthetic Diamond, a New Electrode Material for Electroanalysis. *J. Anal. Chem.* **2000**, *55*, 1045–1050.
5. Zhao, N.; Wu, S.; He, C.; Shi, C.; Liu, E.; Du, X.; Li, J. Hierarchical Porous Carbon with Graphitic Structure Synthesized by a Water Soluble Template Method. *Mater. Lett.* **2012**, *87*, 77–79.
6. Casalini, S.; Bortolotti, C. A.; Leonardi, F.; Biscarini, F. Self-Assembled Monolayers in Organic Electronics. *Chem. Soc. Rev.* **2017**, *46*, 40–71.
7. Zhang, L.; Lin, X. Covalent Modification of Glassy Carbon Electrodes with Glycine for Voltammetric Separation of Dopamine and Ascorbic Acid. *Anal. Bioanal. Chem.* **2001**, *370*, 956–962.
8. Gooding, J. J.; Ciampi, S. The Molecular Level Modification of Surfaces: From Self-Assembled Monolayers to Complex Molecular Assemblies. *Chem. Soc. Rev.* **2011**, *40*, 2704–2718.
9. Hanna, C. M.; Sanborn, C. D.; Ardo, S.; Yang, J. Y. Interfacial Electron Transfer of Ferrocene Immobilized onto Indium Tin Oxide through Covalent and Noncovalent Interactions. *ACS Appl. Mater. Interfaces* **2018**, *10*, 13211–13217.
10. Wang, Y.; Yao, X.; Wang, J.; Zhou, F. Attachment of Amine- and Maleimide-Containing Ferrocene Derivatives onto Self-Assembled Alkanethiol and Alkanedithiol Monolayers: Voltammetric Evaluation of Cross-Linking Efficiencies and Surface Coverage of Electroactive Groups. *Electroanalysis,* **2004**, *16*, 1755–1761.
11. Chidsey, C. E. D.; Bertozzi, C. R.; Putvinski, T. M.; Mujsce, A. M. Coadsorption of Ferrocene-Terminated and Unsubstituted Alkanethiols on Gold: Electroactive Self-Assembled Monolayers. *J. Am. Chem. Soc.* **1990**, *112*, 4301–4306.
12. Barbier, B.; Pinson, J.; Desarmot, G.; Sanchez, M. Electrochemical Bonding of Amines to Carbon Fiber Surfaces Toward Improved Carbon-Epoxy Composites. *J. Electrochem. Soc.* **1990**, *137*, 1757–1764.
13. Deinhammer, R. S.; Ho, M.; Anderegg, J. W.; Porter, M. D. Electrochemical Oxidation of Amine-Containing Compounds: A Route to the Surface Modification of Glassy Carbon Electrodes. *Langmuir,* **1994**, *10*, 1306–1313.
14. Xia, N.; Xing, Y.; Wang, G.; Feng, Q.; Chen, Q.; Feng, H.; Sun, X.; Liu, L. Probing of EDC/NHSS-Mediated Covalent Coupling Reaction by the Immobilization of

Electrochemically Active Biomolecules. *Int. J. Electrochem. Sci.* **2013**, *8*, 2459–2467
15. Booth, M. A.; Kannappan, K.; Hosseini, A.; Partridge, A. In-Depth Electrochemical Investigation of Surface Attachment Chemistry via Carbodiimide Coupling. *Langmuir,* **2015**, *31*, 8033–8041.
16. Liu, L.; Deng, D.; Xing, Y.; Li, S.; Yuan, B.; Chen, J.; Xia, N. Activity Analysis of the Carbodiimide-Mediated Amine Coupling Reaction on Self-Assembled Monolayers by Cyclic Voltammetry. *Electrochim. Acta,* **2013**, *89*, 616–622.
17. Crivillers, N.; Mas-Torrent, M.; Vidal-Gancedo, J.; Veciana, J.; Rovira, C. Self-Assembled Monolayers of Electroactive Polychlorotriphenylmethyl Radicals on Au(111). *J. Am. Chem. Soc.* **2008**, *130*, 5499–5506.
18. Porter, M. D.; Bright, T. B.; Allara, D. L.; Chidsey, C. E. Spontaneously Organized Molecular Assemblies. 4. Structural Characterization of n-Alkyl Thiol Monolayers on Gold by Optical Ellipsometry, Infrared Spectroscopy, and Electrochemistry. *J. Am. Chem. Soc.* **1987**, *109*, 3559–3568.
19. Smalley, J. F.; Feldberg, S. W.; Chidsey, C. E. D.; Linford, M. R.; Newton, M. D.; Liu, Y. P. Kinetics of Electron Transfer through Ferrocene-Terminated Alkanethiol Monolayers on Gold. *J. Phys. Chem.* **1995**, *99*, 13141–13149.
20. Folkers, J. P.; Laibinis, P. E.; Whitesides, G. M. Self-Assembled Monolayers of Alkanethiols on Gold: Comparisons of Monolayers Containing Mixtures of Short- and Long-Chain Constituents with CH_3 and CH_2OH Terminal Groups. *Langmuir* **1992**, *8*, 1330–1341.
21. Yang, Z.; Engquist, I.; Liedberg, B.; Kauffmann, J. M. Electrochemical Characterisation of Mixed Monolayer Assemblies of Thiol Analogues of Cholesterol and Fatty Acids on Gold. *J. Electroanal. Chem.* **1997**, *430*, 189–195.
22. Creager, S. E.; Rowe, G. K. Solvent and Double-Layer Effects on Redox Reactions in Self-Assembled Monolayers of Ferrocenyl-Alkanethiolates on Gold. *J. Electroanal. Chem.* **1997**, *420*, 291–299.
23. Collman, J. P.; Devaraj, N. K.; Chidsey, C. E. D. "Clicking" Functionality onto Electrode Surfaces. *Langmuir* **2004**, *20*, 1051–1053.
24. Dorraji, P. S.; Jalali, F. Electrochemical Fabrication of a Novel ZnO/Cysteic Acid Nanocomposite Modified Electrode and Its Application to Simultaneous Determination of Sunset Yellow and Tartrazine. *Food Chem.* **2017**, *227*, 73–77.
25. Sumner, J. J.; Creager, S. E. Redox Kinetics in Monolayers on Electrodes: Electron Transfer Is Sluggish for Ferrocene Groups Buried within the Monolayer Interior. *J. Phys. Chem. B* **2001**, *105*, 8739–8745.
26. Gagne, R. R.; Koval, C. A.; Lisensky, G. C. Ferrocene as an Internal Standard for Electrochemical Measurements. *Inorg. Chem.* **1980**, *19*, 2854–2855.
27. Chidsey, C. E. D. Free Energy and Temperature Dependence of Electron Transfer at the Metal-Electrolyte Interface. *Science* **1991**, *251*, 919–922.
28. Creager, S. E.; Rowe, G. K. Competitive Self-Assembly and Electrochemistry of Some Ferrocenyl-n-Alkanethiol Derivatives on Gold. *J. Electroanal. Chem.* **1994**, *370*, 203–211.
29. Guo, L. H.; Facci, J. S.; McLendon, G. Distance Dependence of Electron Transfer Rates in Bilayers of a Ferrocene Langmuir-Blodgett Monolayer and a Self-Assembled Monolayer on Gold. *J. Phys. Chem.* **1995**, *99*, 8458–8461.

30. Valincius, G.; Niaura, G.; Kazakevičiene, B.; Talaikyte, Z.; Kažemekaite, M.; Butkus, E.; Razumas, V. Anion Effect on Mediated Electron Transfer through Ferrocene-Terminated Self-Assembled Monolayers. *Langmuir* **2004**, *20*, 6631–6638.
31. Lee, L. Y. S.; Sutherland, T. C.; Rucareanu, S.; Lennox, R. B. Ferrocenylalkylthiolates as a Probe of Heterogeneity in Binary Self-Assembled Monolayers on Gold. *Langmuir* **2006**, *22*, 4438–4444.
32. Yokota, Y.; Fukui, K. I.; Enoki, T.; Hara, M. Origin of Current Enhancement through a Ferrocenylundecanethiol Island Embedded in Alkanethiol SAMs by Using Electrochemical Potential Control. *J. Phys. Chem. C* **2007**, *111*, 7561–7564.
33. Sun, Q. W.; Murase, K.; Ichii, T.; Sugimura, H. Anionic Effect of Ionic Liquids Electrolyte on Electrochemical Behavior of Ferrocenylthiol/Alkanethiol Binary SAMs. *J. Electroanal. Chem.* **2010**, *643* (1–2), 58–66.
34. Murray, R. W. Chemically Modified Electrodes. *Electroanal. Chem*.**1984**, 13, 191.
35. Bard, A. J.; Faulkner, L. R. Electrochemical Methods; John Wiley & Sons: New York, **1980**.
36. Laviron, E. Adsorption, Autoinhibition and Autocatalysis in Polarography and in Linear Potential Sweep Voltammetry. *J. Electroanal. Chem.* **1974**, *52*, 355–393.
37. Le Goff, A.; Artero, V.; Metaye, R.; Moggia, F.; Jousselme, B.; Razavet, M.; Tran, P. D.; Palacin, S.; Fontecave, M. Immobilization of FeFe Hydrogenase Mimics onto Carbon and
Gold Electrodes by Controlled Aryldiazonium Salt Reduction: An Electrochemical, XPS and ATR-IR study. *Int. J. Hydrogen Econ.* **2010**, *25*, 10790-10796.
38. Menanteau, T.; Levillain, E.; Downard, A. J.; Breton, T. Evidence of Monolayer Formation via Diazonium Grafting with a Radical Scavenger: Electrochemical, AFM and XPS Monitoring. *Phys. Chem. Chem. Phys.* **2015**, *17*, 13137–13142.
39. Marrani, A. G.; Caprioli, F.; Boccia, A.; Zanoni, R.; Decker, F. Electrochemically Deposited ZnO Films: An XPS Study on the Evolution of their Surface Hydroxide and Defect Composition upon Thermal Annealing. *J. Solid State Electrochem.* **2014**, *18*, 505-513.
40. Ruther, R. E.; Cui, Q.; Hamers, R. J. Conformational Disorder Enhances Electron Transfer through Alkyl Monolayers: Ferrocene on Conductive Diamond. *J. Am. Chem. Soc.* **2013**, *135* (15), 5751–5761.
41. Strojnik, M.; Specific Resistivity of Glassy-Carbon and its Temperature Dependence, Unconventional Imaging II, edited by Victor L. Gamiz, Paul S. Idell, Marija S. Strojnik, Proc. of SPIE Vol. 6307, 63070S, **2006**.
42. Williams, G.; Calvo, J.A.; Faili, F.; Dodson, J.; Obeloer, T.; Twitchen, D.J. Thermal Conductivity of Electrically Conductive Highly Boron Doped Diamond and its Applications at High Frequencies. In Proceedings of the 2018 17th IEEE Intersociety Conference on Thermal and Thermomechanical Phenomena in Electronic Systems (ITherm), San Diego, CA, USA, 29 May–1 June **2018**; pp. 235–239.

Chapter 7: Conclusions and Future Directions

The primary motivation of this dissertation is to design and develop new electrocatalyst materials for the oxygen reduction reaction (ORR) and the oxygen evolution reaction (OER) using non-precious metal catalysts for energy conversion and storage. At present, Pt-based catalysts display the best performance for the ORR, which is a fundamental electrochemical reaction occurring at the cathode of fuel cells. H_2 is an alternative fuel that can be produced from the electrolysis of water in a clean and sustainable manner, but technical challenges have heretofore limited the efficiency of water electrolyzers. To generate H_2 in a green manner, water can be electrolyzed using electricity from renewable sources. The OER is the rate-limiting reaction for water electrolysis. The catalysts based on Ir have the best performance for the OER. Yet the high cost and scarcity of Pt- and Ir-based catalysts have resulted in a search for alternatives.

I prepared a catalyst consisting of a copper complex of benzyl triazole alkyne (BTA) by covalently attaching a Au electrode with differing chain lengths of thiol-linked self-assembled monolayers (SAMs). I continued by using the phospholipid 1,2-dimyristoyl-sn-glycerol-3-phosphocholine to form a thin film held to the SAM catalyst with weak Van der Waals interactions. These steps allowed for the completion of the electrode architecture by appending a lipid monolayer with 1-dodecylboronic acid as a proton carrier on the top of the SAM. The designed novel electrode architecture modulates the electron transfer rate to a given catalyst by altering the length of the SAM and also controls the proton transfer rate to the catalyst by appending a lipid membrane modified

with proton carriers. Thus, the designed new electrochemical platform allows for the identification of the optimal kinetic and thermodynamic parameters for ORR catalysts.

Also, I designed a hybrid bilayer membrane (HBM) with active proton carriers bearing nitrile groups found in protonphores. The designer small-molecule proton carriers synthesized are among the first demonstrated examples of proton delivery enhancement in alkaline conditions for ORR electrocatalysis in an HBM. The transmembrane proton delivery mechanism was elucidated using a series of temperature, head group modification, and deuteration studies. These results contribute to a complete understanding of the role of proton transfer kinetics in ORR and other renewable energy conversion and electrocatalytic processes.

In addition, I prepared bimetallic electrocatalysts based on Ni and Cu for the OER. I used thin films of Cu_2O modified with an overlayer of Ni to construct novel electrocatalysts and determined the optimal ratio of Ni to Cu_2O for performing OER in alkaline conditions by tuning the amount of Ni electrodeposited on the Cu_2O. Then, I proceeded to develop nanostructured Ni-Cu systems by synthesizing both metallic and bimetallic Ni-Cu nanoclusters and nanoparticles. I discovered that, for both nanoclusters and nanoparticles, the ratio of Ni to Cu is highly associated with OER electrocatalysis efficiency.

Furthermore, I modified carbon electrodes using various compositions and chain lengths of alkyl amine and diamine SAMs with different proportions of diluent. The role of defect sites in the SAMs was investigated to understand the electron transfer properties of the ferrocene modified SAMs with ZnO electrodeposits. Interestingly, I found that the

electron transfer rates as a function of SAM chain length changes significantly only when the SAM defect sites are blocked with ZnO electrodeposits. The surface modification protocol developed in this study could be useful in a wide range of applications, including electroanalysis, biosensors, and energy catalysis.

The non-precious metal electrocatalysts such as those based on Cu and Ni for ORR and OER developed in this dissertation showed improved catalytic activity. However, these electrocatalysts degrade over time. Therefore, future research should focus on how to improve the stability of these materials under ORR and OER conditions. Electrochemical impedance spectroscopy (EIS) study can give important catalyst stability information. To understand what makes these Ni-Cu systems better OER electrocatalysts, transmission electron microscopy (TEM) can be helpful. TEM can provide atomic-level resolution, which could be helpful to better understand the chemistry undergoing on bimetallic Ni-Cu nanostructured systems. Also, the use of different ligands for the synthesis of Ni-Cu bimetallic nanoclusters could improve the stability issue of these electrocatalyst materials under OER conditions.

Chapter 8: Appendices

8.1. Supporting Information for Chapter 2

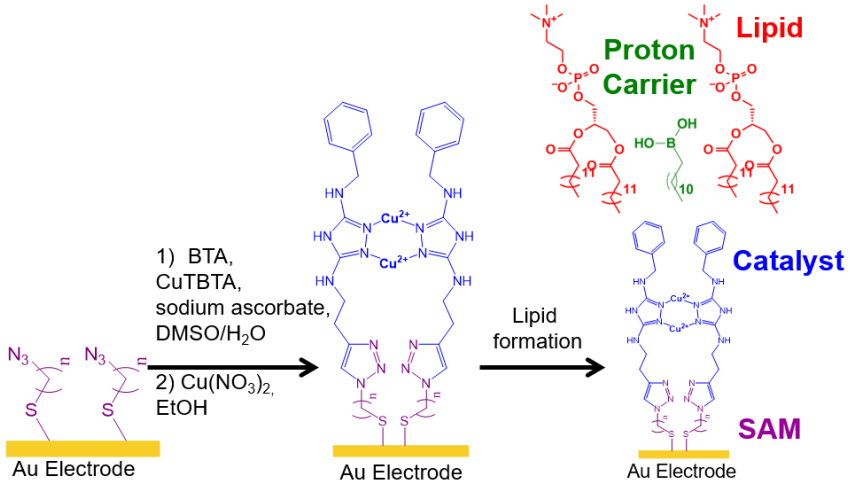

Figure S2.1. Schematic of the fabrication of lipid-modified SAMs used to control the electron and proton transfer rates to a molecular O_2 reduction catalyst.

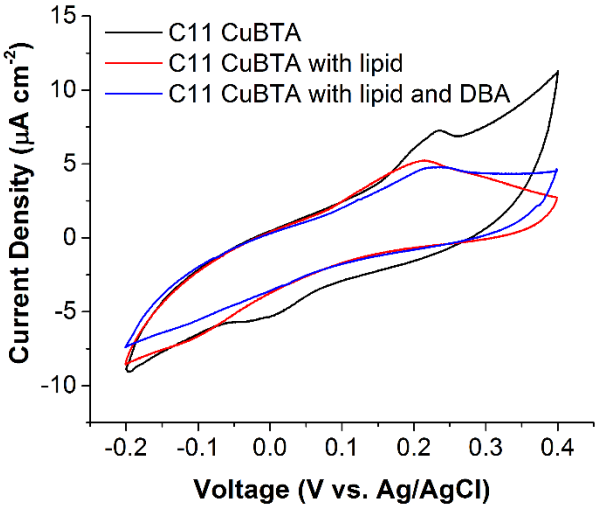

Figure S2.2. Cyclic voltammograms of the CuBTA catalyst (black) covered by a lipid monolayer (red) with 10 mol% DBA (blue) using an azide-terminated thiol SAM containing 11 methylene groups at 10 mV/s in N_2-saturated pH 7 buffer. The midpoint potentials of the Cu(I)/Cu(II) are +112 mV, +54 mV, and +62 mV, for the no lipid, lipid, and lipid with DBA cases, respectively.

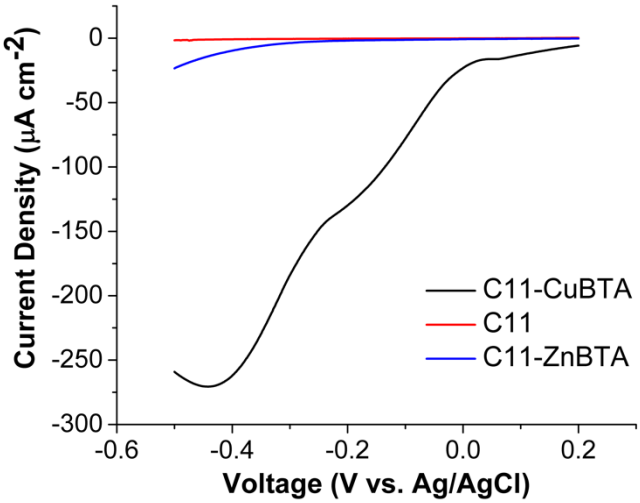

Figure S2.3. Linear sweep voltammograms of O_2 reduction by the CuBTA catalyst (black), the ZnBTA control (blue), and the no catalyst modification control (red) using an azide-terminated thiol SAM containing 11 methylene groups at 10 mV/s in O_2-saturated pH 7 buffer.

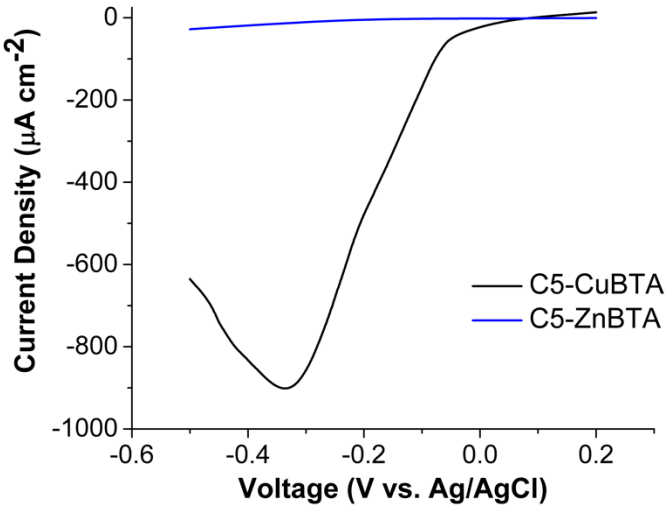

Figure S2.4. Linear sweep voltammograms of O_2 reduction by the CuBTA catalyst (black) and the ZnBTA control (blue) using an azide-terminated thiol SAM containing 5 methylene groups at 10 mV/s in O_2-saturated pH 7 buffer.

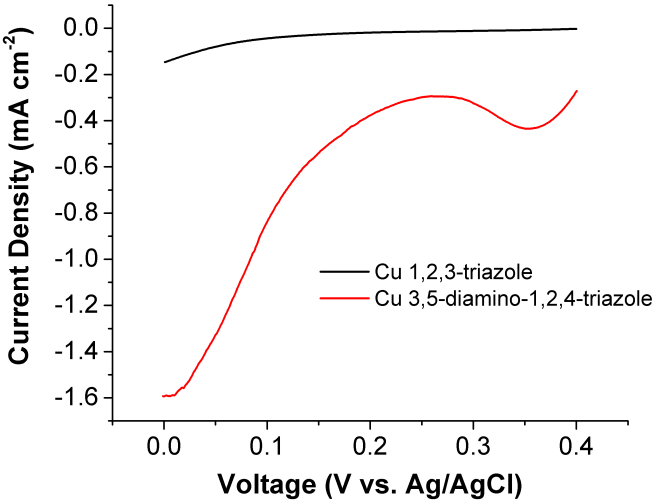

Figure S2.5. Linear sweep voltammograms of a glassy carbon electrode modified with Cu complexes of 1,2,3-triazole (black) and 3,5-diamino-1,2,4-triazole (red) in O_2-sparged pH 7 buffer at a scan rate of 10 mV/s.

$$t = \frac{\langle x \rangle^2 \pi}{4D}$$

Figure S2.6. Equation describing the time (t) it takes a gas molecule to diffuse across an average path length (x) based on its diffusion coefficient (D).

O_2 has a partition coefficient of greater than 2 in DMPC relative to water at 25 °C.[1]

The diffusion coefficient of O_2 at 25 °C in a DMPC bilayer is 1.8 x 10^{-5} cm^2/s,[2] which is

comparable to that of water (1.9×10^{-5} cm^2/s).[3] The time required for a molecule of O_2 to diffuse through 21 Å (the experimental length of the lipid layer as determined by ellipsometry[4]) of the HBM can be calculated using the equation below and is less than 2 ns.[5] In comparison, it is calculated that the fastest catalyst reported in this work (CuBTA with a C_5 SAM and 10 mol % proton carrier) takes an average of 12 ms to react with an O_2 molecule. Therefore, the catalyst cannot be limited by O_2 diffusion through the lipid layer since this process is about 10^6 times faster than the intrinsic kinetics of the ORR.

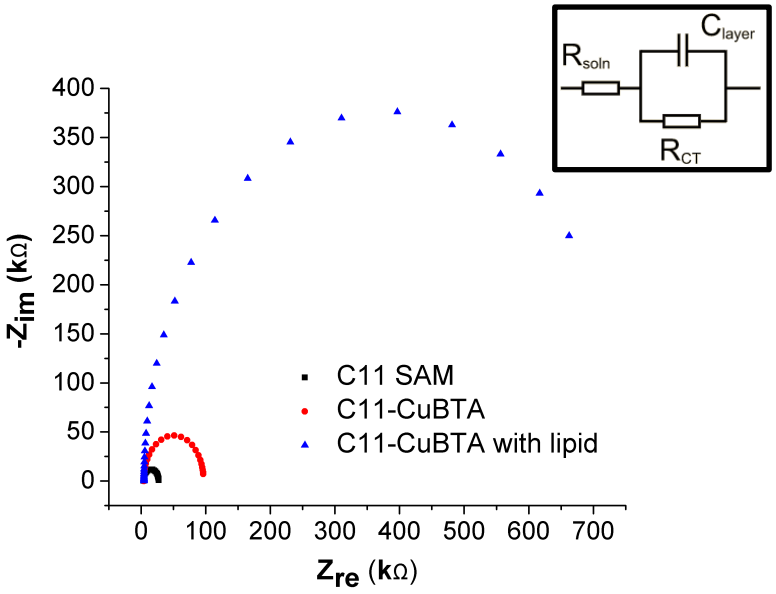

Figure S2.7. Electrochemical impedance spectroscopy (EIS) Nyquist plots of an azide-terminated thiol SAM containing 11 methylene groups (black) modified using the CuBTA catalyst (red) covered by a DMPC lipid monolayer (blue) in O_2-saturated pH 7 buffer. (Inset) Circuit diagram used for modeling the EIS results (Table S1).

	R_{sln} (kΩ)	C_{layer} (nF)	R_{CT} (kΩ)	Experimental Length (Å)	Theoretical Length (Å)
C11 SAM	4.0	220	23.4	20.4	18.0
C11-CuBTA	4.1	132	92.8	34.1	29.6
C11-CuBTA with lipid	4.6	80	753	56.0	51.6

Table S2.1. SAM and HBM modeling data from EIS Nyquist plots in Figure S7 of an azide-terminated thiol SAM containing 11 methylene groups modified using the CuBTA catalyst covered by a DMPC lipid monolayer at 10 mV/s in O_2-saturated pH 7 buffer. A dielectric constant of 2.1 was used for all calculations. [6,7]

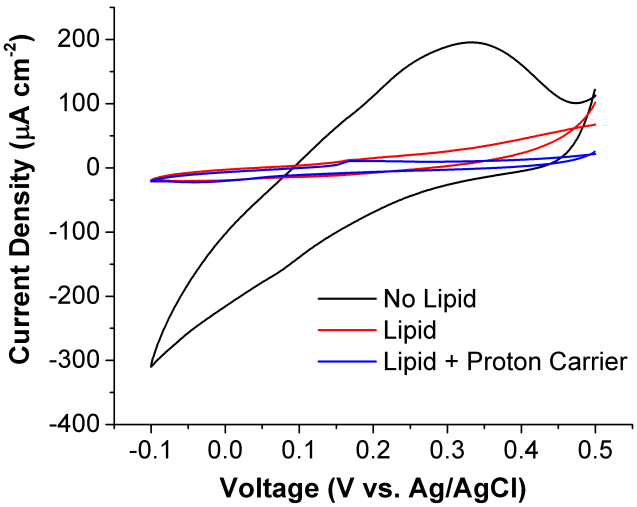

Figure S2.8. Cyclic voltammograms of a SAM containing 11 methylene groups with the CuBTA catalyst (black) with a lipid layer (red) containing 1 molar equivalent of DBA proton carrier (blue) in an aqueous solution containing 1 mM $K_3Fe(CN)_6$ and 100 mM NaCl at a scan rate of 50 mV/s.

These electrochemical "blocking" experiments probe the integrity of the lipid layer and are conducted after performing each O_2 reduction LSV. Analogous experiments have been reported previously.[8] The presence of a clear, but irregularly shaped $Fe(CN)_6^{3-}$/$Fe(CN)_6^{4-}$ wave in the absence of the lipid indicates that electron transfer occurs from the Au electrode to the $K_3Fe(CN)_6$ in bulk solution. Electron transfer is slightly impeded by the presence of the SAM, giving rise to the irregularly shaped wave. In contrast, when a lipid layer covers the electrode the wave is almost entirely suppressed indicating that the lipid effectively blocks electron transfer to the $K_3Fe(CN)_6$ in bulk solution. These

experiments indicate that the lipid layer both with and without proton carrier remains intact after O_2 reduction.

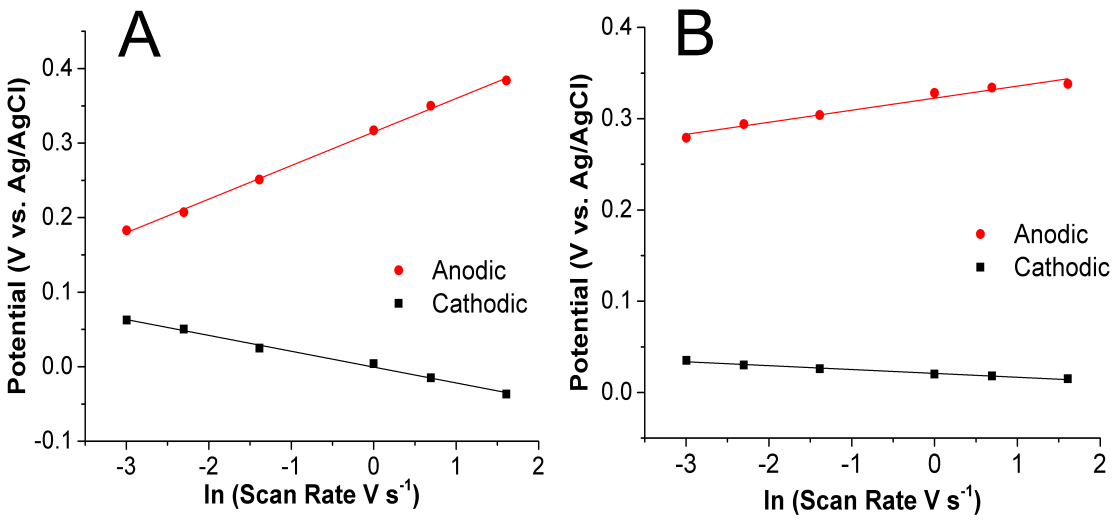

Figure S2.9. Laviron plots of the cathodic (black) and anodic (red) peak potential versus the natural log of scan rates for the CuBTA catalyst using an azide-terminated thiol SAM containing (A) 11 and (B) 5 methylene groups at 10 mV/s in N_2-saturated pH 7 buffer. Electron transfer rates calculated from the above plots **(Table S2).**

SAM	Cathodic Rate (s^{-1})	Anodic Rate (s^{-1})
C_{11}	1.2 ± 0.2	0.6 ± 0.1
C_5	39 ± 3	15 ± 3

Table S2.2. Cathodic and anodic electron transfer rates found for the CuBTA catalyst using an azide-terminated thiol SAM containing 11 and 5 methylene groups.

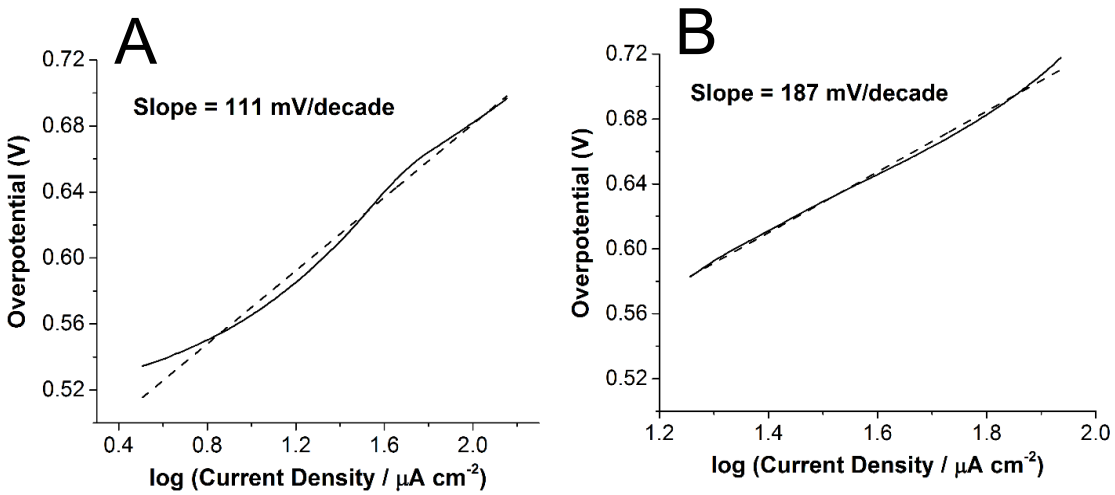

Figure S2.10. Tafel plots of the ORR currents of the CuBTA catalyst using an azide-terminated thiol SAM containing (A) 5 and (B) 11 methylene groups at 10 mV/s in O_2-saturated pH 7 buffer. The change in Tafel slope with varying chain length of SAMs has been observed previously [9,10]

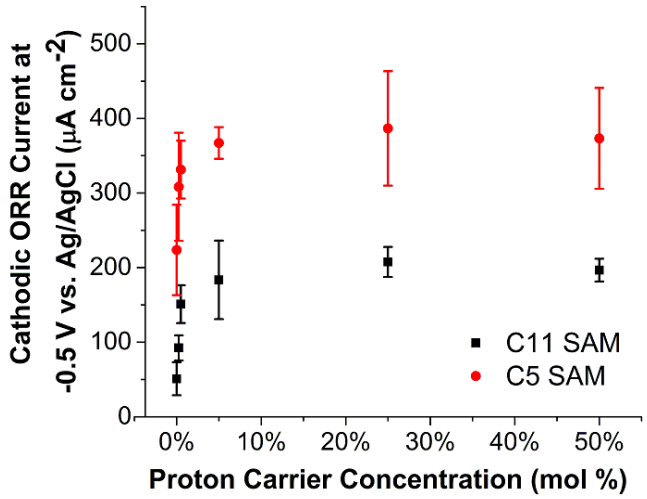

Figure S2.11. Plot of the cathodic ORR current versus the amount of proton carrier in the lipid layer of the CuBTA catalyst using an azide-terminated thiol SAM containing 11 (black) and 5 (red) methylene groups at 10 mV/s in O_2-saturated pH 7 buffer.

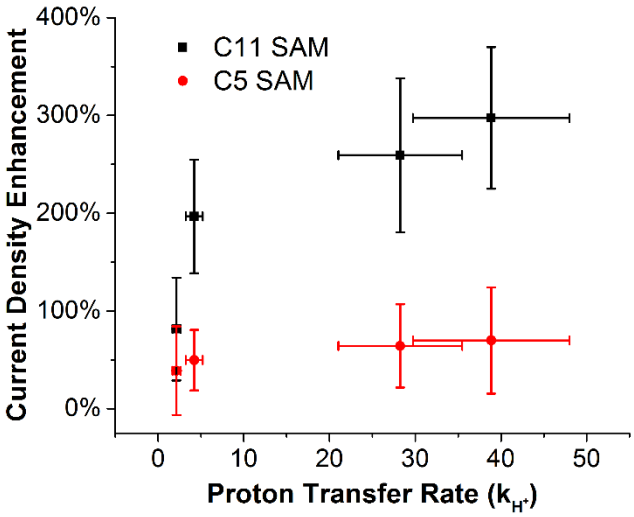

Figure S2.12. O_2 reduction current density enhancement by CuBTA imparted by the incorporation of the DBA proton carrier in the lipid as a function of the proton transfer rate (k_{H+}) in units of protons transferred per second per CuBTA catalyst using an azide-terminated thiol SAM containing 5 (red points) and 11 (black points) methylene groups.

SAM	k_{H+}/k_{e-}	Current Density Enhancement
C_5	0.06 ± 0.01	(39 ± 45) %
C_5	0.11 ± 0.02	(50 ± 31) %
C_5	0.72 ± 0.18	(64 ± 43) %
C_5	1.0 ± 0.23	(70 ± 54) %
C_{11}	1.8 ± 0.49	(82 ± 53) %
C_{11}	3.5 ± 1.0	(197 ± 58) %
C_{11}	24 ± 6.7	(259 ± 79) %
C_{11}	32 ± 10	(297 ± 73) %

Table S2.3. Tabulated values of current density enhancement and the ratio of proton and electron transfer rates (k_{H+}/k_{e-}). These values are displayed graphically in Figure 4.

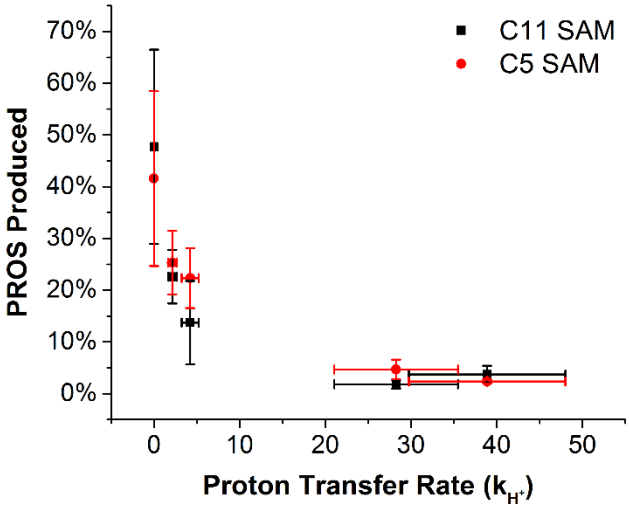

Figure S2.13. Amount of partially reduced oxygen species (PROS) detected using a spectroelectrochemical assay during ORR by the lipid-covered CuBTA as a function of the proton transfer rate (k_{H+}) in units of protons transferred per second with the azide-terminated thiol SAM containing 5 (red points) and 11 (black points) methylene groups.

The assay used follows a literature protocol [10] and is based on horseradish peroxide and an Amplex Red dye, which enables the quantification of the total amount of H_2O_2 and O_2^- generated. The data indicate that increasing the proton transfer rate by increasing the concentration of DBA proton carrier in the lipid layer decreases the amount of PROS produced from ~50% to 1-2%, thus favoring the 4 e^- reduction of O_2 to H_2O. By comparison, the CuBTA without a lipid produces (12 ± 2) % and (16 ± 2) % PROS when using the C_5 and C_{11} SAMs, respectively. These results demonstrate that the selectivity of the catalyst can be improved through the use of a lipid and proton carrier and are comparable to previous studies of an analogous electrochemical platform. [10]

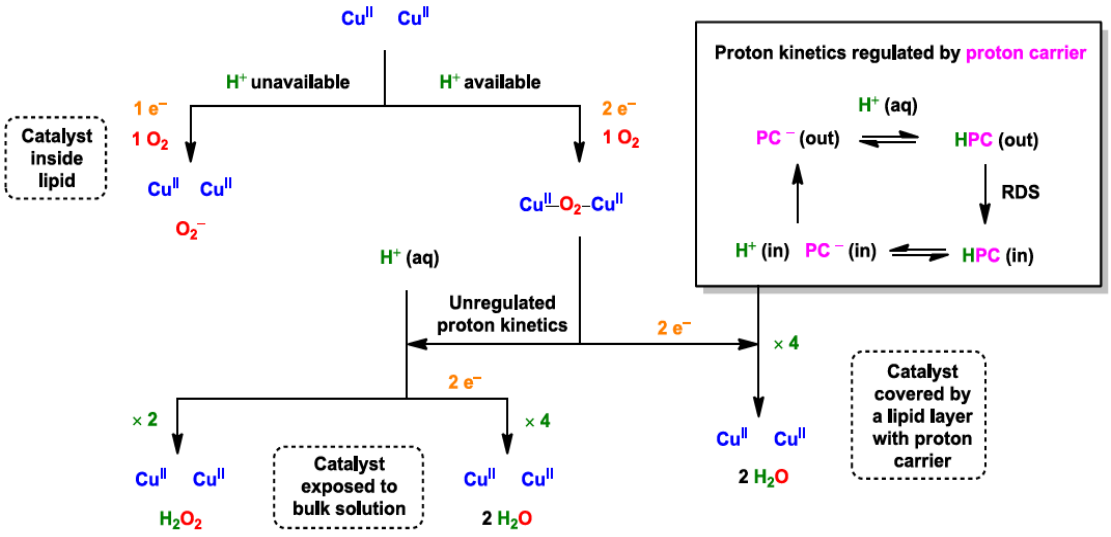

Figure S2.14. O_2 reduction pathways as a function of different proton transfer rates and electrochemical environments, PC = proton carrier.

8.2. References

1. W. K. Subczynski, J. S. Hyde, *Biophys. J.* **1983**, *41*, 283-286.
2. D. A. Windrem, W. Z. Plachy, *Biochim. Biophys. Acta* **1980**, *600*, 655-665.
3. P. Chang, C. R. Wilke, *J. Phys. Chem.* **1955**, *59*, 592-596.
4. C. J. Barile, E. C. M. Tse, Y. Li, T. B. Sobyra, S. C. Zimmerman, A. Hosseini, A. A. Gewirth, *Nat. Mater.* **2014**, *13*, 619-623.
5. I. N. Levine, *Physical Chemistry*. 6th ed.; McGraw Hill: New York, NY, 2009.
6. F. S. Damos, R. C. S. Luz, L. T. Kubota, *Langmuir* **2005**, *21*, 602-609.
7. K. Slowinski, R. V. Chamberlain, R. Bilewicz, M. Majda, *J. Am. Chem. Soc.* **1996**, *118*, 4709-4710.
7. X. Han, L. Wang, B. Qi, X. Yang, E. Wang, *Anal. Chem.* **2003**, *75*, 6566-6570.
8. C. Miller, P. Cuendet, M. Gratzel, *J. Phys. Chem.* **1991**, *95*, 877-886.
9. H. O. Finklea, L. Liu, M. S. Ravenscroft, S. Punturi, *J. Phys. Chem.* **1996**, *100*, 18852-18858.
10. E. C. M. Tse, C. J. Barile, N. A. Kirchschlager, Y. Li, J. P. Gewargis, S. C. Zimmerman, A. Hosseini, A. A. Gewirth, *Nat. Mater.* **2016**, *15*, 754-759.

8.3. Supporting Information for Chapter 3

8.3.1. General Procedures

All reagents were purchased from commercial suppliers and were of analytical grade and used without further purification unless otherwise noted. Reaction progress was monitored by thin-layer chromatography on EMD 60 F254 plates, visualized with a hand-held UV lamp and $KMnO_4$ stain. Compounds were purified via flash column chromatography using Davisil 60 Å 40-63 micron silica gel. Anhydrous solvents acetonitrile (MeCN), dichloromethane (DCM), methanol (MeOH), tetrahydrofuran (THF), dimethylformamide (DMF) and lithium diisopropylamide (LDA) were purchased from J&K in Sure/Seal™ bottles and used without further treatment. *N*,*N*-Diisopropylethylamine (DIPEA) was purchased from J&K and incubated with freshly activated molecular sieve prior use. All reaction vessels were dried in an oven (85 °C) prior to use. NMR spectra were acquired with Bruker Advanced spectrometers. All spectra were acquired at 298 K. ^{1}H-NMR spectra were acquired at 500 MHz. ^{13}C-NMR spectra were acquired at 125 MHz. Chemical shifts are reported in ppm relative to residual non-deuterated NMR solvent, and coupling constants (J) are provided in Hz. All NMR spectra were analyzed using MestReNova reader software.

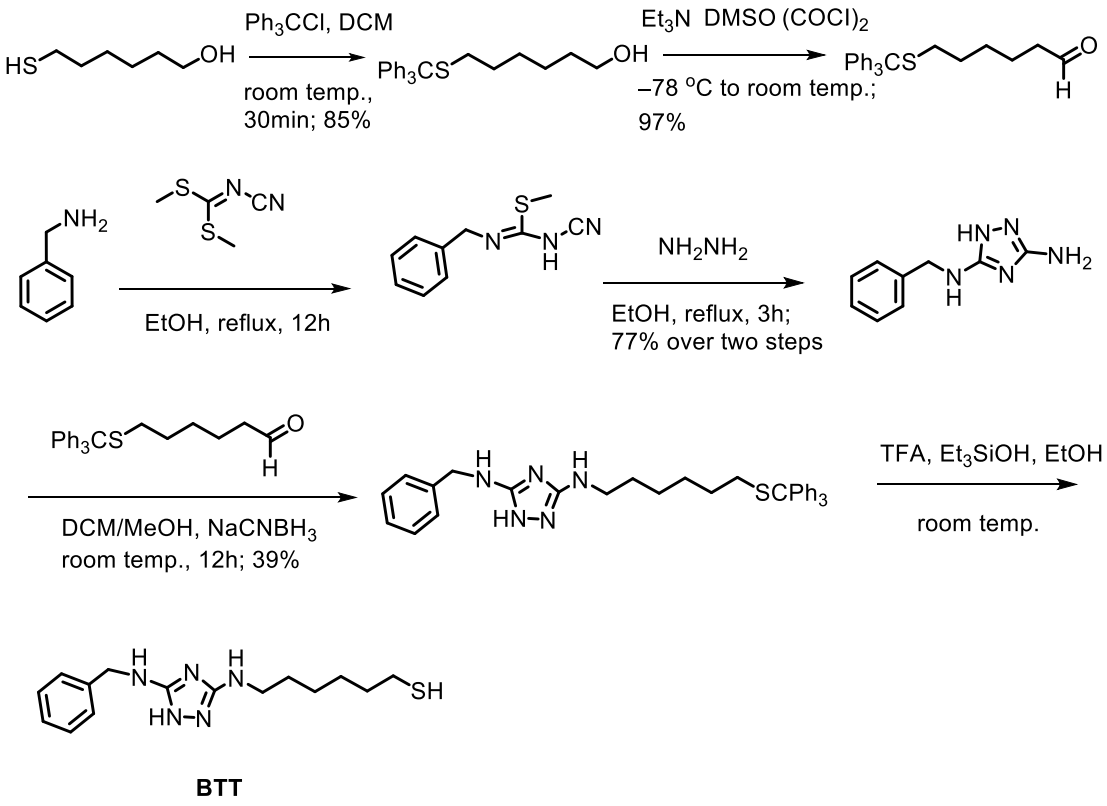

Scheme S3.1. Synthesis of BTT.

BTT was synthesized following our published protocol.[1] NMR and mass spectrometry data were consistent with our previous report.[2]

8.3.2. Synthesis Methods

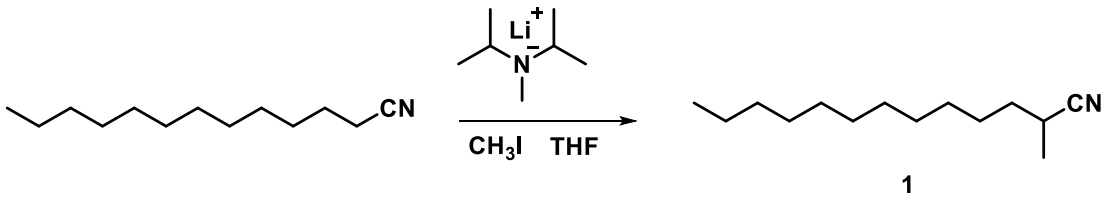

Compound 1. To a solution of lithium diisopropylamide (2.5 mL, 5 mM) in 2 mL of dry THF cooled to –78 °C was added tridecanenitrile (0.5 mL, 2.1 mmol) in 2 mL of dry THF. The mixture was stirred for 1 hour at –78 °C. To the mixture was added CH_3I (0.2 mL, 3.21 mmol). The solution was warmed up to room temperature and stirred for another 18 hours. The solvent was removed using a rotary evaporator. The residue was dissolved in ethyl acetate and washed by H_2O and aqueous saturated brine. The organic layer was dried over Na_2SO_4, concentrated down using a rotary evaporator and purified by column chromatography (ethyl acetate: hexanes = 1:80) to afford the final product as a light-yellow oil (0.23 g, 53 %). ^{1}H NMR (400 MHz, $CDCl_3$) δ 2.59 (dd, J = 14.1, 7.0 Hz, 1H), 1.60 (d, J = 10.5 Hz, 1H), 1.56 – 1.45 (m, 2H), 1.29 (dd, J = 14.9, 8.0 Hz, 18H), 0.88 (t, J = 6.8 Hz, 3H). ^{13}C NMR (101 MHz, $CDCl_3$) δ 123.31 (s), 34.22 (s), 32.05 (s), 29.74 (s), 29.66 (s), 29.51 (s), 29.48 (s), 29.22 (s), 27.18 (s), 25.66 (s), 22.83 (s), 18.18 (s), 14.26 (s).

^{1}H NMR of **1**:

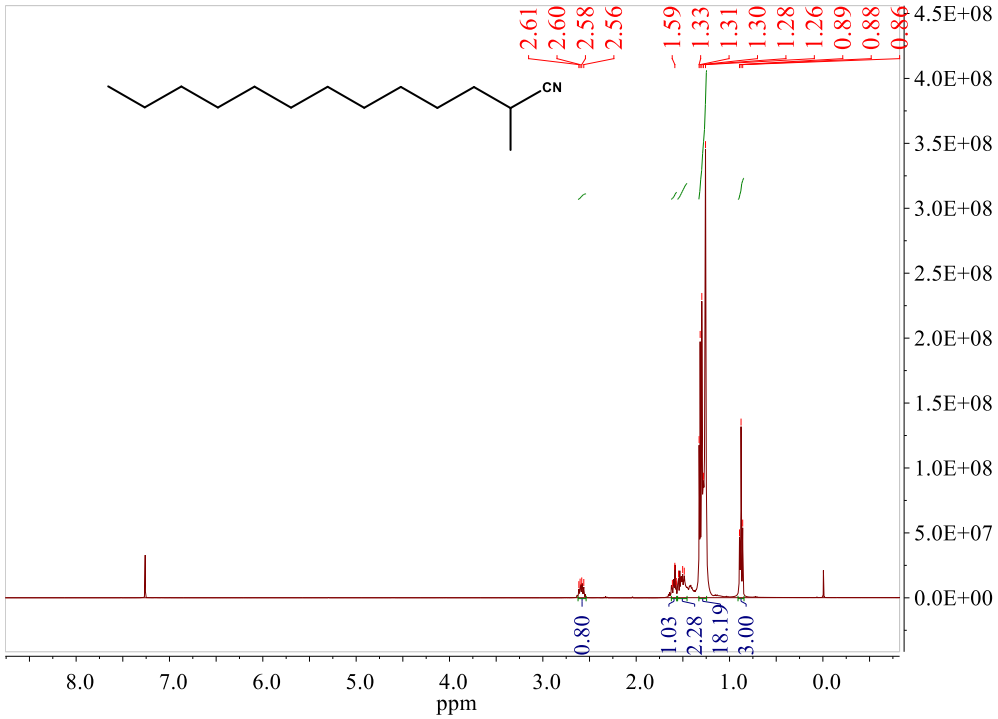
CN
2.61
2.60
2.58
2.56
1.59
1.33
1.31
1.30
1.28
1.26
0.89
0.88
0.86
0.80
1.03
2.28
18.19
3.00
4.5E+08
4.0E+08
3.5E+08
3.0E+08
2.5E+08
2.0E+08
1.5E+08
1.0E+08
5.0E+07
0.0E+00
8.0
7.0
6.0
5.0
4.0
3.0
2.0
1.0
0.0
ppm

^{13}C NMR of **1**:

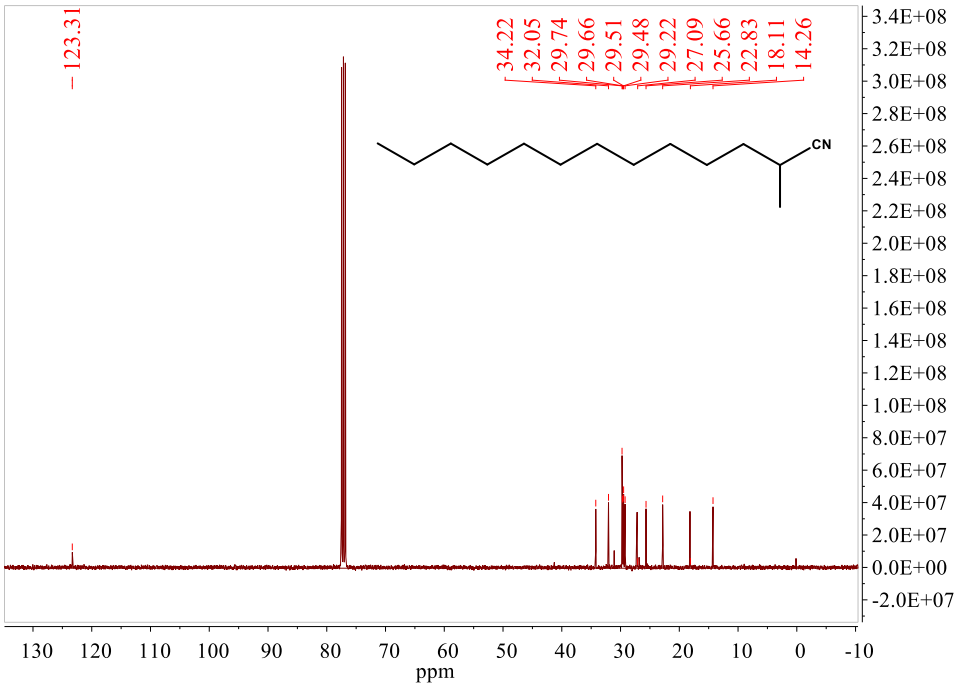
123.31
34.22
32.05
29.74
29.66
29.51
29.48
29.22
27.09
25.66
22.83
18.11
14.26
CN
3.4E+08
3.2E+08
3.0E+08
2.8E+08
2.6E+08
2.4E+08
2.2E+08
2.0E+08
1.8E+08
1.6E+08
1.4E+08
1.2E+08
1.0E+08
8.0E+07
6.0E+07
4.0E+07
2.0E+07
0.0E+00
-2.0E+07
130 120 110 100 90 80 70 60 50 40 30 20 10 0 -10
ppm

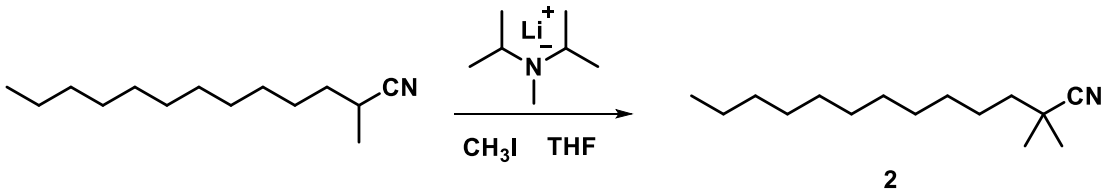

2

Compound 2. To a solution of lithium diisopropylamide (2.5 mL, 5 mM) in 2 mL of dry THF cooled to –78 °C was added compound 1 (0.234 g, 1.12 mmol) in 1 mL of dry THF. The mixture was stirred for 1 hour at –78 °C. To the mixture was added CH_3I (0.2 mL, 3.21 mmol). The solution was warmed to room temperature and stirred for another 18 hours. The solution was removed using a rotary evaporator. The residue was dissolved in ethyl acetate and washed by H_2O and aqueous saturated brine. The organic layer was dried over Na_2SO_4, concentrated down using a rotary evaporator and purified by column chromatography (ethyl acetate: hexanes = 1:80) to afford the final product as a light-yellow oil (0.11 g, 45 %). ^{1}H NMR (500 MHz, $CDCl_3$) δ 1.42 (dd, J = 6.6, 4.6 Hz, 2H), 1.26 (s, 2H), 1.23-1.20 (m, 18H), 0.82 (t, J = 6.9 Hz, 3H). ^{13}C NMR (101 MHz, $CDCl_3$) δ 125.42 (s), 41.25 (s), 32.52 (s), 32.04 (s), 29.82 – 29.63 (m), 29.55 (s), 29.47 (s), 26.82 (s), 25.39 (s), 22.81 (s), 14.25 (s).

^{1}H NMR of **2**:

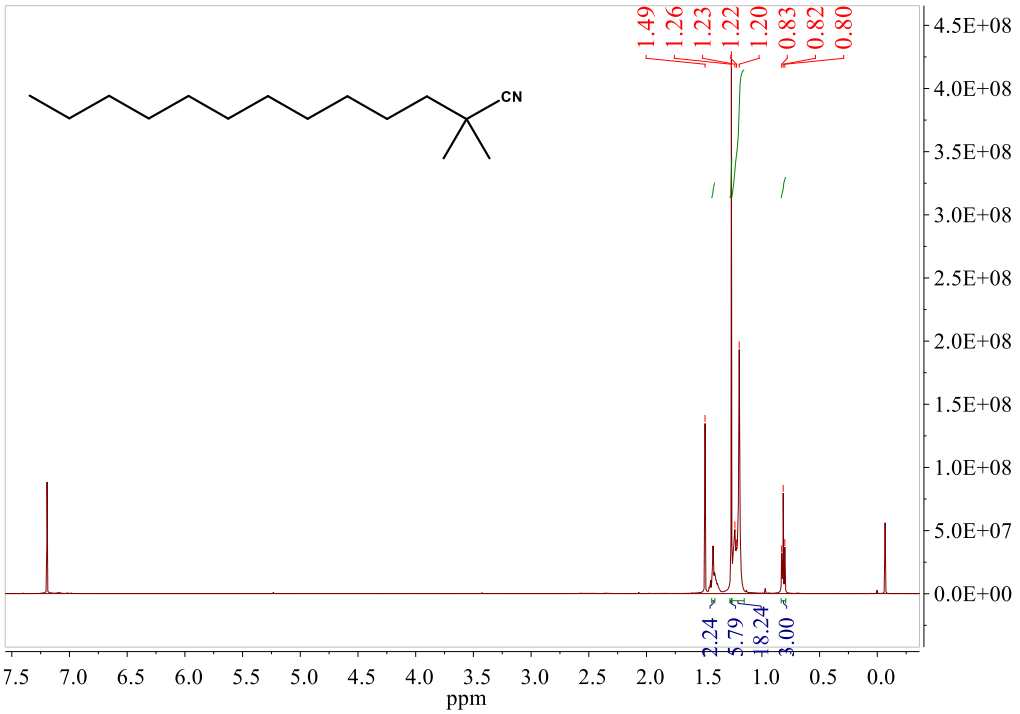
CN
1.49
1.26
1.23
1.22
1.20
0.83
0.82
0.80
4.5E+08
4.0E+08
3.5E+08
3.0E+08
2.5E+08
2.0E+08
1.5E+08
1.0E+08
5.0E+07
0.0E+00
2.24
5.79
18.24
3.00
7.5 7.0 6.5 6.0 5.5 5.0 4.5 4.0 3.5 3.0 2.5 2.0 1.5 1.0 0.5 0.0
ppm

^{13}C NMR of **2**:

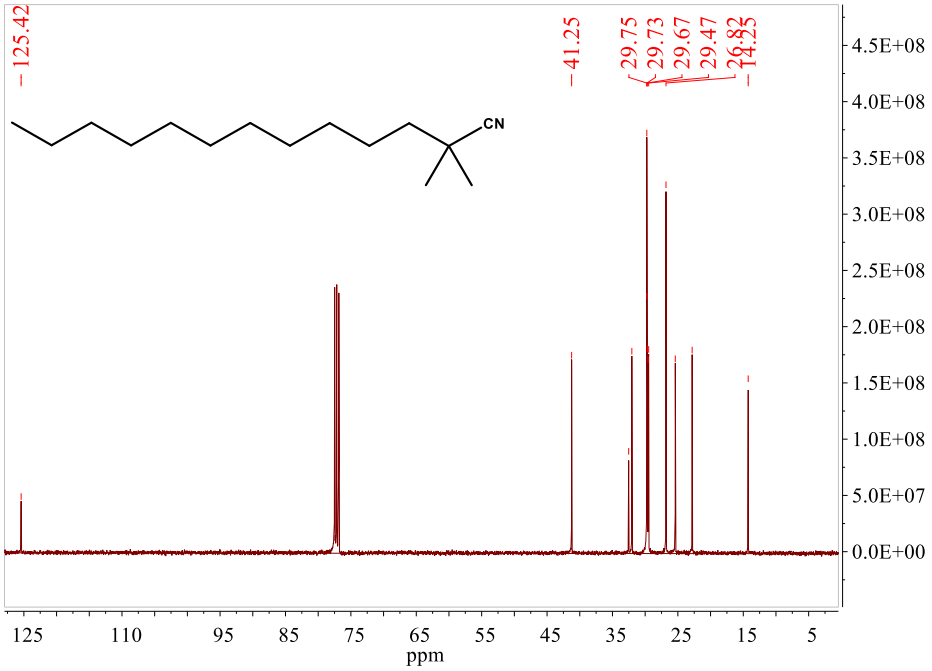
125.42
41.25
29.75
29.73
29.67
29.47
26.82
14.25
CN
4.5E+08
4.0E+08
3.5E+08
3.0E+08
2.5E+08
2.0E+08
1.5E+08
1.0E+08
5.0E+07
0.0E+00
125
110
95
85
75
65
55
45
35
25
15
5
ppm

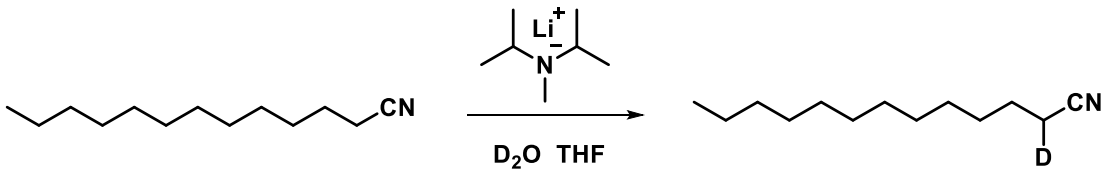

3

Compound 3. To a solution of lithium diisopropylamide (5 mL, 5 mM) in 5 mL of dry THF cooled to –78 °C was added tridecanenitrile (1 mL, 2.1 mmol) in 1 mL of dry THF. The mixture was stirred for 2 hours at –78 °C. To the mixture was added deuterium oxide (1 mL, 100 mmol) in a dropwise fashion. The solution was warmed up to room temperature overnight. The solvent was then removed using a rotary evaporator. The residue was dissolved in ethyl acetate and washed with H_2O and aqueous saturated brine. The organic layer was dried over Na_2SO_4, concentrated down using a rotary evaporator and purified by column chromatography (ethyl acetate: hexanes = 1:9) to afford the final product as a light-yellow oil (0.37 g, 44 %). ^{1}H NMR (400 MHz, $CDCl_3$) δ 2.31 (t, J = 7.2 Hz, 1H), 1.63 (dd, J = 14.9, 7.0 Hz, 2H), 1.46 – 1.37 (m, 2H), 1.24 (s, 16H), 0.86 (t, J = 6.8 Hz, 3H). ^{13}C NMR (101 MHz, $CDCl_3$) δ 119.96 (s), 31.99 (s), 31.00 (s), 29.68 (s), 29.59 (s), 29.42 (s), 29.40 (s), 28.86 (s), 28.74 (d, J = 3.1 Hz), 25.47 (s), 25.37 (s), 22.77 (s), 17.20 (s), 14.20 (s).

^{1}H NMR of **3**:

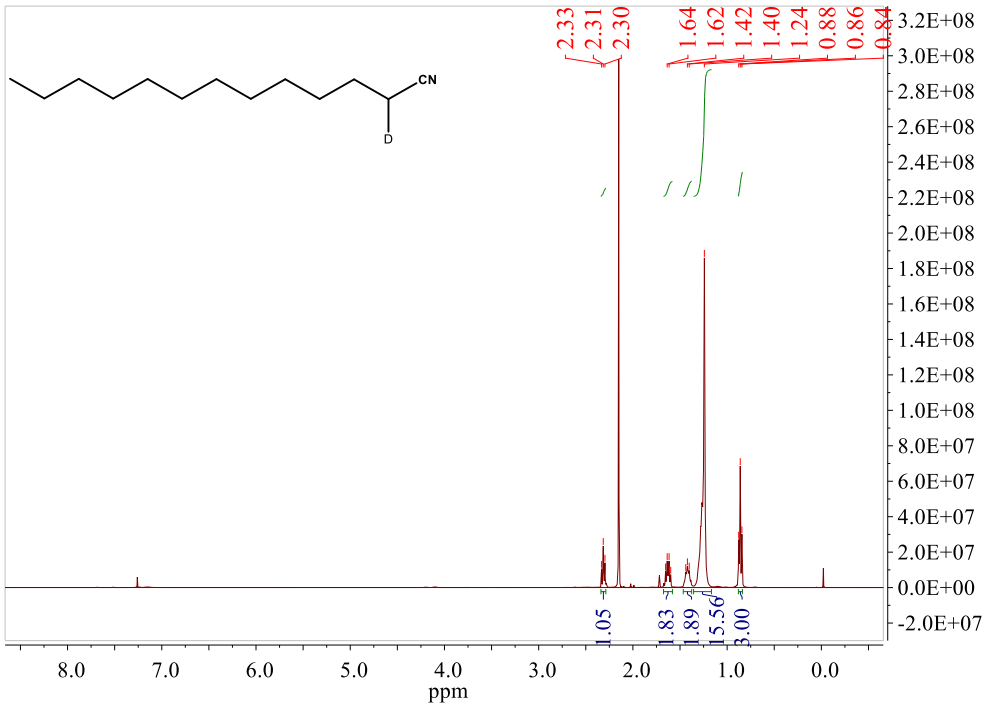
CN
D
2.33
2.31
2.30
1.64
1.62
1.42
1.40
1.24
0.88
0.86
0.84
1.05
1.83
1.89
15.56
3.00
8.0
7.0
6.0
5.0
4.0
3.0
2.0
1.0
0.0
ppm
3.2E+08
3.0E+08
2.8E+08
2.6E+08
2.4E+08
2.2E+08
2.0E+08
1.8E+08
1.6E+08
1.4E+08
1.2E+08
1.0E+08
8.0E+07
6.0E+07
4.0E+07
2.0E+07
0.0E+00
-2.0E+07

^{13}C NMR of **3**:

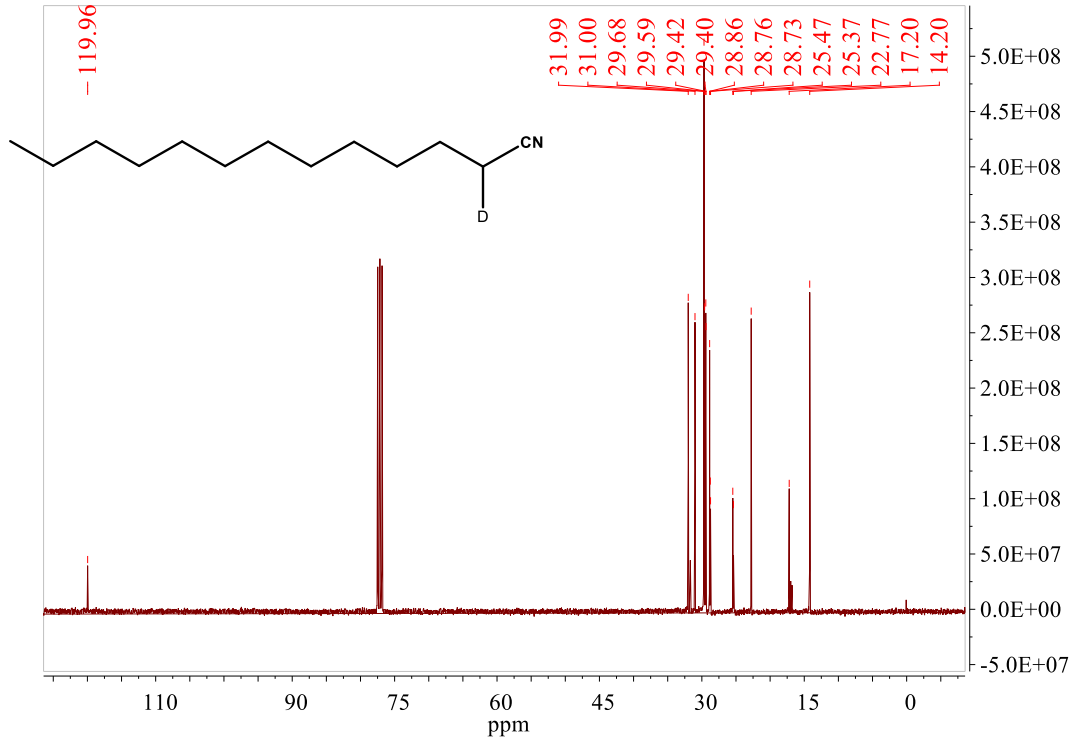
119.96
31.99
31.00
29.68
29.59
29.42
29.40
28.86
28.76
28.73
25.47
25.37
22.77
17.20
14.20
CN
D
5.0E+08
4.5E+08
4.0E+08
3.5E+08
3.0E+08
2.5E+08
2.0E+08
1.5E+08
1.0E+08
5.0E+07
0.0E+00
-5.0E+07
110
90
75
60
45
30
15
0
ppm

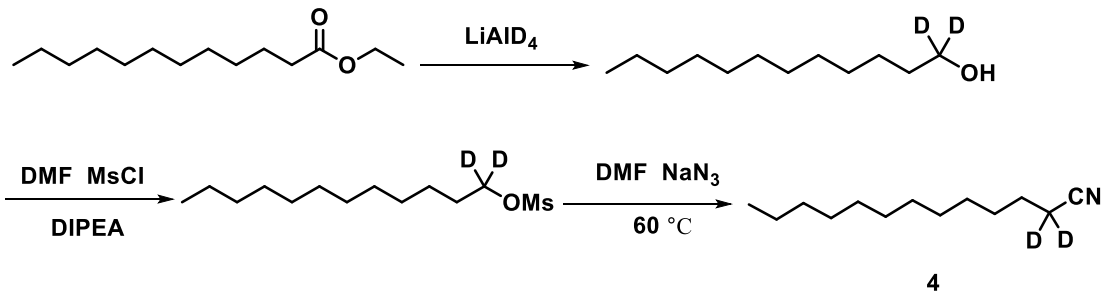

Compound 4. To a dry 25-mL round-bottom flask was added 300 mg $LiAlD_4$ in 10 mL of dry THF, and the suspension was cooled to 0 °C. To the mixture was added ethyl caproate (0.800 g, 3.5 mmol, dried over fresh molecular sieves) in 3 mL of dry THF. The reaction slowly warmed up to room temperature and was stirred overnight. The mixture was cooled to 0 °C, diluted with ether, and H_2O was added to quench the reaction. The organic layer was dried over Na_2SO_4, concentrated down using a rotary evaporator and used without further purification.

To the above crude compound was added 5 mL of dry DMF, methanesulfonyl chloride (MsCl, 0.3 mL, 3.9 mmol) and DIPEA (0.7 mL, 4.2 mmol, dried over fresh molecular sieves) at 0 °C. The mixture was slowly warmed up to room temperature and stirred for additional 3 hours. To the reaction mixture was added NaN_3 (0.23 g, 3.5 mmol), and the mixture was heated to 60 °C overnight. The reaction was diluted with ether and washed with aqueous saturated brine. The organic layer was combined, dried over Na_2SO_4, concentrated down using a rotary evaporator and purified by column chromatography (ethyl acetate: hexanes = 1:9) to afford the final product as a light-yellow oil (0.12 g, 17 % over three steps). ^{1}H NMR (500 MHz, $CDCl_3$) δ 1.66 – 1.60 (m, 2H), 1.46 – 1.39 (m, 2H), 1.26 (d, J = 15.0 Hz, 16H), 0.87 (t, J = 6.8 Hz, 3H). ^{13}C NMR (126 MHz, $CDCl_3$) δ 119.93

(s), 32.01 (s), 29.73 (d, J = 1.6 Hz), 29.69 (s), 29.60 (s), 29.44 (s), 29.40 (s), 28.87 (s), 28.70 (s), 25.28 (s), 22.78 (s), 14.21 (s).

^{1}H NMR of **4**:

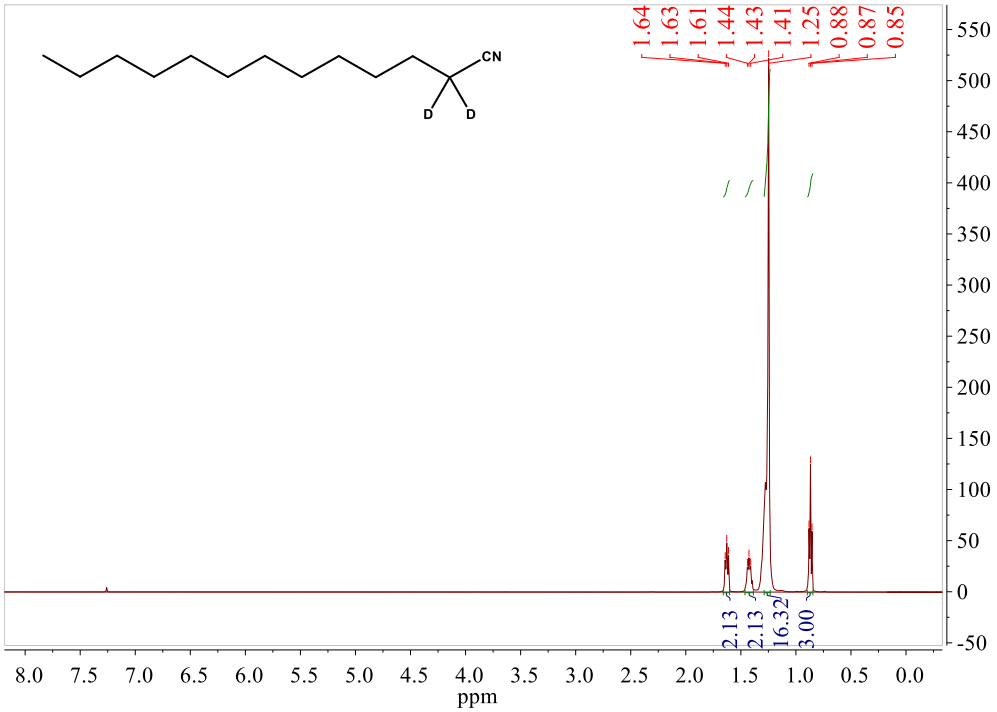

^{13}C NMR of **4**:

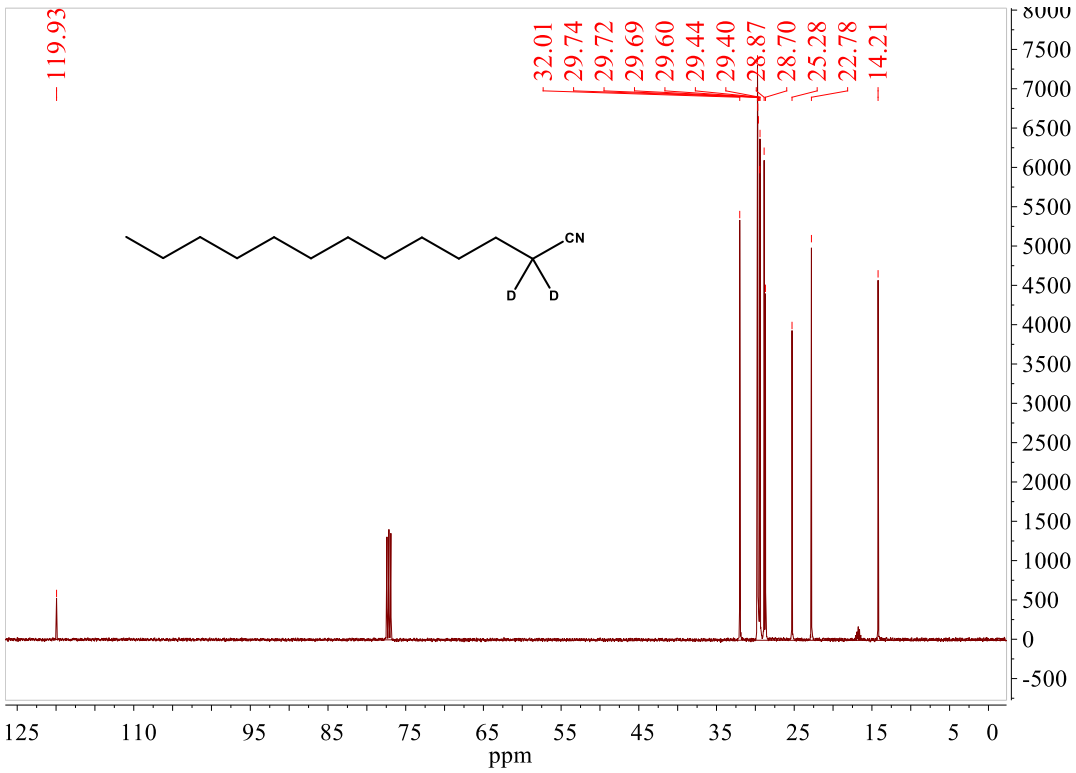
119.93
32.01
29.74
29.72
29.69
29.60
29.44
29.40
28.87
28.70
25.28
22.78
14.21
CN
D
D
8000
7500
7000
6500
6000
5500
5000
4500
4000
3500
3000
2500
2000
1500
1000
500
0
-500
125
110
95
85
75
65
55
45
35
25
15
5
0
ppm

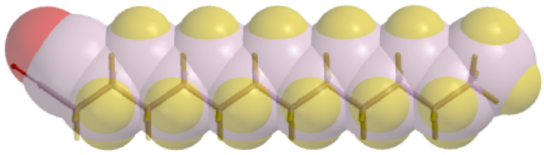

Figure S3.1. Electrostatic potential map of tridecanenitrile (C12-CN).

$$LPP(A^-) = 0.5\chi_{pKa}(HA) + 0.5(1-\chi_{dipole}(HA)) \quad (1)$$

Where χ_{pKa} and χ_{dipole} is a scaling factor defined as:

$$\chi_{pKa}(HA) = \frac{pK_a(HA) - pK_a(HA')_{min}}{pK_a(HA'')_{max} - pK_a(HA')_{min}} \quad (2)$$

$$\chi_{dipole}(HA) = \frac{dipole(HA) - dipole(HA')_{min}}{dipole(HA'')_{max} - dipole(HA')_{min}} \quad (3)$$

The pKa of C12-CN is about 30.9,[3] and the dipole moment of C12-CN is calculated using Spartan '08 (Wavefunction, Inc.) version 1.2.0 to be 4.94 D. Using equations 1, 2, and 3, the LPP of C12-CN is determined to be 1.67. The LPP values of DBA and MDP, which are proton carriers used in previous studies,[2, 4] are 1.11 and 0.57, respectively. The larger the LPP value, the more readily that molecule diffuses across lipids.[5] Therefore, the membrane crossing capacity of C12-CN is expected to be higher than those of DBA and MDP.

8.3.3. Probing the Integrity of HBMs containing DMPC with and without C12-CN Incorporated

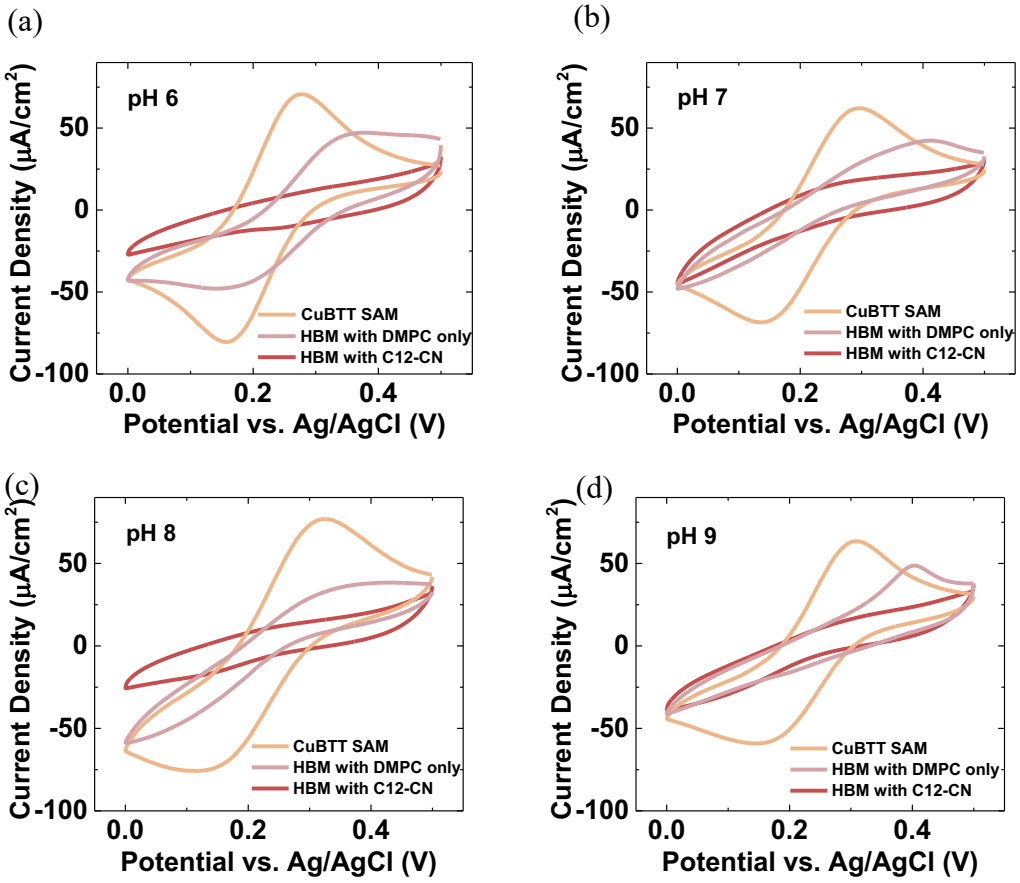

Figure S3.2. Cyclic voltammograms (CVs) of a SAM of the CuBTT, a SAM of CuBTT covered by a monolayer of DMPC, and the HBMs containing DMPC with one equivalent of C12-CN in a solution of $K_3Fe(CN)_6$ (1 mM) with KCl (100 mM) at a scan rate of 50 mV/s after testing the O_2 reduction performance in (a) pH 6, (b) pH 7, (c) pH 8, and (d) pH 9.

(a)

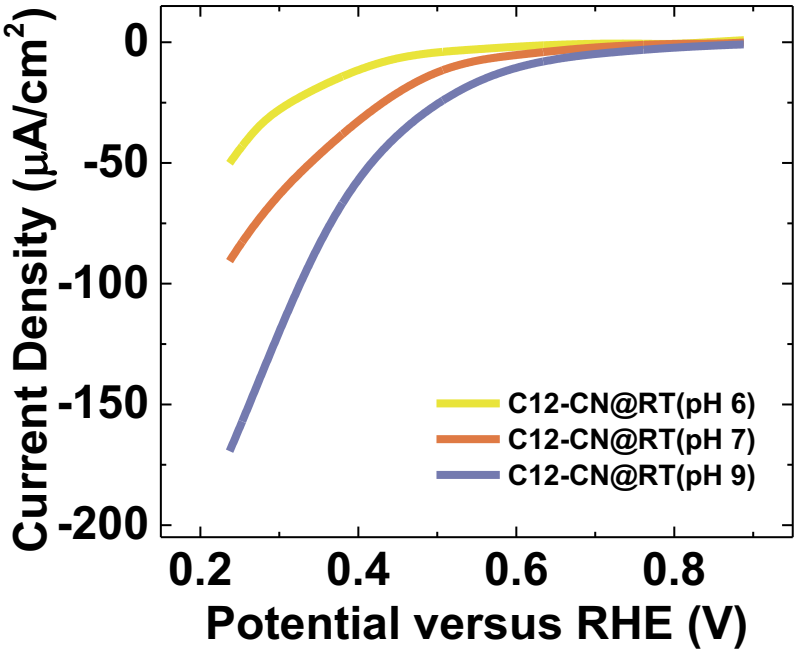
Current Density (μA/cm²)
0
-50
-100
-150
-200
0.2
0.4
0.6
0.8
Potential versus RHE (V)
C12-CN@RT(pH 6)
C12-CN@RT(pH 7)
C12-CN@RT(pH 9)

(b)

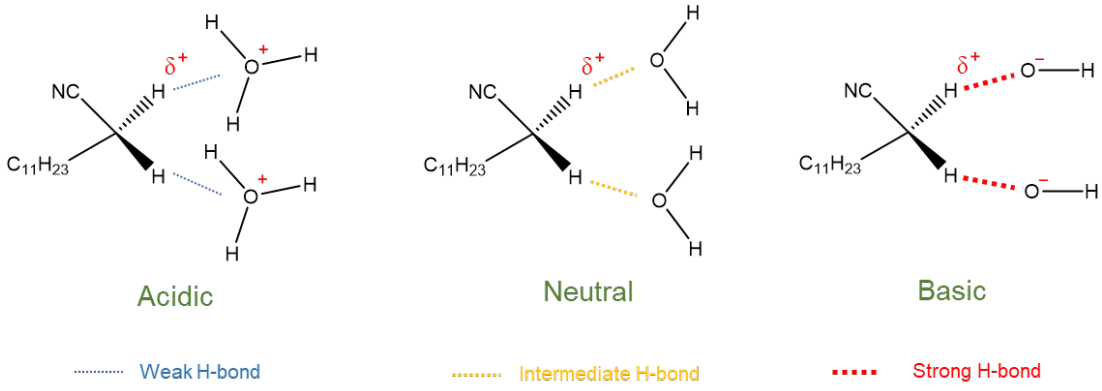
Acidic
Neutral
Basic
Weak H-bond
Intermediate H-bond
Strong H-bond

(c)

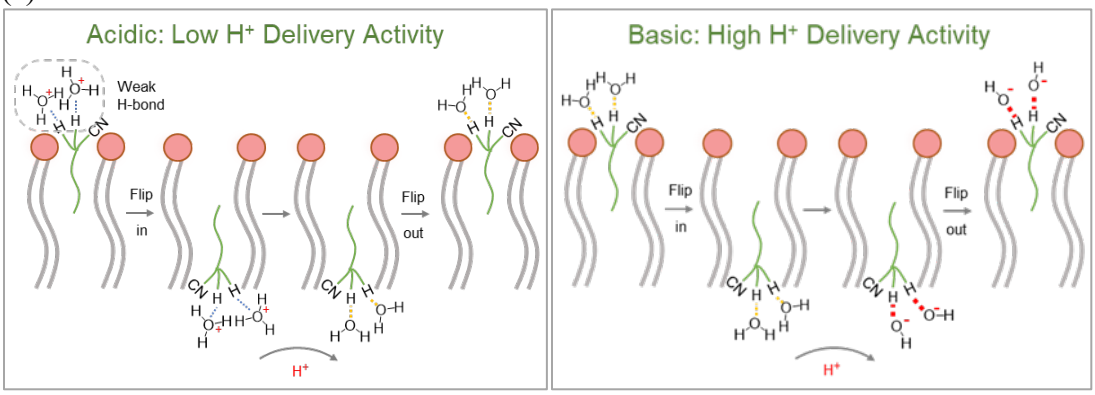
Acidic: Low H⁺ Delivery Activity
Basic: High H⁺ Delivery Activity
Weak H-bond
Flip in
Flip out
H⁺

Figure S3.3. (a) O_2 reduction reaction (ORR) linear sweep voltammograms (LSVs) of a SAM of CuBTT with a monolayer of DMPC appended and with 1 equivalent of C12-CN in the lipid layer in O_2-saturated pH 6 (yellow), 7 (orange), and 9 (blue) phosphate buffer at a scan rate of 10 mV s^{-1}. (b) Qualitative relative H-bonding strengths between the α-protons of C12-CN (H-bond donors) and species in water (H-bond acceptors) under acidic, neutral and basic environment. (c) Schematic of two plausible transmembrane proton delivery pathways that involve (left) H_3O^+ and H_2O species and (right) H_2O and ^-OH species.

The pH-dependent transmembrane proton delivery activity can be understood as follows (Figure 3.3b and S3.3a). Results from low-temperature, methylation, and deuteration experiments suggest that CN-based proton carriers transfer protons via hydrogen-bonded water through a "flip-flop" diffusion mechanism (Figure 3.4-3.5 and S3.4-S3.7). The α-protons on CN-based proton carriers remain as H-bond donors under the mild acidic to mild basic aqueous conditions used in this study (Figure S3.3b). H_3O^+, H_2O, and ^-OH are weak, intermediate, and strong H-bond acceptors in acidic, neutral, and basic environments, respectively.[6] Under acidic condition, because the association of H_3O^+ to C12-CN is weak, proton transfer efficiency across the lipid layer of a HBM is thus low. On the other hand, an increase in the bulk solution pH strengthens the H-bond between C12-CN and water species, therefore leading to the observed increase in the transmembrane proton delivery activity (Figure S3.3c).

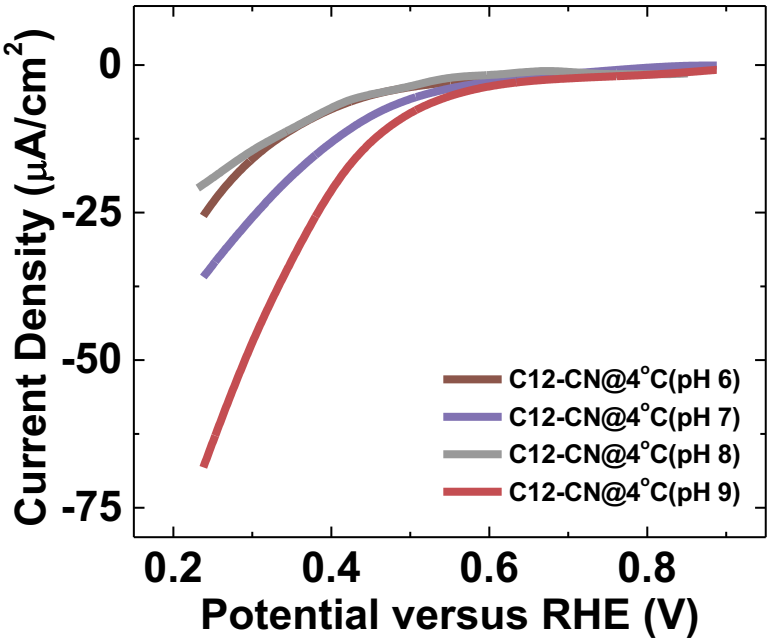

Figure S3.4. O_2 reduction CVs of a SAM of CuBTT covered by a monolayer of DMPC with 1 equivalent of C12-CN in the lipid layer in O_2-saturated pH 6, 7, 8 and 9 phosphate buffer at 4 °C at a scan rate of 10 mV s^{-1}.

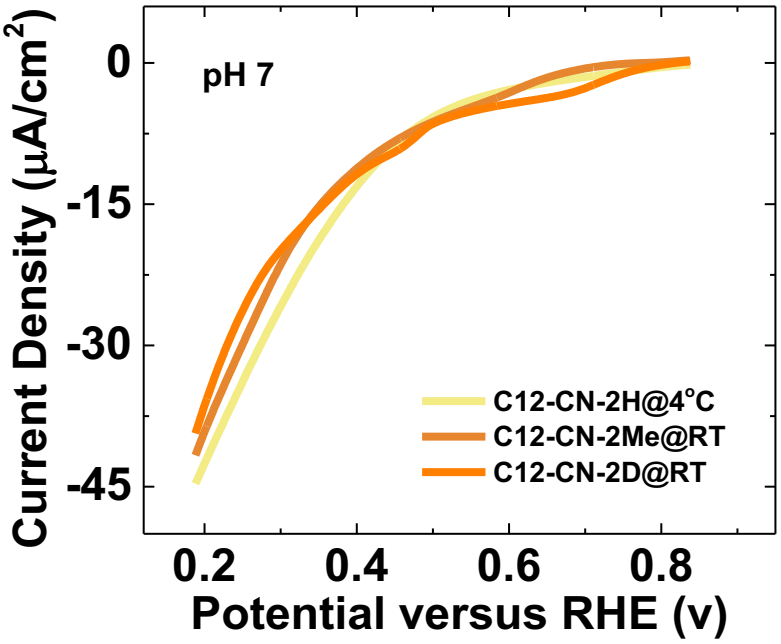

Figure S3.5. O_2 reduction CVs in O_2-saturated pH 7 phosphate buffer with a scan rate of 10 mV s^{-1} of HBMs containing C12-CN-2Me and C12-CN-2D at room temperature and a HBM containing C12-CN-2H at 4 °C.

The proton switch is considered to be in the "off" state in all three cases in Figure S3.5. Though C12-CN-2H is an active proton carrier at room temperature, its proton delivery ability is inhibited at temperatures below the gel-phase transition temperature of DMPC because the proton carrier is frozen in place inside the gel-like lipid matrix. Since C12-CN-2Me does not have α-protons available for hydrogen bonding with water, its proton transfer capability is suppressed. In all three cases, the proton delivery outcome is similar to the DMPC only case (Figure S3.7, black dashed line).

8.3.4. Estimating the Number of Protons Needed to Revive the Activity of C12-CN-2D

The lateral packing density of DMPC is 3.3×10^{-10} mol·cm^{-2}.[7] By assuming that the lateral packing density of HBMs containing DMPC with and without proton carriers are comparable to each other, the density of C12-CN-2D in HBMs containing DMPC with one equivalent of C12-CN-2D system is expected to be 1.7×10^{-10} mol·cm^{-2}. Given that each C12-CN-2D molecule contains 2 deuterons, the deuteron density in the DMPC layer of a HBM is calculated to be 3.3×10^{-10} mol·cm^{-2}. With a Au surface area of 0.219 cm^2, the total number of deuterons present on a HBM-modified Au surface is computed to be 7.3×10^{-11} mol. If all the deuterons of C12-CN-2D are replaced by protons during the ORR process, the number of protons required is 7.3×10^{-11} mol. For ORR, 1 H^+ is transferred for every e^-, so the number of electrons required is 7.3×10^{-11} mol. The amount of total charge transferred therefore equals to 7.0×10^{-6} C, which is equivalent to the point at which the ORR current density reaches 4.0 μA/cm^2. This overestimation places an upper bound on the protons needed to replace the deuterons on C12-CN-2D because it excludes the amount of charge passed before reaching 4.0 μA/cm^2. Since the ORR current density recorded for C12-CN-2D remains low after passing 7.0×10^{-6} C, it is highly likely that the deuterons in C12-CN-2D remain intact and are not replaced by protons during ORR.

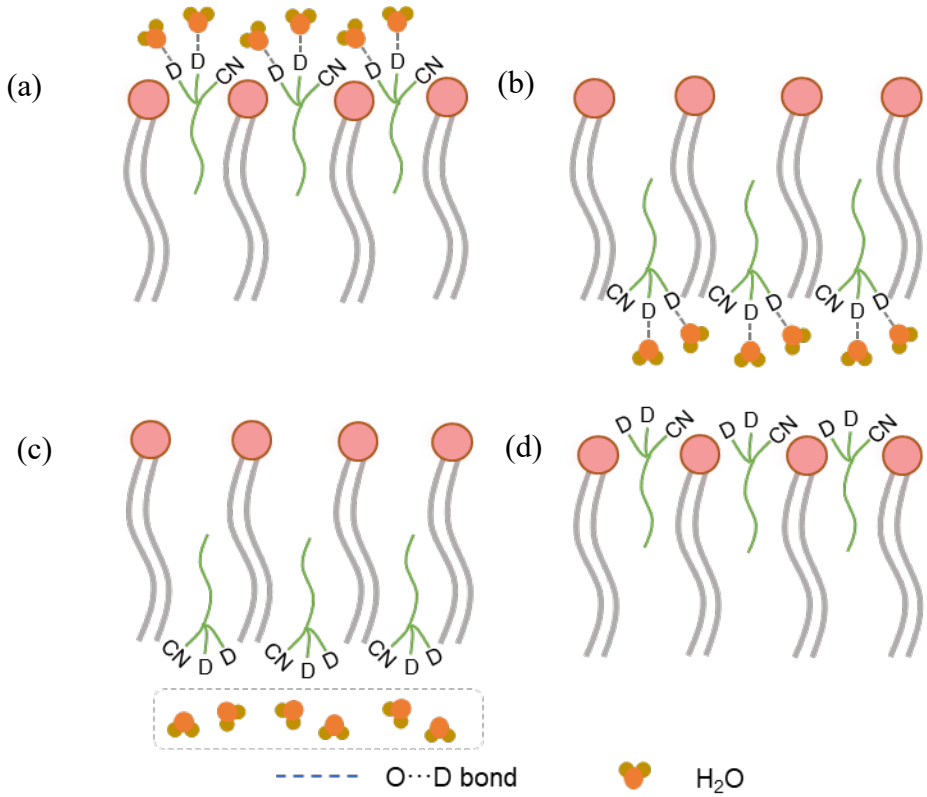

Figure S3.6. Schematic showing how C12-CN-2D transfers protons from bulk solution through the lipid layer to the interior of a HBM during ORR. Hydrogen bonds are established between water molecules and the deuterons on the proton carrier (a). The proton carrier then undergoes flip-flop diffusion in the lipid layer (b) before it releases the water molecules on the opposite side of the membrane (c). Finally, the dehydrated proton carrier reorients itself with its head group at the lipid-water interface (d) where it can associate with additional water molecules.

8.3.5. Deuterated Buffer Inhibits Deuteron Delivery across the HBM Lipid Layer

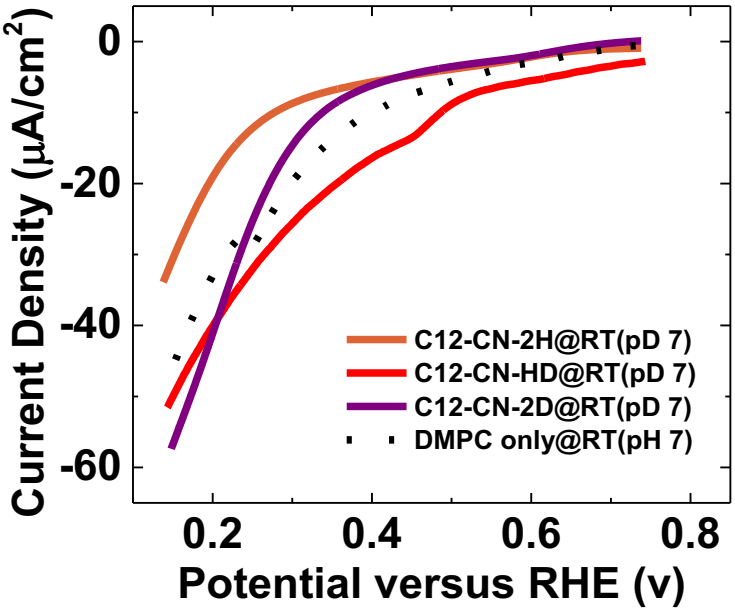

Figure S3.7. O_2 reduction CVs of HBMs containing C12-CN-2H, C12-CN-HD, and C12-CN-2D in O_2-saturated pD 7 phosphate buffer (solid lines) and a HBM that contains DMPC only in O_2-saturated pH 7 phosphate buffer with a scan rate of 10 mV s^{-1} at room temperature.

The proton switch is considered to be in the "off" state in all cases in Figure S3.7. When the experiments were done in pD 7 buffer, the ORR activities of HBMs carrying proton carriers were found to be as low as that of the DMPC only case, suggesting that deuteron delivery is not as efficient as proton delivery for this class of CN-based proton transfer agents.

8.4. References

1. Li Y., Tse E. C. M., Barile C. J., Gewirth A. A., Zimmerman S. C. Photoresponsive Molecular Switch for Regulating Transmembrane Proton-Transfer Kinetics. *J. Am. Chem. Soc.* **137**, 14059-14062 (2015).
2. Barile C. J.*, et al.* Proton switch for modulating oxygen reduction by a copper electrocatalyst embedded in a hybrid bilayer membrane. *Nat. Mater.* **13**, 619-623 (2014).
3. Richard J. P., Williams G., Gao J. Experimental and Computational Determination of the Effect of the Cyano Group on Carbon Acidity in Water. *J. Am. Chem. Soc.* **121**, 715-726 (1999).
4. Tse E. C. M.*, et al.* Proton transfer dynamics control the mechanism of O2 reduction by a non-precious metal electrocatalyst. *Nat. Mater.* **15**, 754-759 (2016).
5. Tse E. C. M., Barile C. J., Gewargis J. P., Li Y., Zimmerman S. C., Gewirth A. A. Anion Transport through Lipids in a Hybrid Bilayer Membrane. *Anal. Chem.* **87**, 2403-2409 (2015).
6. Gilli P., Pretto L., Bertolasi V., Gilli G. Predicting Hydrogen-Bond Strengths from Acid−Base Molecular Properties. The pKa Slide Rule: Toward the Solution of a Long-Lasting Problem. *Acc. Chem. Res.* **42**, 33-44 (2009).
7. Albrecht O., Gruler H., Sackmann E. Polymorphism of phospholipid monolayers. *J. Phys. France* **39**, 301-313 (1978).

8.5. Supporting Information for Chapter 4

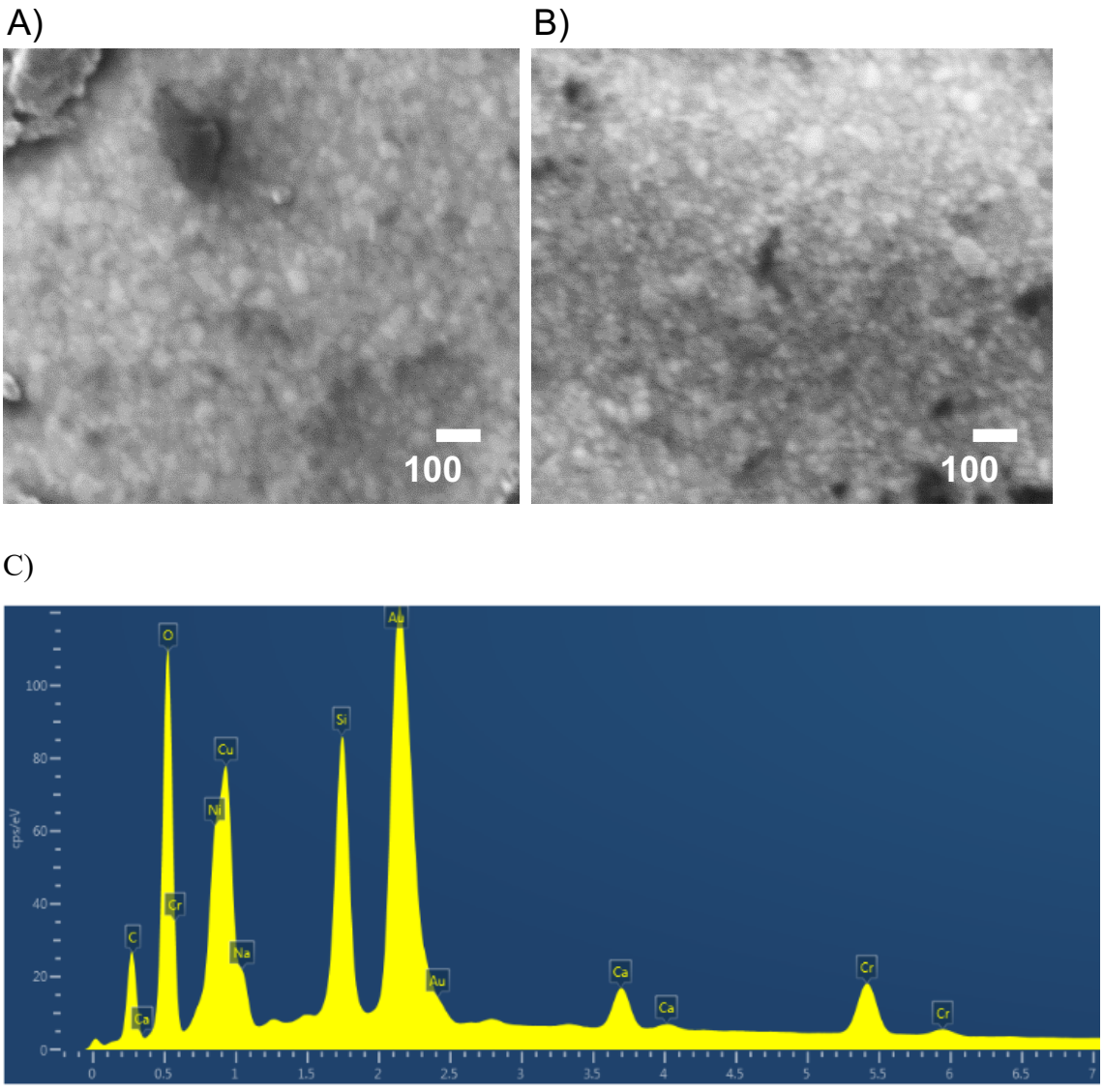

Figure S4.1. SEM images of 46:54 mol % (A) and 71:29 mol % (B) Ni-Cu NPs. Representative energy-dispersive X-ray (EDX) spectrum of Ni-Cu bimetallic nanoparticles on a 100 nm-thick Au on Cr on glass substrate (C). The elements detected are Ni, Cu, Au, Cr, O, C, Si, Ca, and Na. The Au, Cr, O, Si, Ca, and Na detected is from the substrate. C is a common impurity detected in EDS measurements.

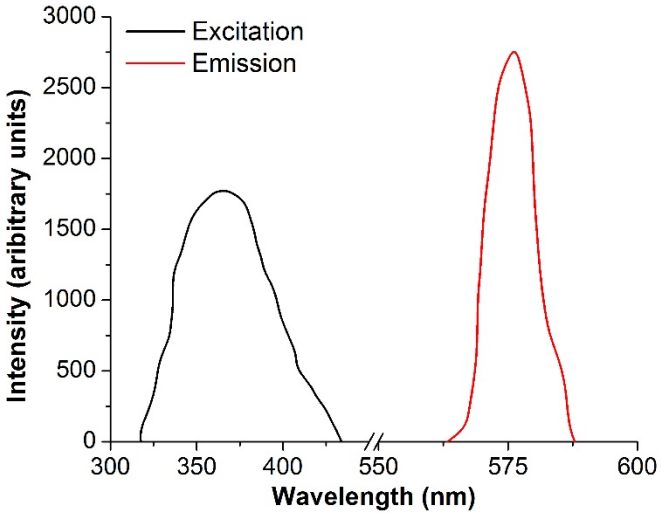

Figure S4.2. Fluorescence spectra of Cu nanoclusters.

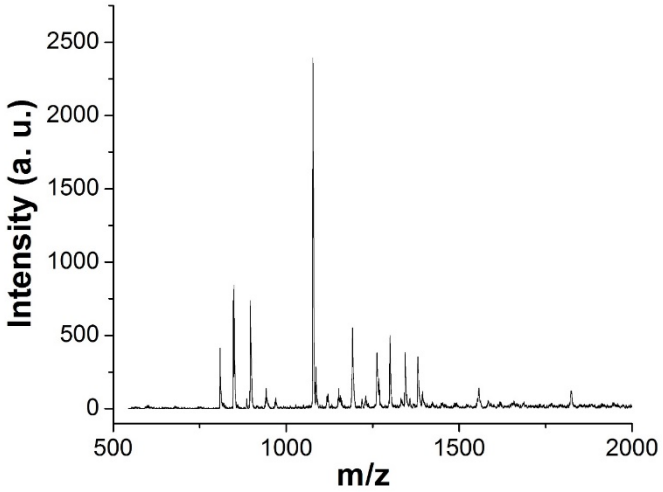

Figure S4.3. The positive-mode MALDI-TOF MS of the as synthesized 100 mol % Cu nanoclusters.

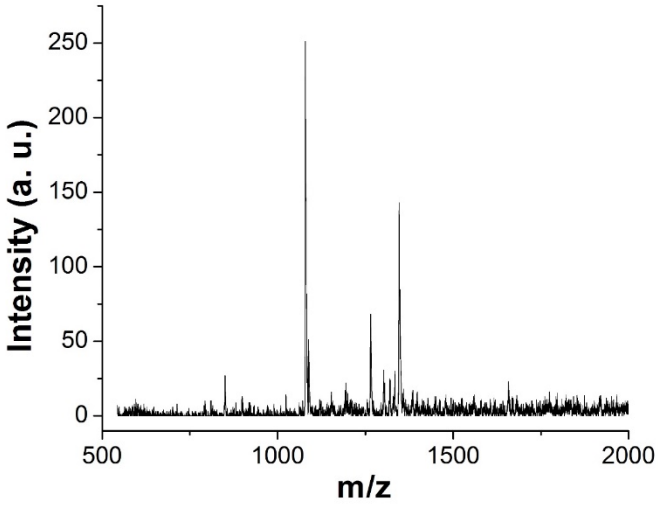

Figure S4.4. The positive-mode MALDI-TOF MS of the as synthesized 25:75 mol % Ni-Cu nanoclusters.

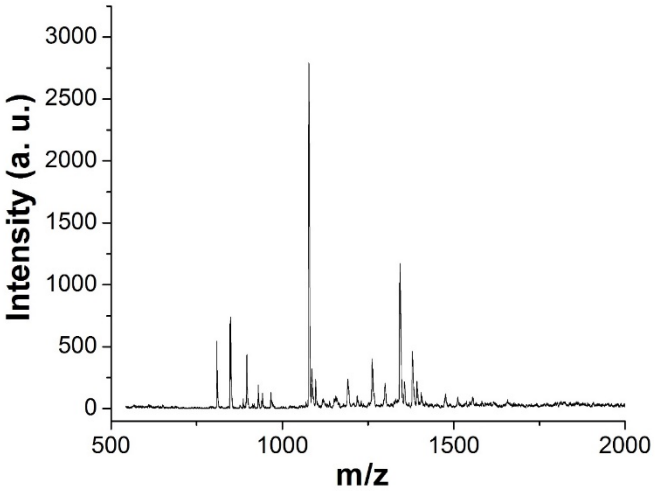

Figure S4.5. The positive-mode MALDI-TOF MS of the as synthesized 43:57 mol % Ni-Cu nanoclusters.

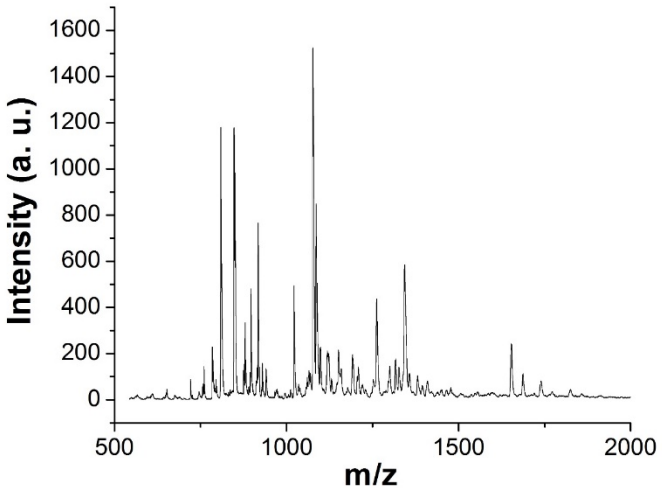

Figure S4.6. The positive-mode MALDI-TOF MS of the as synthesized 100 mol % Ni nanoclusters.

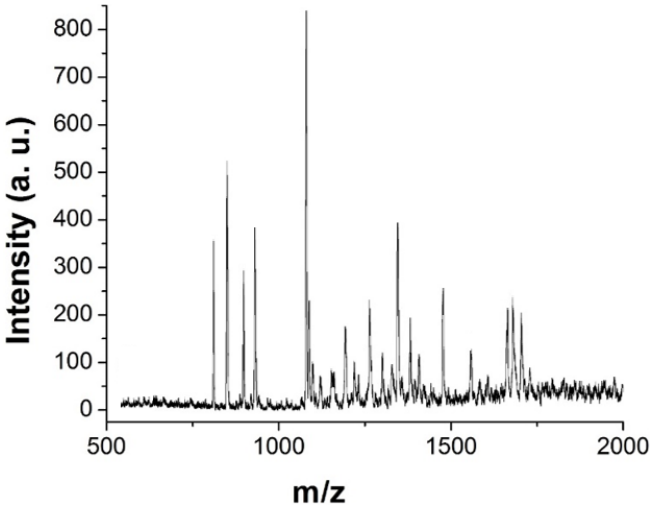

Figure S4.7. Positive-mode MALDI-TOF mass spectrum of the 52:48 mol % Ni-Cu nanoclusters after being immersed overnight in 1 M NaOH and washed with water.

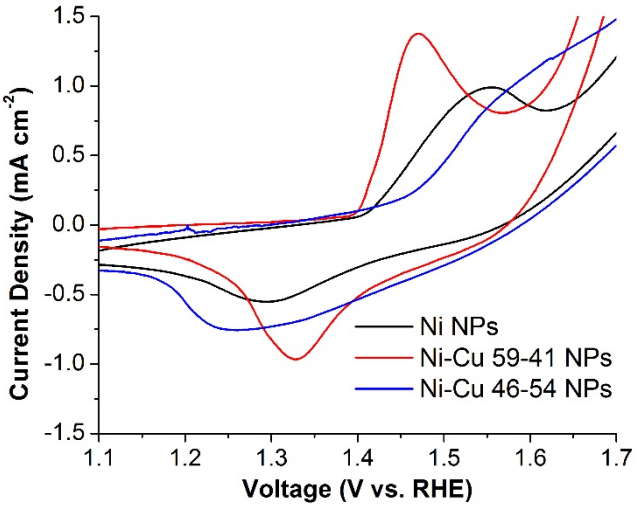

Figure S4.8. Cyclic voltammetry at a scan rate of 10 mV s^{-1} of glassy carbon electrodes modified with Ni nanoparticles (black line), 59:41 mol % Ni-Cu nanoparticles (red line), and 46:54 mol % Ni-Cu nanoparticles (blue line) along with Vulcan XC-72 and PVDF.

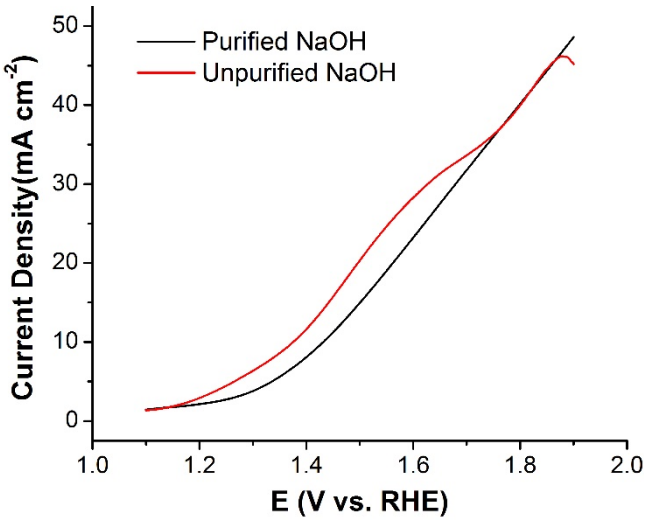

Figure S4.9. Linear sweep voltammograms of the oxygen evolution reaction in purified (2 ppb Fe, black line) and unpurified (115 ppb Fe, red line) 1 M NaOH using a glassy carbon electrode modified with a mixture of 52:48 mol % Ni-Cu nanoclusters, Vulcan XC-72, and PVDF at a scan rate of 10 mV s^{-1}.

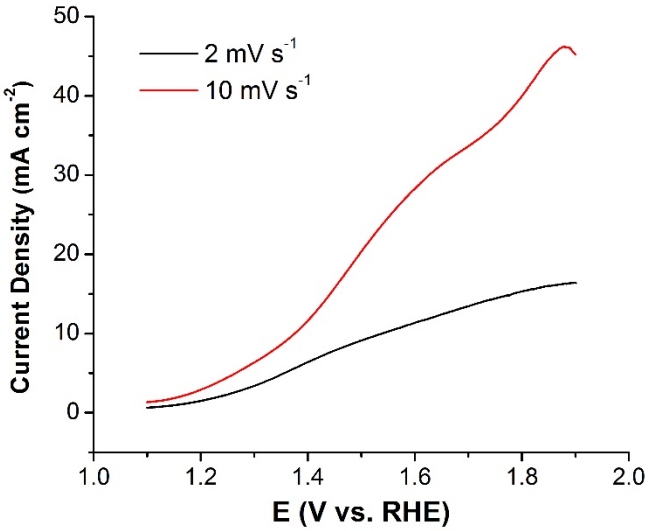

Figure S4.10. Linear sweep voltammograms of the oxygen evolution reaction in 1 M NaOH at a scan rate of 2 mV s^{-1} (black line) and 10 mV s^{-1} (red line) on glassy carbon electrodes modified with 52:48 mol % Ni-Cu nanoclusters, Vulcan XC-72, and PVDF.

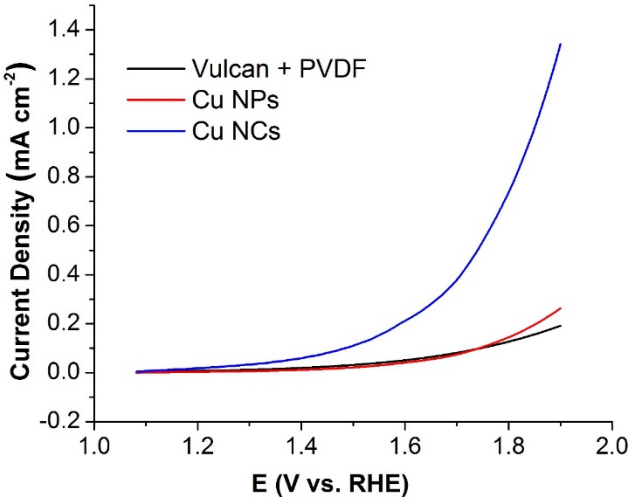

Figure S4.11. Linear sweep voltammograms of the oxygen evolution reaction in 1 M NaOH on glassy carbon working electrodes that have been modified with Cu nanoclusters (100 mol % Cu NCs, blue line) and Cu nanoparticles (100 mol % Cu NPs, red line). A control with the electrode modified with only Vulcan XC-72 and PVDF is also shown (black line).

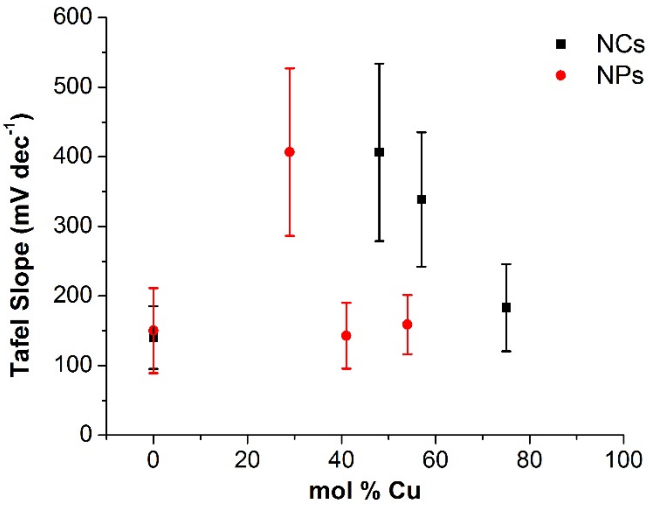

Figure S4.12. Tafel slopes calculated from linear sweep voltammograms of the oxygen evolution reaction in 1 M NaOH on glassy carbon working electrodes that have been modified with nanoclusters (NCs, black line) and nanoparticles (NPs, red line).

A)

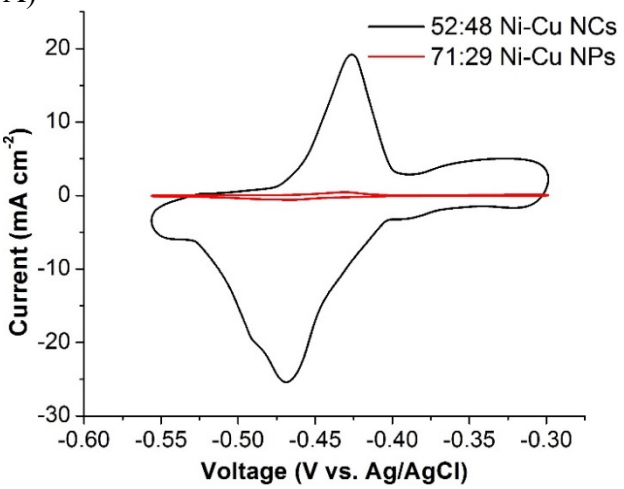

B)

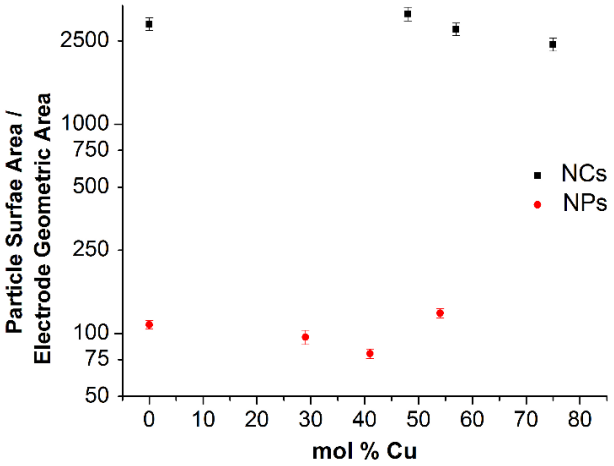

Figure S4.13. Pb UPD experiments of nanoclusters (black) and nanoparticles (red) in an Ar-sparged solution containing 100 mM $HClO_4$, 1 mM $Pb(ClO_4)_2$, and 20 mM KCl at a scan rate of 10 mV/s (A). Calculated electrochemically active surface areas of the nanoclusters (black) and nanoparticles (red) as a function of Cu composition in the catalysts (B).

A)

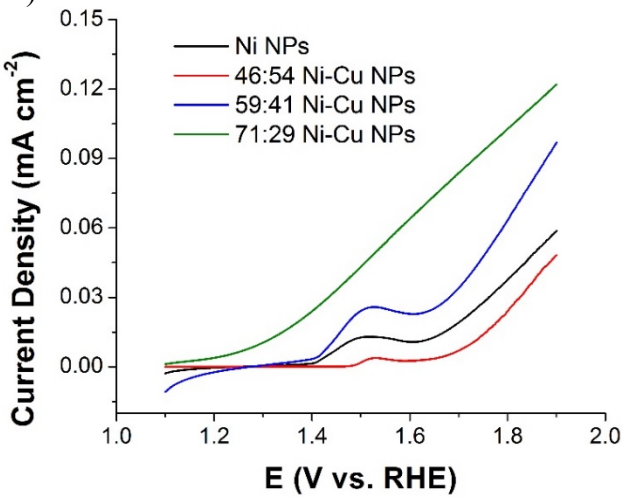

B)

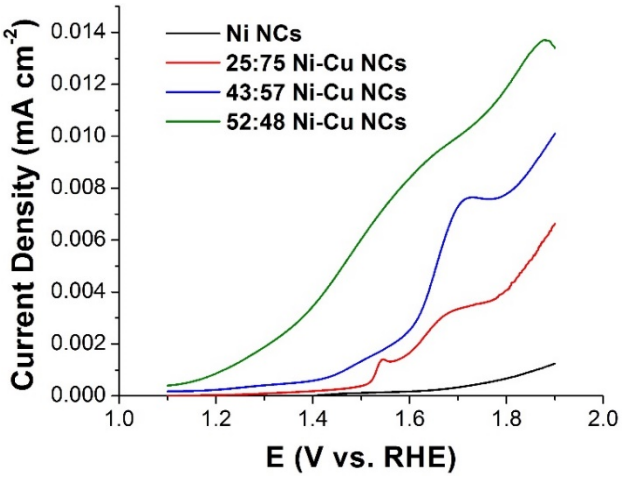

Figure S4.14. Linear sweep voltammograms at 10 mV s^{-1} of the oxygen evolution reaction in 1 M NaOH using a glassy carbon working electrode modified with a mixture of Ni-Cu bimetallic nanoparticles (NPs, A) or nanoclusters (NCs, B), Vulcan XC-72, and PVDF. Ni-Cu bimetallic NPs and NCs with various molar ratios were tested (colored lines) along with pure Ni NPs and NCs (black lines). Current densities are reported against the electrochemically active surface areas reported in Figure S9.

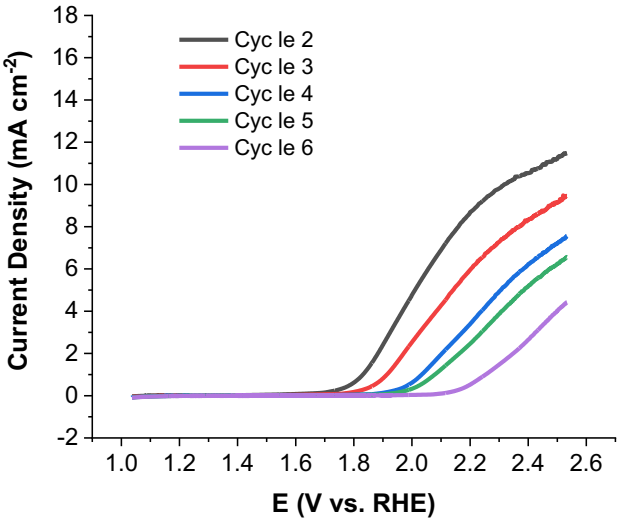

Figure S4.15. Linear sweep voltammograms of multiple cycles of the oxygen evolution reaction in 1 M NaOH using 52:48 mol % Ni-Cu nanoclusters.

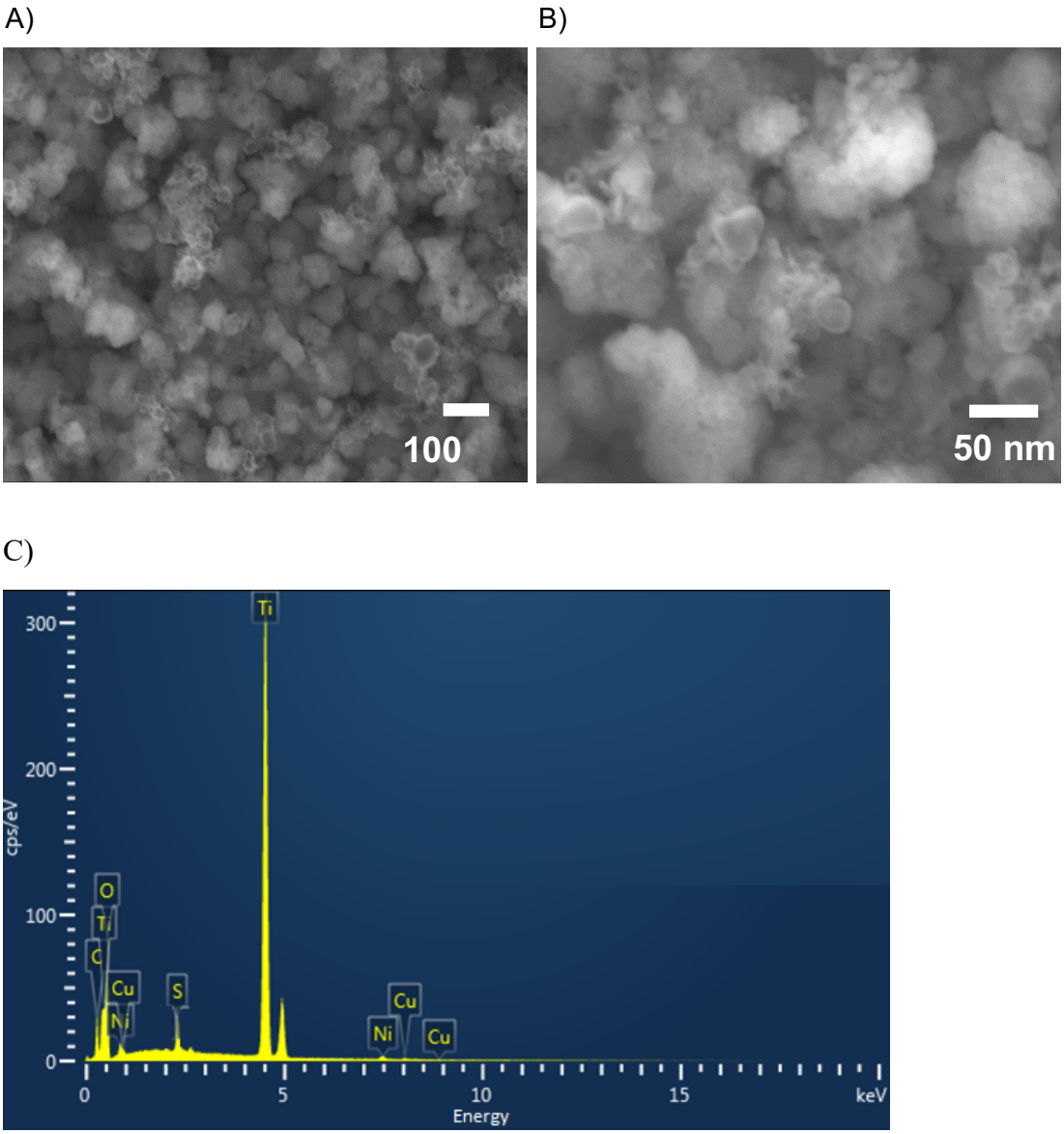

Figure S4.16. SEM images of an electrode containing 52:48 mol % Ni-Cu nanoclusters on TiO_2 nanoparticles on carbon paper (A, B). The EDX spectrum of the electrode (C) demonstrates the presence of Ni and Cu from the core of the Ni-Cu nanoclusters, S from the glutathione ligand of the nanoclusters, and Ti and O from the TiO_2 nanoparticles.

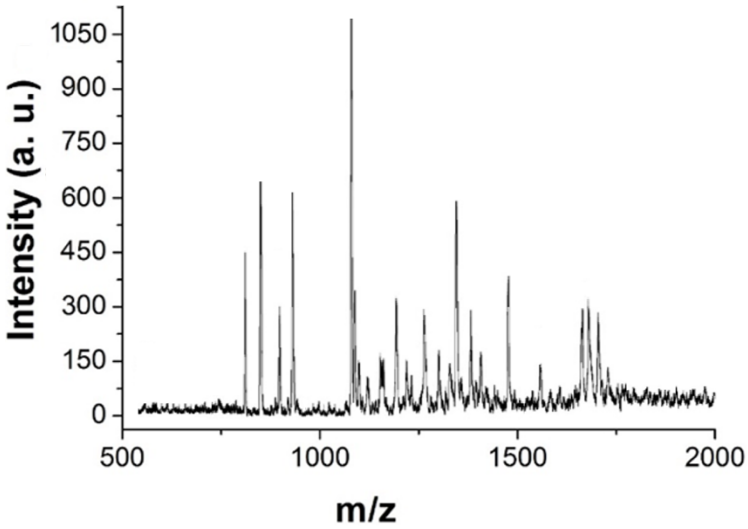

Figure S4.17. Positive-mode MALDI-TOF mass spectrum of the 52:48 mol % Ni-Cu nanoclusters after OER catalysis at 10 mA cm^{-2} for 1 hr.

Assignment	m/z Calculated	100% Cu	25%:75% Ni:Cu	43:57 Ni:Cu	52:48 Ni:Cu	100% Ni
$[Cu_2Ni_2GS + Na]^+$ or $[Cu_9 + H]^+$ or $[Cu_5Ni_4 + Na]^+$ or $[Cu_3NiGS + Na]^+$	572.79 or 573.37 or 575.37 or 577.79				575.5 (18%)	
$[CuNi_{10} + Na]^+$ or **$[Cu_3Ni_3GS + H]^+$** or **$[Cu_6Ni_5 + H]^+$** or **$[Cu_2Ni_9 + Na]^+$**	673.26 or 673.67 or 674.25 or 676.26				673.8 (15%)	
$[Cu_3GS_2 + H]^+$	803.95	806.5 (18%)				
$[Cu_2Ni_6GS + Na]^+$ or **$[Cu_9Ni_4 + H]^+$** or **$[Cu_5Ni_8 + Na]^+$** or **$[Cu_7NiGS + H]^+$**	806.53 or 807.11 or 809.11 or 809.52			807.9 (20%)		
$[Ni_3GS_2 + Na]^+$	810.94					809.7 (78%)
$[Cu_5Ni_8 + Na]^+$ or $[Cu_7NiGS + H]^+$ or $[Ni_3GS_2 + Na]^+$ or $[Cu_3Ni_5GS + Na]^+$ or $[Cu_{10}Ni_3 + H]^+$	809.11 or 809.52 or 810.94 or 811.52 or 812.1				811.0 (32%)	
$[Ni_4GS_2 + H]^+$	846.9					846.5 (77%)
$[Cu_5Ni_9 + H]^+$ or $[Ni_4GS_2 + H]^+$ or $[Cu_3Ni_6GS + H]^+$ or $[Cu_6Ni_8 + H]^+$	845.06 or 846.9 or 849.47 or 850.05			847.6 (26%)	847.6 (59%)	
$[Ni_4GS_2 + H]^+$ or $[Cu_3Ni_6GS + H]^+$ or $[Cu_6Ni_8 + H]^+$ or $[CuNi_3GS_2 + H]^+$	846.9 or 849.47 or 850.05 or 851.89		849.3 (11%)			

$[Ni_{10}GS + H]^+$	892.42					895.4 (32%)
$[Cu_8NiGS + Na]^+$ or **$[CuNi_9GS + H]^+$**	896.43 or 897.42			896.6 (16%)	897.9 (32%)	
$[Cu_9GS + Na]^+$	901.43	899.5 (31%)				
$[Ni_{10}GS + Na]^+$	914.41					916.3 (50%)
$[Ni_5GS_2 + Na]^+$	926.81					927.9 (11%)
$[Cu_5Ni_{10} + Na]^+$ or $[Cu_7Ni_3GS + H]^+$ or $[Cu_{10}Ni_5 + H]^+$ or $[Cu_3Ni_7GS + Na]^+$ or $[Cu_5GS_2 + H]^+$ or $[Cu_6Ni_9 + Na]^+$ or $[Cu_8Ni_2GS + H]^+$ or $[CuNi_4GS_2 + Na]^+$	926.97 or 927.39 or 929.97 or 929.39 or 929.81 or 931.97 or 932.38 or 931.81				929.9 (59%)	
$[Ni_7GS_2 + H]^+$	1022.7					1020.9 (32%)
$[Cu_8Ni_4GS + Na]^+$ or **$[Cu_6NiGS_2 + Na]^+$**	1072.23 or 1074.65			1073.9 (100%)		
$[Cu_7GS_2 + Na]^+$	1079.65	1077.0 (100%)				
$[Cu_9Ni_3GS + Na]^+$ or $[Cu_7GS_2 + Na]^+$	1077.23 or 1079.65				1078.5 (100%)	
$[Cu_9Ni_3GS + Na]^+$ or $[Cu_7GS_2 + Na]^+$ or $[Cu_{10}Ni_2GS + Na]^+$ or $[Ni_8GS_2 + H]^+$	1077.23 or 1079.65 or 1082.22 or 1082.63		1079.9 (100%)			
$[Ni_8GS_2 + H]^+$	1082.63					1082.5 (100%)

$[Ni_8GS_2 + H]^+$ or $[Cu_3Ni_{10}GS + H]^+$ or $[CuNi_7GS_2 + H]^+$ or $[Cu_4Ni_9GS + H]^+$	1082.63 or 1083.21 or 1087.63 or 1088.21			1085.5 (12%)		
$[CuNi_7GS_2 + H]^+$ or **$[Cu_4Ni_9GS + H]^+$**	1087.63 or 1088.21		1089.0 (20%)			
$[CuNi_7GS_2 + H]^+$ or **$[Cu_4Ni_9GS + H]^+$** or **$[Cu_2Ni_6GS_2 + H]^+$**	1087.63 or 1088.21 or 1092.62				1089.9 (30%)	
$[Ni_3GS_3 + H]^+$	1095.04					1095.1 (56%)
$[Cu_3Ni_5GS_2 + H]^+$ or **$[CuNi_2GS_3 + H]^+$** or **$[Cu_6Ni_7GS + H]^+$** or **$[Cu_9Ni_9 + H]^+$** or **$[Cu_4Ni_4GS_2 + H]^+$**	1097.62 or 1100.03 or 1098.2 or 1100.77 or 1100.61				1099.1 (13%)	
$[Ni_3GS_3 + Na]^+$	1117.02					1118.6 (14%)
$[Cu_3NiGS_3 + Na]^+$ or $[Cu_6Ni_3GS_2 + Na]^+$ or $[Cu_9Ni_5GS + Na]^+$ or $[Cu_4GS_3 + Na]^+$	1189.94 or 1192.52 or 1193.1 or 1194.93				1192.8 (23%)	
$[CuNi_4GS_3 + H]^+$ or $[Cu_4Ni_6GS_2 + H]^+$ or $[Cu_7Ni_8GS + H]^+$ or $[Ni_{10}GS_2 + Na]^+$ or $[Cu_2Ni_3GS_3 + H]^+$ or $[Cu_{10}Ni_{10} + H]^+$	1217.9 or 1218.48 or 1221.06 or 1220.48 or 1222.9 or 1221.64				1220.3 (13%)	
$[CuNi_{10}GS_2 + H]^+$ or **$[Cu_9NiGS_2 + Na]^+$**	1263.43 or 1265.44		1264.8 (27%)	1262.8 (14%)	1263.7 (30%)	
$[Cu_6GS_3 + H]^+$	1300.81	1299.8 (21%)				

$[CuNi_5GS_3 + Na]^+$ or $[Cu_4Ni_7GS_2 + Na]^+$ or $[Cu_7Ni_9GS + Na]^+$ or $[Cu_6GS_3 + H]^+$ or $[Cu_2Ni_4GS_3 + Na]^+$ or $[Cu_9Ni_2GS_2 + H]^+$	1297.82 or 1300.39 or 1300.97 or 1300.81 or 1302.81 or 1301.39				1300.3 (16%)	
$[Cu_7Ni_9GS + Na]^+$ or $[Cu_6GS_3 + H]^+$ or $[Cu_2Ni_4GS_3 + Na]^+$ or $[Cu_9Ni_2GS_2 + H]^+$ or $[Cu_5Ni_6GS_2 + Na]^+$ or $[Cu_8Ni_8GS + Na]^+$ or $[Cu_{10}NiGS_2 + H]^+$	1300.97 or 1300.81 or 1302.81 or 1301.39 or 1305.39 or 1305.97 or 1306.39		1303.7 (12%)			
$[Cu_5NiGS_3 + Na]^+$ or **$[Cu_8Ni_3GS_2 + Na]^+$**	1317.8 or 1318.38		1319.6 (10%)			
$[Cu_2Ni_{10}GS_2 + H]^+$ or $[Cu_{10}NiGS_2 + Na]^+$ or $[Ni_7GS_3 + H]^+$	1326.36 or 1328.37 or 1328.78				1327.7 (13%)	
$[Cu_3Ni_9GS_2 + H]^+$ or **$[CuNi_6GS_3 + H]^+$**	1331.35 or 1333.77		1333.3 (12%)			
$[Cu_5Ni_7GS_2 + H]^+$ or **$[Cu_8Ni_9GS + H]^+$** or **$[Cu_3Ni_4GS_3 + H]^+$** or **$[Cu_6Ni_6GS_2 + H]^+$**	1341.34 or 1341.92 or 1343.76 or 1346.34				1343.8 (57%)	
$[Cu_9Ni_8GS + H]^+$ or **$[Cu_8Ni_9GS + H]^+$** or **$[Cu_3Ni_4GS_3 + H]^+$** or **$[Cu_6Ni_6GS_2 + H]^+$**	1346.92 or 1341.92 or 1343.76 or 1346.34			1344.5 (42%)		
$[Cu_2Ni_{10}GS_2 + Na]^+$ or **$[Cu_9Ni_8GS + H]^+$** or **$[Cu_4Ni_3GS_3 + H]^+$** or **$[Cu_6Ni_6GS_2 + H]^+$**	1348.34 or 1346.92 or 1348.75 or 1346.34		1347.0 (57%)			
$[Cu_8Ni_4GS_2 + Na]^+$ or **$[Cu_6NiGS_3 + Na]^+$**	1378.31 or 1380.73			1379.5 (16%)		

$[Cu_6NiGS_3 + Na]^+$ or **$[Cu_9Ni_3GS_2 + Na]^+$**	1380.73 or 1383.3				1382.6 (25%)	
$[Cu_3Ni_5GS_3 + H]^+$ or **$[Cu_6Ni_7GS_2 + H]^+$** or **$[Cu_9Ni_9GS + H]^+$**	1403.69 or 1404.27 or 1406.85				1405.5 (16%)	
$[Cu_4Ni_{10}GS_2 + Na]^+$ or $[Cu_6Ni_3GS_3 + H]^+$ or $[Cu_2Ni_7GS_3 + Na]^+$ or $[Cu_9Ni_5GS_2 + H]^+$ or $[Cu_5Ni_9GS_2 + Na]^+$ or $[Cu_4GS_4 + H]^+$ or $[Cu_7Ni_2GS_3 + H]^+$ or $[Ni_4GS_4 + Na]^+$	1476.2 or 1476.61 or 1478.61 or 1477.19 or 1481.19 or 1479.03 or 1481.61 or 1481.03				1478.7 (23%)	
$[Cu_3Ni_2GS_4 + Na]^+$ or **$[Cu_6Ni_4GS_3 + Na]^+$** or **$[Cu_9Ni_6GS_2 + Na]^+$** or **$[Cu_4NiGS_4 + Na]^+$** or **$[Cu_7Ni_3GS_3 + Na]^+$**	1555.95 or 1556.53 or 1559.11 or 1560.94 or 1561.52				1558.7 (20%)	
$[CuNi_6GS_4 + Na]^+$ or **$[Cu_8Ni_4GS_3 + H]^+$** or **$[Cu_4Ni_8GS_3 + Na]^+$** or **$[Cu_6NiGS_4 + H]^+$** or **$[Cu_2Ni_5GS_4 + Na]^+$**	1661.83 or 1662.4 or 1664.41 or 1664.82 or 1666.82				1663.9 (22%)	
$[Cu_9Ni_8GS_2 + Na]^+$ or **$[Cu_7Ni_5GS_3 + Na]^+$** or **$[Cu_5Ni_2GS_4 + Na]^+$** or **$[Cu_{10}Ni_7GS_2 + Na]^+$**	1676.97 or 1679.39 or 1681.81 or 1679.97				1679.9 (24%)	
$[Cu_2Ni_6GS_4 + H]^+$ or **$[Cu_5Ni_8GS_3 + H]^+$** or **$[Cu_8Ni_{10}GS_2 + H]^+$**	1704.77 or 1705.35 or 1707.93				1705.0 (22%)	
$[Cu_{10}Ni_3GS_3 + H]^+$ or **$[Cu_2Ni_6GS_4 + Na]^+$** or **$[Cu_9Ni_4GS_3 + H]^+$** or **$[Cu_5Ni_8GS_3 + Na]^+$** or	1726.76 or 1725.33 or 1727.34 or 1729.75 or				1727.9 (12%)	

$[Cu_7NiGS_4 + H]^+$ or **$[Cu_8Ni_{10}GS_2 + Na]^+$**	1729.91 or 1730.33					
$[Cu_6Ni_8GS_3 + Na]^+$ or **$[Cu_8NiGS_4 + H]^+$** or **$[Cu_4Ni_5GS_4 + Na]^+$** or **$[Cu_9Ni_{10}GS_2 + Na]^+$**	1792.26 or 1792.68 or 1794.68 or 1792.84				1794.2 (25%)	
$[Cu_7Ni_{10}GS_3 + Na]^+$ or **$[Cu_9Ni_3GS_4 + H]^+$** or **$[Cu_5Ni_7GS_4 + Na]^+$**	1973.06 or 1973.48 or 1975.48				1974.8 (10%)	

Table S4.1. MALDI-TOF peak assignments for Cu, Ni, and Ni-Cu nanoclusters. Assignments in bold are peaks that can only be ascribed to a bimetallic species. Assignments in blue are bimetallic species detected in the spectra of all three bimetallic nanoclusters compositions. Normalized peak intensities are listed in parenthesis after each found m/z value. Peaks were considered present if they possessed a normalized intensity of at least 10%. Peaks were assigned to a species if the calculated m/z value for the isotopically most abundant peak matched within 3 amu.

Catalyst	Electrolyte	Onset E (V_{RHE})	Onset overpotential (V_{RHE} – 1.23 V)	Overpotential (mV) at specific current density	Ref-erence
Precious metal					
Ru_{60}-Co_{40}	0.1 M $HClO_4$	1.41	0.18	-	4
Ru_{70}-Ir_{30}	0.1 M $HClO_4$	1.40	0.27	-	4
RuO_2	0.1 M KOH	1.44	0.21	425 @ 20 mA/cm^2	5
IrO_2	1 M KOH	1.51	0.28	340 @ 10 mA/cm^2	6
Spinel family					
$CoFe_2O_4$ on GCE	0.1 M KOH	1.58	0.35	443 @ 10 mA/cm^2	7
Mn_3O_4 on GCE	1 M KOH	1.68	0.45	>600 @ 3 mA/cm^2	8
Co_3O_4 on Au	1 M KOH	1.56	0.33	400 @ 10 mA/cm^2	9

$Mn_{2.1}Co_{0.9}O_4$	1 M KOH	1.64	0.41	490 @ 3 mA/cm^2	8
$ZnCo_2O_4$ on Pt	1 M KOH (pH 13.8)	1.62	0.39	450 @ 20 mA/cm^2	10
$NiCo_2S_4$ nanostructure	1 M KOH	1.50	0.27	260 @ 10 mA/cm^2	24
FeCo oxide on Ni foam	1 M KOH	1.49	0.26	205 @ 10 mA/cm^2	25
Layer-structure type family					
CoOOH on PtO/AuO	0.1 M KOH/LiOH	1.48	0.25	450 @ 5 mA/cm^2	11
3D Ni-Fe LDH on Ni foam	0.1 M KOH	1.46	0.23	280 @ 30 mA/cm^2	12
Co-Ni LDH on FTO	0.1 M potassium phosphate (pH 7)	1.623	0.393	490 @ 1 mA/cm^2	13
Co-Co LDH	0.1 M potassium phosphate (pH 7)	1.638	0.408	610 @ 1 mA/cm^2	13
Zn-Co LDH on GCE	0.1 M KOH (pH 13)	1.57	0.34	-	14
Co-Fe LDH (1:0.35) on GCE	0.1 M KOH	1.52	0.29	350 @ 10 mA/cm^2	15
Co-Cr LDH (2:1) on GCE	0.1 M KOH	1.47	0.24	340 @ 10 mA/cm^2	5
Ni-Fe-Mn LDH on CFP	1 M KOH	1.43	0.20	289 @ 20 mA/cm^2	16
□□$Ni(OH)_2$ nanoparticle film	0.1 M KOH	1.55	0.32	450 @ 30 mA/cm^2	12
Co-Ni based nanotubes/nanosheets on Cu	1 M KOH	1.50	0.27	280 @ 10 mA/cm^2	17
Exfoliated Ni-Fe nanosheets on GCE	1 M KOH	1.49	0.26	300 @ 10 mA/cm^2	6
Exfoliated Ni-Co nanosheets on GCE	1 M KOH	1.52	0.29	385@ 10 mA/cm^2	6
Exfoliated Co-Co nanosheets on GCE	1 M KOH	1.53	0.30	390 @ 10 mA/cm^2	6
Fe-Ni nanoparticles on GCE	1 M NaOH	1.40	0.17	256 @ 1 mA/cm^2 311 @ 10 mA/cm^2	18

Fe-$Ni_{4.34}$ on FeNi foil	1 M KOH	1.49	0.26	283 @ 10 mA/cm^2	26
NiCu-MOF nanosheet on Ni foam	1 M KOH	1.35	0.12	309 @ 10 mA/cm^2	27
3D Cu-Ni oxide on Ni foam	1 M NaOH	1.42	0.19	319 @ 10 mA/cm^2	28
Ir-Ni oxide thin film	0.1 M $HClO_4$	1.49	0.26	-	29
Ni-Ir thin film	0.1 M KOH	1.48	0.25	-	30
NiO-Fe on Ni foam	1 M KOH	1.46	0.23	240 @ 10 mA/cm^2	31
2D Ir-Ni oxide nanoframes	0.1 M $HClO_4$	1.50	0.27	-	32
$NiCo_{2.7}(OH)_x$ Amorphous double hydroxide	1 M KOH	1.48	0.25	350 @ 10 mA/cm^2	33
3D FeCoW	1 M KOH	1.42	0.19	191 @ 10 mA/cm^2	34
CNTs or carbon fiber supported					
NiFe-LDH/CNT	1 M KOH	1.45	0.22	149 @ 10 mA/cm^2	19
M-CNTs-Arc	1 M KOH	1.48	0.25	152 @ 10 mA/cm^2	20
$NiFeO_x$/CFP	1 M KOH	1.43	0.20	146 @ 10 mA/cm^2	21
20%Ir/C	1 M KOH	1.50	0.27	152 @ 10 mA/cm^2	22
FeNi on N-doped CNT	0.1 M KOH	1.59	0.36	810 @ 10 mA/cm^2	35
$Co_6Mo_6C_2$ on N-doped reduced graphene oxide film	1 M KOH	1.46	0.23	260 @ 10 mA/cm^2	36
Other					
Fe nanoparticles	1 M NaOH	1.56	0.33	421 @ 1 mA/cm^2	18
Ni nanoparticles	1 M NaOH	1.34	0.11	476 @ 1 mA/cm^2	18
Ni-FeO_x/C (69:31) nanoparticle on carbon black	1 M KOH	1.41	0.18	280 @ 10 mA/cm^2	23
Ir/C catalyst	0.1 M KOH	1.50	0.27	390 @ 30 mA/cm^2	12
NiFe phosphide nanoparticles	1 M KOH	1.51	0.28	270 @ 10 mA/cm^2	37

$NiCuO_x$ nanoparticles	1 M Na2CO3	1.55	0.32	680 @ 5 mA/cm^2	38
Ni-Cu nanoparticles in MOF	1 M KOH	1.68	0.45	640 @ 6 mA/cm^2	39
Ni@Pt core-shell nanoplates	1 M KOH	1.51	0.28	330 @ 10 mA/cm^2	40
CoNiPO	1 M KOH	1.49	0.26	320 @ 10 mA/cm^2	41
Ni-Co oxide hollow nanosponges	0.1 M KOH	1.50	0.27	362 @ 10 mA/cm^2	42
$Ni_{0.6}Co_{1.4}P$ nanocages	1 M KOH	1.52	0.29	300 @ 10 mA/cm^2	43
Nanoporous $(Co_{1-x}Fe_x)_2P$	1 M KOH	1.49	0.26	64 @ 10 mA/cm^2	44
Nanoporous Co_3Ni_1P	1 M KOH	1.48	0.25	281 @ 10 mA/cm^2	45

Table S4.2. Summary of performance of various OER electrocatalysts reported in the literature arranged by catalyst family.

8.6. References

1. L. Argueta-Figueroa, T. A. Morales-Luckie, R. J. Scougall-Vilchis, O. F. Olea-Mejia, *Prog. Nat. Sci. Mater.* 2014, ***24*****,** 321-328.
2. X. Gao, Y. Lu, M. Liu, S. He, W. Chen, *J. Mat. Chem. C* **2015,** *3*, 4050-4056.
3. Y. C. Huang, Z. Getahun, Y. Zhu, J. Klemke, W. DeGrado, W. F. Gai, F., *Proc. Natl. Acad. Sci.* **2002**, *99*, 2788-2793.
4. R. Forgie, G. Bugosh, C. K. Neyerlin, Z. Liu, P. Strasser, *Electrochem. Solid State Lett.* **2010**, *13*, B36-B39.
5. C. Dong, X. Yuan, X. Wang, X. Liu, W. Dong, R. Wang, Y. Duan, F. Huang, *J. Mater. Chem. A* **2016**, *4*, 11292–11298.
6. F. Song, X. Hu, Catalysis. *Nat. Commun.* **2014**, *5*, 1–9.
7. K. Liu, C. Zhang, Y. Sun, G. Zhang, X. Shen, F. Zou, H. Zhang, Z. Wu, C. E. Wegener, C. J. Taubert, *ACS Nano* **2018**, *12*, 158–167.
8. S. Hirai, S. Yagi, A. Seno, M. Fujioka, T. Ohno, T. Matsuda, *RSC Adv.* **2016**, *6*, 2019–2023.
9. A. J. Koza, Z. He, S.A. Miller, A. J. Switzer, *Chem. Mater.* **2012**, *24*, 3567–3573.
10. W.T. Kim, A. M. Woo, M. Regis, S. K. Choi, *J. Phys. Chem. Lett.* **2014**, *5*, 2370–2374.
11. R. Subbaraman, D. Tripkovic, C. K., Chang, D. Strmcnik, P. A., Paulikas, P. Hirunsit, M. Chan, J. Greeley, V. Stamenkovic, M. N. Markovic, Nat. *Mater.* **2012**, *11*, 550–557.
12. Z. Lu, W. Xu; W. Zhu, Q. Yang, X. Lei, J. Liu, Y. Li, X. Sun, X. Duan, *Chem. Commun.* **2014**, *50*, 6479–6482.
13. Y. Zhang, B. Cui, C. Zhao, H. Lin, J. Li, *Phys. Chem. Chem. Phys.* **2013**, *15*, 7363–7369.
14. X. Zou, A. Goswami, T. Asefa, *J. Am. Chem. Soc.* **2013**, *135*, 17242–17245.
15. F. Yang, K. Sliozberg, I. Sinev, H. Antoni, A. Bïhr, K. Ollegott, W. Xia, J. Masa, W. Grïnert, R. B. Cuenya, *Chem. Sus. Chem.* **2017**, *10*, 156–165.
16. Z. Lu, L. Qian, Y. Tian, Y. Li, X. Sun, X. Duan, *Chem. Commun.* **2016**, *52*, 908–911.
17. S. Li, Y. Wang, S. Peng, L. Zhang, M. A. Al-Enizi, H. Zhang, X. Sun, G. Zheng, *Energy Mater*. **2016**, *6*, 1501661-1501667.
18. L. S. Candelaria, M. N. Bedford, J. T. Woehl, S. N. Rentz, R. A. Showalter, S. Pylypenko, A. B. Bunker, S. Lee, B. Reinhart, Y. Ren*ACS Catal.* **2017**, *7*, 365–379.
19. M. Gong, Y. Li, H. Wang, Y. Liang, Z. J. Wu, J. Zhou, J. Wang, T. Regier, F. Wei, H. Dai, *J. Am. Chem. Soc.* **2013**, *135*, 8452–8455.
20. Y. Cheng, C. Liu, H. Cheng, P. S. Jiang, *ACS Appl. Mater. Interfaces* **2014**, *6*, 10089–10098.
21. H. Wang, H. Lee, Y. Deng, Z. Lu, P. Hsu, Y. Liu, D. Lin, Y. Cui, *Nat. Commun.* **2015**, *6*, 7261.
22. Y. Liu, H. Wang, D. Lin, C. Liu, P. Hsu, W. Liu, W. Chen, Y. Cui, *Energy Environ. Sci.* **2015**, *8*, 1719–1724.

23. Y. Qiu, L. Xin, W. Li, *Langmuir* **2014**, *30*, 7893–7901.
24. S. Hyun, S. Shanmugam, *ACS Omega* **2018**, 3, 8621-8630.
25. K. W. Gao, Q. J. Chi, B. Z. Wang, H. J. Lin, P. D. Liu, B. J. Zeng, F. J. Yu, L. Wang, M. Y. Chai, B. Dong, *J. Colloid Interface Sci*. **2019**, 537, 11-19.
26. Y. U. Qazi, Z. C. Yuan, N. Ullah, F.Y. Jiang, M. Imran, A. Zeb, J. S. Zhao, R. Javaid, W. A. Xu, *ACS. Appl. Mater. Interfaces*. **2017**, 9, 28627-28634.
27. X. Zheng, X. Song, X. Wang, Z. Zhang, Z. Sun, Y. Guo, *New J. Chem*. 2018, 42, 8346-8350.
28. C. Li, B. Zhang, Y. Li, S. Hao, X. Cao, G. Yang, J. Wu, Y. Huang, *Appl. Catal. B*. **2019**, 244, 56-62.
29. T. Reier, Z. Pawolek, S. Cherevko, M. Bruns, T. Jones, D. Teschner, S. Selve, A. Bergmann, N. H. Nong, R. Schlogl, J.K. Mayrhofer, P. Strasser, *JACS* **2015**, 137, 13031-13040.
30. E. Ozer, I. Sinev, M. A. Mingers, J. Araujo, T. Kropp, M. Mavrikakis, J. J. K. Mayrhofer, R. B. Cuenya, P. Strasser, *Surfaces*, **2018**, 1, 165-186.
31. F. Song, M. M. Busch, B. Lassalle-Kaiser, S. C. Hsu, E. Petkucheva, M. Bensimon, M. H. Chen, C. Corminboeuf, X. Hu, *ACS Cent. Sci*. **2019**, 5, 558-568.
32. F. Godinez-Salomon, L. Albiter, M. S. Alia, S.B. Pivovar, E. L. Camacho-Forero, B.P. Balbuena, R. Mendoza-Cruz, M. J. Arellano-Jimenez, C. P. Rhodes, *ACS Catal*. **2018**, 8, 10498-10520.
33. J. Nai, H. Yin, T. You, L. Zheng, J. Zhang, P. Wang, Z. Jin, Y. Tian, J. Liu, Z. Tang, L. Guo, *Adv. Energy Mater*. **2015**, 5, 1401880.
34. B. Zhang, X. Zheng, O. Voznyy, R. Comin, M. Bajdich, M. Garcia-Melchor, L. Han, J. Xu, M. Liu, L. Zheng, F. P. Garcia de Arquer, C. T. Dinh, F. Fan, M. Yuan, E. Yassitepe, N. Chen, T. Regier, P. Liu, Y. Li, P. De Luna, A. Janmohamed, H. L. Xin, H. Yang, A. Vojvodic, E. H. Sargent, *Science*, **2016**, 352, 333-337.
35. Y. Cheng, S. He, P. J. Veder, R. De Marco, Z. S. Yang, S. P. Jiang, *ChemElectroChem* **2019**, 6, 3478-3487.
36. Y.J. Tang, C.H Liuk, W. Huang, X. L. Wang, L. Z. Dong, S. L. Li, Y. Q. Lan, *Appl. Mater. Interface*. **2017**, 9, 16977-16985.
37. W. K. Gao, J. Q. Chi, Z. B. Wang, J. H. Lin, D. P. Liu, J. B. Zeng, J. F. Yu, L. Wang, Y. M. Chai, B. Dong, *J. Colloid Interface Sci*. **2019**, 537, 11-19.
38. L. Wang, X. Ge, Y. Li, J. Liu, L. Huang, L. Feng, Y. Wang, *J. Mater. Chem. A*. **2017**, 5, 4331-4334.
39. X. Ma, K. Qi, S. Wei, L. Zhang, X. Cui, *J. Alloys Compd*. **2019**, 770, 236-242.
40. F. Wang, G. Chen, X. Liu, F. Chen, H. Wan, L. Ni, N. Zhang, R. Ma, G. Qiu, *ACS Sustainable Chem. Eng*. **2018**, 7, 341-349.
41. J. Wu, L. Lin, F. J Morvan, J. Du, W. Fan, *Inorg. Chem. Front*. **2019**, 6, 2014-2023.
42. C. Zhu, D. Wen, S. Leubner, M. Oschatz, W. Liu, M. Holzschuh, F. Simon, S. Kaskel, A. Eychmuller, *Chem. Commun*. **2015**, 51, 7851-7854.

43. B. Qiu, L. Cai, Y. Wang, Z. Lin, Y. Zuo, M. Wang, Y. Chai, *Adv. Funct. Mater*. **2018**, 28, 1706008.
44. Y. Tan, H. Wang, P. Liu, Y. Shen, C. Cheng, A. Hirata, T. Fujita, Z. Tang, M. Chen, *Energy Environ. Sci*. **2016**, 9, 2257-2261.
45. S. Fu, C. Zhu, J. Song, M. H. Engelhard, X. Li, D. Du, Y. Lin, *ACS Energy Lett*. **2016**, 1, 792-796.

8.7. Supporting Information for Chapter 5

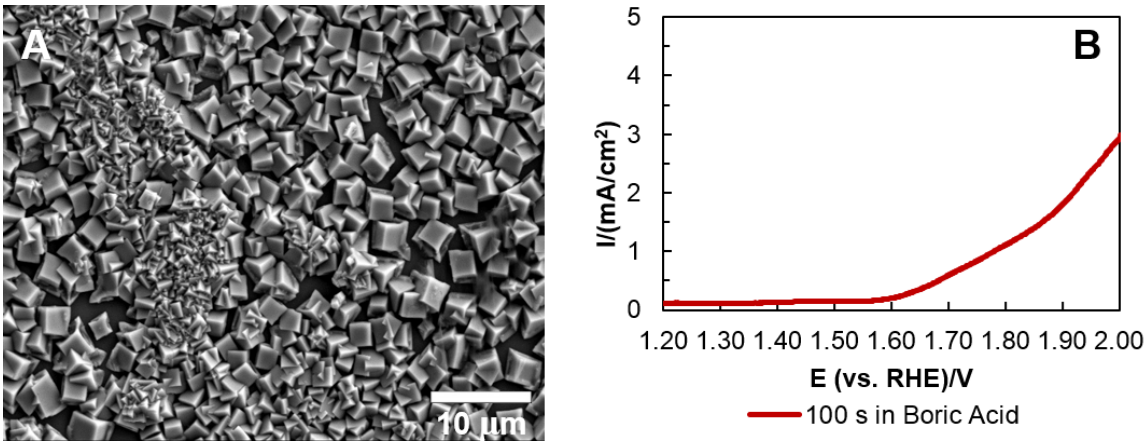

Figure S5.1. SEM images of a Cu_2O on ITO working electrode that has been soaked in 0.4 M boric acid for 100 s (A) and a linear sweep voltammogram of the same electrode in 1 M NaOH at a scan rate of 10 mV/s (B).

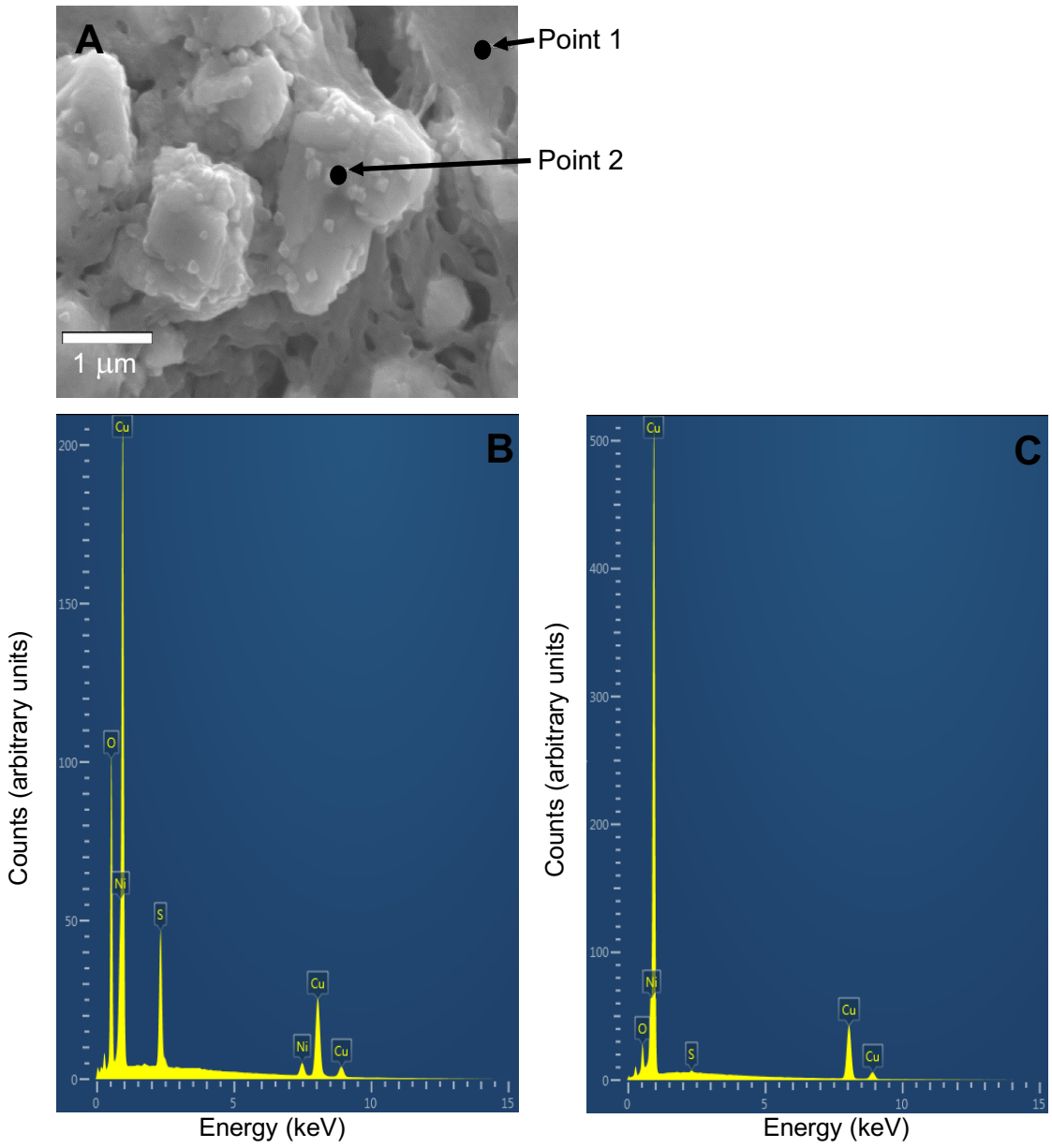

Figure S5.2. SEM image (A) of a Cu_2O on ITO electrode with a Ni overlayer formed using 100 s of Ni electrodeposition and EDS spectra taken at points 1 (B) and 2 (C) of the SEM image.

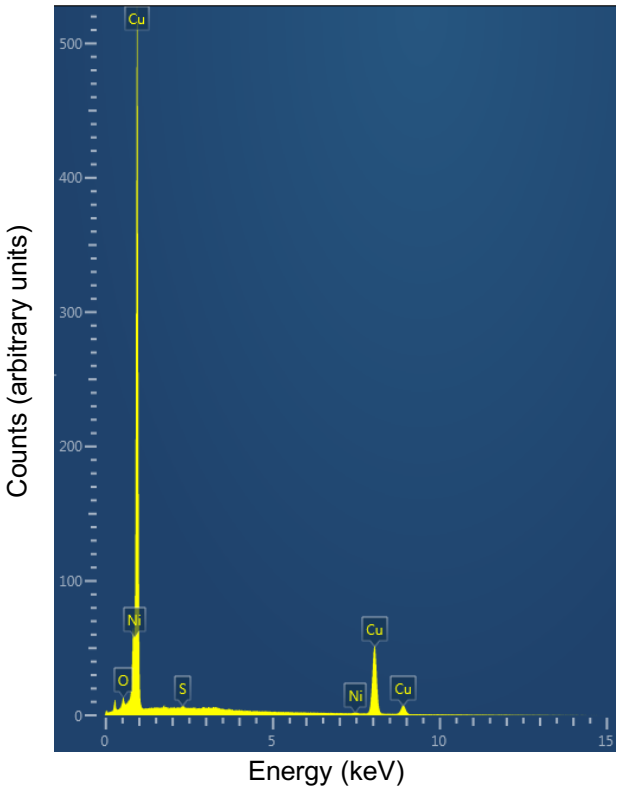

Figure S5.3. EDX spectrum of a Cu_2O on ITO electrode with a Ni overlayer formed using 500 s of Ni electrodeposition. The corresponding SEM image is shown in Figure 5F.

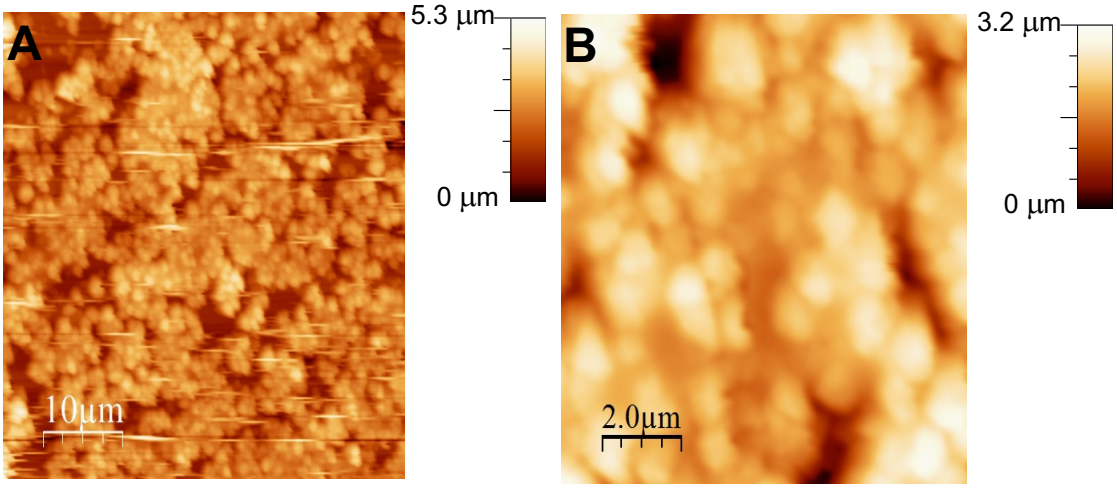

Figure S5.4. AFM images of a Cu_2O on ITO electrode with a Ni overlayer formed using 100 s of Ni electrodeposition.

Catalyst	Electrolyte	Onset E (V_{RHE})	Onset overpotential (V_{RHE} – 1.23 V)	Overpotential (mV) at specific current density	Ref-erence
Precious metal					
Ru_{60}-Co_{40}	0.1 M $HClO_4$	1.41	0.18	-	1
Ru_{70}-Ir_{30}	0.1 M $HClO_4$	1.40	0.27	-	1
RuO_2	0.1 M KOH	1.44	0.21	425 @ 20 mA/cm^2	2
IrO_2	1 M KOH	1.51	0.28	340 @ 10 mA/cm^2	3
Spinel family					
$CoFe_2O_4$ on GCE	0.1 M KOH	1.58	0.35	443 @ 10 mA/cm^2	4
Mn_3O_4 on GCE	1 M KOH	1.68	0.45	>600 @ 3 mA/cm^2	5
Co_3O_4 on Au	1 M KOH	1.56	0.33	400 @ 10 mA/cm^2	6
$Mn_{2.1}Co_{0.9}O_4$	1 M KOH	1.64	0.41	490 @ 3 mA/cm^2	5
$ZnCo_2O_4$ on Pt	1 M KOH (pH 13.8)	1.62	0.39	450 @ 20 mA/cm^2	7
Layer-structure type family					
CoOOH on PtO/AuO	0.1 M KOH/LiOH	1.48	0.25	450 @ 5 mA/cm^2	8

3D Ni-Fe LDH on Ni foam	0.1 M KOH	1.46	0.23	280 @ 30 mA/cm^2	9
Co-Ni LDH on FTO	0.1 M potassium phosphate (pH 7)	1.623	0.393	490 @ 1 mA/cm^2	10
Co-Co LDH	0.1 M potassium phosphate (pH 7)	1.638	0.408	610 @ 1 mA/cm^2	10
Zn-Co LDH on GCE	0.1 M KOH (pH 13)	1.57	0.34	-	11
Co-Fe LDH (1:0.35) on GCE	0.1 M KOH	1.52	0.29	350 @ 10 mA/cm^2	12
Co-Cr LDH (2:1) on GCE	0.1 M KOH	1.47	0.24	340 @ 10 mA/cm^2	2
Ni-Fe-Mn LDH on CFP	1 M KOH	1.43	0.20	289 @ 20 mA/cm^2	13
□□$Ni(OH)_2$ nanoparticle film	0.1 M KOH	1.55	0.32	450 @ 30 mA/cm^2	9
Co-Ni based nanotubes/nanosheets on Cu	1 M KOH	1.50	0.27	280 @ 10 mA/cm^2	14
Exfoliated Ni-Fe nanosheets on GCE	1 M KOH	1.49	0.26	300 @ 10 mA/cm^2	3
Exfoliated Ni-Co nanosheets on GCE	1 M KOH	1.52	0.29	385@ 10 mA/cm^2	3

Exfoliated Co-Co nanosheets on GCE	1 M KOH	1.53	0.30	390 @ 10 mA/cm^2	3
Fe-Ni nanoparticles on GCE	1 M NaOH	1.40	0.17	256 @ 1 mA/cm^2 311 @ 10 mA/cm^2	15
CNTs or carbon fiber supported					
NiFe-LDH/CNT	1 M KOH	1.45	0.22	149 @ 10 mA/cm^2	16
M-CNTs-Arc	1 M KOH	1.48	0.25	152 @ 10 mA/cm^2	17
$NiFeO_x$/CFP	1 M KOH	1.43	0.20	146 @ 10 mA/cm^2	18
20%Ir/C	1 M KOH	1.50	0.27	152 @ 10 mA/cm^2	19
Other					
Fe nanoparticles	1 M NaOH	1.56	0.33	421 @ 1 mA/cm^2	15
Ni nanoparticles	1 M NaOH	1.34	0.11	476 @ 1 mA/cm^2	15
Ni-FeO_x/C (69:31) nanoparticle on carbon black	1 M KOH	1.41	0.18	280 @ 10 mA/cm^2	20
Ir/C catalyst	0.1 M KOH	1.50	0.27	390 @ 30 mA/cm^2	9

Table S5.1. Summary of performance of various OER electrocatalysts reported in the literature arranged by catalyst family.

8.8. References

1. Forgie, R.; Bugosh, G.; Neyerlin, K. C.; Liu, Z.; Strasser, P. Bimetallic Ru Electrocatalysts for the OER and Electrolytic Water Splitting in Acidic Media. *Electrochem. Solid-State Lett.* **2010**, *13*, B36-B39.
2. Dong, C.; Yuan, X.; Wang, X.; Liu, X.; Dong, W.; Wang, R.; Duan, Y.; Huang, F. Rational Design of Cobalt-Chromium Layered Double Hydroxide as a Highly Efficient Electrocatalyst for Water Oxidation. *J. Mater. Chem. A* **2016**, *4*, 11292–11298.
3. Song, F.; Hu, X. Exfoliation of Layered Double Hydroxides for Enhanced Oxygen Evolution Catalysis. *Nat. Commun.* **2014**, *5*, 1–9.
4. Liu, K.; Zhang, C.; Sun, Y.; Zhang, G.; Shen, X.; Zou, F.; Zhang, H.; Wu, Z.; Wegener, E. C.; Taubert, C. J.; et al. High-Performance Transition Metal Phosphide Alloy Catalyst for Oxygen Evolution Reaction. *ACS Nano* **2018**, *12*, 158–167.
5. Hirai, S.; Yagi, S.; Seno, A.; Fujioka, M.; Ohno, T.; Matsuda, T. Enhancement of the Oxygen Evolution Reaction in Mn^{3+}-Based Electrocatalysts: Correlation between Jahn-Teller Distortion and Catalytic Activity. *RSC Adv.* **2016**, *6*, 2019–2023.
6. Koza, J. A.; He, Z.; Miller, A. S.; Switzer, J. A. Electrodeposition of Crystalline Co_3O_4-A Catalyst for the Oxygen Evolution Reaction. *Chem. Mater.* **2012**, *24*, 3567–3573.
7. Kim, T. W.; Woo, M. A.; Regis, M.; Choi, K. S. Electrochemical Synthesis of Spinel Type $ZnCo_2O_4$ Electrodes for Use as Oxygen Evolution Reaction Catalysts. *J. Phys. Chem. Lett.* **2014**, *5*, 2370–2374.
8. Subbaraman, R.; Tripkovic, D.; Chang, K. C.; Strmcnik, D.; Paulikas, A. P.; Hirunsit, P.; Chan, M.; Greeley, J.; Stamenkovic, V.; Markovic, N. M. Trends in Activity for the Water Electrolyser Reactions on 3d M(Ni,Co,Fe,Mn) Hydr(Oxy)Oxide Catalysts. *Nat. Mater.* **2012**, *11*, 550–557.
9. Lu, Z.; Xu, W.; Zhu, W.; Yang, Q.; Lei, X.; Liu, J.; Li, Y.; Sun, X.; Duan, X. Three-Dimensional NiFe Layered Double Hydroxide Film for High-Efficiency Oxygen Evolution Reaction. *Chem. Commun.* **2014**, *50*, 6479–6482.
10. Zhang, Y.; Cui, B.; Zhao, C.; Lin, H.; Li, J. Co-Ni Layered Double Hydroxides for Water Oxidation in Neutral Electrolyte. *Phys. Chem. Chem. Phys.* **2013**, *15*, 7363–7369.
11. Zou, X.; Goswami, A.; Asefa, T. Efficient Noble Metal-Free (Electro)Catalysis of Water and Alcohol Oxidations by Zinc-Cobalt Layered Double Hydroxide. *J. Am. Chem. Soc.* **2013**, *135*, 17242–17245.
12. Yang, F.; Sliozberg, K.; Sinev, I.; Antoni, H.; Bïhr, A.; Ollegott, K.; Xia, W.; Masa, J.; Grïnert, W.; Cuenya, B. R.; et al. Synergistic Effect of Cobalt and Iron in Layered Double Hydroxide Catalysts for the Oxygen Evolution Reaction. *Chem. Sus. Chem.* **2017**, *10*, 156–165.
13. Lu, Z.; Qian, L.; Tian, Y.; Li, Y.; Sun, X.; Duan, X. Ternary NiFeMn Layered Double Hydroxides as Highly-Efficient Oxygen Evolution Catalysts. *Chem. Commun.* **2016**, *52*, 908–911.
14. Li, S.; Wang, Y.; Peng, S.; Zhang, L.; Al-Enizi, A. M. ; Zhang, H.; Sun, X.; Zheng,

G. Co–Ni-Based Nanotubes/Nanosheets as Efficient Water Splitting Electrocatalysts. *Adv. Energy Mater*. **2016**, *6*, 1501661-1501667.

15. Candelaria, S. L.; Bedford, N. M.; Woehl, T. J.; Rentz, N. S.; Showalter, A. R.; Pylypenko, S.; Bunker, B. A.; Lee, S.; Reinhart, B.; Ren, Y.; et al. Multi-Component Fe-Ni Hydroxide Nanocatalyst for Oxygen Evolution and Methanol Oxidation Reactions under Alkaline Conditions. *ACS Catal.* **2017**, *7*, 365–379.
16. Gong, M.; Li, Y.; Wang, H.; Liang, Y.; Wu, J. Z.; Zhou, J.; Wang, J.; Regier, T.; Wei, F.; Dai, H. An Advanced Ni–Fe Layered Double Hydroxide Electrocatalyst for Water Oxidation. *J. Am. Chem. Soc.* **2013**, *135*, 8452–8455.
17. Cheng, Y.; Liu, C.; Cheng, H.; Jiang, S. P. One-Pot Synthesis of Metal–Carbon Nanotubes Network Hybrids as Highly Efficient Catalysts for Oxygen Evolution Reaction of Water Splitting. *ACS Appl. Mater. Interfaces* **2014**, *6*, 10089–10098.
18. Wang, H.; Lee, H.; Deng, Y.; Lu, Z.; Hsu, P.; Liu, Y.; Lin, D.; Cui, Y. Bifunctional Non-Noble Metal Oxide Nanoparticle Electrocatalysts through Lithium-Induced Conversion for Overall Water Splitting. *Nat. Commun.* **2015**, *6*, 7261.
19. Liu, Y.; Wang, H.; Lin, D.; Liu, C.; Hsu, P.; Liu, W.; Chen, W.; Cui, Y. Electrochemical Tuning of Olivine-Type Lithium Transition-Metal Phosphates as Efficient Water Oxidation Catalysts. *Energy Environ. Sci.* **2015**, *8*, 1719–1724.
20. Qiu, Y.; Xin, L.; Li, W. Electrocatalytic Oxygen Evolution over Supported Small Amorphous Ni-Fe Nanoparticles in Alkaline Electrolyte. *Langmuir* **2014**, *30*, 7893–7901.

8.9. Supporting Information for Chapter 6

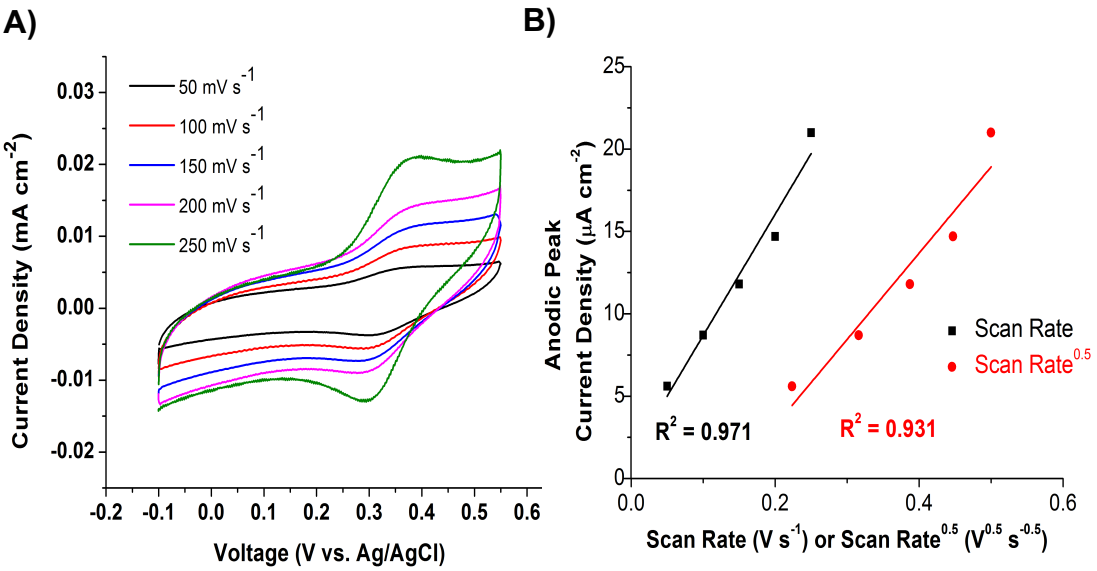

Figure S6.1. Cyclic voltammograms at 50 mV s^{-1} (black), 100 mV s^{-1} (red), 150 mV s^{-1} (blue), 200 mV s^{-1} (pink), and 250 mV s^{-1} (green) in pH 7 buffer of ferrocene attached to SAMs on glassy carbon electrodes using 50 mM $NH_2(CH_2)_2OH$ diluent and 50 mM $NH_2(CH_2)_2NH_2$ (A). Randles-Sevcik analysis of the anodic peak current density (B) as a function of the scan rate (black) and the square root of the scan rate (red). The better linear fit obtained from the data plotted versus the scan rate indicates that the ferrocene is attached to the glassy carbon electrode as opposed to freely diffusing in solution.

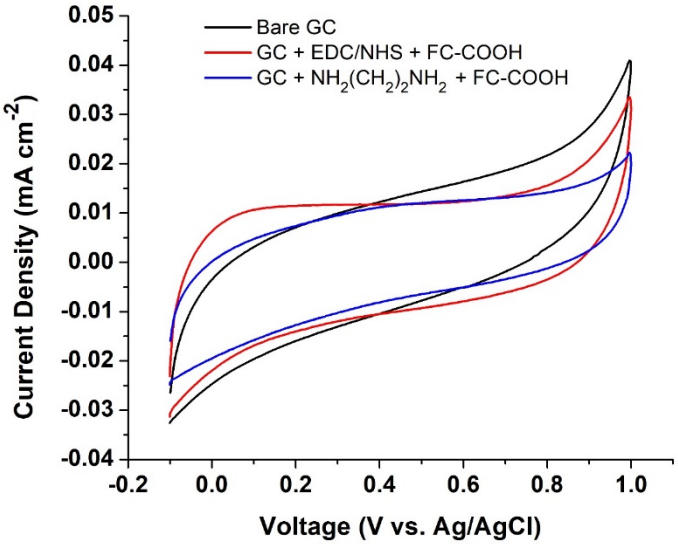

Figure S6.2. Control experiments showing cyclic voltammograms at 300 mV s^{-1} in pH 7 buffer of a bare glassy carbon electrode (black), a glassy carbon electrode immersed in

EDC/NHS/Fc-COOH without SAM (red), and a glassy carbon electrode modified with $NH_2(CH_2)_2NH_2$ without EDC/NHS/Fc-COOH (blue).

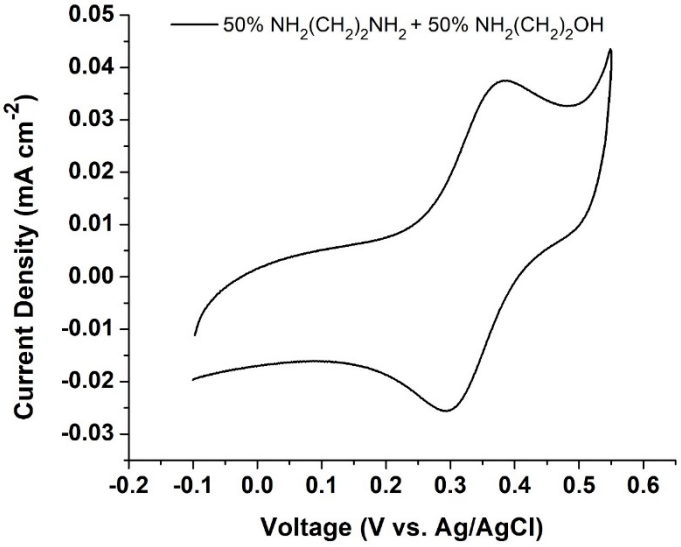

Figure S6.3. Cyclic voltammogram at 300 mV s^{-1} in pH 7 buffer of ferrocene attached to a SAM on a glassy carbon electrode using 50 mM $NH_2(CH_2)_2NH_2$ and 50 mM $NH_2(CH_2)_2OH$ after immersion in EDC/NHS/Fc-COOH for 48 h.

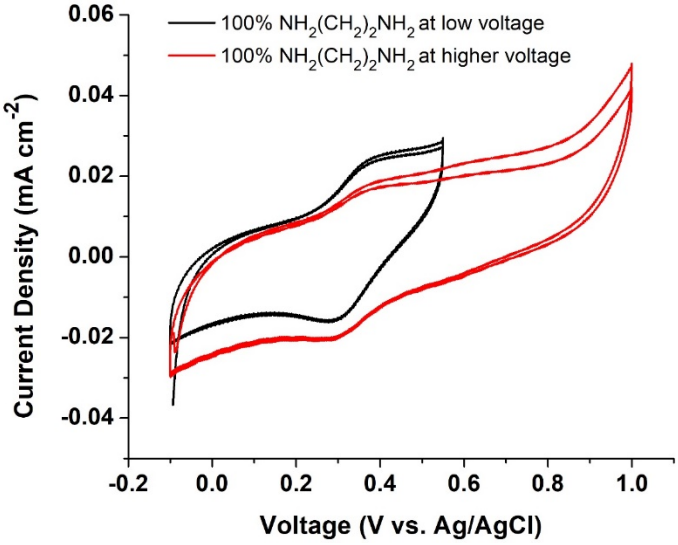

Figure S6.4. Cyclic voltammograms at 250 mV s^{-1} in pH 7 buffer of ferrocene attached to C2 SAMs on glassy carbon electrodes using 100 mM $NH_2(CH_2)_2NH_2$ at different voltage ranges.

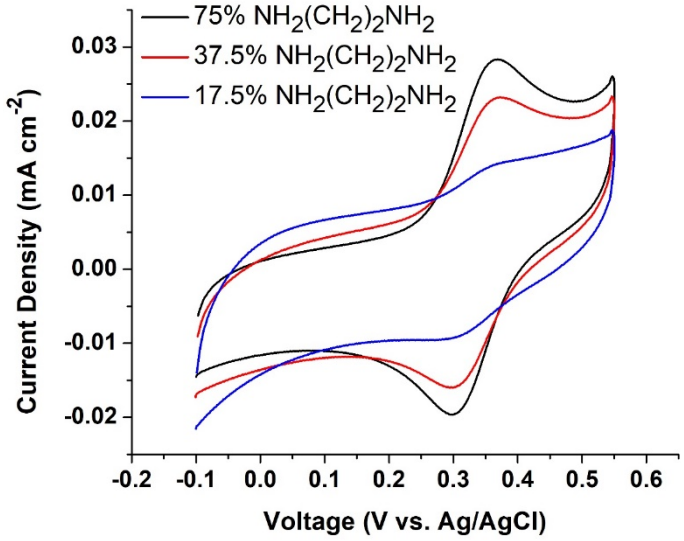

Figure S6.5. Cyclic voltammograms at 300 mV s^{-1} in pH 7 buffer of ferrocene attached to C2 SAMs on glassy carbon electrodes using 100 mM $NH_2(CH_2)_2NH_2$ and $NH_2(CH_2)_2OH$ in various molar ratios.

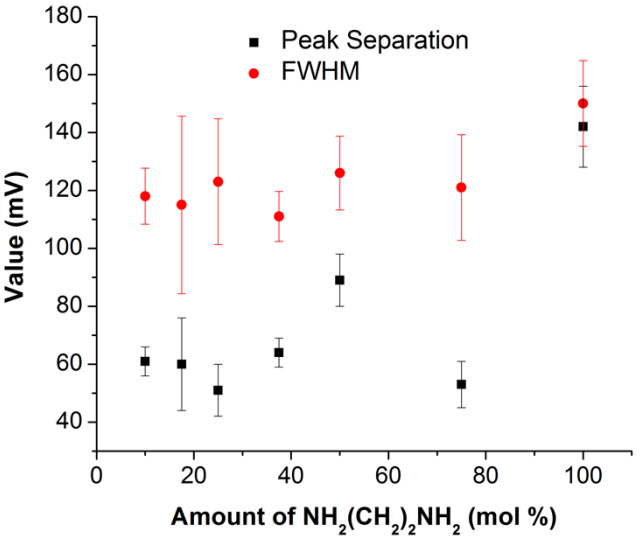

Figure S6.6. Peak separation (black) and full width at half maximum values of the anodic peaks (red) of cyclic voltammograms at 300 mV s^{-1} in pH 7 buffer of ferrocene attached to C2 SAMs on glassy carbon electrodes using 100 mM $NH_2(CH_2)_2NH_2$ and $NH_2(CH_2)_2OH$ in various molar ratios.

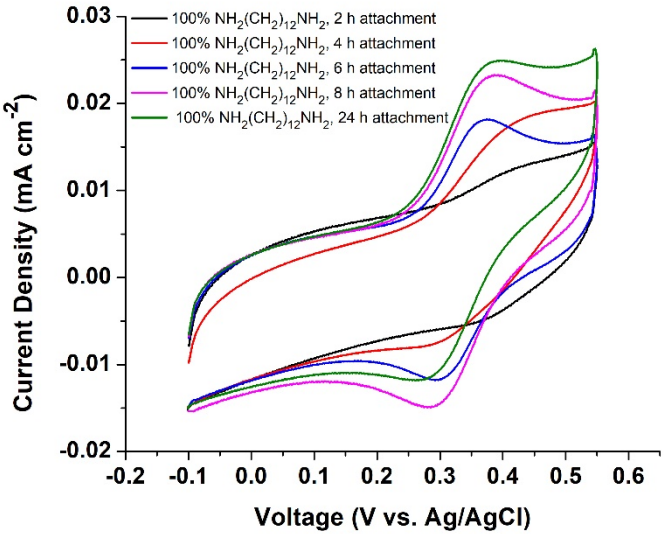

Figure S6.7. Cyclic voltammograms at 300 mV s^{-1} in pH 7 buffer of ferrocene attached to C12 SAMs on glassy carbon electrodes using a 10 mM $NH_2(CH_2)_{12}NH_2$ and 100 mM tetrabutyl ammonium tetrafluoroborate in acetonitrile for different amounts of time.

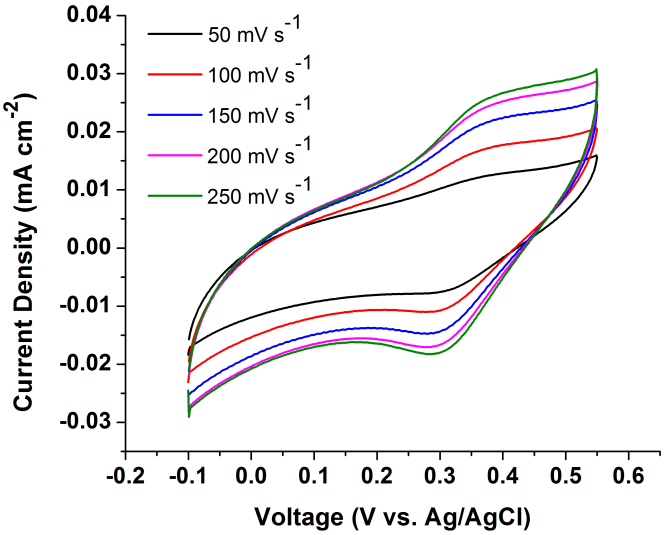

Figure S6.8. Cyclic voltammograms at 50 mV s^{-1} (black), 100 mV s^{-1} (red), 150 mV s^{-1} (blue), 200 mV s^{-1} (pink), and 250 mV s^{-1} (green) in pH 7 buffer of ferrocene attached to SAMs on glassy carbon electrodes using 50 mM $NH_2(CH_2)_2OH$ diluent and 50 mM $NH_2(CH_2)_{12}NH_2$.

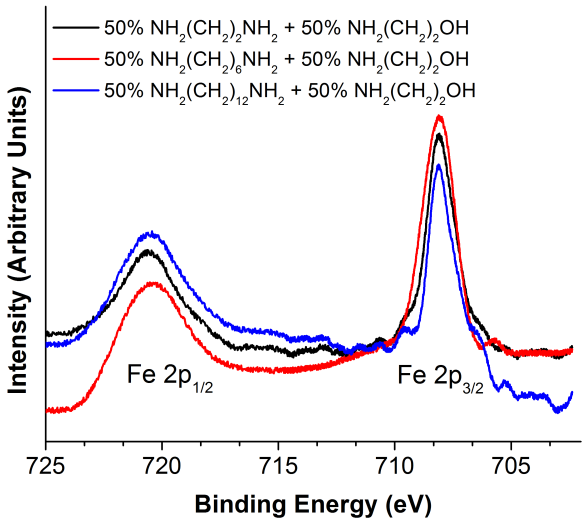

Figure S6.9. XPS Fe 2p spectrum of ferrocene attached to SAMs on glassy carbon electrodes using 50 mM $NH_2(CH_2)_2OH$ diluent and 50 mM $NH_2(CH_2)_2NH_2$ (black), 50 mM $NH_2(CH_2)_6NH_2$ (red), and 50 mM $NH_2(CH_2)_{12}NH_2$ (blue).

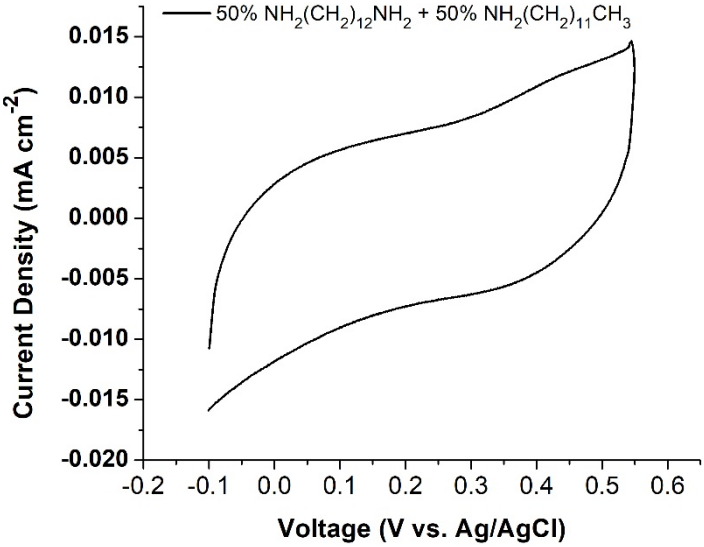

Figure S6.10. Cyclic voltammograms at 300 mV s^{-1} in pH 7 buffer of ferrocene attached to a SAM on a glassy carbon electrode using 5 mM $NH_2(CH_2)_{12}NH_2$ and 5 mM $NH_2(CH_2)_{11}CH_3$ and 100 mM tetrabutyl ammonium tetrafluoroborate in acetonitrile.

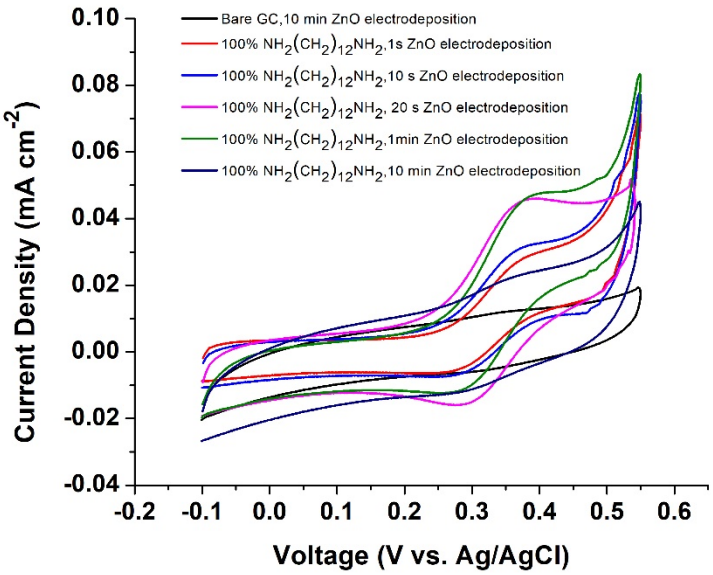

Figure S6.11. Cyclic voltammograms at 300 mV s^{-1} in pH 7 buffer of ferrocene attached to C12 SAMs on glassy carbon electrodes using 10 mM $NH_2(CH_2)_{12}NH_2$ and 100 mM tetrabutyl ammonium tetrafluoroborate in acetonitrile with ZnO electrodeposition for different amounts of time.

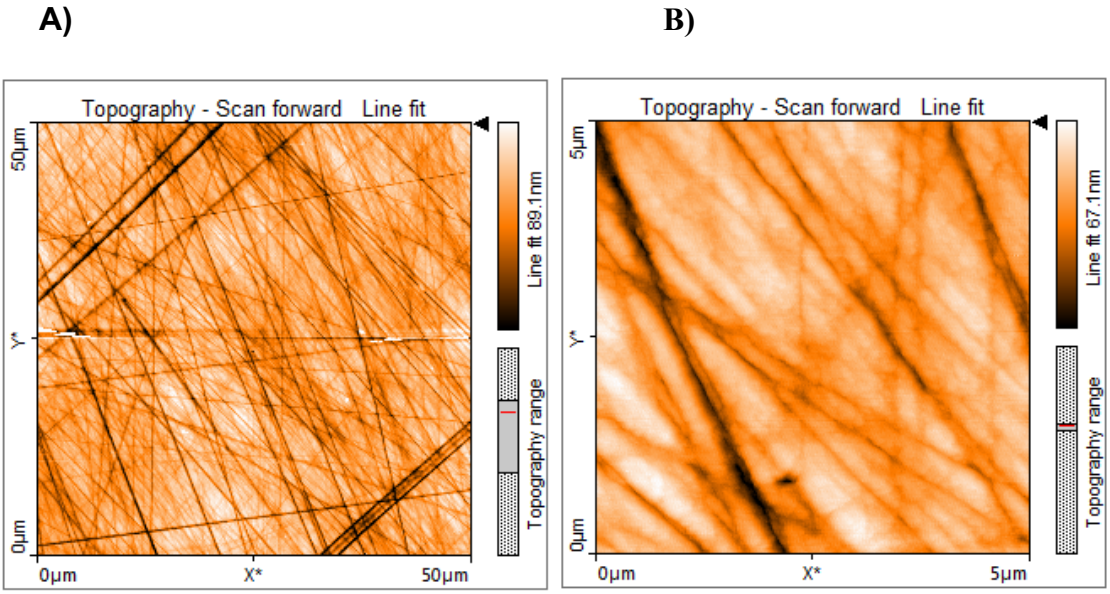

Figure S6.12. Atomic force microscopy images of 50 x 50 µm (A) and 5 x 5 µm (B) of a bare glassy carbon electrode.

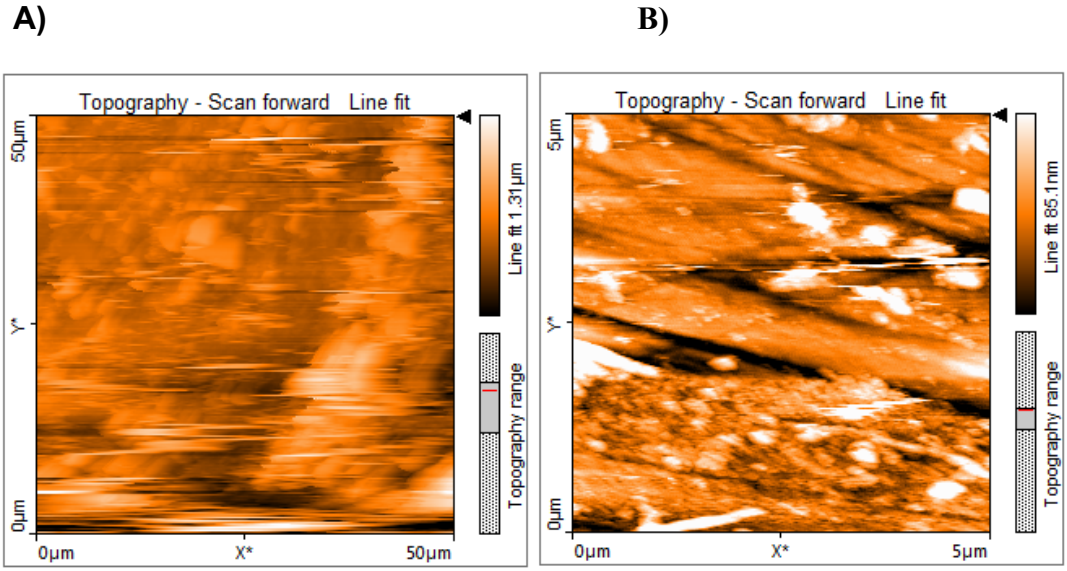

Figure S6.13. Atomic force microscopy images of 50 x 50 µm (A) and 5 x 5 µm (B) of a SAM of ferrocene on a glassy carbon electrode formed using 50 mM $NH_2(CH_2)_{12}NH_2$ and 50 mM $NH_2(CH_2)_2OH$.

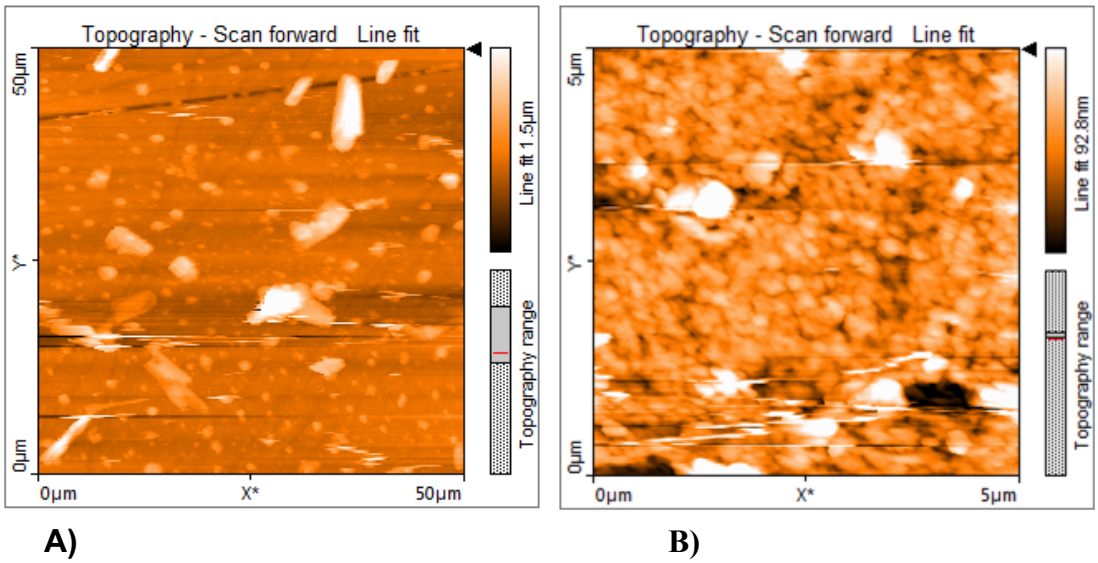

Figure S6.14. Atomic force microscopy images of 50 x 50 µm (A) and 5 x 5 µm (B) of a SAM of ferrocene on a glassy carbon electrode formed using 50 mM $NH_2(CH_2)_{12}NH_2$ and 50 mM $NH_2(CH_2)_2OH$ with ZnO electrodeposition conducted using 20 s of chronoamperometry.

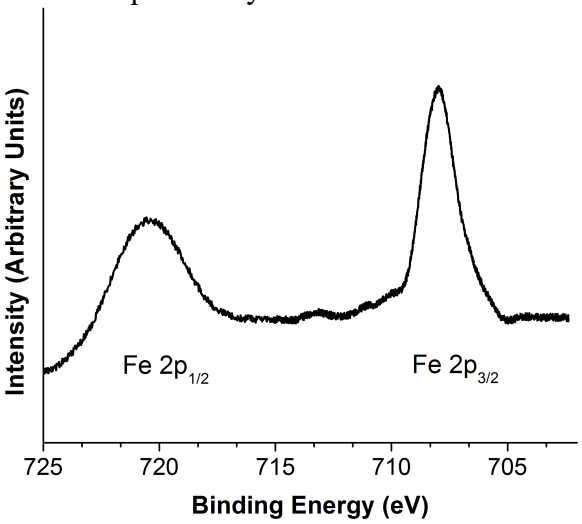

Figure S6.15. XPS Fe 2p spectrum of ferrocene attached to a SAM on a glassy carbon electrode using 50 mM $NH_2(CH_2)_2NH_2$ and 50 mM $NH_2(CH_2)_2OH$ with ZnO electrodeposition conducted using 20 s of chronoamperometry.

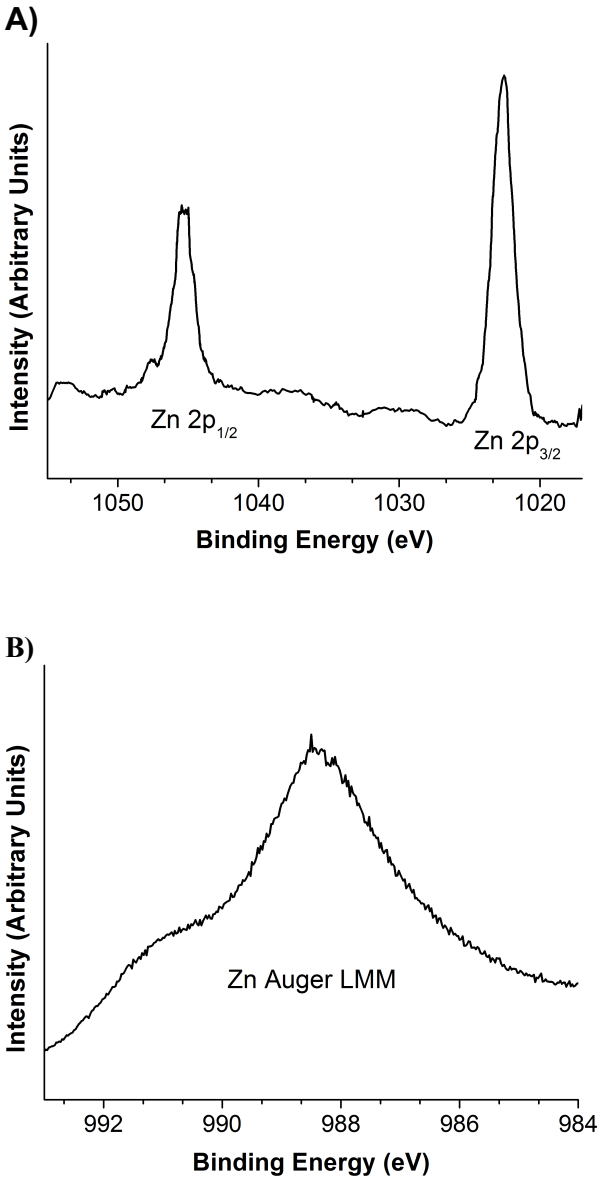

Figure S6.16. XPS Zn 2p spectrum (A) and Auger LMM spectrum (B) of ferrocene attached to a SAM on a glassy carbon electrode using 50 mM $NH_2(CH_2)_2NH_2$ and 50 mM $NH_2(CH_2)_2OH$ with ZnO electrodeposition conducted using 20 s of chronoamperometry.

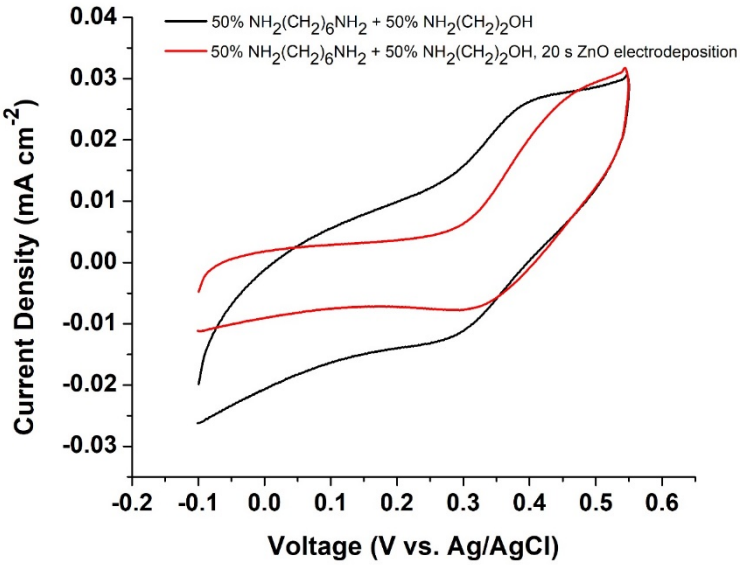

Figure S6.17. Cyclic voltammograms at 300 mV s^{-1} in pH 7 buffer of ferrocene attached to SAMs on glassy carbon electrodes using 50 mM $NH_2(CH_2)_6NH_2$ and 50 mM $NH_2(CH_2)_2OH$ with (red) and without (black) 20 s of ZnO electrodeposition.

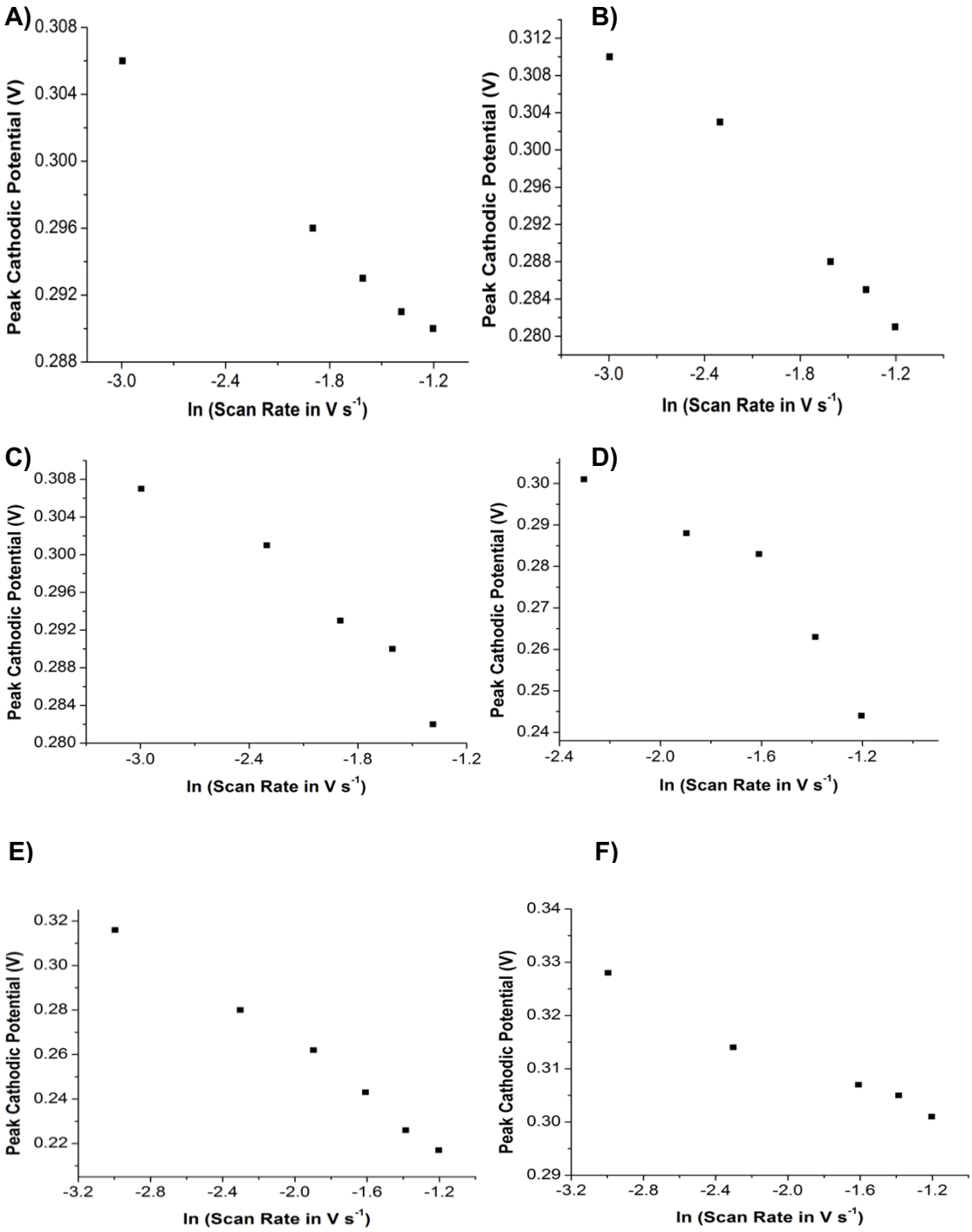

Figure S6.18. Representative Laviron plots of ferrocene SAMs using 50 mM $NH_2(CH_2)_2OH$ and 50 mM of $NH_2(CH_2)_2NH_2$ (A, B), $NH_2(CH_2)_6NH_2$ (C, D), or $NH_2(CH_2)_{12}NH_2$ (E, F) with (B, D, F) and without (A, C, E) 20 s of ZnO electrodeposition.

The cathodic Laviron rates were calculated using the following equation:

$$E_p = E^0 + (RT/\alpha nF) \ln (RTK_{et}/\alpha nF) + (RT/\alpha nF) \ln \nu$$

where E_p is the peak cathodic potential, E^0 is the formal redox potential, T = 298 K is the absolute temperature, R = 8.314 J/K-mol is the universal gas constant, n = 1 is the number of electrons transferred during the redox process, F = 96485 C/mol is Faraday's constant, ν is the scan rate, α is the transfer coefficient, and K_{et} is the cathodic Laviron electron transfer rate.

Figure S18 above plots E_p vs ln ν for the different electrodes. The slopes of the best linear fits of these plots were used to calculate α from the following relationship.

$$\text{slope} = (RT/\alpha nF)$$

Once α is determined, the x-intercepts of the E_p vs ln ν plots were then used to calculate K_{et} from the following relationship.

$$\text{intercept} = E^0 + (RT/\alpha nF) \ln (RTK_{et}/\alpha nF)$$

Rearranging this equation allows K_{et} to be solved.

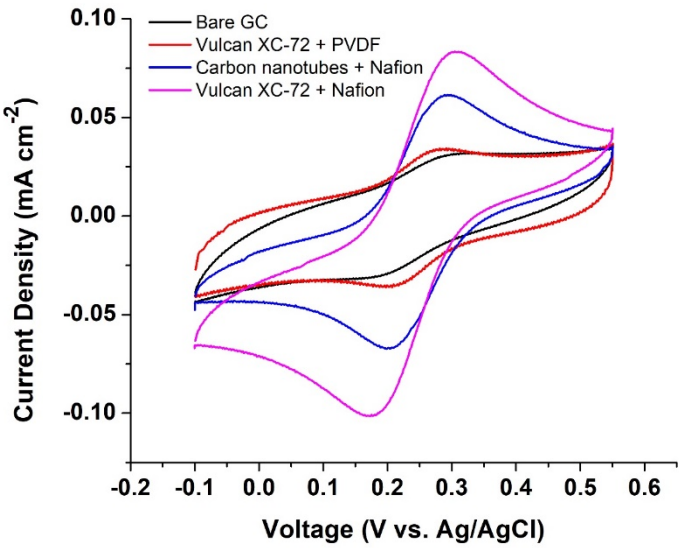

Figure S6.19. Cyclic voltammograms at 300 mV s^{-1} in 1 mM of $K_3Fe(CN)_6$ and 100 mM of KCl on glassy carbon electrodes (black) modified with Vulcan XC-72 and PVDF (red), carbon nanotubes and Nafion (blue), and Vulcan XC-72 and Nafion (pink).